Engineering Dwarfs at Galaxy formation's Edge

Matthew Orkney
Supervisor: Prof. Justin Read
Co-Supervisor: Dr. Michelle Collins

Astrophysics PhD
University of Surrey
June 7, 2021

Abstract

Dwarf galaxies provide unique insights into the cosmology of our Universe. They are at the scale most sensitive to the properties of dark matter and the physical processes governing their evolution. They are, therefore, an ideal laboratory for testing dark matter and galaxy formation models. Furthermore, due to new surveys like SDSS and DES, the number of known dwarf galaxies in the Local Group and beyond continues to grow, with upwards of 50 detected within the Milky Way to date. Due to their close proximity, we can resolve these into their individual stars, providing stellar velocities, metallicities, and star formation histories for hundreds to thousands of members. In this work I present a suite of cosmological simulations designed to probe the low-mass dwarf regime in a Lambda Cold Dark Matter (ΛCDM) cosmology at a mass and spatial resolution of $100\,\mathrm{M}_\odot$ and 3 pc respectively.

First, I present a selection of dwarf galaxies produced as part of the Engineering Dwarfs at Galaxy formation's Edge (EDGE) simulation suite and show they conform to all known observations of dwarf galaxies to date.

Then, I investigate the cusp-core problem in the very smallest dwarf galaxies. I find that even galaxies with $M_* \sim 10^5\,\mathrm{M}_\odot$ can have their inner dark matter density lowered by baryonic processes. This proceeds via two heating mechanisms, the typical 'gas flow' mechanism and a subdominant 'minor merger' mechanism. I also show that cusps can be regrown as a result of dense mergers.

Next, I follow up with more detailed analyses to test whether my simulations can explain the lone star cluster discovered in the ultra faint dwarf galaxy Eridanus II. This includes the development of a large suite of star cluster simulations. I find that none of the $1 \times 10^9 \leqslant M_{200}/\mathrm{M}_\odot \leqslant 2 \times 10^9$ EDGE dwarf simulations run to date produce a core substantial enough to explain the properties of the star cluster in Eridanus II. I discuss possible explanations for this discrepancy and how these can be tested.

Finally, I explore whether the aforementioned dark matter heating has any measurable impact on the halo shape in EDGE simulation. Above $M_{200} \sim 3 \times 10^9\,\mathrm{M}_\odot$, halo shapes become more oblate and aligned with the angular momentum vector of the gas out to 5-10 times the stellar half light radius. This effect owes to gas dissipation rather than cusp-core transformations. Below $M_{200} \sim 2 \times 10^9\,\mathrm{M}_\odot$, haloes retain their typically prolate shapes as in pure dark matter ΛCDM simulations. I predict, therefore, that reionisation fossils should be triaxial, providing a novel means to test cosmological models and the nature of dark matter.

Declaration

I confirm that the submitted work is my own work and that I have clearly identified and fully acknowledged all material that is entitled to be attributed to others (whether published or unpublished) using the referencing system set out in the programme handbook. I agree that the University may submit my work to means of checking this, such as the plagiarism detection service Turnitin® UK. I confirm that I understand that assessed work that has been shown to have been plagiarised will be penalised.[1]

Parts of Chapter 3 and Chapter 4 have been submitted, and passed review, to the Monthly Notices of the Royal Astronomical Society (MNRAS).

---

[1] This declaration is not in my own words but was downloaded from `https://www.surrey.ac.uk/sites/default/files/2018-09/b2-regulations-for-academic-integrity-2018-19.pdf`

Acknowledgements

I would like to make the following acknowledgements to those who have helped me throughout my PhD:

- My supervisors for their amazing guidance, encouragement and support at all stages of my PhD.
- Collaborators Dr. Martin Rey and Dr. Stacy Kim for all of their useful advice and assistance, which has been greatly appreciated.
- The EDGE collaboration and many co-authors for their useful discussion and efforts in shaping my research.
- My examiners Prof. Alyson Brooks and Dr. Denis Erkal for sacrificing their time to review this thesis and conduct my viva examination.
- All those PhD students with whom I have shared office space: Pol Massana Zapata, Michele De Leo, Kate Attard, Sophia Lilleengen, David Hendriks, Dr. Alex Gregory, and Dr. Imran Nasim. Their intelligent discussion and friendship have been critical throughout my PhD.
- The University of Surrey Astrophysics research group, past and present, for their outstanding support. A special thanks to Dr. Maxime Delorme, for his tireless efforts solving my innumerable computer bugs, and Dr. Giovanni Mirouh for his keen observations and moral support.
- My family and friends for keeping me sane (sometimes).
- UKRI Science and Technology Facilities Council (STFC) for their support (grant ST/R505134/1).
- The DiRAC Data Intensive service at Leicester, operated by the University of Leicester IT Services, which forms part of the STFC DiRAC HPC Facility (`www.dirac.ac.uk`). The equipment was funded by BEIS capital funding via STFC capital grants ST/K000373/1 and ST/R002363/1 and STFC DiRAC Operations grant ST/R001014/1. DiRAC is part of the National e-Infrastructure.
- The EUREKA high performance computer facility at the University of Surrey.

Contents

Acronyms

AGB	Asymptotic Giant Branch
AGN	Active Galactic Nuclei
AMR	Adaptive Mesh Refinement
BBN	Big Bang Nucleosynthesis
CC	cusp-core problem
CDM	Cold Dark Matter
CMB	Cosmic Microwave Background
dE	Dwarf Elliptical galaxy
dIrr	Dwarf Irregular galaxy
DM	Dark Matter
DMO	Dark Matter Only
dSph	Dwarf Spheroidal galaxy
EDGE	Engineering Dwarfs at Galaxy formation's Edge
FTT	Fully Threaded Tree
GC	Globular Cluster
GM	Genetic Modification
HPC	High Performance Computing
ICs	Initial Conditions
IGM	Inter-Galactic Medium
IMF	Initial Mass Function
ISM	Inter-Stellar Medium
JWST	James Webb Space Telescope
ΛCDM	Lambda Cold Dark Matter
LG	Local Group
LHC	Large Hadron Collider
Lya forest	Lyman-Alpha forest
MACHO	MAssive Compact Halo Object
MCMC	Markov Chain Monte Carlo
MoND	Modified Newtonian Dynamics
MS	missing satellite problem
MW	Milky Way
PM	Particle Mesh
PoS	planes of satellites problem
PP	Particle Particle
SC	Star Cluster
SKA	Square Kilometer Array
SMHM	Stellar Mass Halo Mass
SNe	Supernovae
TBTF	Too Big To Fail problem
WDM	Warm Dark Matter
WIMP	Weakly Interacting Massive Particle

List of Figures

List of Tables

Introduction

1.1 The ΛCDM cosmological paradigm

The ΛCDM cosmological paradigm provides an excellent fit to large-scale structure in the Universe (See Figure 1.4 and §1.4), and implies that the evolution of the Universe is governed primarily by two mysterious ingredients. These are the accelerating expansion of space driven by a negative pressure (dark energy), and the invisible mass that provides the scaffolding of cosmic structure (Dark Matter (DM)). These phenomena appear to dominate the mass-energy density of the Universe, with dark energy contributing $\sim 69\%$ and DM $\sim 26\%$ (Planck Collaboration et al., 2014) to the total budget. The baryonic matter we are familiar with (gas, planets, stars) constitutes just under 5%. The dark sector remains poorly understood despite its dominance, and the validity of our models will remain uncertain until we know what dark energy and DM really are. In this first section I give a brief overview of ΛCDM.

1.1.1 An expanding Universe

In the early 20th century, observations of distant galaxies revealed a startling prospect: their light was increasingly redshifted, showing that they were receding from us with a velocity proportional to their distance (Lemaître, 1927; Hubble, 1929). Assuming our Earthly perspective is not special or unique, and that the Universe becomes homogeneous and isotropic on large enough scales, the conclusion is that our Universe is rapidly expanding at all points in space.

In the 1920s, Russian cosmologist Alexander Friedmann developed equations to describe the dynamics of this expanding Universe (Friedmann, 1999)[1]:

$$\dot{R}^2 - \frac{8\pi G}{3}\rho R^2 = -kc^2, \tag{1.1}$$

where R is a scaling parameter, $G = 6.67 \times 10^{-11}\,\mathrm{m}^3\,\mathrm{kg}^{-1}\mathrm{s}^{-2}$ is the gravitational constant, ρ is the matter-energy density, c is the speed of light in a vacuum, and k is the curvature parameter that describes the overall geometry of the Universe. If $k = +1$ then the Universe is considered 'closed', meaning it is sufficiently dense to collapse under self-gravity. If $k = -1$ then the Universe is 'open' and lacks the density to constrain its expansion, consigning it to expand indefinitely. Observations which attempt to quantify the total matter-energy content of the Universe favour a 'flat' geometry with $k = 0$ (Bennett et al., 2003; Planck Collaboration et al., 2016b). A flat universe has a critical density ρ_c, which can be evaluated as:

$$\rho_\mathrm{c} = \frac{3H^2}{8\pi G}, \qquad \Omega = \rho/\rho_\mathrm{c}, \tag{1.2}$$

where H is the Hubble parameter defined as $\dot{R}/R$, and Ω is a convenient density parameter. In the ΛCDM model, the dominant components of the density parameter are the vacuum (Ω_Λ), matter (Ω_m) and radiation (Ω_r) components – all of which evolve differently with

---

[1] For simplicity I quote the non-relativistic form of the equation, with the assumption of a constant mean density.

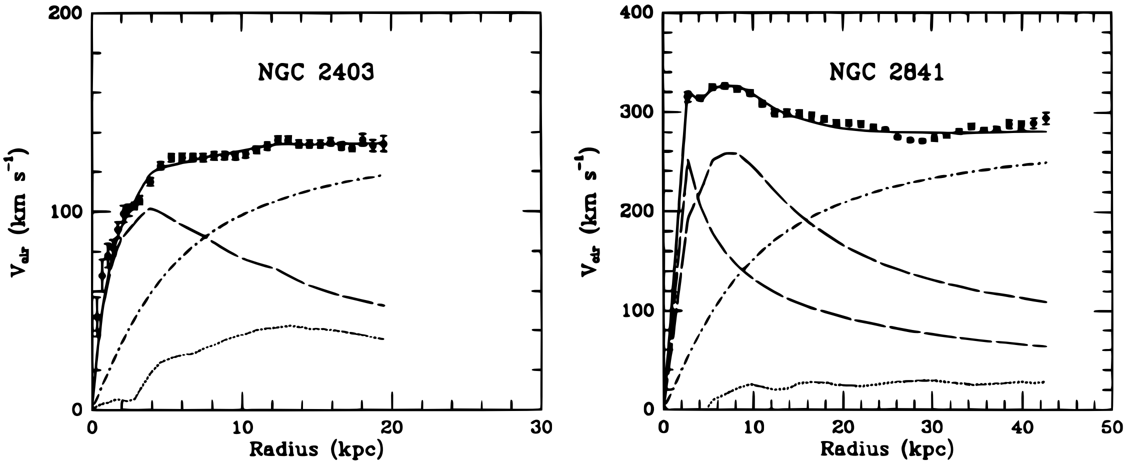

Figure 1.1: Shown here are examples of rotation curves for two galaxies by the authors in Begeman et al. (1991). Black squares indicate the observed rotation curves taken from HI gas, with the solid line representing a total fit based on the prescription in Begeman (1987). This is then partitioned into the luminous component (dashed line), the gaseous component (dotted line), and the dark component (dash-dot line). In both galaxies, the dark component dominates beyond a certain radius.

time. Therefore, one can write:

$$\Omega(t) = \Omega_\Lambda(t) + \Omega_m(t) + \Omega_r(t). \tag{1.3}$$

The evolution of the Universe is then dependent on the contribution of each term. Measurements of the Universal expansion based on using Type Ia Supernovae (SNe) as standard candles and analysis of the Cosmic Microwave Background (CMB) (discussed in Section §1.2.2) find that our Universe today is dominated by the Ω_Λ term, which has been attributed to dark energy. This results in an accelerating expansion of the Universe.

The model assumes Universal homogeneity and isotropy, and is therefore valid only at large scales. The Universe collapses under self-gravity on smaller scales ($\lesssim 70\,$Mpc at the modern day), forming inhomogenous structures that host galaxies and galaxy clusters. A proper modelling of these smaller scales must consider perturbations around the homogeneous isotropic model (Kodama & Sasaki, 1984; Mukhanov et al., 1992 and see §1.4).

1.1.2 Classical evidence for a dark Universe

DM is a mysterious yet pervasive substance which dominates the matter budget of our universe. Historically, the term "dark matter" was first used to refer to baryonic matter that was too faint to see. This included low luminosity stars, gas and/or planets and asteroids (Bessel, 1844; Thomson & Kelvin, 2010; Bertone & Hooper, 2018). It was not until the 20th century that the remarkable nature and pervasiveness of DM in the Universe began to be discovered. We now know that most of the gravitating mass of the Universe is exotic, meaning it does not appear to emit nor absorb light across the electromagnetic spectrum.

The first compelling evidence for this new DM was found by Astronomer Fritz Zwicky in 1933 (Zwicky, 1933, 1937). Whilst trying to infer the mass of the Coma cluster from the relative velocities of its constituent galaxies, Zwicky noticed that these velocities were in excess of those predicted by classical Newtonian dynamics. The measurements suggested a true mass 400× that of the observable, luminous portion of the cluster. Though important in retrospect, Zwicky's claims were initially met with great skepticism in the scientific community.

Similar anomalous masses were later found in the rotation curves of individual galaxies (Babcock, 1939; Volders, 1959; Freeman, 1970) and around the solar neighbourhood (Oort, 1940). Later, astronomer Vera Rubin and collaborators were able to show that these unexpected rotation curves were an ubiquitous property of galaxies in general (Rubin & Ford, 1970; Rubin, 1983; Rubin et al., 1985). These observations suggested that this invisible 'dark' mass pervades the universe on intergalactic *and* sub-galactic scales. The rotation curve due exclusively to the dark component of a galaxy can be estimated with rotation curves based on the visible stellar and gaseous components. This exercise not only identifies the dark mass fraction, but also its distribution within galaxies. These studies reveal that DM does not trace the distribution of stars and gas, but extends to fill an expansive 'halo' (van Albada et al., 1985; Kent, 1986; Begeman et al., 1991), as shown in Figure 1.1.

The broad academic acceptance that DM enjoys today was far from instantaneous, and it was not until the 1970s that the problem of 'missing mass' began to be recognised as a serious issue in astronomy (Freeman, 1970; Ostriker et al., 1974; Faber & Gallagher, 1979). In large part, this was due to the growing need for an exotic matter to solve cosmological challenges (Bertone & Hooper (2018) and see Sections §1.1.1, §1.2.2, §1.2.3). DM has now become a staple in the modelling of galaxies and cosmological structure, and adopted into the current ΛCDM cosmological paradigm.

1.2 Dark Matter: beyond the classical evidence

Many unique approaches have converged upon the problem of 'missing mass', and the evidence in favour of a new exotic form of matter has been accruing steadily over the last century.

1.2.1 Gravitational lensing

Perhaps the most direct observations of DM can be made by exploiting the phenomenon of gravitational lensing. According to Einstein's relativity, light follows geodesics in spacetime. As spacetime is warped by gravity, so are the geodesics that light follows. Matter between an observer and a background light source can therefore act as a lens, and careful analysis of the distortions can infer both the quantity and distribution of that matter.

Gravitational lensing is evaluated in two main forms, strong and weak lensing. In strong lensing, the warping effect is so great that background sources are bent into arcs, rings, or even multiple sources. In contrast, weak lensing is a more minor effect that can often only be resolved through the statistical analysis of multiple background sources. These effects are normally caused by high-mass galaxies and galaxy clusters.

Lensing, both weak and strong, has many applications in detecting and constraining the properties of DM (reviewed in Massey et al., 2010). These include mapping the DM mass profiles of galaxies and galaxy clusters (Geiger & Schneider, 1998; Hoekstra et al., 2004; Limousin et al., 2005; Nightingale et al., 2019) and the detection of DM substructure (Vegetti et al., 2014; Hezaveh et al., 2016; Gilman et al., 2020; Hsueh et al., 2020).

Gravitational lensing can also help distinguish between different types of DM (condensed baryons, alternative gravity, exotic particles, which are all discussed further in

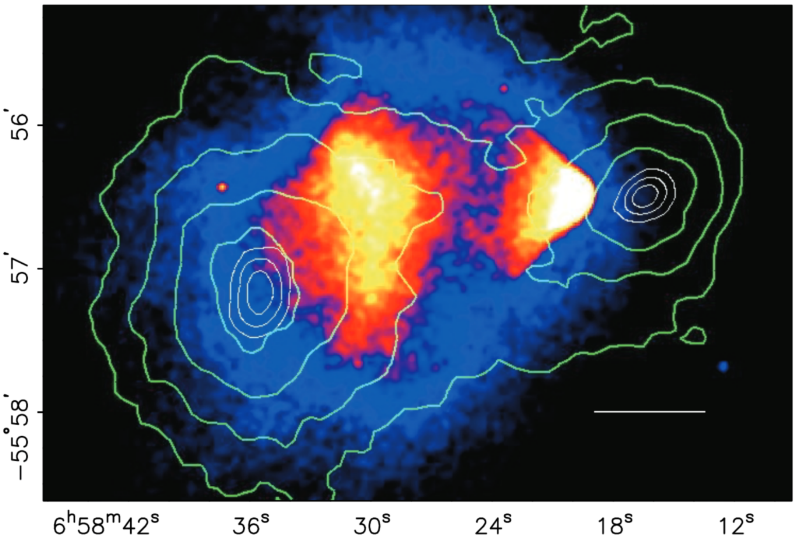

Figure 1.2: Chandra image of the Bullet Cluster as in Clowe et al. (2006), showing a colour-relief of the X-ray emitting plasma surrounding the cluster. The green contours indicate the gravitational mass reconstruction from weak-lensing observations. The thin white bar in the lower-right corner marks 200 kpc.

Section §1.3). Observations of the Bullet Cluster, a pair of colliding galaxy clusters in the constellation of Carina, is a critical example (Clowe et al., 2006). According to velocity measurements, the cores of the clusters should have passed through each other around 100 Myr ago (Barrena et al., 2002). The hot plasma in these clusters makes up the majority of the luminous mass within the system, and has become shocked as the clusters have sailed through one another. Whilst the gas content has slowed due to ram pressure (defined in §1.6.2), the effectively collisionless stellar component of the cluster has continued unimpeded. This has resulted in a segregation between the dominant gaseous component and the stars. As is shown in figure 1.2, the mass inferred from gravitational lensing traces the stellar component of the clusters, and not the X-ray observations of the hot plasma. This suggests the majority of the cluster mass is in the form of a collisionless and exotic DM. Many similar cluster collisions have now been reported, with a range of collision severity that places further limits on the self interaction cross-section of DM (summarised in Harvey et al., 2015).

1.2.2 The Cosmic Microwave Background

The CMB is a near-isotropic microwave signal discovered by chance in 1965 (Penzias & Wilson, 1965; Dicke et al., 1965). It is near perfectly described by a black body spectrum at a temperature of $\sim 2.725\,\mathrm{K}$ (Fixsen, 2009).

The origin of this signal was cause for much controversy within the scientific community and beyond, with proposed solutions including a 'Big Bang' scenario or scattered starlight from distant galaxies in a 'steady-state' model (Bondi & Gold, 1948; Hoyle, 1948). Ultimately, the high uniformity and low polarisation of the CMB favoured the Big Bang model.

In Big Bang cosmology, the Universe was initially hot and dense. At this high temperature and pressure, baryons and photons were coupled in a baryon-photon fluid. This fluid was not perfectly uniform, but contained density perturbations inherited from initial quantum fluctuations. As these dense regions developed, the radiation pressure increased

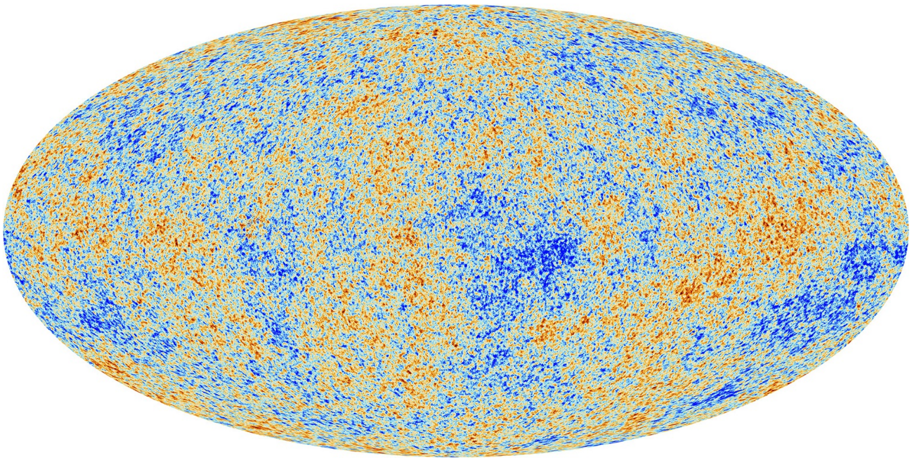

Figure 1.3: Image of the Cosmic Microwave Background signal, as observed by the Planck space telescope (Credit: ESA/Planck collaboration 2018). Colours correspond to under- and over-densities in the temperature, which vary by only ±200 microkelvin. These correlate with the density fluctuations of the Universe at the time of cosmic recombination, which seeded the future growth of structure.

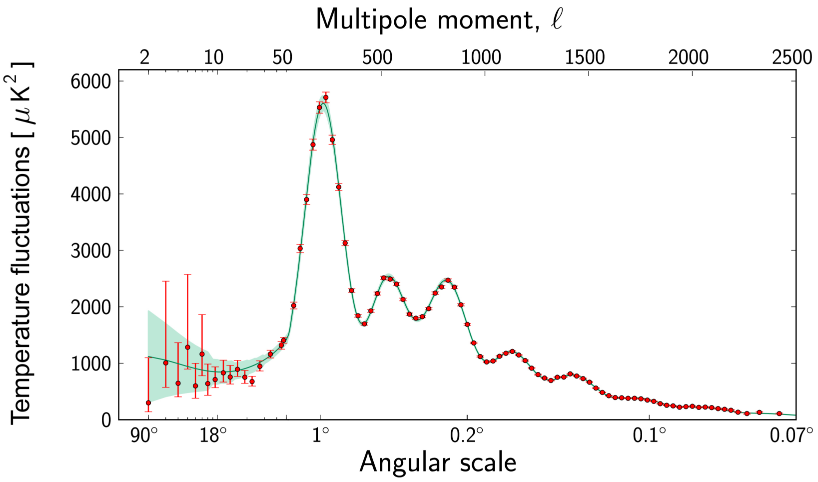

Figure 1.4: A plot of the temperature variations in the CMB with angular scale, known as the power spectrum. Plotted in red are measurements from Planck (Planck Collaboration et al., 2014). The power spectrum is most uncertain at large angular scales because the observable Universe has a limited number of large-scale modes. In green are best fit scenarios for the ΛCDM paradigm, which are generally in excellent agreement with the data points.

and pushed back again, causing the propagation of acoustic waves within the fluid. The Universe cooled as it expanded, and the baryon-photon fluid began to decouple once the universal temperature approached 3000 K (Hinshaw et al., 2009). Electrons and protons were free to bind together to form neutral hydrogen in an event termed 'recombination', which allowed photons to travel unimpeded, turning the universe transparent. This flood of photons, roughly 380,000 years after the Big Bang, manifests as the CMB signal.

Although the CMB is near isotropic, slight anisotropies are present at the 1×10^{-5} K level (Smoot et al., 1992; White et al., 1999), which I show in Figure 1.3. The exact form of these perturbations is typically represented as a matter-power spectrum, as in Figure 1.4. This quantifies the temperature anisotropies in terms of their angular scale on the sky, and shows a distinctive fingerprint pattern that is well fit by a ΛCDM cosmology.

The growth of cosmological structure is seeded by these initial fluctuations, and crucially there are unique predictions for a Universe with and without DM. In a DM-free Universe, the acoustic oscillations resulting from the coupled baryon-photon fluid imprint a strong wave-like signature on the matter-power spectrum (see Dodelson, 2011; Pardo & Spergel, 2020). Conversely, an exotic DM remains uncoupled to the acoustic fluid. When baryons decouple from photons during recombination, they fall into the framework provided by DM and the acoustic signatures are damped. Observations of the CMB strongly favour the damped signature scenario (Blake & Glazebrook, 2003; Eisenstein et al., 2005; Dawson et al., 2013; Planck Collaboration et al., 2014), supporting the existence of a physical DM (though see Section §1.3.2).

1.2.3 Big Bang Nucleosynthesis

The extreme early temperatures and pressures provided by the Big Bang model facilitate the synthesis of light elements through neutron capture, namely Hydrogen and Helium with trace abundances of heavier elements. This formation mechanism was originally postulated as the origin of all the elements (Alpher et al., 1948), but subsequent research showed that islands of instability obstructed the production of the heavier elements. The full roster of elements would later be explained through nucleosynthesis processes, both within stars and during SNe explosions (Cameron, 1955; Burbidge et al., 1957).

Big Bang Nucleosynthesis (BBN) refers to the study of how the first nuclei (anything heavier than the singular proton) came into being during the first few minutes after the Big Bang, a time when the universe was dominated by radiation. BBN is based upon the physics of the Standard Model (Wagoner et al., 1967), and can be used to ascertain the primordial abundances of various light elements, facilitating comparison with observational data (Schramm & Turner, 1998; Steigman, 2007, and references therein). These comparisons are in excellent agreement, and BBN has become a reliable probe of the early Universe (see Schramm & Turner, 1998; Iocco et al., 2009).

A crucial parameter within BBN is the baryon to photon number density η. From this, the baryon number density can be found by combining η with estimates of the photon number density from the CMB. This finds a density $\Omega_{\mathrm{baryonic}} \approx 0.044$, which falls well short of the total mass density $\Omega_{\mathrm{m}} \approx 0.27$ from observations of galaxy clusters (ch.29 Carroll & Ostlie, 2006). Therefore, there is a massive portion of Universal matter required to complete the Friedmann equation (Equation 1.1) which cannot be explained by BBN, and is therefore not baryonic in nature. These investigations reveal the startling prospect that the matter content of the universe is primarily dark, with a ratio of about 5:1 in favor of DM (Dunkley et al., 2009).

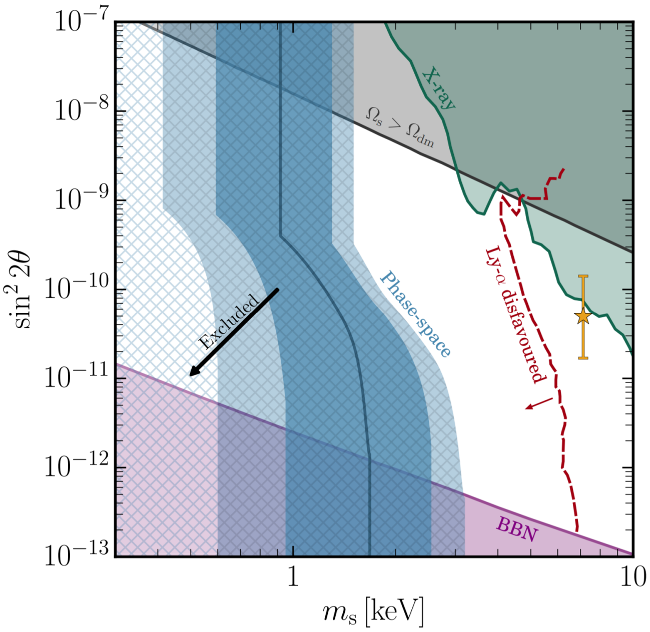

Figure 1.5: Bounds on resonantly produced sterile neutrinos. The blue, hatched area is the phase-space constraint based on Gaussian coarse-graining. The dark blue line indicates the central value of the bound, below which masses are excluded (as indicated by the arrow). The dark (light) blue regions are the $\pm1\sigma(\pm2\sigma)$ confidence intervals. The purple region represents the BBN constraint on the primordial lepton asymmetry, see Sec. 4.2.2 of Alvey et al. (2021) for details. The black line depicts where sterile neutrinos are non-resonantly created and above which the dark matter is overproduced. Complementary constraints from X-ray observations (Boyarsky et al., 2019) and indicative sensitivity of the Lyman-Alpha forest method (Baur et al., 2017) are also included, see Sec. 5.2 of Alvey et al. (2021) for comments. The orange star with error bars denotes the sterile neutrino interpretation of the tentative signal recently observed in X-ray data (Bulbul et al., 2014; Boyarsky et al., 2014). Figure and caption credit to (Alvey et al., 2021).

1.2.4 The Lyman-Alpha forest

As light emitted from distant sources travels through space, it is intercepted by clouds of hydrogen gas. These impart a series of absorption lines from the Lyman-Alpha electron transition in neutral hydrogen, stratified by the cosmological redshift of each cloud. The resulting absorption lines are known as the Lyman-Alpha forest (Lya forest) (reviewed in Meiksin, 2009), so called due to their visual appearance, and were originally discovered in observations of distant quasars by astronomer Roger Lynds in the 1970s (Lynds, 1971).

The Lya forest is useful as a probe of the Inter-Galactic Medium (IGM), and can be used to determine the large-scale structure of gas in the Universe. Among its many applications, the Lya forest is sensitive to the nature of DM. This is because the growth of cosmological structure depends on the properties of DM, and these differences are reflected on the density and size of intergalactic gas clouds. As an example, the authors in Iršič et al. (2017); Murgia et al. (2017, 2018) use the Lya forest to constrain a thermal relic Warm Dark Matter (WDM) particle to a lower limit of 3.5, 3.6 and 2.2 keV respectively.

The Lya forest has a small-scale cutoff in its flux power spectrum below $\sim 30\,\mathrm{km\,s^{-1}}$, implying some lower limit in the formation of small-scale gas clouds. Whilst ΛCDM is able to reproduce the Lya forest to first order (Hernquist et al., 1996), this cutoff can be interpreted as evidence for warmer DM models[2], which would act to delay the onset of structure formation in the early Universe (Boyarsky et al., 2009a). However, the Lya forest is only sensitive to neutral hydrogen, and as such there is a degeneracy between structure formation and the thermal history of the Universe. Increasing the formation of structure provides more potential regions for Lyman-Alpha absorption, but also increases the prevalence of ionising sources. Proper consideration of this degeneracy for reasonable thermal histories in a ΛCDM Universe weaken the constraining power of the Lya forest (Garzilli et al., 2021).

In Figure 1.5 I show parameter-space constraints for sterile neutrino DM as in Alvey et al. (2021). A red dashed line indicates the region prohibited by analysis of the Lya forest.

1.3 What is Dark Matter?

There are three likely interpretations of the DM problem: either there is a huge undiscovered bulk of matter within the Universe, our understanding of gravity is fundamentally flawed on large scales, or a combination of the two. These possible avenues have been explored over the last few decades, but none have proven conclusive so far.

1.3.1 A baryonic solution

Before moving on to more exotic solutions, it is worthwhile reviewing the possibility that non-luminous baryonic matter can solve the missing mass problem.

Both gas and dust are largely ruled out because their presence can be inferred from absorption or re-emission of light. Whilst a proportion of missing mass could be explained by yet undetected gases (Nicastro et al., 2018), it would not be enough to explain the classical evidence for missing mass. Other sources of dark baryons include brown dwarfs, rogue planets, neutron stars, black holes, or even macroscopic baryonic clumps (Witten, 1984; Lynn et al., 1990). At typical galactic densities, these objects would behave as though they were collisionless even though their constituent baryons are not.

Compact baryonic object DM models are known as MAssive Compact Halo Object (MACHO) models, which propose that galactic haloes are populated by many non-luminous baryonic objects that inflate the overall gravitational mass whilst preserving the observed luminosity. The high density of MACHOs means they could be detected indirectly through gravitational micro-lensing observations (Alcock et al., 1997). Surveys specifically designed to hunt for MACHOs in the Magellanic clouds and galactic halo find the detection of such objects falls short of the number required to fill the proposed DM budget (Alcock et al., 1996, 1998; Tisserand et al., 2007). Tackling the problem from a different perspective, the increased dynamical heating from MACHOs has implications on the evolution of wide stellar binaries and compact stellar systems, which are not supported by observational constraints (Yoo et al., 2004; Brandt, 2016). However, these surveys and kinematic arguments are only sensitive to a particular mass range – and MACHOs below $\sim 1\,\mathrm{M}_\odot$ could easily escape detection.

Whilst many MACHO models could solve the missing mass problem, they struggle to acknowledge constraints from the CMB and BBN seen in §1.2.2, §1.2.3. Figure 1.6 shows that observations of galaxy clusters reveal a baryonic mass fraction that approaches that derived from the CMB. This strongly suggests that the baryonic mass fraction from the

---

[2] It could also be caused by an especially high temperature and pressure in the IGM. Arguments for and against are discussed in Garzilli et al. (2017).

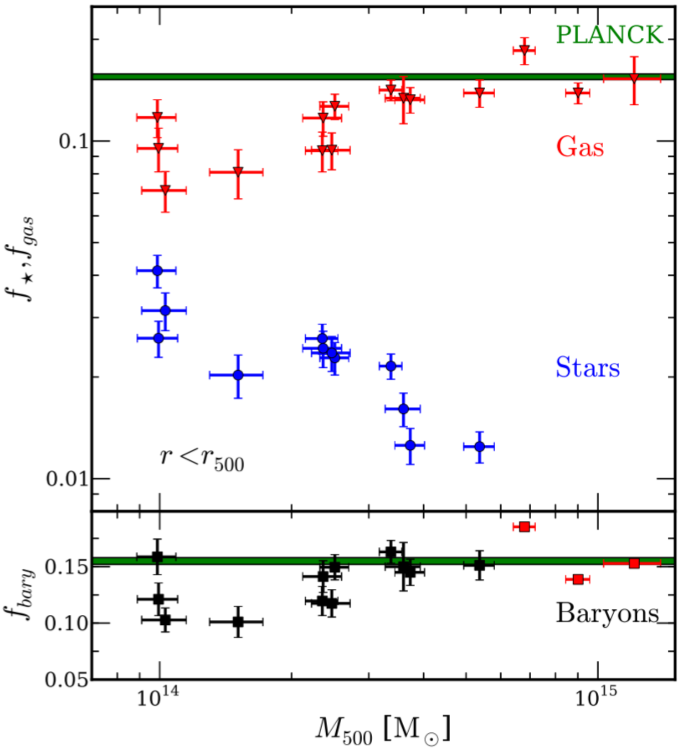

Figure 1.6: Star, gas and baryon fractions as a function of halo mass for twelve galaxy clusters in Gonzalez et al. (2013) and three additional higher mass clusters from Vikhlinin et al. (2006) (which lack stellar fractions). This shows that for clusters of increasingly high mass, for which the IGM is more powerfully illuminated and therefore more completely appraised by X-ray observations, the baryon fraction is in extremely good agreement with measurements based on the CMB from Planck Collaboration et al. (2014). Figure credit to Gonzalez et al. (2013).

CMB is an accurate representation of reality, and that baryonic explanations cannot solve the missing mass problem in isolation.

1.3.2 Alternative gravity

The Newtonian description of gravity is successful at describing our everyday experience. Einstein's general relativity expands this success to the case of extremely strong gravitational fields and scenarios where extreme accuracy is requisite. However, the nature of gravity in the extremely low acceleration regime (the weak-field limit) is much more difficult to measure. This is the gravitational scale that galactic systems operate on.

Modified Newtonian Dynamics (MoND) (Milgrom, 1983) (see Famaey & McGaugh 2012 and Milgrom 2020 for a review) modifies Newtonian gravity in a way that reproduces the phenomena commonly attributed to DM. The model introduces an acceleration constant into the gravitational force formula:

$$m_g\mathbf{a} = \mathbf{F} \rightarrow m_{\rm g}\mu(\frac{a}{a_0})\mathbf{a} = \mathbf{F}, \tag{1.4}$$

with $\mu(x \gg 1) \approx 1$ and $\mu(x \ll 1) \approx x$, where $x = a/a_0$. Here, $m_{\rm g}$ is the gravitational mass of a body and $a_0 \simeq 10^{-10}\,{\rm ms}^{-2}$ is a new fundamental constant termed the 'acceleration constant'. This constant boosts acceleration by a/a_0 in the weak-field regime where $a \ll$

a_0. Newtonian dynamics are restored for accelerations much greater than a_0. By design, MoND is successful in predicting the rotational velocities of galaxies over a range of mass scales.

Alternative gravity, by necessity, applies to all gravitating systems proportionally. Matter based DM schemes do not have this limitation because there are scenarios that might leave systems with more or less than their fair share of DM. Recent observations of possible DM-poor ultra-diffuse galaxies would prove difficult to explain (van Dokkum et al., 2018, 2019)[3], with simulations predicting their formation as a result of tidal stripping (Jing et al., 2019; Haslbauer et al., 2019; Tremmel et al., 2020) and/or major mergers (Wright et al., 2021). The authors in Islam & Dutta (2019) explore different alternative gravity schemes with respect to these galaxies, but find that all schemes agree with the observations to within a 2σ uncertainty. MoND also suffers at reproducing the stellar velocity dispersion in the outskirts of Globular Cluster (GC)s (Ibata et al., 2011), systems which are not expected to contain significant amounts of DM.

Whilst alternative gravity poses a solution to the missing mass problem, and avoids the need for exotic forms of matter, it has been less successful at explaining a variety of observations. Early attempts to embed MoND in a theory that includes Universal expansion have failed to explain the form of the power spectrum measured from the CMB (TeVeS Slosar et al., 2005; Dodelson, 2011; Pardo & Spergel, 2020). A more recent TeVeS-like theory introduces additional parameters that fulfill the role of DM on linear scales whilst transitioning to MoND in the weak-field limit (Skordis & Zlosnik, 2020), though it remains to be tested at the scale of galaxy clusters. This is a crucial scale for MoND, with the authors in Natarajan & Zhao (2008) using gravitational lensing to show that MoND-like theories are unable to sufficiently boost the gravity in galaxy clusters. Tensions remain even on the scales where MoND has typically performed best, such as in dwarf galaxies (Angus et al., 2014; Read et al., 2019a).

With the addition of enough new parameters, an alternative gravity could be designed to solve any challenge thrown at it. However, as the solutions grow more complex it begs the question as to what advantage it holds over the traditional DM approach.

1.3.3 Dark particles

The standard model of particle physics has seen growing success over the course of the 20th century, with the successful discovery of all the originally predicted fundamental particles. There remain many plausible extensions to the standard model, and a natural line of enquiry is whether DM could be explained by a ‘dark particle’. Such a particle would need to have a minimal non-gravitational interaction on megaparsec scales (Gilman et al., 2019), negligible interaction through the electromagnetic force, lifetimes exceeding the age of the Universe, and relic densities comparable to predictions from the CMB. The dynamical temperature of DM is yet another constraint, with hot DM disfavoured. Nevertheless, there is still room for warmer candidates due to the difficulty constraining smaller scales (See Figure 1.7).

This idea is especially compelling because ‘dark particles’ have already been discovered in Neutrinos. Other candidates include particles outside the standard model whose detection may lie beyond the capabilities of facilities such as the Large Hadron Collider (LHC). Of course, there is no special reason why there must be only one candidate, and the dark sector may be populated by a zoo of different particles. A complete review can be found

---

[3] The determination of the mass-light ratio and accuracy of the distance measurements to these objects is controversial and can change the perceived DM content to within normal ranges (Martin et al., 2018; Blakeslee & Cantiello, 2018; Laporte et al., 2019)

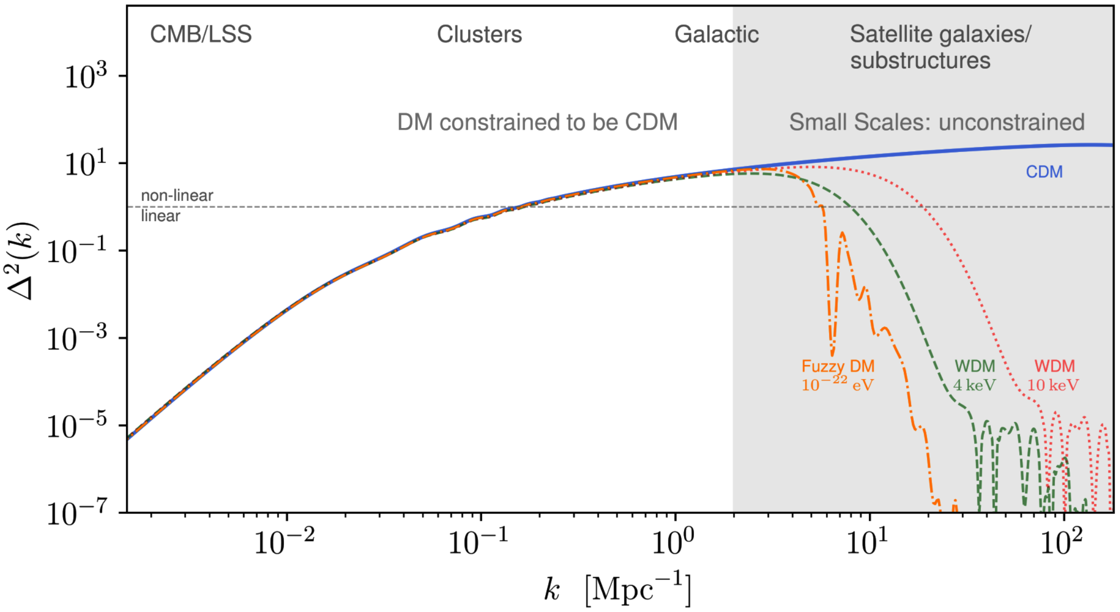

Figure 1.7: This plot shows the dimensionless power spectrum (see Section §1.2.2) as a function of the wavenumber k. The solid blue line represents ΛCDM, the dotted red line represents WDM with a particle mass of 10 keV, the dashed green line represents WDM with a particle mass of 4 keV, and the dot-dashed orange line represents an ultralight DM of particle mass 10^{-22} eV. The text along the upper edge indicates the corresponding physical scales, where the smallest scales are where galaxies reside and are therefore impacted by galaxy formation physics. All DM schemes are indistinguishable at large scales, but make unique predictions at galactic scales. This highlights the importance of understanding galaxy formation. Figure credit to (Kuhlen et al., 2012; Ferreira, 2020).

in Bertone et al. (2005) and references therein, and here I give a brief overview of some key candidates.

Neutrinos

Neutrinos are fermionic particles that interact through gravity and the weak force. They come in three varieties which correspond to the three charged lepton groups (Electron, Muon, Tau). They are the only DM candidate for which the existence has been confirmed experimentally (Cowan et al., 1956), and they are the only electrically neutral and long-lived particles in the standard model. Based on these known properties and predicted abundances in the early Universe, the neutrino mass would need to be approximately 11.5 eV to explain the dark mass fraction (Lesgourgues & Pastor, 2006). Unfortunately, their incredibly low masses ($\leqslant 0.21$ eV, Planck Collaboration et al., 2016b) and relativistic free-streaming velocities make it difficult to reconcile neutrinos with the dynamically cold DM needed to explain cosmic structure. Whilst neutrinos undoubtedly contribute to a proportion of hot DM in the Universe, they cannot solve the missing mass problem alone.

Alternatively, the hypothetical sterile neutrino can be used to justify hot, warm, and cold DM schemes depending on the particle mass (reviewed in Boyarsky et al., 2009b; Drewes, 2013). If they exist, these particles would be the right-chirality counterpart to neutrinos, and may explain the exceedingly low mass of neutrinos via the 'Seesaw' oscillation mechanism (i.e. Mohapatra & Senjanovic, 1980). Sterile neutrinos decay to produce a photon and neutrino (Pal & Wolfenstein, 1982), and detection of these decay channels in DM density centres may confirm their existence (Abazajian et al., 2001; Abazajian, 2019). Searches in galaxy spectra have so far found no such evidence (Anderson et al., 2015).

WIMP

The hypothetical Weakly Interacting Massive Particle (WIMP) particle is one of the most popular DM candidates, which has a non-zero weak force interaction and yields a dynamically cold DM (Ellis et al., 1984).

WIMPs are predicted to have formed in the early Universe during thermal equilibrium, where they would have been in a constant state of creation and annihilation (Bringmann & Hofmann, 2007). As the Universe expanded and cooled to around $1 - 10\,\mathrm{MeV}$ (as for the neutralino WIMP candidate Hofmann et al., 2001), their formation pathways became unattainable and the annihilation rates plummeted. This 'freeze-out' yields a relic number density of WIMPs in the Universe.

WIMPs annihilate because of a non-zero self-interaction cross section, with the end product being gamma-rays and/or neutrinos. This annihilation is crucial because it continues to the present day, albeit at very small rates which depend on the cross section and particle density, generating a potentially detectable signature. DM over-densities, such as galactic nuclei, would be ideal sources for this annihilation signal, but are complicated by the presence of other gamma-ray emitters like Active Galactic Nuclei (AGN). Investigations are typically limited to dwarf galaxies where these alternative gamma-ray sources are uncommon. Analysis of the dwarf galaxies Reticulum II and Tucana II have revealed promising gamma-ray signals that may hint at DM annihilation (Geringer-Sameth et al., 2018; Bhattacharjee et al., 2019).

There are also efforts to detect WIMP annihilation more locally, such as within the Sun. As DM particles scatter off of nuclei in the dense solar interior, there is a small chance they lose sufficient energy to become gravitationally captured (Press & Spergel, 1985). The accumulation of DM particles lead to over-densities that emits a predictable neutrino flux through annihilation processes (Silk et al., 1985; Krauss et al., 1986). The annihilation signal then depends not only on the DM interaction cross-section, but also on the local DM density and velocity distribution, which themselves depend on the properties of DM and on the halo of the Milky Way[4]. Searches for WIMP annihilation within the Sun have revealed no statistically significant results so far (ANTARES Collaboration, 2013; Bernadich & Pérez de los Heros, 2019).

Axions

Axions are a hypothetical particle originally conceived from efforts to solve strong CP-violation (charge and parity symmetry violation, see Peccei & Quinn 1977b,a; Peccei 1999) in the domain of Quantum physics. They are predicted to have formed from oscillations in a new 'axion field'. Axions have weak coupling to the standard model, with long lifetimes, and are therefore a good DM candidate (Preskill et al., 1983).

Axions are predicted to couple with photons, and can convert to and from photons whilst in the presence of magnetic fields (Sikivie, 1983). Axions which are converted into photons in space, such as in neutron star magnetospheres (Pshirkov & Popov, 2009), could then be converted back into axions on Earth. This property means that axions

---

[4] Galactic DM velocity distributions can gain features due to the merger history, and this combined with other uncertainties makes it difficult to constrain DM properties based on local annihilation rates (Nuñez-Castiñeyra et al., 2019)

can be detected both in the lab and in astrophysical environments, and there are ongoing experimental searches in both respects (Hagmann et al., 1998; Vogel et al., 2013; Hook et al., 2018). Axions are also expected to be thermally produced in stellar interiors, with implications on the stellar evolution. This allows for constraints on axion masses to be drawn (e.g. Raffelt & Dearborn, 1987; Friedland et al., 2013).

Since axion candidates are generally lighter than WIMP candidates, they may not be dynamically cold enough to agree with other observational constraints. This challenge can be overcome if axions coalesce into dense mini-haloes of $10^{-19} \leqslant M_{\rm minihalo}/{\rm M}_{\odot} \leqslant 10^{-5}$ (Hogan & Rees, 1988; Kolb & Tkachev, 1993). Substructure such as this would have implications on detection mechanisms, such as transient photon conversion when mini-haloes interact with neutron stars (see Edwards et al., 2020; Kavanagh et al., 2020).

Ultralight particles

Ultralight DM, also known as scalar-field DM or fuzzy DM, assumes a hypothetical boson with either zero or minimal self-interaction and mass $\sim 10^{-22}$ eV. A particle with such a tiny mass has so large a positional uncertainty that it exhibits wavelike behaviour, forming a Bose-Einstein condensate on galactic scales. Due to the uncertainty principle, these particles are less likely to perceive self-gravitation from one another on the smallest scales, leading to a suppression of fine structure formation.

As a result of its wavelike properties, ultralight DM is predicted to form 'soliton' cores in DM halo centres (cores are discussed further in Section §1.5.1). A natural property of these cores is that they undergo a random walk within the central region of the host galaxy, with ramifications on other local structures (e.g. Schive et al., 2020). Interference patterns can also arise, generating a granularity in the DM gravitational field on the scale of a few 100 kpc (Schive et al., 2014b; Mocz et al., 2019). These can leave observable imprints on the condensation of gas in the early Universe.

Recent constraints, based on observations of ultra-faint dwarf galaxies, the Lya forest and Milky Way (MW) satellites, have narrowed the mass range of ultralight DM to above 2×10^{-20} eV (Jowett Chan et al., 2021; Rogers & Peiris, 2021; Nadler et al., 2021). Whilst not ruling out the candidate, this would suggest that it would be unable to solve the small-scale puzzles discussed later in §1.5 by itself.

1.4 The formation of cosmic structure in ΛCDM

1.4.1 Large-scale structure

Seeded by initial quantum fluctuations, DM coalesces under the action of gravity to form bound structures. The over-densities first collapse into two-dimensional sheets, which are themselves gravitationally unstable. Sheets collapse into one-dimensional filaments, which then themselves collapse into zero-dimensional haloes (Zeldovich et al., 1982). The very first DM haloes would have been only as massive as the Earth (Diemand et al., 2005), with the formation of larger haloes proceeding via the hierarchical merging of smaller haloes and smooth accretion of surrounding DM from filaments (White & Rees, 1978). The resulting honeycomb structure of voids and haloes, interconnected with filaments and sheets, is known as the cosmic web (Bond et al., 1996). On the largest scales, the cosmic web is isotropic and homogeneous, and may extend infinitely in all directions. The locally observed distribution of galaxies and quasars is shown in Figure 1.8, which trace the pattern of the cosmic web. This paradigm has proven to be extremely successful in predicting the formation of cosmic structure on large scales (in the range 10 Mpc to 1 Gpc)

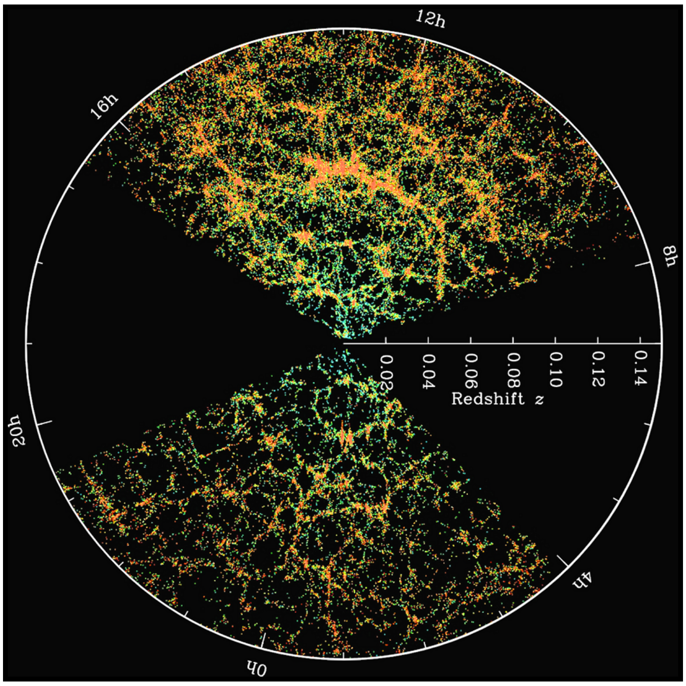

Figure 1.8: A map of the large-scale luminous structure in the Universe, as observed by the Sloan Digital Sky Survey (SDSS) (Blanton, 2008). Dots represent individual galaxies, with hue indicating the g-r colour of the stars. Large black wedges mark regions that could not be mapped because they were obscured by galactic dust lanes. Galaxies trace the underlying DM density, and the cosmic web – with filaments and voids – is clear to see at this scale. The distribution becomes increasingly uniform at larger scales.

(Springel et al., 2006; Clowe et al., 2006; Tegmark et al., 2006; Dawson et al., 2013; Oka et al., 2014; Planck Collaboration et al., 2014; Wang et al., 2016) and observations of the Lya forest (Croft et al., 1998; Baur et al., 2016).

Whilst the prediction of hierarchical structure formation is not unique to ΛCDM, a sufficiently cold DM is required to quantitatively explain the formation of modern structure. If DM was too kinematically warm, then halo formation would see a cutoff below some critical mass scale and the observed growth of Universal structure would have been delayed. This would have implications on the timing of events such as cosmic reionisation (more in §1.6.2) and other key signals (Barkana et al., 2001; Boehm & Schaeffer, 2005; Mesinger et al., 2005; Sitwell et al., 2014).

1.4.2 Small scale structure

As DM haloes form and detach from the Hubble flow[5], they naturally begin to approach a relaxed state of virial equilibrium, defined as:

$$2K + U = 0, \tag{1.5}$$

where K is the total kinetic energy and U is the total gravitational potential energy. This process occurs over a dynamical time, and propagates from the inside-out. Early DM simulations in a ΛCDM cosmology predicted that relaxed DM haloes would assume a universal and self-similar density profile at all scales. This profile is well-fit by the 'NFW'

---

[5] The Hubble flow describes the motion of cosmic structure due solely to the expansion of the Universe.

profile (Navarro et al., 1996b, 1997):

$$\rho_{\mathrm{NFW}}(r) = \frac{\rho_0}{r/r_{\mathrm{s}}\left(1 + r/r_{\mathrm{s}}\right)^2}, \tag{1.6}$$

where ρ_0 is a critical density, r is the radius from galactic center and r_s is the scale radius which marks the transition between an inner density of $\rho \sim r^{-1}$ (a cusp) and an outer density that has $\rho \sim r^{-3}$. The logarithmic divergent density cusp is a consequence of the dissipationless nature of DM, and is only truncated by the resolution limit in simulations.

DM haloes are diffuse objects with no definitive boundary. There are many convenient definitions for the halo edge, each with its own merits.

- The virial radius: This is defined as the radius at which the matter density approaches the Universal average, given by $\rho_{\mathrm{overdensity}} = \rho_{M_0}(1+z)^3$ where $\rho_{\mathrm{overdensity}}$ defines the boundary density. $\rho_{\mathrm{overdensity}}$ can be taken as 178, the critical density for spherical collapse in an Einstein-de Sitter Universe (Einstein & de Sitter, 1932), but is often rounded to 200 for convenience. As a consequence of the accelerating expansion of the Universe, the virial radius expands with time – independent of any local evolution in the DM halo.

- The splashback radius (More et al., 2015; Snaith et al., 2017): This definition attempts to draw a line between the DM halo and its surrounding environment based on accreting material. Here, the edge of the halo is marked by the apocentre of accreted matter after its first orbit. This radius ranges from around $1 - 1.5\times$ the virial radius, depending on the accretion rate.

- The turnaround radius (Pavlidou & Tomaras, 2014; Lee & Yepes, 2016): This definition marks the radius at which halo material detaches from the host and joins the Hubble flow. It is calculated based upon the radial velocity profile of the DM halo. A strength of this definition is its simplicity. The turnaround radius is typically much larger than the virial radius.

All of these definitions assume simple spherical symmetry, an assumption which I discuss further in Chapter 4.

1.5 A crisis at small scales

Despite the success of ΛCDM on large scales, simulations in a pure-DM cosmology struggle to describe various phenomena observed at galactic and sub-galactic scales. These have become collectively known as ‘small-scale puzzles’. The solutions to these puzzles may lie in the ramifications of unmodelled baryonic physics, or arise from a misunderstanding of the observational data.

1.5.1 Cusp-core problem

The oldest and most tenacious challenge to ΛCDM is known as the cusp-core problem (CC) (e.g. Flores & Primack, 1994; Moore, 1994; Read et al., 2017). As mentioned in Section §1.4, DM profiles are expected to adopt a divergent density profile. However, observations of real galaxies reveal a more complicated picture. Analysis based on the rotation curves of many galaxies favour a density profile that scales as $\rho \propto r^0$ within r_{s} (a core) (Carignan & Freeman, 1988; Flores & Primack, 1994; Moore, 1994; McGaugh et al., 2001; Read et al., 2017). In decades past, the numerical resolution in simulations was too low to rule out

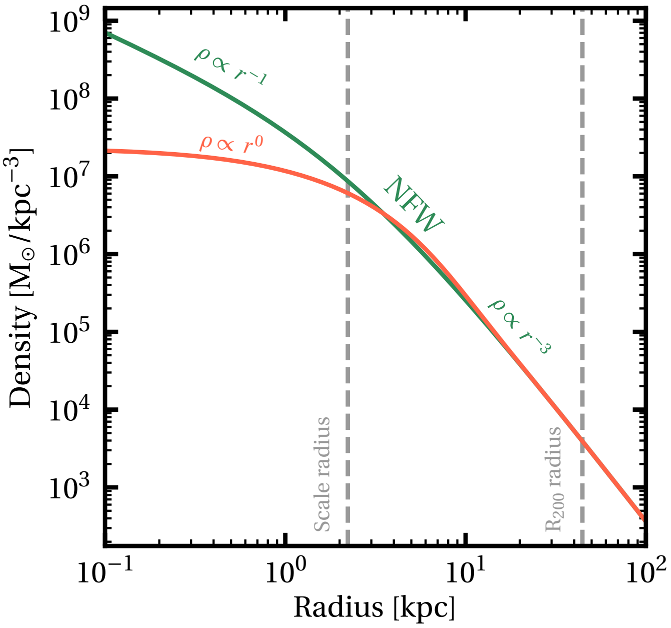

Figure 1.9: Schematic illustrating an example of a cuspy NFW profile (dark green line) and the equivalent cored profile (red line, represented with a coreNFW profile, Read et al. 2016a). This particular example is representative of a low mass dwarf galaxy. Indicated with dashed grey lines are the scale radius r_s and virial radius R_{200}.

density cores below a small scale (i.e. ~ 1.4 kpc in Dubinski & Carlberg, 1991). However, improvements in computing technology have since made clear that the discrepancy is genuine. A schematic, illustrating example cusped and cored density profiles, is shown in Figure 1.9. Many solutions to the CC have been proposed in the literature to date, which I briefly review here.

Observational misunderstanding

If observations are misinterpreted due to incorrect modelling assumptions, then the discovery of central cores may be erroneous. For gas-rich dwarf galaxies, the primary problems are due to systematic error in the estimated inclination angle of the galaxy (e.g. Oman et al., 2016), disequilibrium due to winds and gas bubbles (e.g. Read et al., 2016b), and unmodelled triaxiality (e.g. Rhee et al., 2004; Hayashi et al., 2007; Pineda et al., 2017). For gas-poor dwarf galaxies, for which the potential is derived from stellar kinematics, the primary problem is a degeneracy between the stellar orbit distribution and the inner DM density slope (e.g. Merrifield & Kent, 1990; Read & Steger, 2017; Genina et al., 2020b). An inaccurate photometric centring can also be to blame. Whether any of these effects are able to fully solve the CC on their own remains an active area of ongoing research (Kuzio de Naray & Kaufmann, 2011; Oman et al., 2016).

The authors in Oman et al. (2015) report a significant diversity in the rotation curves of dwarf galaxies, but do not account for these potential sources of observational error. In Read et al. (2016b), this is shown to have disastrous consequences for analysis of the dwarf galaxy IC 1613, which was predicted to host an enormous DM core. Here, a turbulent HI gas profile has kinematics inconsistent with the stellar profile (Oman et al., 2016). HI bubbles generated in galactic starburst cycles are shown to bias fitting models towards higher concentrations and lower masses, and that reconciling these fits with the stellar kinematics yields a normal sized DM core in IC 1613. Analysis of curated observations of isolated gas rich dwarf galaxies over the mass range $5 \times 10^5 \lesssim M_*/\mathrm{M}_\odot \lesssim 10^8$ consistently favour density cores (Read et al., 2017).

Alternative cosmologies

Perhaps the CC problem points to a new cosmology beyond ΛCDM. Alternatives such as WDM (e.g. Hogan & Dalcanton, 2000; Bode et al., 2001; Avila-Reese et al., 2001), self-interacting DM (e.g. Carlson et al., 1992; Spergel & Steinhardt, 2000; Tulin & Yu, 2018) or ultralight DM (e.g. Schive et al., 2014a; Ferreira, 2020) all predict a lower DM density at the centres of dwarf galaxies whilst retaining the predictions of ΛCDM on larger scales (see Figure 1.7).

In the case of WDM schemes, high-frequency modes in the matter power spectrum are suppressed, limiting the formation of structure at small scales (Bond et al., 1980). These schemes are heavily constrained by observations of the CMB, appearance of the first stellar populations (Chatterjee et al., 2019), perturbations in stellar streams (Banik et al., 2019) and gravitational lensing (Gilman et al., 2020; Hsueh et al., 2020), such that only mildy warm DMs are permitted. Whilst this does not yield full-size cores in place of cusps, it does result in much lower central densities and tiny central cores of $\mathcal{O}(10\,\mathrm{pc})$ (Villaescusa-Navarro & Dalal, 2011; Macciò et al., 2012). The small size of these central cores has cast doubt that realistic WDM schemes can explain observations of large cores (Macciò et al., 2012). However, the lower central densities enhance the ease with which other heating processes erode central cusps (see Chapter 4).

For self-interacting DM, particles become kinematically heated through elastic scattering off one another. This causes the DM halo to thermalise, adopting a Maxwell-Boltzmann velocity distribution (Vogelsberger & Zavala, 2013) and more spherically symmetric halo shape. The heating effect is limited to dense regions in the inner halo where particle-particle interactions are most likely, transforming central cusps into cores. The interaction cross-section of self-interacting DM schemes can be constrained by observations of the non-sphericity in DM haloes ($0.1\,\mathrm{cm}^2\,\mathrm{g}^{-1}$ Meneghetti et al., 2001), and of halo mergers such as the bullet cluster ($< 1\,\mathrm{cm}^2\,\mathrm{g}^{-1}$ Randall et al., 2008 and see Figure 1.2). These cast doubt on whether the interaction cross-section can be small enough to reproduce ΛCDM at larger scales. Self-interacting models can evade some constraints if they adopt an interaction cross-section dependent on the collisional velocity (see Kaplinghat et al., 2016). This allows the heating to be tuned depending on the DM velocity dispersion. The authors in Read et al. (2018) show that the required self-interaction cross-section for the dwarf galaxies Draco and Fornax are inconsistent – even with a velocity dependent cross-section – though this may be subject to the impact of accretion history and tidal effects (e.g. Kaplinghat et al., 2016; Nishikawa et al., 2020; Correa, 2021).

Ultralight DM introduces central density cores through an entirely novel mechanism, whereby the DM assumes wavelike properties and forms a soliton core at galactic densities. The implications of this were briefly discussed in Section §1.3.3. A possible defect of this scheme is that cores are formed in *all* DM haloes above a minimum scale, whereas there may be a diversity in the central density profiles (Oman et al., 2015).

Whilst alternative cosmologies can often resolve the CC problem, it is challenging to simultaneously match other constraining criteria from the CMB, BBN and galaxy observations.

Dark matter heating

The CC problem originates from a comparison of pure DM simulations – that do not model stars or gas – with observations. This opens up the possibility that purely gravitational interactions between DM particles and baryons could act to push DM out from the centres of dwarf galaxies, transforming a cusp into a core. Four main mechanisms have been proposed to date:

- Dynamical friction from infalling dense clumps (e.g. El-Zant et al., 2001; Mo & Mao, 2004; Romano-Díaz et al., 2009; Goerdt et al., 2010; Cole et al., 2011; Nipoti & Binney, 2015; Del Popolo & Pace, 2016). These clumps impart energy and angular momentum to the DM halo, causing it to expand.
- Dynamical friction from a central stellar or gaseous bar that acts similarly to infalling clumps, kinematically 'heating' the background DM halo. (e.g. Weinberg & Katz, 2007).
- A fluctuating gravitational potential driven by gas inflow/outflow due to cooling, stellar winds and SNe. This causes DM particle orbits to slowly migrate outwards (e.g. Navarro et al., 1996a; Read & Gilmore, 2005; Mashchenko et al., 2008; Pontzen & Governato, 2012; Governato et al., 2012).
- Impulsive heating and/or dynamical friction from subhalo mergers can reduce the central density in galaxies (Naab et al., 2009; Bédorf & Portegies Zwart, 2013; Boldrini et al., 2020b), with Boldrini et al. (2020a) finding this process occurs in a similar fashion in a model of the Fornax dSph when GCs are embedded in DM haloes.

The common feature underpinning these mechanisms is a time-varying gravitational potential that allows DM particles to exchange orbital energy both with one another and with the stars and gas in the galaxy. The mechanisms are differentiated by the physical mechanism driving the time-dependent gravitational field. In principle, all four mechanisms can act in tandem as galaxies form and evolve.

Despite the diversity of mechanisms in the literature, to date high resolution galaxy formation simulations have typically favoured the gas flow mechanism at the scale of dwarf galaxies (Navarro et al., 1996a; Read & Gilmore, 2005; Pontzen & Governato, 2012; Governato et al., 2012; Pontzen & Governato, 2014; Teyssier et al., 2013; Di Cintio et al., 2014a; Oñorbe et al., 2015; Dutton et al., 2016). Once gas is allowed to cool ($T < 10^4\,\mathrm{K}$) and reach high density ($\rho > 10\,\mathrm{atoms/cc}$; e.g. Pontzen & Governato 2012; Dutton et al. 2016), these simulations find that gas flows drive repeated fluctuations in the central galaxy mass of amplitude $10-20\%$ over a period less than the local dynamical time. Such fluctuations gradually lower the inner DM density on the scale of the stellar half mass radius, transforming a DM cusp to a core (e.g. Chan et al., 2015; Read et al., 2016a). Dwarf galaxies are particularly sensitive to these effects due to their shallow potential wells, and more massive galaxies may retain dense DM due to adiabatic contraction from a centrally concentrated baryonic component (Blumenthal et al., 1986; Jesseit et al., 2002; Gnedin et al., 2004; Davis et al., 2014; Dutton et al., 2016)

Theoretically, the mechanism can be reduced to a simple adiabatic mass inflow followed by a sudden (impulsive) mass outflow. For a DM halo comprised exclusively of particles on circular orbits, the specific angular momentum of each particle will be conserved if the halo mass changes adiabatically:

$$j^2 = GM_{\mathrm{ini}} r_{\mathrm{ini}} = GM_{\mathrm{inflow}} r_{\mathrm{inflow}} \tag{1.7}$$

where M is the halo mass, r is the orbital radius of the particle and subscripts 'ini' and 'inflow' stand for the state of the halo before and after inflow. In the case of gaseous inflow, $M_{\text{inflow}} = M_{\text{ini}} + M_{\text{gas}}$. The orbital radius of each particle is then given by:

$$r_{\text{inflow}} = \frac{M_{\text{ini}} r_{\text{ini}}}{M_{\text{ini}} + M_{\text{gas}}}. \tag{1.8}$$

Therefore, increasingly large M_{gas} result in increasingly contracted orbits. This baryon-induced contraction is seen to increase the concentration in some more massive galaxies (Young, 1980; Blumenthal et al., 1986; Gnedin et al., 2011; Dutton et al., 2016).

The outflows driven by SNe feedback occur on short timescales, and so the removal of mass can be considered to be impulsive. Angular momentum is no longer conserved, but the kinetic energy *is* conserved over these very short timescales:

$$E_{\text{outflow}} = \frac{1}{2} v_{\text{inflow}}^2 - \frac{G(M_{\text{inflow}} - M_{\text{gas}})}{r_{\text{inflow}}}, \tag{1.9}$$

where subscript 'outflow' refers to the system after impulsive outflow. Substituting $v_{\text{inflow}}^2 = GM_{\text{inflow}}/r_{\text{inflow}}$ for particles on circular orbits:

$$E_{\text{outflow}} = -\frac{1}{2} \frac{G(M_{\text{inflow}} - 2M_{\text{gas}})}{r_{\text{inflow}}}. \tag{1.10}$$

Combining both inflow and outflow together, the energy ratio between the initial and final system can be derived as:

$$\frac{E_{\text{ini}}}{E_{\text{outflow}}} = \frac{M_{\text{ini}}^2}{(M_{\text{ini}} - M_{\text{gas}})(M_{\text{ini}} + M_{\text{gas}})}. \tag{1.11}$$

Therefore, a positive M_{gas} pumps energy into the system, with the energy growing for more massive M_{gas}.

Realistically, DM particles occupy a variety of orbits, haloes are not point masses and inflow/outflow cycles are less than ideal. This process is described in more detail in Pontzen & Governato (2012), where it is shown that individual inflow/outflow events cannot significantly alter the DM. However, the effect is cumulative, and repeated cycles of gas flows can have considerable effect.

There is mounting observational evidence that this process occurs in real dwarf galaxies. Reconstructed star formation histories find that the duration of starbursts in observed low-mass galaxies are of the order a dynamical time (Weisz et al., 2012a; Kauffmann, 2014; Hirtenstein et al., 2019), in excellent agreement with simulated bursty star formation in El-Badry et al. (2016); Sparre et al. (2017). This can then be linked to a clear anti-correlation between the stellar mass of galaxies and their DM density at 150 pc (see Read et al., 2019b), in agreement with simulation predictions (Di Cintio et al., 2014b). However, it is worth mentioning that this anti-correlation can be interpreted differently depending on the DM model (e.g. Sameie et al., 2020), and could be impacted by tidal effects (Genina et al., 2020a).

Many authors have argued that core formation ceases in galaxies of stellar masses $10^6\,\mathrm{M}_\odot$ and below (Governato et al., 2012; Munshi et al., 2013; Madau et al., 2014; Chan et al., 2015; Oñorbe et al., 2015; Tollet et al., 2016; Wetzel et al., 2016; Garrison-Kimmel et al., 2017; Fitts et al., 2017; Bose et al., 2019), seemingly in tension with other results (Battaglia et al., 2008; Walker & Peñarrubia, 2011; Amorisco et al., 2013, 2014; Contenta et al., 2018). Much of this apparent disagreement stems from the definition of a core, with the former discussing substantial cores of a fixed size (e.g. $\sim 500\,\mathrm{pc}$). A DM core will still be dynamically important if it has size comparable to the half light radius, because this is the scale that stellar kinematics are typically measured on and has implications for DM annihilation signals in ultra-faints (Lake, 1990; Bonnivard et al., 2015)[6].

If gas flows are truly the dominant mechanism driving cusp-core transitions, then galaxies lacking suitable gas flows should be observed to retain a primordial density cusp. The authors in Peñarrubia et al. (2012) find a lower limit of order $10^{53} - 10^{55}\,\mathrm{erg}$ for cusp removal in haloes with mass $10^9 \leqslant M_{200}/\mathrm{M}_\odot \leqslant 10^{10}$. Most SNe energy will not directly couple to the gas, and so this can only be considered as a lower limit on the energy requirement. As an example, Maxwell et al. (2015) show that a coupling efficiency of at least 1% is needed to justify the 1 kpc core in the Fornax galaxy, though this is easily achievable. The required energies depend highly on the DM mass enclosed within some critical radius (i.e. the half light radius), which in turn depends on the halo mass and concentration. Ultra-faint dwarf galaxies, for which star formation becomes increasingly inefficient at lower halo masses, are an ideal example. While some such galaxies *do* have evidence for a cusp (Richardson & Fairbairn, 2014; Strigari et al., 2017; Read et al., 2018; Shi et al., 2021), others – such as the dwarf galaxies Eridanus II (Bechtol et al., 2015; Koposov et al., 2015) and Andromeda XXV (Richardson et al., 2011; Cusano et al., 2016) – have been argued to be cored (Amorisco, 2017; Contenta et al., 2018). Given the amount of stars within these galaxies, it is energetically challenging to achieve the formation of a core through the typical gas flow mechanism (Contenta et al., 2018). This, then, provides an opening for other sub-dominant processes or even exotic DM schemes. I investigate this further in Chapter 4 and Chapter 5.

1.5.2 Missing satellites

Within galaxies there are a large number of smaller, dense, gravitationally-bound substructures called ‘subhaloes’ (Tormen et al., 1997; Moore et al., 1998). These subhaloes are the remnant cores of merging DM haloes, as described in §1.4, which are accreted predominantly during the early formation of the parent halo (Press & Schechter, 1974). Whilst DM subhaloes in ΛCDM are expected to exist at incredibly low masses, only those above a certain mass scale can reasonably be expected to host galaxies, and only a fraction of these will be luminous enough to meet observational limits. For MW-mass haloes, early models of ΛCDM predicted there should be more than a hundred easily observable luminous satellites ($L > 10^6\,\mathrm{L}_\odot$ Kauffmann et al., 1993).

The real MW hosts only around ten such satellites, and this discrepancy was heralded as the missing satellite problem (MS) (Klypin et al., 1999; Moore et al., 1999). There are many physical processes which act to suppress galaxy formation, which will be discussed further in Section §1.6, and these have often been quoted as potential explanations for the MS problem. Whether these processes can actually explain the problem in practice is an area of continued investigation, and if they fail then new cosmologies may need to be invoked.

For a long time this under-representation remained significant despite advances in imaging technology (Klypin et al., 1999; Bullock, 2010). However, the number of missing satellites has decreased as more dwarf galaxies have been discovered within the MW, thanks to deep large-scale sky surveys such as the Sloan Digital Sky Survey (York et al., 2000), VST ATLAS (Shanks et al., 2015), the Dark Energy Survey (Dark Energy Survey

---

[6] The stellar profile of ultra-faint galaxies extends only a short distance, and dense cusps in dwarf galaxies are often considered as possible detection sites of DM self annihilation.

Collaboration et al., 2016), the PAN_STARRS1 survey (Chambers et al., 2016) and the Hyper Suprime-Cam Sub-aru Strategic Program Survey (Aihara et al., 2018). There has also been continued discovery of ultra-faint MW dwarfs with very high DM fractions, which hint at further populations of even fainter galaxies which are as of yet undetectable.

There are many physical effects that could impact the formation of dwarf galaxies, such that a larger fraction of DM substructure is not populated by luminous galaxies. Star formation can be suppressed due to photoionisation of gas, SNe feedback and tidal stripping – to which dwarf galaxies are more vulnerable. The authors in Simon & Geha (2007); Fielder et al. (2019); Nadler et al. (2020) find that the number of haloes generated under ΛCDM approaches observed quantities when such physical effects are accounted for. The massive host itself can also contribute to the problem, with the authors in Brooks et al. (2013) showing that enhanced tidal stripping generated by a baryonic disk reduces the population of observable satellites in the MW.

The solution could also be far more mundane. Perhaps the Local Group (LG) is a statistical outlier, or the variation between galaxies is larger than previously thought. Answering these questions will require detailed analysis of the dwarf galaxy populations in a statistically significant number of galaxies, including those outside the LG. Said work is already underway, with the authors in Tanaka et al. (2018) investigating two galaxies outside the LG and finding one to have a dwarf galaxy population similar to the MW, and the other to have a more abundant population.

1.5.3 Too-Big-To-Fail

If the MS problem can be solved by careful treatment of physics affecting low-mass subhaloes, then the *existing* MW satellites should be attributed to the highest mass subhaloes expected in ΛCDM. If this prediction is accurate, then the observed satellites of the MW should have an internal velocity dispersion matching the highest mass subhaloes in ΛCDM simulations. However, ΛCDM simulations predict more massive subhaloes (Read et al., 2006b; Boylan-Kolchin et al., 2011). Somehow the most massive subhaloes in ΛCDM are failing to produce galaxies, which is described as Too Big To Fail problem (TBTF). There is much contention in the literature over whether the 'Too big to fail' problem is real, with some research suggesting there are instead *too many* star-forming haloes (Jethwa et al., 2018; Kim et al., 2018; Graus et al., 2019).

This problem has recently been re-imagined as a consequence of the cusp-core problem, where bursty SNe feedback is able to solve both problems at once (Ogiya & Burkert, 2015; Read et al., 2016a; Kato et al., 2016). If massive DM subhaloes contain cores rather than cusps then their central velocity dispersion will be systematically lower (by as much as a factor of two Read et al., 2016a), bringing observation in line with simulation. Cored haloes are also more susceptible to tidal stripping upon infall to a host galaxy, which may help to explain the MS problem. The authors in Brooks & Zolotov (2014); Brooks et al. (2013) use cosmological simulations to show that a combination of baryonic heating and tidal stripping lowers the central DM mass in analogues of MW satellites. This brings the number of expected luminous satellites in agreement with observations of the MW and M31.

The TBTF problem has also been extended to dwarf galaxies in the field (Papastergis et al., 2015; Klypin et al., 2015). These are more challenging to explain because there are no tidal fields, and baryonic heating alone struggles to resolve the tension (Papastergis & Shankar, 2016). Simulations in Brooks et al. (2017) suggest that the apparent dearth of field dwarfs is a result of misleading observations, where the measured width of the HI profile at 50% of the peak height systematically underestimates the true peak rotation curve. This is endorsed by Read & Steger (2017) who find no field TBTF problem when observations of spurious quality are excluded, and by Chauhan et al. (2019) who use a mock survey to show that selection effects are the primary driver of the TBTF problem.

1.5.4 Planes of satellites problem

ΛCDM predicts that DM haloes form from the hierarchical assembly of bound structures, which naturally results in host haloes populated by a swarm of lighter satellites. Simulations predict that satellites occupy a highly chaotic and random spread in phase space (Ghigna et al., 1998; Zentner & Bullock, 2003; Diemand et al., 2004b). Whilst there is some anisotropy, which has been linked to the preferential accretion of satellites from filamentary structures and the triaxial shapes of host DM haloes (Zentner et al., 2005), satellites in simulations remain mostly uncorrelated in phase space.

However, it has long been known that the satellites of the MW are spatially distributed in a single plane called the Vast Polar Structure (VPOS) (Lynden-Bell, 1976; Kunkel et al., 1976). More recent observations of our most local galaxies (the MW, the Andromeda galaxy (M31), Centaurus A) have all found flattened satellite distributions with kinematic signs of co-rotation (Pawlowski et al., 2012; Ibata et al., 2013b; Müller et al., 2018), indicating that satellites generally co-orbit in a common plane. Whilst it is not impossible that these alignments are a coincidence, the chance of this is incredibly low ($< 0.5\%$ Kroupa et al., 2005, $< 0.1\%$ Pawlowski & Kroupa, 2020), and so the planes of satellites problem (PoS) was born.

The small-scale problems discussed so far are sensitive to baryonic physics, but the phase-space locations of satellites are controlled by the overall gravitational field – which is dominated by DM. The bulk motions of satellites can be measured with greater certainty than their internal motions, reducing the possibility that the PoS problem is linked to observational error.

A number of possible solutions have been put forward by the astrophysics community, none of which have gained universal support. These all invoke an event or circumstance which encourages satellites to share similar phase-space locations, and are summarised as follows:

- Accretion from filaments: This solution suggests that the anisotropic accretion of satellite material from filamentary structure can explain the PoS. However, such accretion is already built-in to cosmological simulations which fail to predict PoS. The width of cosmological filaments ($> R_{\rm vir}$, Vera-Ciro et al., 2011) is typically much broader than the observed satellite planes (a few tens of kpc), and so it is unlikely to be the cause of the high coherence.

- Group infall: If a significant number of satellites fell into their host as a compact group, then they would already share similar phase space conditions. As with the accretion from filaments scenario, this is already built-in to simulations and it is unlikely that the large number of coherent satellites in LG galaxies could all be part of the same infalling group.

- Tidal Dwarfs: Tidal dwarfs are formed within their host galaxies as a result of large-scale tidal interactions. If a large portion of observed satellites formed from a single tidal tail, then this could justify their similar alignment. However, tidal dwarfs should have both high metallicities (due to being formed from an enriched IGM) and low DM ratios. These properties are not borne out by observation (McConnachie, 2012; Recchi et al., 2015).

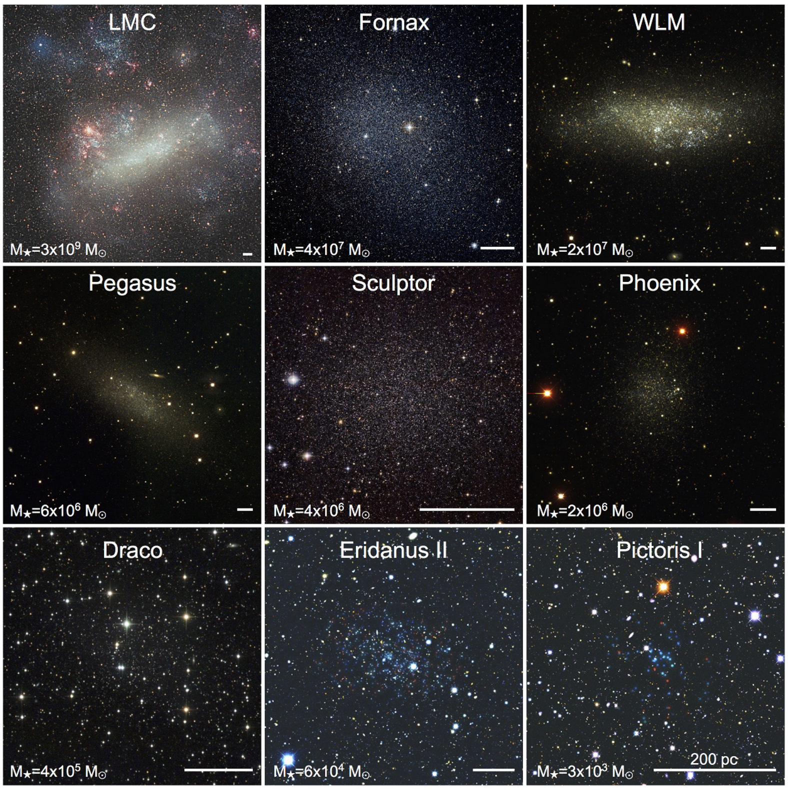

Figure 1.10: A selection of galaxy images from Bullock & Boylan-Kolchin (2017), and references therein. The galaxies are selected to span a range of six orders of magnitude in stellar mass. Only the LMC, WLM and Pegasus continue to form stars today. The bottom row represents ultra-faint dwarf galaxies.

- Halo triaxiality: As will be discussed in Chapter 6, gas condensation onto DM haloes leads to a scattering of the particle orbits and yields a rounder halo shape. This effect can extend to large distances for high mass galaxies ($\sim$ 20 disc scale lengths Debattista et al., 2008). The distribution of substructure naturally tends to trace the host halo shape, and so this mechanism could reduce the phase-space coherence of satellites.

1.6 Dwarf Galaxy formation in ΛCDM

1.6.1 Observational properties of dwarf galaxies

Whilst there is no rigorous definition of a dwarf galaxy, in this thesis I define it as a galaxy inhabiting a DM halo in the mass range $10^8 \leqslant M_{200}/\mathrm{M}_\odot \leqslant 10^{10}$. Following this definition, even the largest dwarf galaxies are around a hundredth of the mass of the MW. Such low masses yield low gravitational potential wells, and dwarf galaxies are particularly susceptible to tidal interactions from other galaxies and internal perturbations like SNe and stellar winds. The luminous component of the galaxy is more sensitive to the influence of the DM halo at this extreme limit, which makes dwarf galaxies excellent laboratories for investigating the properties and behaviour of DM.

Despite their diminutive mass, dwarf galaxies are the most ubiquitous type of galaxy in the visible Universe (Bel et al., 2014). They come in a variety of flavours, and are commonly distinguished by their stellar content, with Bullock & Boylan-Kolchin (2017)

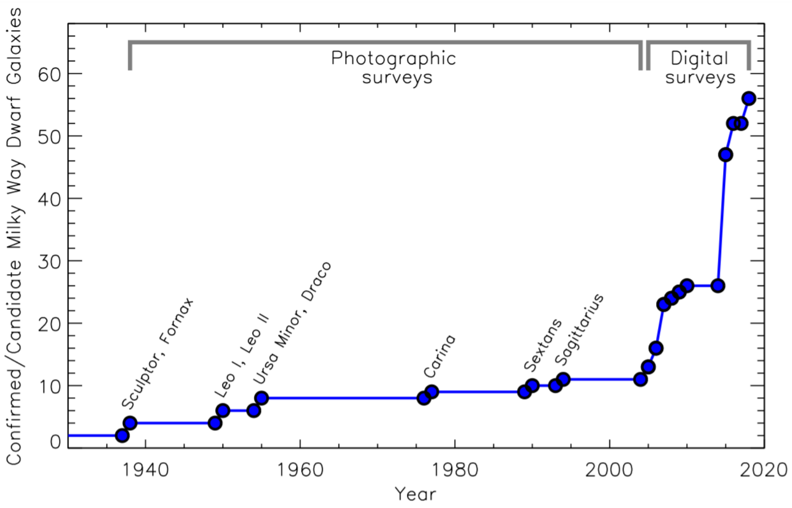

Figure 1.11: This figure from Simon (2019) shows the rapid increase in dwarf galaxy satellite detections within the MW. The introduction of digital surveys after the millennium have contributed the vast majority of dwarf galaxy candidates.

establishing the following definitions:

- Bright Dwarf: Stellar mass of $10^{7-9}\,\mathrm{M}_{\odot}$.
- Classical Dwarf: Stellar mass of $10^{5-7}\,\mathrm{M}_{\odot}$.
- Ultra-faint Dwarf: Stellar mass of $10^{2-5}\,\mathrm{M}_{\odot}$.

Further delineation can be based on morphology and appearance:

- Dwarf Spheroidal galaxy (dSph): These low surface brightness and diffuse galaxies are so named due to their roughly spheroidal shape, and lack the spiral or bar features that are commonly associated with more massive galaxies. The content of dSphs is dominated by their DM, with only trace amounts of gas (e.g. Young, 2000). Analysis of their star formation histories show most stop forming stars in the early Universe, and are rarely actively forming stars today (Karachentsev et al., 2018). They are most frequently found orbiting more massive galaxies.
- Dwarf Elliptical galaxy (dE): These galaxies are distinct from dSphs in that they are elliptical in shape, although there is a lot of overlap depending on the chosen definition (like in Sandage & Binggeli, 1984). dE galaxies are often more massive than dSphs, but still host ancient and quiescent stellar populations.
- Dwarf Irregular galaxy (dIrr): The most common type of dwarf galaxy, dIrrs have an amorphous structure and show little sign of coherent rotation (Binney & de Vaucouleurs, 1981; Lo et al., 1993). Despite different appearances, the overall star forming histories of dIrr are not dissimilar from those of other morphological types (Weisz et al., 2011a), and the *underlying* structure is comparable to dSphs (Kormendy, 1985). dIrrs differ from dSphs in that they have retained their gas, and are more frequently still forming stars today. This may suggest dIrrs are early dSphs that are yet to exhaust/lose their gas (Lin & Faber, 1983). However, observations show that dIrrs of comparable luminosity are more metal-rich and are therefore unlikely to be progenitors

of dSphs (Mateo, 1998; Richer et al., 1998; Grebel et al., 2003), but see also arguments in (Kirby et al., 2013). dIrrs are more frequently isolated than dSphs.

A selection of dwarf galaxy observations across a range in brightness and morphology are shown in Figure 1.10.

Many dwarf galaxies are so faint that they escape direct detection. Investigations are limited to dwarfs within the LG, with almost all of the sub $M_v \simeq -11$ galaxies residing there (Whiting et al., 1997). Fortunately, comparisons between LG dwarfs and other nearby dwarfs indicate that those in the LG are representative of dwarf galaxies in general, such that local investigations can be extrapolated elsewhere (Weisz et al., 2011b; Collins et al., 2013). The number of dwarf galaxy detections has exploded with the introduction of digital imaging surveys, which can be seen in Figure 1.11. A consequence is that the dwarf regime has been extended to increasingly low surface brightness, and the tail-end is becoming difficult to distinguish from GC populations (see Figure 6 of McConnachie, 2012).

Dwarf galaxies are thought to be the most DM dominated systems in the Universe, and can have mass-to-light ratios as high as 1000 (Walker et al., 2009; Wolf et al., 2010). This is in contrast with GCs, for which there is good evidence of no associated DM halo (Heggie & Hut, 1996; Moore, 1996; Baumgardt et al., 2009; Conroy et al., 2011; Bradford et al., 2011; Ibata et al., 2013a). However, it has been suggested that some GCs may have originally formed within DM haloes (Peebles, 1984) which were then stripped through interactions with a host galaxy (Hilker & Richtler, 2000; Bromm & Clarke, 2002; Bekki et al., 2002; Bekki & Freeman, 2003; Ricotti et al., 2016). If correct, the gap between ultra-faint dwarf galaxies and GCs becomes increasingly blurred.

The SMHM relation

The Stellar Mass Halo Mass (SMHM) relation describes the relationship between the stellar mass of a galaxy and its host DM halo (see Moster et al., 2010; Guo et al., 2010). It is one of the most fundamental properties in galaxy evolution, and is connected to the small-scale puzzles in Section §1.5.1 (Bullock & Boylan-Kolchin, 2017). In the absence of more direct mass-modelling, the SMHM relation can be determined through abundance matching techniques that are tuned to cosmological simulation results (e.g. Trujillo-Gomez et al., 2011). It is found that the SMHM relation can be well described by a single power law of $M_* \propto M_{\rm halo}^{\alpha}$ for halo masses below $10^{12}\,{\rm M}_\odot$ (Simon, 2019, and references therein). The scatter in this relation is tight over a large range of masses (< 0.3 dex in Behroozi et al., 2013).

The SMHM relation is less well constrained in the dwarf regime, with varying predictions for α at the lower end of the relation (see Moster et al., 2013; Behroozi et al., 2013; Brook et al., 2014; Garrison-Kimmel et al., 2014; Read et al., 2017). Survey incompleteness and the difficulty in mass-modelling at this scale have contributed to the problem. Abundance matching techniques are less reliable too, with simulation predictions failing to meet expectations from observation (Ferrero et al., 2012; Brook & Di Cintio, 2015). This is unsurprising given that dwarfs approach the scale where DM haloes are no longer populated by luminous galaxies at all, and cosmological simulations predict sizeable scatter in their stellar masses (Munshi et al., 2019; Feldmann et al., 2019; Munshi et al., 2021). The authors in Read & Erkal (2019) suggest that the reliability is improved if abundances are matched to star formation rate rather than final stellar mass.

Whilst the low-mass end of the SMHM relation can be predicted by extrapolation, this does not consider the impact of physics that may have a disproportionate affect on dwarf formation. There is no specific reason to believe the SMHM relation should be extrapolated to lower masses, and (Munshi et al., 2021) show that doing so can lead to an inaccurate portrayal of the number of small galaxies.

1.6.2 Formation pathways

Ram pressure

Dwarf galaxies, due to their low masses, are vulnerable to interactions with their environment, but this vulnerability encompasses more than just gravitational perturbations. As a dwarf sails through a gaseous background, such as a gas filament in the cosmic web or the gaseous halo of a larger host galaxy, it runs the risk of having its own Inter-Stellar Medium (ISM) blasted off in a process called 'ram pressure stripping'. A result of stripping the ISM is that the galaxy is strongly damped or prematurely quenched because it cannot fuel further star formation (Mayer et al., 2006; Yozin & Bekki, 2015; Emerick et al., 2016), with the effect occurring on order of a dynamical time for infalling satellite dwarfs (Wetzel et al., 2015; Fillingham et al., 2016). The authors in Akins et al. (2021) posit a mass limit of $M_* = 10^8\,\mathrm{M}_\odot$, above which satellites are resistant to rapid quenching in MW-mass hosts.

Ram pressure stripping most strongly affects the hottest and least-bound portion of a galactic ISM. The cold, clumpy centralised gas is often retained, as shown by cosmological and wind-tunnel simulations in Hausammann et al. (2019). Cold, central gas is found to resist quenching in dwarf galaxies, and can respond to ram pressure by extending or reigniting star formation under the correct conditions (Marcolini et al., 2003; Bekki & Couch, 2003; Kronberger et al., 2008; Henderson & Bekki, 2016).

Therefore, ram pressure is not always destructive. The authors in Wright et al. (2019); Steyrleithner et al. (2020) suggest that star formation in dwarf galaxies can be enhanced from transits through gas filaments if the surrounding gas pressure is within a suitable range ($1 > P_{\mathrm{Galactic}}/P_{\mathrm{Extragalactic}} > 4$). Within this threshold, the extragalactic gas acts to compress the galactic gas such that star forming HI gas condenses out.

Stellar feedback

Stellar feedback can be counter-productive for continued star formation. A certain fraction of stars will explode in SNe, releasing an energy of order 10^{53} ergs, of which roughly 1% is kinetically coupled to the surrounding environment. These explosions are so powerful that they super-heat and blow-out the surrounding IGM (see Lynds & Sandage, 1963; Larson, 1974), leaving residual 'bubbles' (see Figure 1.12 for a visual example and Meurer et al. (1992); della Ceca et al. (1996); Ott et al. (2001) for evidence that this occurs in dwarfs). Although gas blowout driven by SNe is already discussed in Section §1.5.1, there are further implications. The heating and removal of gas from multiple SNe suppresses the star formation rate, with the impact being particularly large in dwarf galaxies due to their low binding energies (Dekel & Silk, 1986; Efstathiou, 2000; Benson et al., 2003; Puchwein & Springel, 2013).

SNe ejecta are also responsible for enriching the IGM with metals (e.g. Aguirre et al., 2001). This enhances the cooling rate in the IGM by introducing atomic emission lines from the recombination of ionised elements, which in turn encourages gas accretion and star formation (Choi & Nagamine, 2009). However, dwarfs retain less of this enriched gas due to their shallower potential wells (Finlator & Davé, 2008; Peeples & Shankar, 2011), and so experience a diminished increase in gas cooling.

Figure 1.12: Infrared image of star forming molecular clouds in the northern constellation Cassiopeia, taken with the Herschel space telescope. Blue regions correspond to young stars, which have carved out large bubbles with SNe-driven winds. These observations illustrate the extent to which stars can reshape their local environment. Image credit to ESA/Herschel/NASA/JPL-Caltech/R. Hurt.

The Epoch of reionisation

In ΛCDM, the first protogalaxies are expected to appear in early DM haloes a few hundred million years after the big bang. Radiation from these initial light sources spreads out into the IGM, bringing an end to the 'dark ages'. At this early time, the IGM was dominated by neutral Hydrogen gas. This was gradually ionised by radiation exceeding the ionisation threshold of neutral Hydrogen ($\sim 13.6\,\mathrm{eV}$).

This transition from a neutral to an ionised IGM had dire consequences for many of the smallest galaxies. As the IGM was ionised, gas temperatures were raised to around $10^4\,\mathrm{K}$, inhibiting their gravitational collapse. This had two effects on dwarf galaxies: their cold gas evaporated away, and they were starved of further gas accretion. As dwarfs depleted their remaining cold gas, their star formation was prematurely quenched (both in theory and simulation (Efstathiou, 1992; Thoul & Weinberg, 1996; Barkana & Loeb, 1999)).

The authors in Rodriguez Wimberly et al. (2019a) suggest that reionisation is the most likely mechanism by which star formation is quenched on small scales. The susceptibility to quenching strongly depends on the mass scale and self-shielding capabilities of a galaxy. A large galaxy may be reionised at the periphery, but preserve a larger reservoir of cold gas where the ionising radiation struggles to penetrate. However, the gas in dwarf galaxies is also vulnerable to removal via SNe, and it is not always clear which process is the dominant factor in quenching (e.g. Ricotti & Gnedin, 2005; Salvadori & Ferrara, 2009; Gallart et al., 2021a). There are rare examples of dwarf galaxies (such as Leo P, with a low stellar mass of around $5.6 \times 10^5\,\mathrm{M}_\odot$ (McQuinn et al., 2015)) that remain star-forming today. Reconciling these rare galaxies with the reionisation narrative may require close attention to the exact timescale of reionisation and other relevant physical processes.

Reionisation did not occur homogeneously, but began with hot pockets of ionised gas around the first protogalaxies. This ionisation front expanded and spread across the universe from $20 \gtrsim z \gtrsim 6$ (Fan et al., 2002; Planck Collaboration et al., 2016a; Madau, 2017). The authors in Dawoodbhoy et al. (2018a) simulate a large volume of cosmic structure with detailed modeling of radiative transfer to reproduce the patchy evolution of reionisation. They find that dwarf galaxies are unable to maintain their own reionisation, and rely on importing radiation from more luminous galaxies.

The timescale of reionisation depends not only on the ionising output of galaxies but also the escape fraction f_{escape} of this radiation into the IGM. f_{escape} is difficult to observe directly because the IGM had a high opacity during the reionisation epoch, and the main sources of ionising radiation occur at such a high redshift that they escape detection (Paardekooper et al., 2015). f_{escape} is expected to vary with time as the universal population of galaxies evolves, which results in a variable reionisation efficiency (Ferrara & Loeb, 2013)[7]. To further complicate the situation, f_{escape} is often anisotropic due to gaseous discs and dust lanes within larger galaxies, and this can vary f_{escape} by more than an order of magnitude (Gnedin et al., 2008).

Paardekooper et al. (2015) suggests that low-mass galaxies with $M_{200} < 10^8\,\mathrm{M}_\odot$ will have dominated the reionisation landscape due to both their high abundance and higher f_{escape}, despite high-mass galaxies providing more ionising radiation individually (Gnedin et al., 2008). Stellar feedback within such galaxies acts to clear away the local IGM, allowing the ionising radiation to penetrate further. Ricotti (2002); Ma et al. (2020) show that early GCs are also responsible for driving reionisation.

Reionisation is the dominant quenching mechanism for dwarf galaxies (Brown et al., 2014; Benítez-Llambay et al., 2015; Fitts et al., 2017; Dawoodbhoy et al., 2018b; Rodriguez Wimberly et al., 2019b), but this is not to say that all dwarf galaxies quench at the same time scale. Simulations by Oñorbe et al. (2015) show that dwarf galaxies continue to form stars after reionisation until their shielded internal gas reservoir is depleted.

1.7 Thesis overview

In this introduction I have described the foundations underpinning the ΛCDM paradigm, and summarised scientific advancements into the nature of DM and galaxy formation. This sets the scene for my own research into DM and dwarf galaxies.

- In Chapter 2 I present a synopsis of the numerical methods and challenges involved in simulating dwarf galaxies and their cosmological environments. I also discuss the software which I use most extensively throughout this work.
- In Chapter 3 I introduce the EDGE simulation suite. Here I describe my research goals, my particular numerical setup, simulation pipeline and establish the main suite analysed in this work. I then show that EDGE compares favourably with all known observable properties in real dwarf galaxies.
- In Chapter 4 I investigate the cusp-core problem in EDGE, aiming to answer the question of whether cusp-core transformations are operating at this low mass scale and which mechanisms bear responsibility. I perform additional simulations for one dwarf in an attempt to isolate a potential sub-dominant heating mechanism.
- In Chapter 5 I develop the results of Chapter 4 with respect to the ultra faint galaxy Eridanus II, the faintest galaxy known to host a Star Cluster (SC). I create a comprehensive suite of N-body SC simulations to test whether comparable EDGE dwarfs can host a SC with similar properties to that in Eridanus II. I discuss formation scenarios for Eridanus II informed by the results of these simulations and using energetic arguments.
- In Chapter 6 I construct a halo shape algorithm and employ it on the EDGE dwarfs. I compare the halo shape with radius, and the evolution of the central halo shape,

---

[7] The authors in Seiler et al. (2019) argue that the Square Kilometer Array (SKA) will be able to distinguish between different models for how the escape fraction varies with galactic stellar mass.

with the aim of determining the dominant mechanisms for any shape changes. Then, I investigate the velocity anisotropy within EDGE.

- Finally, I summarise my research in Chapter 7 and discuss future prospects for the EDGE project and the field in general.

Numerical methods

2.1 Cosmological simulations

Cosmological simulations aim to model the evolution of the universe from its primordial conditions. This is an extremely challenging task, because it encompasses a wide range of physics (gravitation, hydrodynamics, stellar evolution, to name a few) and scales (the large-scale structure of the cosmic web down to star formation processes). Here I will present a simplified description of the different ingredients and techniques used in modern cosmological simulations. For a more complete review of these methods, see Efstathiou et al. (1985); Colombi (2001); Peter (2001); Aarseth (2003); Bagla (2005); Dehnen & Read (2011).

2.1.1 Initial Conditions

The evolution of cosmic structure began from small perturbations in an otherwise smooth density field (see Chapter 1). To represent this computationally, simulation elements representing mass are initialised on an equally-spaced three-dimensional grid. Each element is then given a small perturbation, creating over-densities within the grid. The exact form of these initial perturbations must be carefully designed to reproduce the density power spectrum from the CMB, such that the evolution of cosmic structure under gravity is realistic. Different initial perturbations can result in entirely unique Universal structures, as is demonstrated in Figure 2.1. Here, the halo in the left panel assumes CDM and the halo in the right panel assumes WDM with a particle mass of 2 keV. Whilst the general forms of the host halo are similar at large scales, truncating the smaller scales in the power spectrum has fundamentally altered the hierarchical formation of structure. The growth of smaller substructure is inhibited, and halo concentrations are reduced. See also Moscardini et al. (1991) for more examples of how different forms of the primordial power spectrum affect structure formation.

Cosmological simulations can be broken down into component ingredients: DM, gas, stars and radiation. The initial simulation elements are split into DM and gas along a Universal baryon fraction, which can be calibrated to observations from the CMB. Stars are then allowed to form from collapsing gas clouds.

2.1.2 Dark Matter

It is convenient to model DM in the form of simulation elements (hereafter particles), where each particle is representative of a mass of DM. This is not the same as actual subatomic particles, but should instead be considered as the discretised sampling of a DM fluid. These simulation particles are typically in excess of hundreds of solar masses – many orders of magnitude above any candidate DM particle. This approximation is a necessity to keep computation costs feasible, but has some undesirable side effects which I discuss later. The force calculation method used in the cosmological code RAMSES is described in Section 2.3.1.

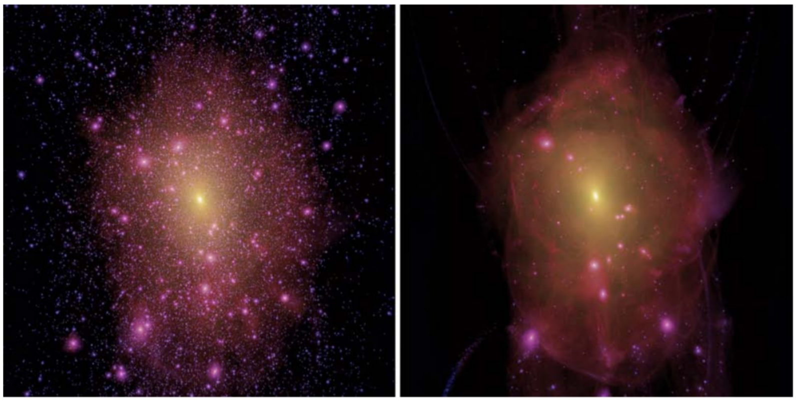

Figure 2.1: Projected density images of DM haloes evolved in CDM (left) and WDM (right) cosmologies from the Aquarius simulations. Both haloes are derived from the same initial conditions, but in the case of WDM the power spectrum is truncated as for a thermal relic 2 keV sterile neutrino (competitive against Lya forest constraints). The colour scheme reveals the DM velocity dispersion (from low dispersions in blue to high dispersions in yellow). Figure credit to Frenk & White (2012).

Force calculation

The most straight-forward approach to simulate a system of particles under gravity is to directly calculate the total gravitational force acting upon one particle from every other particle. For standard Newtonian gravity, this can be written:

$$\boldsymbol{F_{ij}} = \frac{G m_i m_j \left(\boldsymbol{q}_j - \boldsymbol{q}_i\right)}{\|\boldsymbol{q}_j - \boldsymbol{q}_i\|^3}, \tag{2.1}$$

where F_{ij} is the inter-particle force, G is the gravitational constant and $\|\boldsymbol{q}_j - \boldsymbol{q}_i\|$ represents the inter-particle distance.

This is known as the Particle Particle (PP) approach (e.g. Aarseth et al., 1979), and ensures the most accurate force calculations. Unfortunately, the computational cost of these calculations scales with $\mathcal{O}(N^2)$, where N is the number of simulation particles. This renders the PP approach infeasible for large cosmological simulations, and even for simulations of large galaxies. The high force accuracy of the PP approach is excessive for the representation of collisionless environments in cosmological simulations, where close particle interactions make only a minor contribution to the evolution of the system. Therefore, the calculations can be made more efficient by way of approximation.

A popular method is the Tree-code. This method exploits the fact that the gravitational force on a particle m from distant particles can be approximated as a particle group. More distant particles can be approximated as larger groups, based upon the angle that these groups subtend on the particle m. The threshold angle can then be chosen to favour accuracy or speed. This greatly reduces the number of operations needed to calculate the force on each particle, improving efficiency to $\mathcal{O}(N \log N)$.

The first implementation was the Barnes-Hut algorithm (Barnes & Hut, 1986). The simulation space is divided into eight cubes called ‘octs’. Each oct containing > 1 particles is further subdivided until each particle occupies its own cell. The total mass and centre of mass is calculated for every oct in the hierarchical tree structure. Then, the gravitational forces on a particle m from all other particles can be considered on an oct-by-oct basis, where more distant particles are grouped into larger octs higher up in the tree structure.

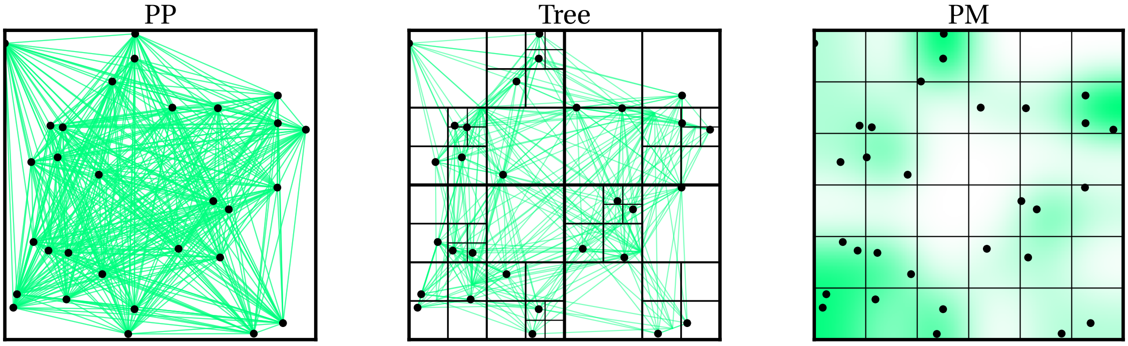

Figure 2.2: Each panel includes a simple schematic illustrating the particle-particle, tree code, and particle-mesh methods for force calculation. Black dots represent the locations of particles, and the force calculation is indicated with green. For the PP method, there are $30 \times 30 = 900$ force calculations. The tree method slashes the number of computations by recursively dividing the simulation space, and minimises the number of force interactions at longer ranges. The PM method divides the simulation space into a grid and calculates the gravitational potential in each cell, then interpolates this potential to find the force on each particle.

Tree-codes are far more efficient than direct-summation, but there is some overhead when calculating the tree structure. However, this is still faster than calculating the forces in the tree (Aarseth, 2003). They also demand a larger memory in order to store the tree, and the reliance on a rigid geometric grid can be restrictive.

Another approximation method is Particle Mesh (PM) (Hockney & Eastwood, 1981), in which the particle distribution is divided amongst a mesh grid. The force on a particle m can then be approximated as the force from each grid cell. This simplifies the computation, but sacrifices the accuracy of the force calculation at short ranges. More complex variations of the PM method include hybridisation with the PP method to accommodate high accuracy force computation at close ranges (see Efstathiou et al., 1985). In mesh type methods, gravitational forces are found from the gravitational potential by solving the Poisson equation:

$$\nabla^2\Phi = 4\pi G\rho, \tag{2.2}$$

where Φ is the gravitational potential and ρ is the density. The potential is then interpolated across the grid structure so that the particles experience a smooth potential. This method can easily exploit fast fourier transforms to improve efficiency to $\mathcal{O}(N \log N)$ (Press et al., 1992). Schematic illustrations of these methods are presented in Figure 2.2.

A further complication comes from the fact that cosmological simulations take place in an expanding Universe, where large scales are better described by a Friedmann-Lamaître-Robertson-Walker spacetime (Komatsu et al., 2011). The equations defining the system must transition from Newtonian gravity at galactic scales to general relativistic expansion at the largest scales (e.g. Colombi, 2001). This is typically achieved by simulating the Universe as an expanding ‘box’ with periodic boundary conditions (i.e. the box tiles in all directions to create a pseudo-infinite system), where the expansion rate is tuned to predictions from observation.

Time-stepping

To evolve the system, the phase-space information of the particles must be updated for a new time. This can be achieved by deriving the positions and velocities from the particle forces over successive time steps, where the accuracy of the evolution is improved with decreasing step size. In the simplest approach, the system of particles can be stepped through time in unison using constant time steps. This can prove expensive, and particles undergoing more extreme interactions will be prone to errors. Many modern integrators use variable time steps that can be tuned to the needs of the simulation, and these can both decrease computational cost and reduce error (Dehnen & Read, 2011).

One example of a time integrator is the Leapfrog scheme (Hockney & Eastwood, 1981), which is a popular choice for orbit calculation due to its simplicity, time reversibility and the fact that it is symplectic (conserves angular momentum). The scheme is so-named because it calculates positions and velocities in alternating steps as if they are leap-frogging over each other. Each calculation that updates the positions is called a 'drift', and each calculation that updates the velocities is called a 'kick'. The Leapfrog scheme can be written:

$$\begin{aligned} x_{i+1} &= x_i + v_i \Delta t + \frac{1}{2} a_i \Delta t^2, \\ v_{i+1} &= v_i + \frac{1}{2} \left(a_i + a_{i+1} \right) \Delta t, \end{aligned} \tag{2.3}$$

where Δt is the timestep, i is the current time step, $i+1$ is the next time step after Δt, x is the position, v is the velocity and a is the acceleration on each particle. Here, kick and drift steps have been combined so that the integrator can be expressed in terms of a single updated position and velocity.

The success of time integrators is generally measured by their accuracy (ability to conserve energy, although this is broken for cosmological simulations with an expanding Universe), their speed, and their adaptability (e.g. variable time steps). The best choice often depends on the goals of the simulation.

Numerical errors

A consequence of representing a DM fluid as discrete particles is the introduction of two-body numerical relaxation, similar in effect to the relaxation time of stars in GCs and galaxies. However, whilst the relaxation time for stellar systems is a physical effect, the relaxation time for DM systems is an undesired numerical artefact. The relaxation time can be approximated as:

$$t_{\text{relax}} \sim \frac{N}{8 \ln \Lambda} t_{\text{dyn}}, \qquad \Lambda = b_{\text{min}} / b_{\text{max}}, \tag{2.4}$$

where N is the number of particles, t_{dyn} is the dynamical time (the time needed for particles to transverse a significant fraction of their orbit), and b_{min} and b_{max} are the maximum and minimum impact parameters for particle-particle interactions. t_{relax} decreases as the DM fluid is resolved by fewer simulation particles, with the result that the densest regions experience artificial kinematic heating. This jeopardises the physical accuracy of the simulation in the very centres of DM haloes, which are precisely the regions of interest for the small-scale puzzles in Section §1.5. The numerical heating can be reduced by increasing N, though this is computationally expensive (Dehnen & Read, 2011).

In a similar vein, close particle encounters can result in divergent forces that are difficult to compute, i.e. $\|\boldsymbol{q}_j - \boldsymbol{q}_i\| \to 0$. These effects are reduced with the introduction of a force softening length ϵ (Dyer & Ip, 1993):

$$\boldsymbol{F_{ij}} = \frac{G m_i m_j \left(\boldsymbol{q}_j - \boldsymbol{q}_i\right)}{\left(\|\boldsymbol{q}_j - \boldsymbol{q}_i\|^2 + \epsilon^2\right)^{3/2}}, \qquad \Psi = -\frac{1}{\sqrt{r^2 + \epsilon^2}}. \tag{2.5}$$

This parameter lowers the inter-particle force within a chosen distance, smoothing the granularity of the gravitational potential. Thus, the potential of each particle is represented as a Plummer sphere (Plummer, 1911), for which the peak potential is truncated. Despite limiting the close-range interactions between particles, force softening only slightly improves the relaxation time of the system. Whilst close-range interactions significantly perturb particle orbits, they are much less common than long-range interactions, and the combination of many long-range interactions are dominant even with force softening (Theis, 1998). A natural side-effect of ϵ is that Newtonian gravity is broken at small scales, and care has to be taken to ensure that gravity is faithfully represented at the scales of interest.

2.1.3 Gas

Modelling baryonic gas presents a challenge beyond that of DM: gas interacts via the electro-magnetic force, meaning it has temperature, pressure and is dissipative. Gas is well described with Newtonian fluid dynamics, and adheres to the Navier-Stokes equations, which are then simplified to the Euler equations by assuming negligible viscosity:

$$\begin{gathered}
\frac{\delta \rho}{\delta t} + \nabla \cdot (\rho \boldsymbol{u}) = 0, \\
\frac{\delta}{\delta t}(\rho \boldsymbol{u}) + \nabla \cdot (\rho \boldsymbol{u} \otimes \boldsymbol{u}) + \nabla p = -\rho \nabla \phi, \\
\frac{\delta}{\delta t}(\rho e) + \nabla \cdot [\rho \boldsymbol{u})(e + p/\rho)] = -\rho \boldsymbol{u} \cdot \nabla \phi,
\end{gathered} \tag{2.6}$$

where ρ is the density, $\boldsymbol{u}$ is the fluid velocity, e is the specific total energy, and p is the thermal pressure (equations as in Teyssier, 2002). These equations conserve mass, momentum and energy. The equations as written here assume a static Universal background, and as with DM they must be adapted to accommodate an expanding Universe.

There are two popular methods to model gas in cosmological simulations, which have inherent benefits and detractors respectively.

- Lagrangian approach: Gas is modelled with a distorted mesh or particles that trace the form of the gas. This approach is well-suited to simulations with a wide dynamical range because the mesh/particles can naturally condense and expand to best sample the gas properties.

- Eulerian approach: The gas properties are calculated for grid cells on a mesh. The resolution of this mesh can be refined following Adaptive Mesh Refinement (AMR) techniques to allow for large dynamical ranges. The flux of gas properties are then convected across cell boundaries with time. This has the disadvantage that the movement of gas flows throughout the cosmological volume cannot be tracked without the addition of tracer particles. However, the approach allows for refinement on any desired property rather than simply the mass. This approach tends to perform better under gas shocks and instabilities due to the rigidity of the mesh, but suffers from diffusion errors if gas is moving through the grid at high velocities (e.g. Pontzen et al., 2021a).

Modern methods such as the 'moving-mesh' employ tessellated grid cells in a Voronoi mesh, in which cell position and size evolve to follow the flow of gas (as in Vogelsberger et al., 2014). This method mitigates the direction dependent errors of rigid grids.

2.1.4 Radiative transfer

Commonly, ionising radiation in cosmological simulations is either ignored entirely or approximated as a uniform background field with a time-dependent intensity. Generally this is a reasonable approximation, but as described in Chapter 1, the radiation landscape of the Universe is far from homogeneous and can have important repercussions on quenching timescales.

A complete solution would directly model the propagation of various kinds of radiation (including photoionisation, collisional ionisation, collisional excitation, recombination, bremsstrahlung, homogeneous Compton cooling/heating of the cosmic-microwave background, di-electronic recombination, etc). Resolving these effects is extremely difficult, and carries a heavy computational cost.

The cosmological equation for radiative transfer can be described as (Gnedin & Ostriker, 1997; Abel et al., 1999):

$$\frac{1}{c}\frac{\partial I_v}{\partial t} + \frac{\hat{n}\cdot\nabla I_v}{\bar{a}} - \frac{H(t)}{c}\left(v\frac{\partial I_v}{\partial v} - 3I_v\right) = \eta_v - \chi_v I_v, \tag{2.7}$$

where I_v describes the intensity of the radiation field at a given time, distance, direction and photon frequency, $\hat{n}$ is the unit vector for the radiation direction, and $\hat{a}$ accounts for the change in photon frequency v due to cosmic expansion. η_v and χ_v are the emission and absorption coefficients for the radiation. The parameters c and $H(t)$ correspond to the speed of light in a vacuum and the time-dependent Hubble constant, respectively. This equation is incredibly complicated to solve, includes many dimensions, and is difficult to implement in massively parallel cosmological codes.

Radiative transfer calculations can be achieved using a variety of ray-tracing (e.g. Mihalas & Mihalas, 1984; Haardt & Madau, 1996; Madau et al., 1999; Abel et al., 1999) and moment schemes (e.g. Gnedin & Abel, 2001; Aubert & Teyssier, 2008; Petkova & Springel, 2009). Ray-tracing schemes follow the propagation of light as 'rays' which then spread and interact with the chosen hydrodynamics solver. A standard approach is to integrate the equation over a set of interconnected hydrodynamic cells, for which the computational cost scales with the number of cells and with their level of inter-connectivity. Moment schemes reduce the number of dimensions involved by tracking only the lower-order moments of Equation 2.7, and approximating the contribution of higher-order moments. Whilst this is more efficient, it is also less accurate and can lead to over-ionisation (Wu et al., 2021).

2.1.5 Cooling

Gas cooling is responsible for the collapse of gas clouds and ultimately the formation of stars, which I discuss in Section §2.2. The principle processes are radiative energy losses like Bremsstrahlung (which dominates the cooling at high temperatures) and enhancement from metal-line cooling (which dominates the cooling at lower temperatures). The presence of metals increases the cooling rate by introducing new atomic emission lines (Omukai, 2000, 2001). Therefore, the cooling rate of the gas depends in part on metal enrichment

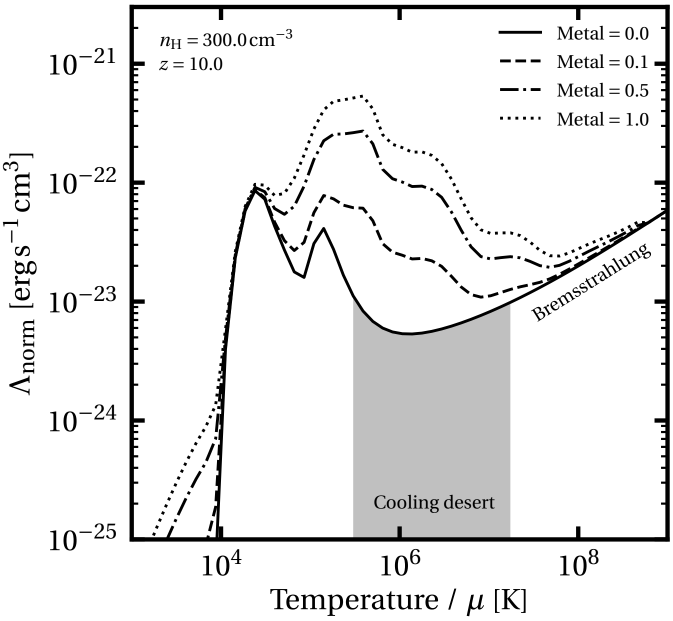

Figure 2.3: Normalised net cooling rates from all radiative processes versus gas temperature divided by the molecular weight μ, as defined by the cooling tables in RAMSES for an EDGE simulation. The rates are taken at $z = 10$ (prime star forming time), for a hydrogen number density of 300 atoms cm^{-3} (the threshold for star formation in EDGE) and a selection of metallicities. At this early time, gas enrichment is typically low. The grey shaded region indicates a 'cooling desert' where radiative cooling is especially inefficient. At high temperatures, radiative cooling is dominated by Bremsstrahlung.

from stellar physics. Correctly modelling metal-line cooling is crucial because it not only increases the star formation efficiency within a galaxy, but the ejection of metals into the IGM also promotes the condensation of gaseous fuel into the galactic centre (Madau et al., 2001).

Modelling the cooling rate becomes challenging in extreme scenarios such as SNe explosions. Realistically, each SNe results in an enormous gas blowout as in Figure 1.12, with important consequences for galaxy evolution as in Section §1.5. The pressure of this blowout is dependent on the temperature of the gas. If SNe energy is injected directly onto a hydrodynamics grid, then the energy will be distributed across a cell and its neighbours ($3^3 = 27$ gas cells). The resulting temperature on the grid cells can be calculated as:

$$T_\mathrm{cell} = \frac{2}{3k_\mathrm{B}}\left[\frac{N_\mathrm{SN}\times\epsilon_\mathrm{SN}}{n_\mathrm{H}\frac{\mathrm{M}_\odot}{m_\mathrm{p}}\Delta x^2 N_\mathrm{cell}^3}\right], \tag{2.8}$$

where $k_\mathrm{B} = 1.38\times10^{-23}\,\mathrm{m}^2\,\mathrm{kg}\,\mathrm{s}^{-2}\,\mathrm{K}^{-1}$ is the Boltzmann constant, N_SN is the number of SNe events, ϵ_SN is the individual SNe energy, n_H is the number density of hydrogen, m_p is the mass of a proton, Δx is the width of a grid cell and N_cell is the number of grid cells. Diluting of SNe energy over an unrealistically large volume causes gas temperatures to be artificially depressed. Therefore, the gas temperature is limited by the resolution of the hydrodynamics grid. Particle-based Lagrangian codes are subject to a comparable problem related to the mass resolution of the gas particles (see Springel & Hernquist, 2002).

An example cooling function from the EDGE simulation suite (see Chapter 3) is presented in Figure 2.3 with a selection of different metallicities. This highlights the efficient radiative cooling at low (reaching its peak just above $10^4\,\mathrm{K}$) and high temperatures, mediated by an inefficient 'cooling desert'. The maximum resolution sets a natural minimum gas temperature, below which the gas collapses into stars. In simulation codes this temperature is often around $10^4\,\mathrm{K}$. This means the energy deposited by SNe is quickly radiated away before it impacts the ISM, resulting in less violent explosions (Katz, 1992). This is known as the over-cooling problem (discussed in Smith et al., 2018)[1].

Potential solutions to this problem include modifying the cooling of the gas surrounding SNe (Springel, 2000; Thacker & Couchman, 2000; Stinson et al., 2006), preheating the gas to push it past the cooling peak near $10^4\,\mathrm{K}$ (Bialek et al., 2001; Muanwong et al., 2002), depositing some of the SNe energy in the form of kinetic energy (Navarro & White, 1993; Mihos & Hernquist, 1994), depositing larger amounts of energy (Dalla Vecchia & Schaye, 2012), amongst others. These strategies all have associated side-effects, which risk the physical accuracy of galaxy formation. Ideally, the gas is resolved at sufficiently high resolution that it can cool to temperatures of $\sim 100\,\mathrm{K}$, which alleviates the over-cooling problem (Ceverino & Klypin, 2009).

2.2 Stars

The physics governing the birth and evolution of stars operate at scales far below the resolution limit in modern cosmological simulations. Instead, they must be described using so-called "sub-grid" physics. In the field, stars form from the collapse of dense molecular gas clouds. Whether the gas collapses or not is determined by a competition between potential and kinetic energy. When potential energy dominates kinetic energy, instability leads to collapse. The fate of gas clouds is then dependent on density and temperature, leading to the Jeans length and Jeans mass – the scales on which gas collapses:

$$\begin{aligned} L_{\mathrm{Jeans}} &= \left(\frac{15 k_{\mathrm{B}} T}{4\pi G m_{\mathrm{p}} \mu \rho}\right)^{1/2}, \\ M_{\mathrm{Jeans}} &= \left(\frac{5 k_{\mathrm{B}} T}{G m_{\mathrm{p}} \mu}\right)^{3/2} \left(\frac{3}{4\pi\rho}\right)^{1/2}, \end{aligned} \tag{2.9}$$

where T is the gas temperature, ρ is the gas density, μ is the mean molecular weight and m_{p} is the proton mass. By rearranging Equation 2.9, a critical threshold density for star formation can be derived. Gas clouds exceeding this critical threshold density have sufficient gravitational potential energy to overwhelm the kinetic energy, leading to collapse. Observations of molecular clouds predict that these densities are extremely high (atoms $\mathrm{cm}^{-3} > 10^3$ Lada et al., 2010; Evans et al., 2014).

Of course, the minimum size and mass scales in simulations are set by their resolution, and anything below those scales must be treated as if it becomes Jeans unstable. In Figure 2.4 I show how the critical threshold density in Eulerian schemes is set by the choice of spatial resolution and temperature floor. A similar relationship exists for simulations using the Lagrangian approach, where the minimum spatial scale is replaced by the minimum mass scale. Kim & Ostriker (2015) present a detailed discussion of the resolution required to capture SNe feedback without falling prey to the over-cooling problem. They find that for dwarf galaxies, the ideal spatial resolution is between 1 and 10 pc.

---

[1] Not to be confused with a similar over-cooling problem which stipulates that feedback is needed to prevent excessive gas cooling in early galaxies (see Katz & White, 1993).

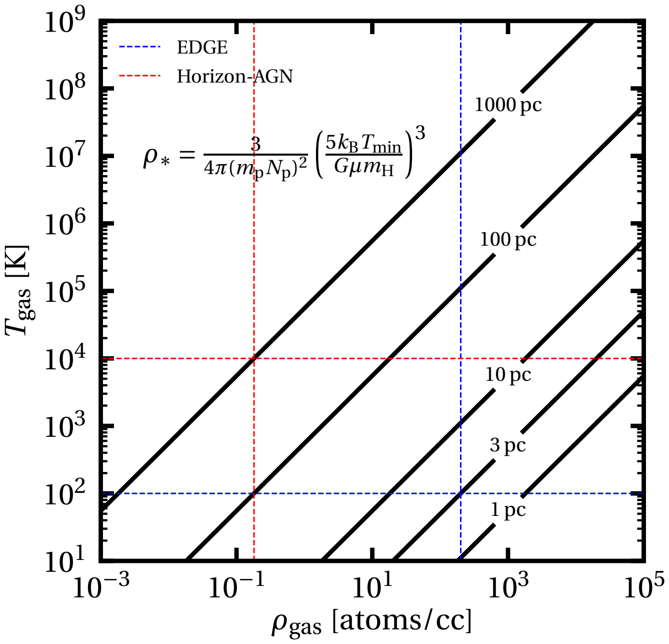

Figure 2.4: Here I show the Jeans length L_{Jeans} (black lines) as calculated over a range of gas temperature and density. Over-plotted are coloured dashed lines that represent the maximum gas densities allowed by the chosen minimum gas temperature and scales in simulations. I compare the large-scale survey simulation Horizon-AGN (Kaviraj et al., 2017) with the cosmological-zoom EDGE simulations (Agertz et al., 2020). Improved spatial resolution, combined with lower temperature floors, allows for higher density gas clouds to be resolved.

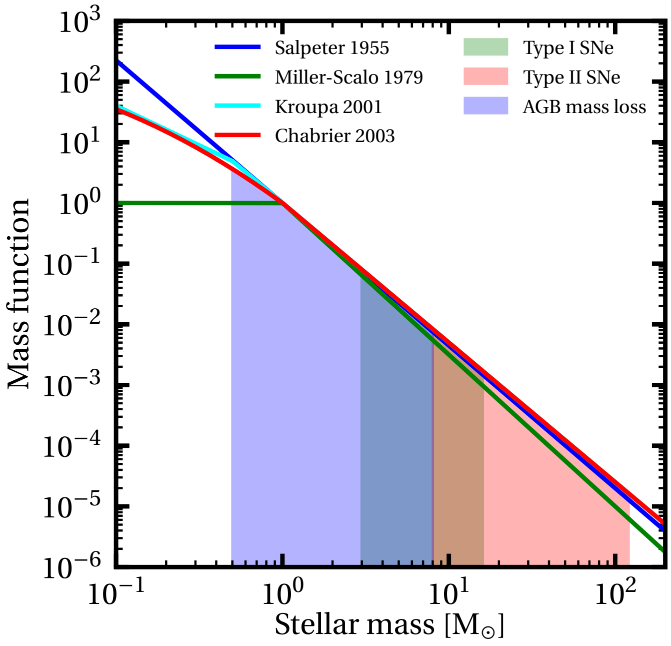

Figure 2.5: This plot shows a selection of IMFs (Salpeter, 1955; Miller & Scalo, 1979; Kroupa, 2001; Chabrier, 2003). I also overlay regions corresponding to different stellar processes, which are covered in Chapter 3.

The star formation rate in simulated gas cells can then be approximated using a Schmidt law (Schmidt, 1959; Wechsler et al., 2002; Zhao et al., 2003; Li et al., 2007).

$$\dot{\rho_*} = \epsilon_{\mathrm{ff}} \frac{\rho_g}{t_{\mathrm{ff}}} \text{ for gas cells with } \rho_g > \rho_\star \text{ and } T_g < T_\star, \tag{2.10}$$

where ρ_* is the critical threshold density and $T_\star$ is a temperature above which star formation is prohibited. Here, ρ_g is the density per gas cell, $t_{\mathrm{ff}} = \sqrt{3\pi/32G\rho_g}$ is the local free-fall time of the gas, and ϵ_{ff} is the star formation efficiency per free-fall time. Essentially, any gas cell meeting certain temperature and density requirements will begin converting mass into stars at a rate calibrated to best match observation or theoretical predictions.

It would be computationally expensive to model every individual star, and so groups of stars are represented with “stellar particles”. These stellar particles inherit the phase-space information and chemistry from their progenitor gas cells. Each stellar particle represents a single stellar population, with a range of masses that can be drawn from an IMF. In Figure 2.5 I show a selection of popular IMFs. These are found to be universal, meaning that stellar populations are well described by these IMFs everywhere in the Universe. The IMF has seen a gradual refinement over the years as observational techniques have improved, with the biggest difference occurring at the highly populated low-mass end of the mass spectrum. Galaxy formation is affected not only by the chosen IMF, but also the way in which it is sampled. Applebaum et al. (2020) find that a stochastically sampled IMF (more physically representative, but cannot sample stars with higher masses than the star particle) results in burstier stellar feedback.

More complicated stellar physics such as stellar evolution, winds, and SNe can also be considered if necessary.

2.2.1 Resolution strategy

The resolution employed in simulations must be carefully chosen to support the science goals and physical processes involved. The simplest scheme is to have a single level of resolution throughout a cosmological volume. As the dark matter particles coalesce, they naturally begin to sample regions of higher density more effectively. Simulations of this type are normally used to produce a large-volume within which there are a significant number of dark matter haloes, allowing for statistical analysis (e.g. Klypin et al., 2011; Vogelsberger et al., 2014; Schaller et al., 2015). These simulations are incredibly costly, and are limited in the maximum resolution they can realistically attain. If a simulation has a mass resolution of $\mathcal{O}(10^7\,\mathrm{M}_\odot)$ (acceptable for a modern large-volume simulation) then dwarf galaxies of $10^9\,\mathrm{M}_\odot$ will only be resolved by one hundred particles and little meaningful analysis can be made.

Many galaxy properties demand higher resolutions in order to be resolved, such as central density profiles, small-scale gas turbulence and the formation of SCs. In some cases, galaxies can be simulated at incredibly high resolutions in fully isolated conditions. However, a cosmological context is necessary to model the full evolution of a galaxy. To solve this problem, the ‘zoom-in’ technique was developed to focus computer expenditure on one (or a subset) of galaxies within the full volume (Katz et al., 1994; Navarro & White, 1994; Tormen et al., 1997; Hahn & Abel, 2011). In a zoom simulation, the region of interest is simulated to an extremely high resolution while the surrounding box is left at a coarser resolution. The region of interest must be carefully selected to ensure the coarser surroundings do not collapse into and mix with it. A buffer region, where the resolution is incrementally improved, is usually included to discourage unrealistic particle interactions at the boundary. Simulations of this type are able to resolve individual galaxies

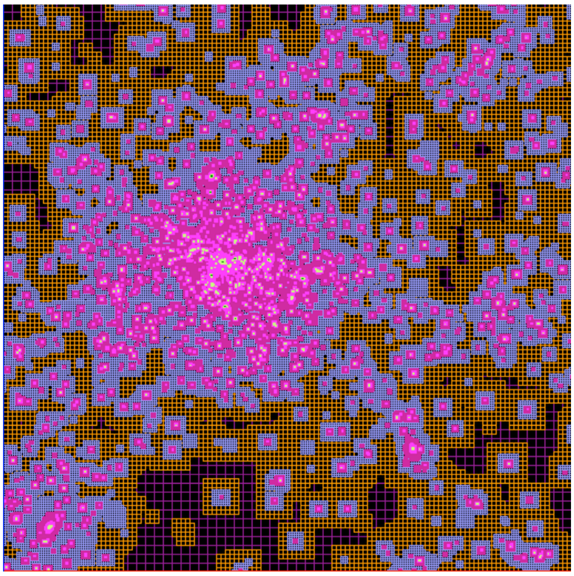

Figure 2.6: The cover image of the RAMSES userguide as it appears in Teyssier (2002). This shows a two-dimensional snapshot of an AMR grid, where octs of each resolution level are shown in a unique colour. This gives an indication of the adaptability of the AMR grid to a non-uniform background density. Harsh boundaries are avoided by enforcing a rule that octs can only border octs of an equal or ±1 resolution level.

in incredible detail, whilst submerging them in an environment of realistic gravitational torques (e.g. Springel et al., 2008; Hopkins et al., 2014; Grand et al., 2017).

2.3 Software

This project makes use of several simulation and analysis tools, which I describe now.

2.3.1 RAMSES

RAMSES (Teyssier, 2002) is a massively parallelisable dual N-body and hydrodynamics solver purpose built for cosmological and galaxy simulations. It makes use of AMR to optimise force integration. I use RAMSES for all my cosmological simulations, which form the bedrock of this project.

The N-body component of the code is used for the stars and DM particles. It is based upon an advanced PM scheme called a Fully Threaded Tree (FTT), which incorporates contributions from the PP scheme for close-range particles. Particles are grouped into a hierarchical tree structure comprising of octs, where the integration time-stepping increases by a factor of two for each successive resolution level. This tree structure is modified every timestep as the particles move through the simulation space (creating an AMR grid). The evolution of particles under gravity is found by solving the Poisson equation. This process is expedited by only resolving the force resolution as far as the current resolution level, ie, the coarse grid will experience forces from the fine grid as if they were the overall force from their parent oct.

The propagation of gas properties are computed by solving the Euler equations using a second-order Gudanov method, as in Saltzman (1994), with Riemann solvers. The flux of gas properties are calculated at the oct boundaries in the AMR grid, meaning that the resolution of gas properties traces the AMR grid.

The code units use conformal time such that co-moving coordinates are supported, as in Martel & Shapiro (1998). This allows for the easy implementation of cosmological expansion.

2.3.2 Nbody6

Nbody6 is a direct-summation N-body integrator designed for the evolution of GC systems. It represents the amalgamation of the N-body integrator Nbody5 with the detailed stellar evolution models of Eggleton, Tout and Hurley (Eggleton et al., 1989; Tout et al., 1997; Hurley et al., 2000). Nbody6 models individual stars with high force accuracy using the PP method, which is necessary for collisional systems such as GCs. Regularisation is used to model binary and higher-order stellar encounters, a crucial component in the long-term evolution of dense stellar systems which contributes to the 'core-collapse' phenomena (Lightman & Fall, 1978; Heggie, 1979).

In this project, I use a variant of Nbody6 called Nbody6DF which incorporates a semi-analytic solution to dynamical friction (Petts et al., 2015). This approximates the orbital decay of a GC in a host galactic potential based on Chandrasekhar's formalism (Chandrasekhar, 1943). Remarkably, the software is able to reproduce 'core-stalling' whereby orbital decay stalls within a cored potential profile.

2.3.3 Pynbody

Pynbody is an analysis and data reduction Python package for astrophysical simulations (Pontzen et al., 2013). It reads the outputs from a variety of popular simulation codes, and includes a library of analysis and post-processing tools which are well optimised and of high quality.

I use pynbody throughout my analysis pipeline, and have also contributed to its development through both bug fixes and a custom function
(see `pynbody.analysis.halo.halo_shape()`).

2.3.4 Tangos

Large cosmological simulations are unwieldy, calculating and storing fundamental halo properties is a difficult task. The tangos Python package provides a convenient solution to this problem (Pontzen & Tremmel, 2018a). With tangos, a user can generate database files which house halo properties, simulation metadata, and hierarchical merger trees. This data can be rapidly recalled with single-line commands. Combined with pynbody, this makes a powerful data storage tool.

A strength of tangos is the combination of halo properties with hierarchical merger trees. This allows for the rapid access of halo properties over the entire main progenitor branch, allowing for quick investigation into evolutionary trends.

I use tangos to calculate and store a comprehensive selection of halo and profile properties for all resolved haloes at every timestep, on the condition that they are below a certain contamination threshold.

2.3.5 GenetIC

When investigating galaxy formation and evolution, one may ask the question "How would a different formation scenario impact this galaxy?". To answer this question, one would need to find a candidate galaxy in the simulation volume which is *similar* to the original galaxy but with a differing formation scenario. Of course, this candidate galaxy may be the product of many unique formation events, and could be a poor comparison despite best intentions. It is here that the Genetic Modification (GM) technique is useful (Roth et al., 2016). Using the GM technique, the Initial Conditions (ICs) of a simulation can be forensically altered to change the formation of target galaxies in a controlled way. This allows for a direct comparison to be made.

The GM technique is implemented within the GenetIC code (Stopyra et al., 2021a). In general, a set of ICs used for a cosmological simulation assume a background density field with linear perturbations. In GenetIC, the approach is to map an existing initial density field to a new density field that satisfies a desired modification, whilst keeping the overall change to a minimum. This transformation is solved with the Hoffman-Ribak equation (Hoffman & Ribak, 1991). By minimising the overall change, the new density field is kept as close to a random realisation of a density field in ΛCDM as possible. GenetIC outputs the χ^2 value between initial and modified fields, allowing the user to judge the likelihood of the modified field. This allows users not only to discard improbable modifications, but also to quantify the rarity that certain formation scenarios have in a ΛCDM Universe.

Complications arise in the case of zoom-in ICs, whereby the Hoffman-Ribak equation cannot be consistently solved across boundaries between differing resolution levels. This causes discontinuities in the modified field that cause unrealistic ICs. The GenetIC code solves this problem by decomposing the density fields across resolution boundaries into high- and low-frequency Fourier modes. The higher resolution level is then given the low-frequency modes from the lower resolution level, forming a single consistent field which retains the high frequency modes inside the higher resolution level.

The EDGE project

3.1 What is EDGE?

3.1.1 Motivation and overview

As discussed in Chapter 1, there are various unsolved problems within the ΛCDM cosmological model. Resolving these problems is key to understanding the nature of DM and galaxy evolution. The ultra-faint dwarf regime is a natural laboratory for investigating these problems. Firstly, it is this mass range where the cracks in the ΛCDM paradigm are most severe. Secondly, the DM domination in dwarf galaxies makes them particularly susceptible to DM physics, feedback processes, and events such as reionisation. Finally, their low mass allows them to be simulated at much higher resolutions. This last reason is fortuitous, because extremely high numerical resolutions are required to accurately resolve the very centres of dwarf galaxies and the relevant physical processes.

Previous simulation projects have attempted to shed light on the low-mass dwarf regime, around the halo mass range $10^8 \leqslant M/\mathrm{M}_\odot \leqslant 10^{10}$. These include NIHAO (Wang et al., 2015), FIRE (Chan et al., 2015; Wheeler et al., 2015; Wetzel et al., 2016; Fitts et al., 2017), cosmological simulations in Munshi et al. (2017, 2019); Revaz & Jablonka (2018); Munshi et al. (2021), and ultra-faints in a LG context (Jeon et al., 2017; Applebaum et al., 2021). Despite their many achievements, different simulations tend to make varying predictions for galaxy formation. As an example, in Figure 3.3 I show the SMHM relation between these projects, demonstrating a large scatter. The EDGE project was designed to explore this mass regime at an unprecedented mass and spatial resolution, within a full cosmological context.

Over time, the collaboration has grown to involve a wide group of researchers from the University of Surrey, University College London (UCL) and Lund University. These have included Prof. Justin Read, Prof. Andrew Pontzen, Dr. Oscar Agertz, Dr. Martin Rey, Dr. Stacy Kim, Ethan Taylor, Alex Goater, and myself. Close to 75 RAMSES simulations have been run, spanning a range of resolutions, physics, and GMs. These have exhausted over 13 million CPU hours on the DiRAC[1] High Performance Computing (HPC) facility alone, with another few million on HPC systems at Surrey and UCL. Combined, the project occupies around 100 Tb of storage space. The EDGE collaboration have published 5 research papers to date, with many more in development.

My own role in EDGE has involved running and managing the main (non-GM) simulation suite. I have led the analysis and interpretation of the impact that baryons have on the EDGE dwarf DM haloes.

3.1.2 Science goals

EDGE was conceived to address a variety of science goals, which I quote verbatim from the original DiRAC project bid:

---

[1] DiRAC, or Distributed Research utilising Advanced Computing, is one of the UK's foremost high performance computing systems. They are dedicated to supporting scientific research to the Science and Technology Facilities Council (STFC). `https://dirac.ac.uk/`

Table 3.1: Details of all RAMSES simulations. The simulation labels denote different reference haloes selected from the initial void simulation. From left to right the columns are: the simulation label, the physics scheme employed, the mass resolution, the halo mass (M_{200c}) at $z = 0$, total stellar mass within the virial radius (r_{200c}) at $z = 0$, the projected half light radius of halo stars at $z = 0$, the mean stellar metallicity at $z = 0$, and the V-band magnitude at $z = 0$.

Name	**Physics**	**Resolution** $[m_{\rm DM}, m_{\rm gas}, m_*]/\mathbf{M_\odot}$	M_{200} **[M$_\odot$]**	r_{200} **[kpc]**	M_* **[M$_\odot$]**	$R_{\rm half}$ **[pc]** (projected)	**[Fe/H]**	M_V **(mag)**
Halo1445 fiducial DMO	DM-only	[1112, -, -]	1.66×10^9	24.94	-	-	-	-
Halo1459 fiducial DMO	DM-only	[1112, -, -]	1.70×10^9	25.17	-	-	-	-
Halo600 fiducial DMO	DM-only	[1112, -, -]	4.55×10^9	33.68	-	-	-	-
Halo605 fiducial DMO	DM-only	[1112, -, -]	3.95×10^9	33.31	-	-	-	-
Halo624 fiducial DMO	DM-only	[1112, -, -]	4.08×10^9	34.91	-	-	-	-
Halo1445 fiducial	Agertz+2020	[939, 147, 300]	1.35×10^9	23.31	7.91×10^4	0.16	-2.58	-6.35
Halo1459 fiducial	Agertz+2020	[939, 147, 300]	1.43×10^9	23.76	2.63×10^5	0.20	-2.40	-7.62
Halo600 fiducial	Agertz+2020	[939, 147, 300]	2.55×10^9	31.54	5.11×10^5	0.17	-2.43	-8.77
Halo605 fiducial	Agertz+2020	[939, 147, 300]	3.20×10^9	31.08	1.74×10^6	0.21	-2.21	-9.73
Halo624 fiducial	Agertz+2020	[939, 147, 300]	3.35×10^9	28.81	5.86×10^5	0.26	-2.30	-8.93
Halo1445 DMO	DM-only	[139, -, -]	1.65×10^9	24.92	-	-	-	-
Halo1459 DMO	DM-only	[139, -, -]	1.71×10^9	25.20	-	-	-	-
Halo600 DMO	DM-only	[139, -, -]	4.25×10^9	33.62	-	-	-	-
Halo605 DMO	DM-only	[139, -, -]	3.94×10^9	33.31	-	-	-	-
Halo624 DMO	DM-only	[139, -, -]	4.06×10^9	34.13	-	-	-	-
Halo1459 DMO GM:Later	DM-only	[139, -, -]	1.47×10^9	25.34	-	-	-	-
Halo1459 DMO GM:Latest	DM-only	[139, -, -]	1.47×10^9	23.34	-	-	-	-
Halo1445	Agertz+2020	[117, 18, 300]	1.32×10^9	23.10	1.35×10^5	0.10	-2.49	-6.93
Halo1459	Agertz+2020	[117, 18, 300]	1.43×10^9	23.75	3.77×10^5	0.10	-2.03	-8.03
Halo600	Agertz+2020	[117, 18, 300]	2.65×10^9	31.17	9.84×10^5	0.11	-2.50	-9.19
Halo605	Agertz+2020	[117, 18, 300]	3.13×10^9	31.08	1.93×10^6	0.10	-1.98	-9.91
Halo624	Agertz+2020	[117, 18, 300]	3.23×10^9	29.18	1.08×10^6	0.11	-2.20	-9.44
Halo1459 GM:Later	Agertz+2020	[117, 18, 300]	1.43×10^9	23.73	1.11×10^5	0.17	-2.62	-6.70
Halo1459 GM:Latest	Agertz+2020	[117, 18, 300]	1.38×10^9	23.45	8.65×10^4	0.30	-2.76	-6.44

1. What is the expected scatter in the $M_* - M_{200}$ relation below $M_{200} = 10^{10}\,\mathrm{M}_\odot$?
2. At what mass scale does reionisation quench galaxy formation?
3. Can we reproduce a galaxy like Leo T that has formed stars at a rate of $10^{-5}\,\mathrm{M}_\odot\,\mathrm{yr}^{-1}$ for a Hubble time, yet has somehow escapes quenching by reionisation?
4. Can dark matter cusp-core transformations occur in dwarfs below $M_{200} \sim 10^{10}\,\mathrm{M}_\odot$?
5. How many new dwarf galaxies will upcoming HI and photometric surveys find?
6. How many visible satellites do we expect to find orbiting nearby dwarf galaxies?
7. Can we form (dense) star clusters in 'ultra-faint' dwarfs, like those recently reported in Eridanus II, Andromeda XXV and Andromeda I?

These questions are all key to addressing the nature of DM and are particularly relevant given current and upcoming observational surveys which will explore dwarf galaxies to unprecedented depths (e.g. Gaia, SKA, James Webb Space Telescope (JWST), amongst others). I have focused on investigating goals 2, 4 and 7, whilst other goals have been addressed by members of the EDGE collaboration.

3.1.3 Philosophy

The EDGE project is designed with two key novelties that make it a powerful investigative tool. Firstly, the simulations are run at high resolution (cell lengths below 3 pc and particle masses of $100\,\mathrm{M}_\odot$). The spatial resolution is sufficient to capture the cooling radius of supernovae events (Kimm et al., 2015), thereby avoiding the over-cooling problem. This reduces the need for complicated subgrid physics models[2], and so the simulation results are more physically motivated. It also means that the centres of DM haloes are better resolved, which are key regions of interest for the small-scale puzzles in Section §1.5 and for comparison with observation. Galaxies can be simulated with increasingly high mass as computing power affords, with calibration to our original simulations when a reduction in resolution is necessary. This "bottom up" approach is distinct from the more traditional "top down" approach, where galaxies are simulated at increasingly high resolutions as computing power affords. The advantage to the approach in EDGE is that the subgrid models are "locked-in" with our original simulations, and do not need to be rebuilt when running galaxies of higher masses.

Secondly, all the initial conditions are designed with the GenetICs code (Rey & Pontzen, 2018; Stopyra et al., 2021a). This allows for the roles of mass assembly history and environment to be efficiently explored.

3.2 Subgrid physics

3.2.1 Star particles

Star particles are generated on a cell-by-cell basis when the local gas density exceeds $300\,m_\mathrm{p}\,\mathrm{cm}^{-3}$ and is below the threshold temperature of 100 K. The formation rate follows a Schmidt law as in Equation 2.10, where the number of new stars is decided using Poisson statistics. As shown in Agertz et al. (2020), galaxy formation in EDGE is relatively insensitive to the star formation rate. Each star particle is initialised at approximately

---

[2] Such as delayed cooling, artificially inflated SNe energies, and certain sub-grid wind models.

$300\,\mathrm{M}_\odot$, and is representative of a single stellar population described by a Chabrier IMF (Chabrier, 2003). This mass choice is great enough to allow for a statistically appropriate sampling of the IMF, and is necessary to accommodate mass loss from the feedback recipes that EDGE employs. Resolving individual stars would be more expensive, and demand physics such as magnetic fields (Krumholz & Federrath, 2019) which are not well understood. The star formation efficiency per free-fall time is set to 10%, motivated by findings in Grisdale et al. (2019) that this efficiency reproduces the observed star formation rates in giant molecular clouds.

Supernovae

Stellar evolution is calibrated on the stellar evolution code STARBURST99 (Leitherer et al., 1999). The number of stars exiting the main sequence to produce type I and II SNe follow equations 6 and 7 in Agertz et al. (2013), and is based upon the age-mass-metallicity fit given in Raiteri et al. (1996). The key mass regimes where these processes occur in EDGE are shown in Figure 2.5, and are as follows:

$$\begin{aligned} 3 \geqslant \text{Type Ia SNe}/\mathrm{M}_\odot \geqslant 16, \\ 8 \geqslant \text{Type II SNe}/\mathrm{M}_\odot \geqslant 40, \end{aligned} \tag{3.1}$$

where for Type Ia, it is assumed that this mass corresponds to a binary pair rather than an individual star.

Each SNe is modelled as a discrete event for stars greater than $8\,\mathrm{M}_\odot$, where the exact number of explosions is sampled following a Poisson law. For SNe where the cooling radius is resolved by at least six hydrodynamic grid cells (see Agertz et al. 2015), a thermal energy of 10^{51} erg is injected into the gas and the hydrodynamics solver then computes the propagation of momentum. If the hydrodynamic grid surrounding the SNe is too poorly resolved then there is a risk of over-cooling, and so the momentum is injected directly following the method described in Kim & Ostriker (2015). The vast majority ($> 90\%$) of SNe in EDGE are sufficiently well-resolved to avoid the over-cooling problem naturally (Agertz et al., 2020).

After each SNe event, a certain amount of mass is returned to the ISM through ejecta, leaving behind only a remnant Chandrasekhar mass of $1.4\,\mathrm{M}_\odot$. This has the effect of enriching the local gas with metals, of which only Iron and Oxygen are tracked in EDGE. The details are governed by equations 9 and 10 in Agertz et al. (2013).

Mass loss through winds

As lower mass stars reach the end of their evolution, they swell into red giants called Asymptotic Giant Branch (AGB) stars. Stars lose a large portion of their mass through stellar winds during the AGB phase of their evolution, and the contribution to the ISM is tracked in EDGE. Mass loss is considered for stars in the following mass range (and shown in Figure 2.5):

$$0.5 \geqslant \mathrm{AGB}/\mathrm{M}_\odot \geqslant 8, \tag{3.2}$$

where the loss is calculated continuously and averaged over the stellar IMF for all stars in the AGB phase following equation 17 in Agertz et al. (2013), and then deposited in the local hydrodynamic grid cell.

3.2.2 Hydro

Cooling

The metal line gas cooling for hot gas ($T > 10^4\,\mathrm{K}$) is computed with CLOUDY (Ferland et al., 1998). Then, for cold gas ($T \leqslant 10^4\,\mathrm{K}$) the cooling is calculated based on fine structure rates from (Rosen & Bregman, 1995). An example of the net cooling rates were shown earlier in Figure 2.3, and are increased with metal enrichment.

The gas field is initialised with a background Oxygen metallicity of $10^{-3}\,\mathrm{Z}_\odot$. This is to provide coolant to encourage the formation of stars, which would naturally be provided by Population III stars that are not included in EDGE[3]. It is noted in Agertz et al. (2020) that the star formation rate is not sensitive to this background metallicity due to the presence of other coolants and cooling pathways.

Reionisation

The epoch of reionisation is modelled with a spatially uniform and time-dependent UV background, as implemented in the public version of RAMSES. The luminosity of the UV background follows that of Haardt & Madau (1996), but with a cut-off at the earliest times ($z > 10$) to avoid overheating the IGM (Oñorbe et al., 2017). The outcome of this UV background is to mimic a delayed reionisation, such as could be expected for dwarf galaxies in a cosmic void where there are less ionising sources nearby (see Keating et al., 2020). This background radiation is necessary, independent of whether radiative transfer physics are included, because the volume in EDGE is only 50 Mpc wide and cannot account for distant ionising sources. An artificial 'self-shielding' prescription is included so that dense gaseous regions are ionised at a reduced rate, as is expected for the centres of galaxies. See Appendix A in Rey et al. (2020) for a full description.

A discussion of the sensitivity of EDGE to the timing of reionisation is presented in Rey et al. (2020). There, a duplicate simulation is designed with a modified UV background, which reionises at an earlier time more consistent with that expected in non-void environments (Aubert et al., 2018). It is found that star formation is quenched earlier ($\sim z = 7$ as opposed to $\sim z = 4$), but rejuvenates at later times in a manner similar to the reference simulation. This has minimal consequence for the results of that paper, but could significantly change early-time gas flows that are critical for the gas flow mechanism in Section §1.5.1.

3.3 Design method

The EDGE suite began life as a simulation of a 50 cMpc Dark Matter Only (DMO) cosmic void[4] at a maximum particle resolution of 2048^3 in the zoom region, run over a full Hubble time. This void simulation was designed to accommodate a large number of dwarf galaxy haloes, from which zoom simulations can subsequently be run. The void environment was chosen to guarantee a large number of isolated halo environments within the simulation box. This progenitor simulation – and all those subsequently run – assumed cosmological parameters $\Omega_m = 0.309$, $\Omega_\Lambda = 0.691$, $\Omega_b = 0.045$ and $H_0 = 67.77\,\mathrm{km\,s^{-1}\,Mpc^{-1}}$, in line with data from the PLANCK satellite (Planck Collaboration et al., 2014)

A selection of candidate DM haloes were chosen from the void, with masses $10^9 \leqslant M_{200\mathrm{c}}/\mathrm{M}_\odot \leqslant 5 \times 10^9$. This is the mass contained within a radius $r_{200\mathrm{c}}$, defined as the

---

[3] While it would be feasible to include a Population III model, their physical description is uncertain and could introduce faulty results. See the discussion in Boley et al. (2009).

[4] The 'c' stands for comoving, meaning that the simulation space is 50 Mpc at $z = 0$ but smaller at earlier times due to cosmic expansion.

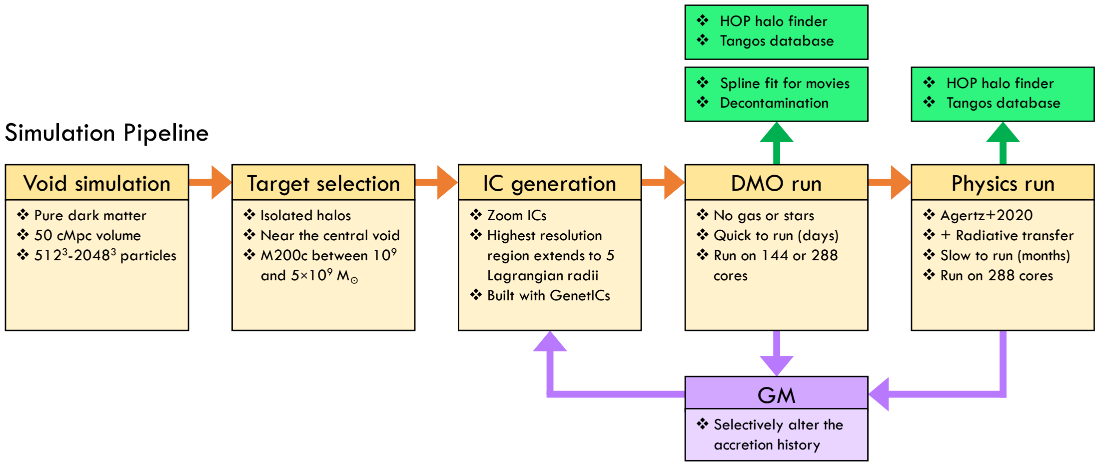

Figure 3.1: A visual map of the EDGE simulation pipeline.

limit where the DM halo is 200 times the critical density of the Universe at the current time. A set of ICs were created for each candidate halo using the zoom technique (Katz & White, 1993; Oñorbe et al., 2014), with resolution levels of 512^3, 1024^3, 2048^3, 4096^3, 8192^3, 16384^3, 32768^3. The maximum resolution region was chosen to extend for five Lagrangian radii around the target galaxy, so that the risk of contamination from lower resolution particles was minimised. In an additional step novel to EDGE, the velocity of the ICs were adjusted to match the velocity of the target halo. This reduces the impact of numerical diffusion effects innate to grid schemes, which have been shown to have undesired consequences for star formation (see Pontzen et al., 2020).

Each of these ICs were then integrated in RAMSES over the range $99 \geqslant z \geqslant 0$. Outputs were written to file in steps of $a = 0.01$, where a is the dimensionless scalefactor ($a = 1/(1+z)$). Refinement for the AMR grid was set to a minimum of 8 and maximum of 24 levels. Following simple arithmetic, $50\,\mathrm{Mpc}/2^{24} \approx 3\,\mathrm{pc}$, which is the minimum grid cell length supported in EDGE.

A suite of DMO simulations were run first, which affords the opportunity to tag any lower-resolution DM particles which entered the target galaxy by $z = 0$. These particles were upgraded to the highest resolution before running the full-physics simulations. The trajectory of the target halo was used to fit a cubic spline, which RAMSES uses to track the target halo and record movies. Simulations with baryonic physics, and/or with GM, were then run with these decontaminated ICs and movie parameters.

For each simulation, distinct bound structures were identified with the HOP halo finder (Eisenstein & Hut, 1998). Tangos databases were compiled for each simulation, including merger trees and halo properties. Throughout this thesis, the virial radius, $r_{200\mathrm{c}}$, is defined as the spherical region that is at least 200 times the critical mass density of the universe at that redshift. The halo mass $M_{200\mathrm{c}}$, is then the total mass of all matter contained within that radius. A visual summary of the entire pipeline is shown in Figure 3.1.

The EDGE suite simulations are summarised in Table 3.1, and include all simulations relevant to this thesis. Not included are lower resolution simulations run for testing purposes, simulations run with the inclusion of radiative transfer physics, various GM simulations, and simulations with otherwise modified physics recipes. The full void simulation is shown as a surface density plot in Figure 3.2, where the locations of each target halo are marked with zoomed-in subplots. This highlights that all EDGE haloes are chosen from a

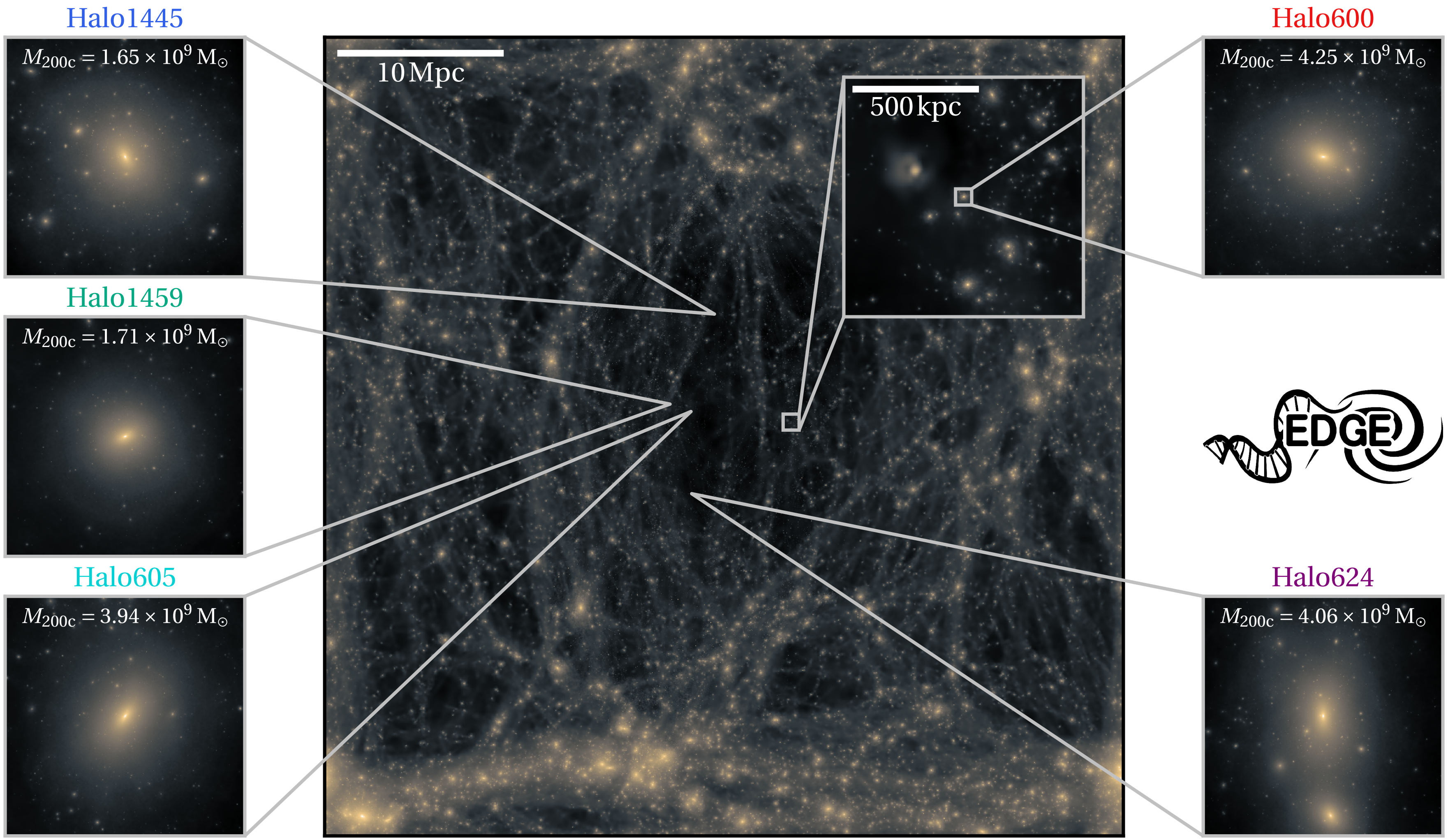

Figure 3.2: The location of the EDGE dark matter haloes selected for higher resolution resimulation from a lower resolution void at $z = 0$. Each panel shows a surface density plot of a cube. The zoomed panels for each halo are taken from the 'DMO' simulations out to r_{200c} (see Table 3.1), and show the corresponding M_{200c} mass, as marked. For Halo600, there is a partial-zoom to help illustrate how small the selected haloes are in comparison to the total box size (50 Mpc).

particularly under-dense region, without any major cosmic structure in the near vicinity.

3.4 How well does EDGE perform?

3.4.1 Comparisons

Generally, simulations are viewed favourably if they are able to reproduce observed galaxy properties. However, this can not be considered confirmation that the simulations are realistic or complete. It may be the case that errors conveniently act to eliminate each others effects, or that subgrid recipes have been over-calibrated to produce realistic outputs in spite of unrealistic physics. Furthermore, future observations may disagree with the simulation results. Nonetheless, here I make some broad comparisons between EDGE and observations.

In Figure 3.3 I show the SMHM relation for the dwarf galaxy regime, including results from EDGE (black stars) and abundance matching relations. The observed relations do not probe below $\sim 10^{10}\,\mathrm{M}_\odot$, and so observed data for individual dwarf galaxies are plotted in magenta. The EDGE simulation results are in broad agreement with the extrapolated abundance matching relations, but there are too few data points to draw firm conclusions.

In Figure 3.4, results from the 'fiducial' EDGE simulation suite are compared against observational data. The parameters shown are all key observables which are heavily relied upon in the literature. All simulated dwarfs lie within the parameter space mapped out by observational analogues. Though not shown here, the parameters of each EDGE dwarf tend to evolve along the observed scaling relations.

In Figure 3.5, a similar comparison is made between EDGE dwarfs and observed data but for the stellar metallicity versus absolute V-band magnitude. The magnitudes and metallicities for the EDGE dwarfs are averaged within the projected half light radius, because peripheral stars are likely below the limiting surface brightness threshold for observational surveys. This has the effect of removing particularly metal-poor stars, with are preferentially situated at the outskirts of the dwarfs. The EDGE dwarfs are all isolated, and should therefore only be compared against tidally isolated dwarfs. Fortunately, this is the case for most LG dwarfs. The Sagittarius (Sag) dSph is an example of a tidally disrupted dwarf (Johnston et al., 1995), and is an outlier on this figure. However, the pre-infall stellar mass can be reconstructed from inspection of its tidal tails (Niederste-Ostholt et al., 2012), yielding a brighter dwarf that moves back onto the relation (represented by the red 'x'). In (Agertz et al., 2020) it was shown that the metallicity versus absolute V-band magnitude is sensitive to the choice of feedback scheme, and is also the most difficult relation to get right in simulations.

3.4.2 Known caveats

The EDGE simulation suite is far from perfect, and there are known physical processes which are unresolved and/or unmodelled:

- The EDGE simulations that include radiative transfer are missing certain radiation components, including photoelectric heating (see Draine, 1978), cosmic rays, and resonantly scattered Ly-α photons. These effects are excluded due to their computational difficulty, and are expected to diminish the stellar mass formed in dwarf galaxies.

- Binary stars are not included in the modelling of the stellar particles, beyond the basic consideration of Type Ia SNe. This has implications on the production of ionising

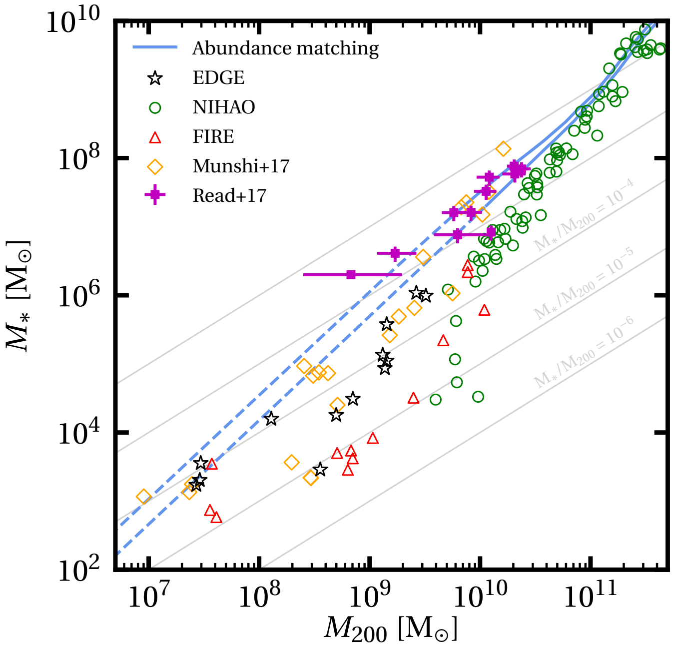

Figure 3.3: The SMHM relation for a selection of EDGE dwarfs (black stars, also including GM simulations that are not present in Table 3.1), the NIHAO project (Wang et al., 2015) (green circles), the FIRE project (Chan et al., 2015; Wheeler et al., 2015; Wetzel et al., 2016; Fitts et al., 2017) (red triangles) and simulations from Munshi et al. (2017) (orange diamonds). In light blue lines are abundance matching relations from Moster et al. (2010); Behroozi et al. (2013); Read et al. (2017), where the lines transition to a dashed linestyle below a stellar mass of 2×10^7 M$_\odot$ – where the abundance matching is less certain. Also included are individual dwarf galaxy observations which explore below the limit of observed relations (magenta stars) Read et al. (2017). Lines of constant M_*/M_{200} are added in light grey.

radiation (e.g. Ma et al., 2016), stellar feedback (Jeon et al., 2015), and on long-term stellar evolution as binary mergers inflate the proportion of high-mass stars.

- There is no modelling of cosmological magnetic fields. Simulated magnetic fields act to enhance the pressure of the IGM, leading to suppressed star formation (Marinacci & Vogelsberger, 2016). Magnetic fields can be more critical in larger galaxies, where interactions between magnetic loops and rotating disks generate a dynamo which amplifies the magnetic effect (Steenbeck et al., 1966; Rieder & Teyssier, 2017). There is minimal disk formation, or coherent gas rotation, in EDGE.

- The existence of black holes, and therefore of AGN, are not considered. The collapse of material onto a central black hole generates a huge amount of radiation, which is hypothesised to be the dominant source of feedback and galaxy quenching in the most massive galaxies (Croton et al., 2006; McNamara et al., 2006; Li et al., 2020; Su et al., 2021). Whilst AGN are far less prevalent in the dwarf regime, there is growing evidence for their existence (Lemons et al., 2015; Pardo et al., 2016; Baldassare et al., 2017; Mezcua et al., 2018; Bellovary et al., 2019; Birchall et al., 2020). It remains uncertain whether AGN, in addition to reionisation and stellar feedback, must be invoked to fully explain quenching in dwarf galaxies (Silk, 2017; Dashyan et al., 2018).

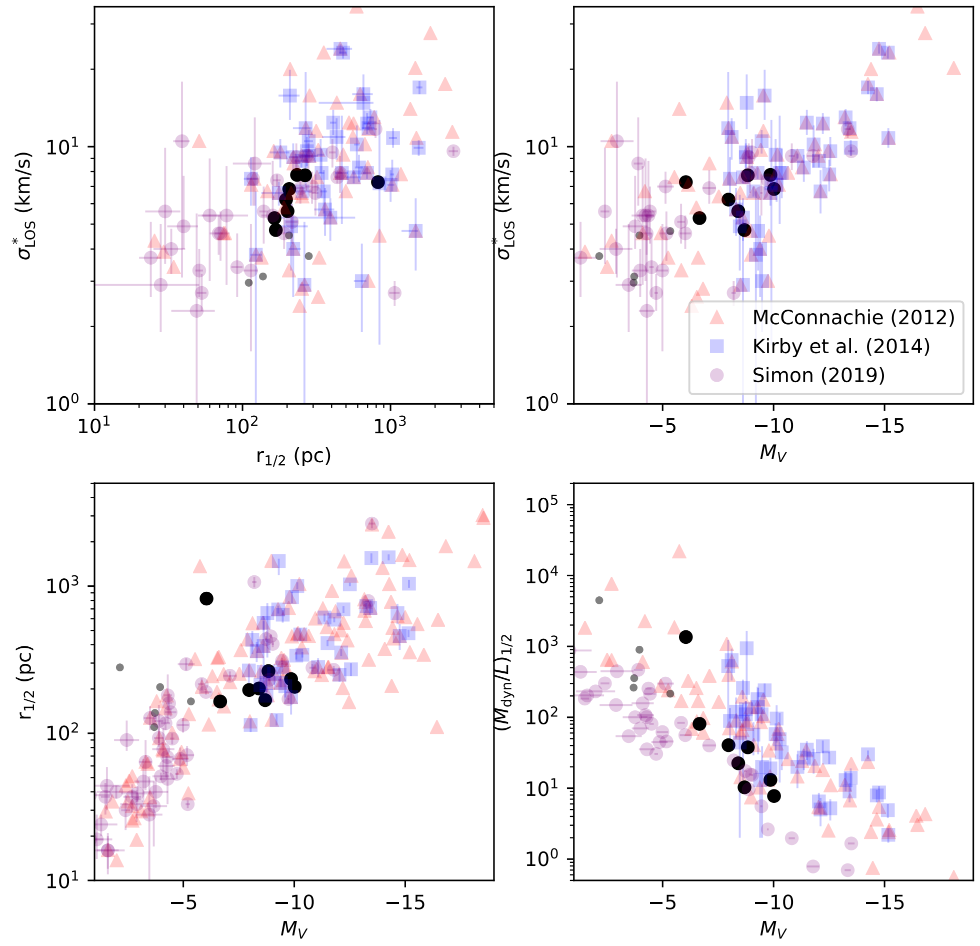

Figure 3.4: A selection of plots comparing EDGE simulation data (black/grey circles) to observational data from McConnachie (2012) (red triangles), Kirby et al. (2014) (blue squares) and Simon (2019) (purple circles). Black circles represent primary haloes, as listed in Table 3.1, whereas grey circles represent other well-resolved dwarfs in the simulation space. For simulation data, the stellar velocity dispersion are calculated as $\sigma^*_{\rm LOS} = \sigma^*_{\rm 3D}/\sqrt{3}$, $r_{1/2}$ is the projected stellar half light radius, M_V is the absolute V-band magnitude and $M_{\rm dyn} = 3\sigma^2 r_{1/2}/G$ is the dynamical mass estimator as in Kirby et al. (2014). Figure credit to Dr. Stacy Kim.

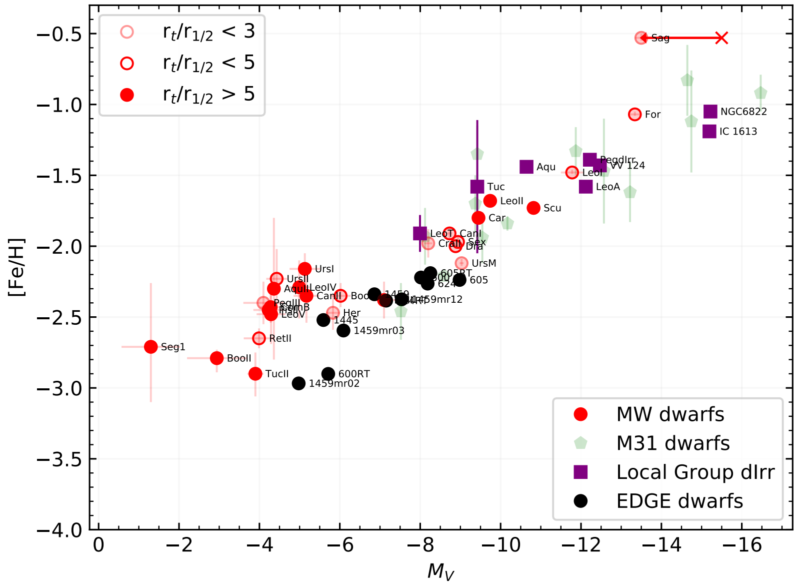

Figure 3.5: Comparison of metallicity versus absolute V-band magnitude relations between EDGE dwarfs and observational data from Kirby et al. (2013); Simon (2019). The metallicity for EDGE dwarfs is calculated as in Equation 3 from Escala et al. (2018) for stellar particles within the half light radius. For the MW dwarf candidates, the point style represents the ratio of the tidal radius to the half light radius. This indicates how isolated the dwarfs are, with solid data points being the most isolated. The EDGE dwarfs are isolated, and should be compared only with tidally isolated dwarfs. For Sagitarrius (Sag), a red 'x' and arrow indicate the pre-infall brightness (Niederste-Ostholt et al., 2012). Figure credit to Dr. Stacy Kim.

In spite of these missing or inaccurate mechanisms, Section 3.4.1 shows that EDGE simulations are in good agreement with a variety of observations. In many cases, the missing physics have subdominant effects compared to the processes which are resolved. For others, it is possible that processes act to cancel each other's effect.

3.5 Key results from EDGE

The EDGE collaboration has already resulted in several research outputs for which I am coauthor, with many interesting results. I summarise some of these here.

- In Agertz et al. (2020) a comprehensive grid of simulations found that galaxy properties such as size, velocity dispersion, V-band magnitudes and mass-to-light ratios are all relatively insensitive to subgrid recipes and physics (with the exception of removing stellar feedback). I show this in Figure 3.6. The stellar mass-metallicity relation is the only observable property found to distinguish different physics schemes.
- Rey et al. (2019, 2020) find a new kind of galaxy at $2-5\times10^9\mathrm{M}_\odot$ that rejuvenates due to a slow gas and mass accretion, possibly explaining the nature of galaxies like Leo T and Leo P (Irwin et al., 2007; Weisz et al., 2012b; Clementini et al., 2012). A prediction is made for two new classes of galaxy: gas rich quenched ultra-faints that may have

already been found in Janesh et al. (2019), and ultra-faints with no intermediate-age stars.

- Rey et al. (2019) finds the scatter in assembly histories of an ultra-faint dwarf galaxy generate significant scatter in their present-day surface brightness and stellar mass. A prediction is made for the existence of ultra-diffuse ultra-faint dwarfs below a surface brightness of $32\,\mathrm{mag\,arcsec}^{-2}$.
- From a more technical perspective, the work in Pontzen et al. (2021a) found that a high velocity of a simulated galaxy with respect to its hydrodynamic grid results in a numerical diffusion that suppresses the gas filaments feeding the galaxy. The consequence is to delay the onset of star formation and increase the burstiness of star formation at later times. This increased burstiness yields shallower dark matter cores through the gas flow mechanism discussed in Chapter 1. Fortunately, the effects can be mitigated by zeroing the initial grid velocity on the target halo. This zeroing is employed throughout EDGE.

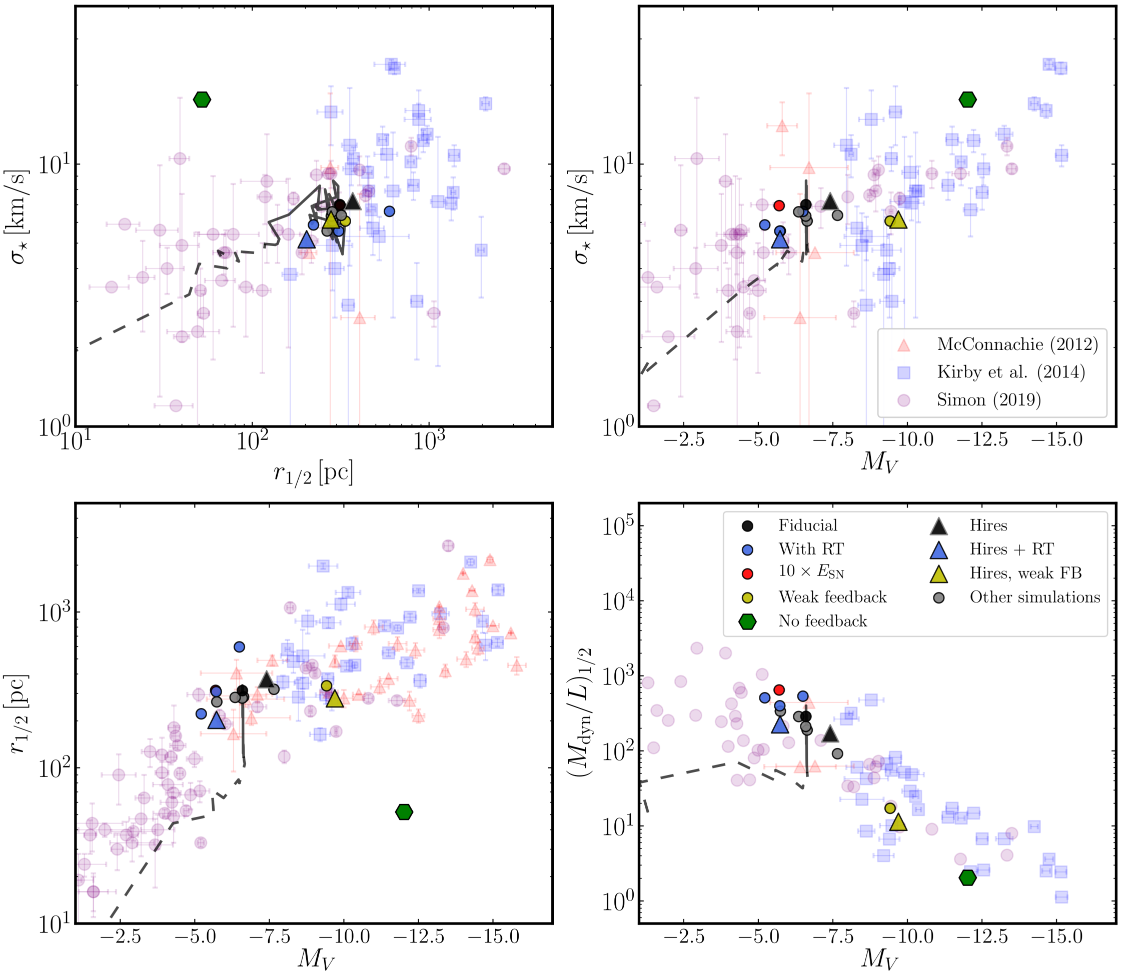

Figure 3.6: Plots showing various observable properties of EDGE simulations in Agertz et al. (2020) compared to observational data from McConnachie (2012) (red triangles), Kirby et al. (2014) (blue squares) and Simon (2019) (purple circles). These demonstrate that the EDGE simulations, which involve various physics schemes, are all within the scatter of observational data (with the exception of the 'No feedback' simulation). The 'Fiducial' physics simulation includes a tail to indicate its evolution with time, where the solid line is from $4 \leqslant z \leqslant 0$ and the dotted line $z > 4$.

Two routes to dark matter core formation in ultra-faint dwarfs

The content of this chapter has been submitted, and passed review, to Monthly Notices of the Royal Astronomical Society as "*EDGE: Two routes to dark matter core formation in ultra-faint dwarfs*". Section 4.4.3 makes use of simulations run in the GRIFFIN code. Whilst I designed these simulations, created their ICs and analysed them, the simulations were themselves run by Dr. Imran Nasim.

4.1 Abstract

In the standard Lambda cold DM paradigm, pure DM simulations predict dwarf galaxies should inhabit DM haloes with a centrally diverging density 'cusp'. This is in conflict with observations that typically favour a constant density 'core'. I investigate this 'cusp-core problem' in 'ultra-faint' dwarf galaxies simulated as part of the 'Engineering Dwarfs at Galaxy formation's Edge' (EDGE) project. I find, similarly to previous work, that gravitational potential fluctuations within the central region of the simulated dwarfs kinematically heat the DM particles, lowering the dwarfs' central DM density. However, these fluctuations are not exclusively caused by gas inflow/outflow, but also by impulsive heating from minor mergers. I use the GM approach on one of my dwarf's ICs to show how a delayed assembly history leads to more late minor mergers and, correspondingly, more DM heating. This provides a mechanism by which even ultra-faint dwarfs ($M_* < 10^5\,\mathrm{M}_\odot$), in which star formation was fully quenched at high redshift, can have their central DM density lowered over time. In contrast, I find that late major mergers can regenerate a central DM cusp, if the merging galaxy had sufficiently little star formation. The combination of these effects leads me to predict significant stochasticity in the central DM density slopes of the smallest dwarfs, driven by their unique star formation and mass assembly histories.

4.2 Introduction

The ΛCDM paradigm presents us with a Universe that has an energy budget dominated by DM and dark energy, and in which galaxies are assembled through successive hierarchical mergers (White & Rees, 1978). It has proven to be extremely successful in predicting the formation of cosmic structure on large scales (Springel et al., 2006; Clowe et al., 2006; Tegmark et al., 2006; Dawson et al., 2013; Oka et al., 2014; Planck Collaboration et al., 2014; Wang et al., 2016).

However, disagreements between theory and observation endure at (sub-)galactic scales that have become collectively known as 'small scale puzzles' (e.g. Bullock & Boylan-Kolchin, 2017). The oldest, and perhaps most challenging, of the small scale puzzles is the CC problem (e.g. Flores & Primack, 1994; Moore, 1994; Read et al., 2017). Pure DM structure formation simulations in ΛCDM predict a self-similar radial DM density profile – the NFW profile (Navarro et al., 1997). This scales as $\rho \propto r^{-1}$ within a scale radius r_s, referred to as a 'cusp' due to its divergence towards the origin. By contrast, observations of rotation curves in dwarf galaxies appear to favour instead a constant inner

DM density, referred to as a 'core' (e.g. Carignan & Freeman, 1988; Flores & Primack, 1994; Moore, 1994; McGaugh et al., 2001; Read et al., 2017).

Many solutions to the CC have been proposed in the literature to date. Firstly, observations could have been misinterpreted due to incorrect modelling assumptions. Typical assumptions include spherical symmetry, circular orbits and dynamical pseudo-equilibrium, all of which can be reasonably questioned (e.g. Kuzio de Naray & Kaufmann, 2011; Oman et al., 2016; Read et al., 2016b). Secondly, the assumed underlying DM model could be incorrect. Alternatives such as WDM (e.g. Hogan & Dalcanton, 2000; Bode et al., 2001; Avila-Reese et al., 2001), self-interacting DM (e.g. Spergel & Steinhardt, 2000; Tulin & Yu, 2018) or ultra-light DM (e.g. Schive et al., 2014a; Ferreira, 2020) all predict a lower DM density at the centres of dwarf galaxies whilst retaining the predictions of ΛCDM on larger scales. However, in recent years a third class of solution has been gaining traction.

The CC problem originates from a comparison of pure DM simulations – that do not model stars or gas (hereafter baryons) – with observations. This opens up the possibility that purely gravitational interactions between DM particles and baryons could act to push DM out from the centres of dwarf galaxies, transforming a cusp into a core. The three main mechanisms proposed to date are described in Chapter 1 Section §1.5.1, and ultimately owe to a time-varying gravitational potential. To recap, a fluctuating potential driven by gas inflow/outflow is found to be the dominant process in dwarf galaxies.

While DM heating may solve the CC problem in isolated gas rich dwarfs, a new puzzle has recently presented itself: there is a growing body of evidence for small DM cores even within 'ultra-faint' dwarf galaxies, typically defined to have stellar masses $M_* < 10^5\,\mathrm{M}_\odot$ (e.g. Amorisco, 2017; Contenta et al., 2018; Sanders et al., 2018; Malhan et al., 2020; Simon et al., 2021a). Several papers have suggested that galaxies with so few stars have insufficient energy from stellar feedback to carve out a DM core of size $0.5-1\,\mathrm{kpc}$ (e.g. Peñarrubia et al. 2012; Munshi et al. 2013; Oñorbe et al. 2015; Tollet et al. 2016). However, DM cores form on the scale of the half mass radius, $R_{1/2}$ (Read et al., 2016a), which can be as small as $30-300\,\mathrm{pc}$ in ultra-faint dwarfs (e.g. Simon, 2019). Such small cores form much more rapidly and require significantly less energy, raising the possibility that DM core formation could proceed 'all the way down' to even the smallest dwarfs (e.g. Read et al., 2016a; Contenta et al., 2018). Furthermore, such small cores remain dynamically important by construction since they exist precisely where the stars and gas do – i.e. precisely where we can hope to measure the inner DM potential.

In this chapter, I use a suite of high resolution cosmological zoom simulations from the EDGE project (Rey et al., 2019; Agertz et al., 2020; Rey et al., 2020; Pontzen et al., 2020) to explore whether DM core formation can proceed even in the very smallest dwarf galaxies. The simulations model galaxies over the mass range $M_{200\mathrm{c}} \sim 1-4\times10^9\,\mathrm{M}_\odot$, consistent with ultra-faint dwarfs, and reach a spatial resolution of $\sim 3\,\mathrm{pc}$, sufficient to resolve even very small DM cores.

This chapter is organised as follows. In Section §4.3.1, I describe my numerical methods. In Section §4.3.3, I present an overview of the EDGE simulation suite. In Section §4.4.1, I investigate how gas flows driven by bursty star formation drive early-time core formation in the simulations. In Section §4.4.2, I show that minor mergers can also drive the formation of cores in EDGE and I validate the robustness of my results using the N-body code GRIFFIN. In Section §4.4.4, I show how late major mergers can reintroduce a DM cusp. In Section §4.5, I discuss the implications of my results for DM cusps and cores in the smallest dwarf galaxies. Finally, in Section §4.6 I present my conclusions.

4.3 Method

4.3.1 Simulations

The EDGE project is described in detail in Agertz et al. (2020), and the full description of our setup is also included in Chapter 3.

To further test my numerical results, I use the GRIFFIN code (Dehnen, 2014) to run a controlled investigation into the effects of the merger history on the DM halo of one of the EDGE dwarfs. The motivation for these additional simulations will be made clear in Section §4.4.3. GRIFFIN is a high performance N-body integrator that exploits the fast multipole method (FMM), and is an ideal tool to compare against RAMSES because it is based on a fundamentally different numerical integration scheme that has comparable force accuracy to direct summation codes (e.g. Dehnen, 2014; Gualandris et al., 2017; Nasim et al., 2020; Nasim et al., 2021). These simulations are run at both the equivalent and 10× better mass resolution compared to the RAMSES runs, with the former being used as a convergence study. I employ a force softening length of 10 pc in all of these simulations. Additional tests with a softening length of 5 pc showed no measurable change in the results.

4.3.2 Halo finding

I use the HOP halo finder (Eisenstein & Hut, 1998) to identify all distinct bound structures in each simulation output. HOP does not identify haloes within haloes (subhaloes), and so, where necessary, my analysis is supplemented with the AHF (Amiga Halo Finder) (Knollmann & Knebe, 2009). Merger trees and halo properties are calculated using PYNBODY (Pontzen et al., 2013) and TANGOS (Pontzen & Tremmel, 2018b), respectively. I locate the centre of each bound structure using the shrinking spheres method of Power et al. (2003), performed exclusively on the DM component, as implemented in PYNBODY. Results from the DMO simulations are in all cases corrected for the universal baryon fraction.

4.3.3 An overview of the simulations

Several EDGE dwarfs presented in this chapter have been discussed already in previous EDGE collaboration papers[1], however run at a lower 'fiducial' resolution ($m_{\rm DM} = 1112\,{\rm M}_{\odot}$). Here, since I am interested in resolving potentially very small DM cores, the same dwarfs are resimulated at the 'hires' resolution ($m_{\rm DM} = 117\,{\rm M}_{\odot}$). I show convergence tests between these two resolutions in Appendix A, demonstrating that the results presented here do not depend on resolution.

For a general view of the simulations within their greater cosmological contest, I refer the reader back to Figure 3.2 in Chapter 3. Here, I show each EDGE dwarf in greater detail. Figure 4.1 includes a visual representation of each high resolution baryonic simulation at $z = 0$. The left-most panels show the centred DM surface density out to $r_{200{\rm c}}$, which is indicated by a dashed circle. The middle panels show the central gas density averaged in a 0.2 kpc thick slice through the z-axis. The plot is zoomed into the inner five half light radii, where the 3D half light radius is marked with a solid circle. Each halo is oriented side-on on the angular momentum vector of the central cold gas ($< 10^4$ K), where available, which represents the central gas disc if it is present. The right-most panels are a PYNBODY rendering of the halo stars.

---

[1] Halo1459, Halo1459 GM:Later and Halo1459 GM:Latest appear in Rey et al. (2019). Halo600, Halo605 and Halo624 appear in Rey et al. (2020)

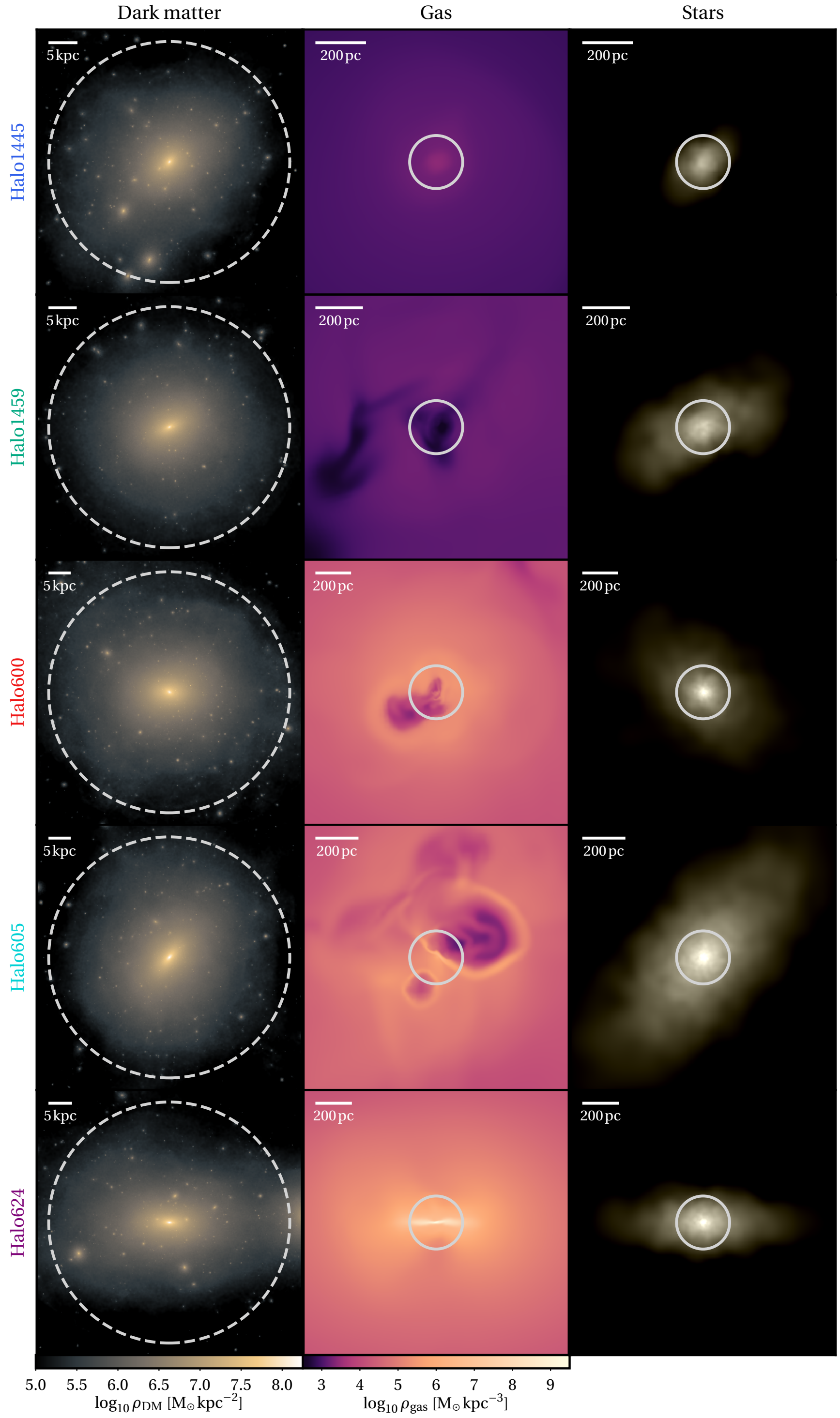

Figure 4.1: A visual representation of the high resolution baryonic simulations in Table 3.1. *Left panels*: The DM surface density out to $r_{200\rm c}$ (dashed circle). *Middle panels*: The gas density averaged along a 0.2 kpc slice through z. The 3D half light radius is indicated by the solid circle. *Right panels*: The halo stars are rendered in PYNBODY with the i, v and u-bands over the range $23 \leqslant \text{mag arcsec}^{-2} \leqslant 28$, shown at the same scale as the gas density panels. All images are oriented side-on along the angular momentum vector of the cool gas ($< 10^4$ K) within 1 kpc of the halo centre. The physical size of each frame is indicated by a scale bar in the top left corner.

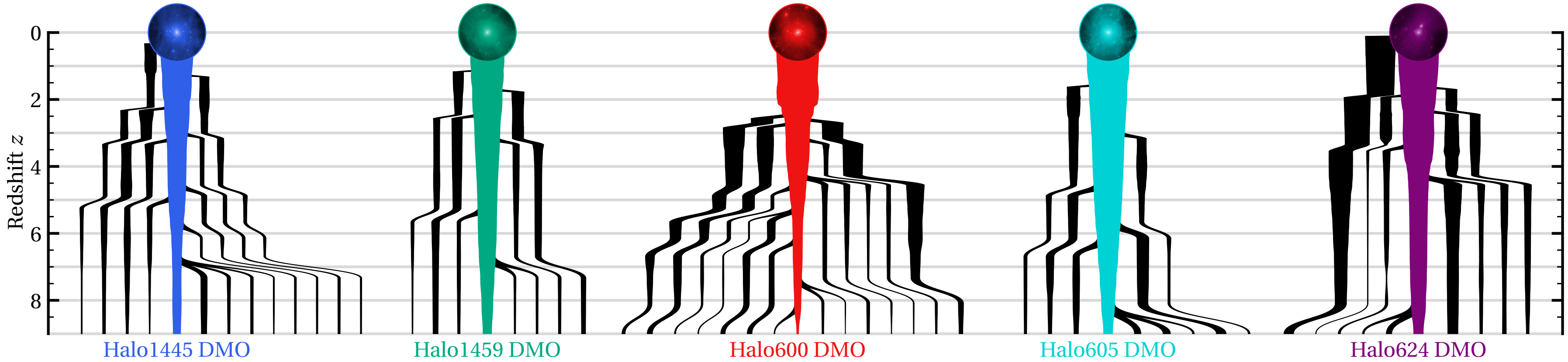

Figure 4.2: The accretion history of each halo as taken from the 'DMO' simulations, where $< 1/30$ mass ratio mergers and sub-mergers are excluded for clarity. The central coloured branch is the main progenitor halo and the line thickness represents the $M_{200\mathrm{c}}$ mass of each DM halo.

For Halo1445 and Halo1459, the gas is extremely under-dense and shows little structure, with the exception of some mild stirring due to late Type Ia SNe (most apparent in Halo1459). Both Halo600 and Halo605 have denser gas, with bubbles forming due to ongoing bursty star formation. Halo624 is the only galaxy to form a structured gas disc, which is both dense and rotating at $z = 0$. A detailed study of the observational properties of these simulated dwarfs will be presented in forthcoming work. In this chapter, I focus on their DM content and structure.

In Figure 4.2, I present merger trees for each of the haloes using the 'DMO' simulations. For simplicity, only $\geqslant 1/30$ mergers onto the main progenitor (coloured line) are shown. The line thickness is representative of each halo mass. The general form of these merger trees are identical for different resolutions and physics, with the one exception that the final merger in Halo624 DMO occurs just after $z = 0$ in Halo624. The present-day main progenitor halo is not necessarily the most massive halo at all times (for instance, Halo600 DMO at $z = 6$). This is because the main progenitor is defined as the most massive halo at the time of each merger. This plot exhibits the unique personality belonging to the accretion history of each EDGE dwarf.

4.4 Results

4.4.1 Core formation from gas flows

In Figure 4.3, I show the evolution of the central DM density for all of the EDGE dwarfs. In the upper panels, the inner 3D DM density is plotted at a radius of 40 pc. This approaches the inner limit of the region that I consider numerically resolved (see Appendix B). The opaque lines are the results for the baryonic simulations, whereas faint lines are the results for the DMO simulations. The corresponding star formation rates of both the main progenitor and all progenitors for the baryonic simulation are plotted in the middle panels, averaged over 100 Myr bins. Included in the lower panels are the 3D density profiles for both baryonic and DMO simulations at $z = 0$.

From Figure 4.3, I see that the inner DM density of the baryonic simulations – that include star formation, gas cooling and stellar feedback – is in all cases lower than the DMO simulations after ~ 1 Gyr. This disparity is driven by the early star formation period seen in all EDGE dwarfs. The reduction in inner density occurs over this star forming period, as expected from the gas-flow mechanism. Star formation reignites at later times in some examples, a result that is explored in detail for the fiducial resolution simulations in Rey et al. (2020). The intensity of this late rejuvenation is insufficient to drive a further reduction of the inner density in Halo624 and Halo605, but is great enough in Halo600 to manifest as a sudden dip in the inner density. However, the late rejuvenation in Halo600 lacks the continuous bursts of star formation necessary to grow a large core (Read & Gilmore, 2005; Pontzen & Governato, 2012).

The lower panels of Figure 4.3 show at which radius the density profile slopes in the baryonic simulations depart from the DMO simulations. In all cases, the bulk of the profile flattening occurs within the 3D half light radius (black dashed line) at approximately 100 pc. This is also consistent with prior work on the gas flow mechanism (see e.g. Chan et al. 2015; Read et al. 2016a; and Section §4.2).

In Figure 4.4, I show the gas-to-DM central density ratio ($\rho_{\mathrm{gas}}/\rho_{\mathrm{DM}}$) for two representative dwarf galaxies. This is computed at time intervals of $\Delta a = 0.01$ (the cadence of the simulation outputs), and so the true peak $\rho_{\mathrm{gas}}/\rho_{\mathrm{DM}}$ may be higher. The upper panel shows Halo1445, which is quenched permanently by $z = 4$ due to the effects of

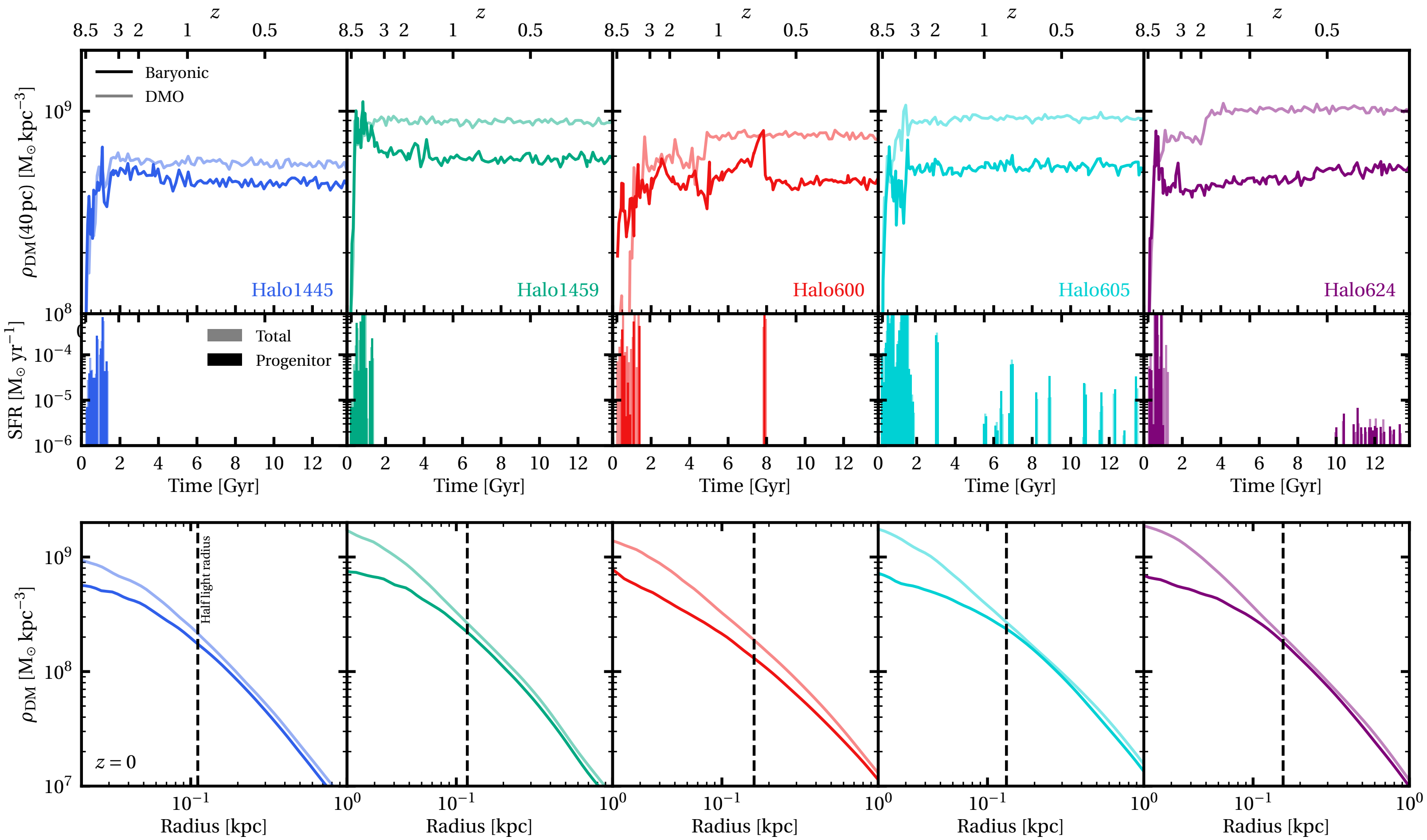

Figure 4.3: *Upper panels:* The evolution of the 3D DM density at 40 pc in the main progenitor halo for the high resolution dwarf galaxies. The opaque lines show simulations run with baryonic physics, whereas the faint lines show pure DM (DMO) simulations using the same ICs. The results are qualitatively similar when selecting the density at different inner radii. *Middle panels:* The star formation rate of the baryonic simulations averaged over bins of 100 Myr. The opaque bars show stars formed within r_{200c} of the main progenitor, whereas fainter bars include stars that are brought in with mergers. *Lower panels:* A comparison of the 3D DM density profiles between the baryonic and DMO simulations at $z = 0$. The black dashed lines mark the 3D half light radii in each case.

reionisation. There are large-scale fluctuations in the density ratio before quenching, corresponding to gas outflow/inflow triggered by bursty star formation. These fluctuations cease after quenching, and the gas gradually photo-evaporates. The lower panel shows Halo624, which is a more massive dwarf that is able to rejuvenate at late times. As in Halo1445, there are large-scale density ratio fluctuations at early times that diminish after the initial quenching. However, as the halo grows more massive it is able to increase its central gas density (see Rey et al., 2020). Star formation then rejuvenates after 10 Gyr, but the intensity of this late star formation is not sufficient to drive large enough fluctuations in $\rho_{\rm gas}/\rho_{\rm DM}$ to further heat the central DM.

4.4.2 Core formation from minor mergers

My results so far are in line with previous studies in the literature that suggest that forming kpc scale DM cores becomes inefficient in ultra-faint dwarfs (Peñarrubia et al., 2012; Garrison-Kimmel et al., 2013; Di Cintio et al., 2014a; Madau et al., 2014; Maxwell et al., 2015; Tollet et al., 2016; Read et al., 2016a). However, the puzzle of apparent DM cores in at least some ultra-faints remains (Amorisco, 2017; Contenta et al., 2018), Section §4.2.

Perhaps the most compelling case for a small dark core in an ultra-faint dwarf comes from the survival of a lone and extended SC, offset from the centre of the Eridanus II galaxy (Amorisco, 2017; Contenta et al., 2018; Simon et al., 2021a). Eridanus II is substantially more extended than any of the reference EDGE dwarfs, with $R_{\rm half} = 299 \pm 12$ pc. Using the GM approach (Roth et al., 2016; Rey & Pontzen, 2018; Stopyra et al., 2021b), alternative mass accretion histories for a galaxy can be created. Rey et al. (2019) modified one of the fiducial resolution EDGE dwarfs, Halo1459, such that it assembled later. They found that this leads to a larger, lower surface brightness, and lower metallicity dwarf – more similar to Eridanus II. Furthermore, Boldrini et al. (2020b) have recently shown that eccentric minor mergers can themselves fluctuate the inner gravitational potential, flattening a DM cusp. As such, in this section, I resimulate the genetically modified later forming dwarfs from Rey et al. (2019) at higher resolution to study how late formation impacts the central DM density.

I run two modifications of Halo1459 which I call Halo1459 GM:Later and Halo1459 GM:Latest (Table 3.1). The assembly histories of these modifications were already shown at the fiducial resolution in Figure 1 of Rey et al. (2019); they are indistinguishable from the higher resolution trajectories which I show in Figure 4.5. The modified haloes are approximately 3× (2×) less massive at $z = 8.5$ for Halo1459 GM:Later (Halo1459 GM:Latest), but grow to the same mass within a 4% margin by $z = 0$.

In the upper panel of Figure 4.6, I plot the evolution of the central density in Halo1459 GM:Later. Now, the inner DM density continues to fall long after star formation has ceased. This occurs in both the simulation with baryonic physics and in the DMO simulation. The baryonic simulation is extremely gas deficient after quenching, with $M_{\rm gas}/M_{\rm DM}(< r_{\rm halflight}) < 10^{-5}$, so any gas flows driven by residual feedback from old stars (as in Rey et al., 2020) have a negligible impact on the overall mass distribution. This reduction in the central density is not seen to the same extent in Halo1459 GM:Latest. I will discuss the reasons for this in Section §4.4.4.

The lower panel of Figure 4.6 shows the radial DM density profiles of Halo1459 GM:Later (darker) and Halo1459 DMO GM:Later (lighter) at $z = 4$ (dashed) and $z = 0$ (solid). A schematic illustrates the expected density slopes for a cusp and a core, indicating that whilst the central density slope has declined by $z = 0$, it still has a slope of $\rho \propto r^{-0.5}$.

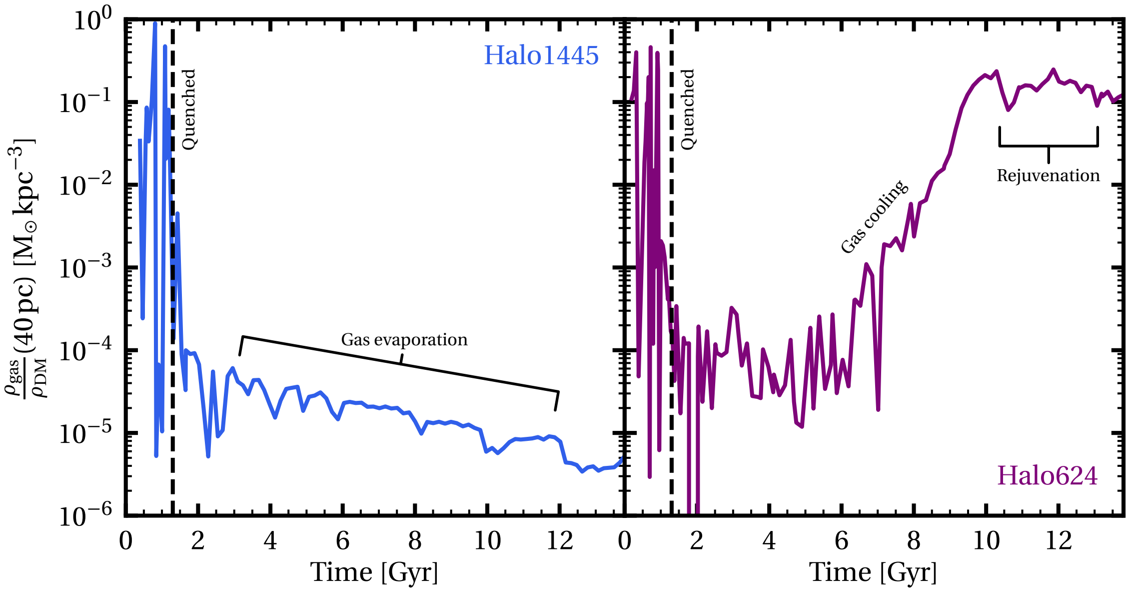

Figure 4.4: Evolution of the inner gas-to-DM density ratio at 40 pc ($\rho_{\rm gas}/\rho_{\rm DM}$) for two representative EDGE dwarfs. Prior to quenching by reionisation (black dashed line), there are large fluctuations in $\rho_{\rm gas}/\rho_{\rm DM}$ caused by repeated cycles of gas cooling, star formation and stellar feedback. These fluctuations excite 'DM heating' that lowers the central DM density (Figure 4.3). Halo1445 experiences no further star formation or DM heating after it quenches. By contrast, Halo624 grows in mass, accumulating cold gas and rejuvenating its star formation after ~ 10 Gyr. Subsequent fluctuations are orders of magnitude smaller than at early times, and so there is no late time DM heating.

It is important to rule out the possibility that any apparent DM heating is caused by numerical relaxation. In Appendix B, I calculate the 'relaxation radius', $r_{\rm relax}$, for the EDGE simulations. This is the radius inside which the numerical relaxation time is equal to the simulation run time and so numerical relaxation will become important. From this calculation, I conclude that the simulations should still be well-resolved above $r_{\rm relax} > 25\,{\rm pc}$ at $z = 0$, yet the density clearly evolves on scales larger than this at *all* times. Therefore, there must be some other mechanism by which the central DM density is lowering. It is well established that dynamical friction heating from dense clumps can contribute to core formation (e.g. El-Zant et al. 2001; Mo & Mao 2004; Romano-Díaz et al. 2009; Goerdt et al. 2010; Cole et al. 2011; Nipoti & Binney 2015; Del Popolo & Pace 2016; and Section §4.2). In Halo1495 GM:Later, the only dense clumps available to drive such a process at late times are merging DM subhaloes.

To investigate the veracity of the above late time DM heating, and to explore whether merging DM subhaloes are indeed the culprit, in the next section I resimulate the sequence of mergers that form Halo1459 GM:Later using the non-cosmological N-body FMM code GRIFFIN (Dehnen, 2014), as described in Section §4.3.1. This allows me to isolate the heating effects of minor mergers in a non-cosmological setting, and to verify that numerical effects unique to RAMSES are not responsible for the heating.

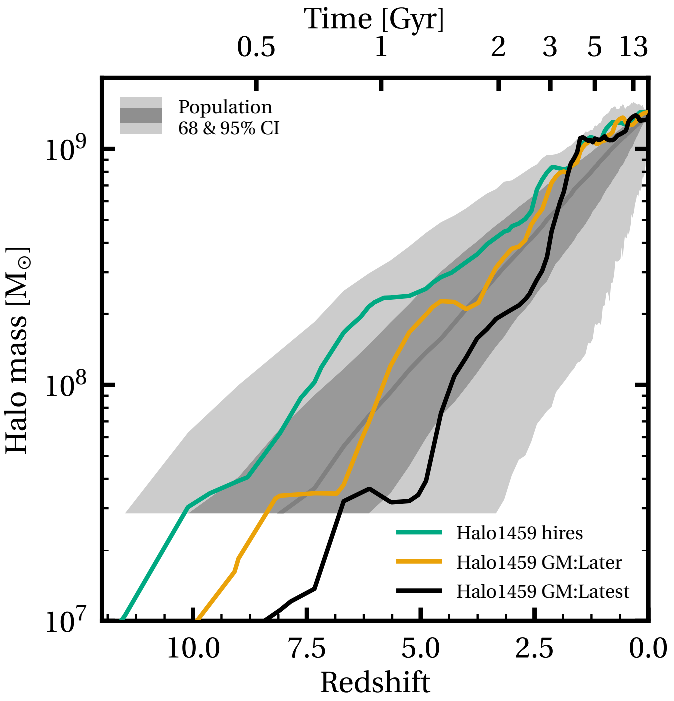

Figure 4.5: The halo mass growth history of Halo1459 and two modified variants which I call Halo1459 GM:Later and Halo1459 GM:Latest. Included are grey bands indicating the 68% and 95% scatter for the mass growth histories of haloes throughout the lower resolution void simulation. The bands are truncated at $\sim 3 \times 10^7$ due to the resolution limit of the void simulation. This shows that the modified haloes are within the expected scatter of assembly histories in ΛCDM.

4.4.3 Testing minor merger induced DM core formation with the GRIFFIN code

In this section, I use the GRIFFIN N-body code to reproduce the assembly history of Halo1459 GM:Later in a controlled manner. For this, I simulate a series of halo mergers based upon profile fits to the reference RAMSES simulation. I use the coreNFW profile as in Read et al. (2016a):

$$\rho_{\text{cNFW}}(r) = f^n \rho_{\text{NFW}} + \frac{n f^{n-1}\left(1-f^2\right)}{4\pi r^2 r_c} M_{\text{NFW}},$$
$$f^n = \left[\tanh\left(\frac{r}{r_c}\right)\right]^n \tag{4.1}$$

which is a NFW profile (Navarro et al., 1997) adapted to include a parameter n that controls the flatness of the central density slope ($n = 1$ being a core and $n = 0$ being a cusp). Here, r_c is a 'core radius' and ρ_{NFW} and M_{NFW} are the typical NFW density and mass profiles.

I first fit the spherically symmetric DM density profile of the main progenitor halo at $z = 4$. By this time, the central DM halo is well-established and star formation has permanently quenched. The total stellar mass is low ($\sim 10^5\,\text{M}_\odot$) and the gas content is negligible, so the system can be safely resimulated using exclusively its DM component.

Mergers are defined based on every halo identified with HOP at $z = 4$, on the condition

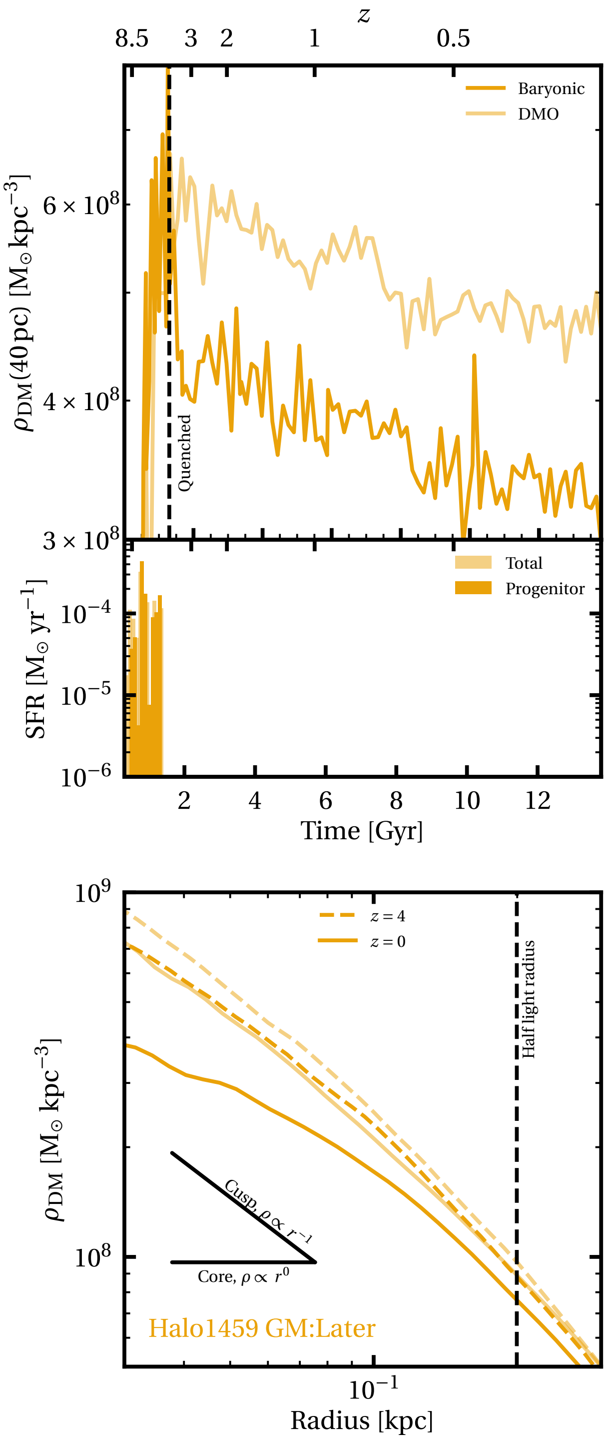

Figure 4.6: *Upper panel:* The evolution of the 3D DM density at 40 pc, but for a modified simulation that has a delayed formation history (Halo1459 GM:Later). A black dashed line marks the approximate time at which the galaxy is permanently quenched. *Middle panel:* The star formation rate of the baryonic simulation, averaged over bins of 100 Myr. Opaque bars are stars formed within r_{200c} of the main progenitor, whereas faint bars include stars that are brought in with mergers. *Lower panel:* A comparison of the 3D DM density profiles between the baryonic and DMO simulations at both $z = 4$ (after quenching) and $z = 0$. A black dashed line marks the 3D half light radius at $z = 0$.

Table 4.1: The GRIFFIN simulations used to investigate the late-time density reduction in Halo1459 GM:Later. From left to right, the columns give: the simulation names, whether mergers were included or the main progenitor was isolated, the DM particle mass resolution, and the force softening length.

Name	**Mergers**	**Resolution** [$m_{\rm DM}/{\rm M}_\odot$]	**Force softening** [pc]
Isolated low	✗	117	10
Mergers low	✓	117	10
Isolated	✗	11.7	10
Mergers	✓	11.7	10

that they contain at least 800 DM particles and are destined to merge with the main progenitor. Each merging halo is tracked until the snapshot prior to infall (defined as the point where the merger crosses over r_{200c} of the main progenitor), by which time many of them have coalesced. Despite the large number of individual haloes at $z = 4$, there are a manageable 38 distinct subhaloes at the time of merging.

For each of these mergers, I perform a spherically symmetric coreNFW profile fit and generate ICs using AGAMA (Vasiliev, 2018). I use a multipole potential approximation with one hundred grid nodes, an isotropic velocity distribution function, and model the density out to $3 \times r_{200c}$ for each coreNFW profile fit (which is necessary to ensure there is sufficient dynamical friction between interacting haloes at large radii; e.g. Read et al., 2008). A further improvement could include fitting the halo triaxiality, but should not be necessary for resolving the leading order effects of halo mergers. The resulting merger masses range from $5 \times 10^5 \leqslant M_{\rm merger}/{\rm M}_\odot \leqslant 10^8$, with the majority falling around the $2 \times 10^6\,{\rm M}_\odot$ mark.

The ICs of the main progenitor are integrated forward in time with the GRIFFIN code, as described in Section §4.3.1. As the simulation reaches the time of each merger infall, the corresponding ICs are inserted at the same phase-space location as in the reference RAMSES simulation. In this way, the merger history of the EDGE dwarf from $4 \leqslant z \leqslant 0$ is recreated.

The above method has a few caveats. Firstly, the number density of mergers in a ΛCDM cosmology increases with decreasing halo mass (Stewart et al., 2009; Rodriguez-Gomez et al., 2015). Therefore, a significant amount of mass accretion is neglected by only considering mergers above a certain mass threshold. This yields a final $z = 0$ mass roughly 1.5× less that of the original RAMSES simulation, although much of this missing mass is located in the halo outskirts ($\sim 80\%$ of the missing mass is exterior to 5 kpc). I also see that the orbits of merging haloes begin to diverge from the reference simulation after two pericentre passages, and it is already established that reproducing exact orbital behaviour of mergers is challenging (e.g. Lux et al., 2010). Lastly, any mergers already within the virial radius of the main progenitor by $z = 4$ are ignored, meaning that the onset of dynamical heating due to mergers may be delayed as compared to the reference simulation.

I also run a control simulation without mergers to distinguish any physical reduction in density from numerical relaxation. The GRIFFIN simulations are summarised in Table 4.1.

The evolution of the central density for the isolated control (grey) and full assembly (black) GRIFFIN simulations is shown in Figure 4.7. At 40 pc, there is still a small numerical heating effect in the isolated simulation (grey line). The inner density falls by $\approx 2.6 \times 10^7\,{\rm M}_\odot\,{\rm kpc}^{-3}$ over 12 Gyr. However, this contrasts with a much more substantial drop in

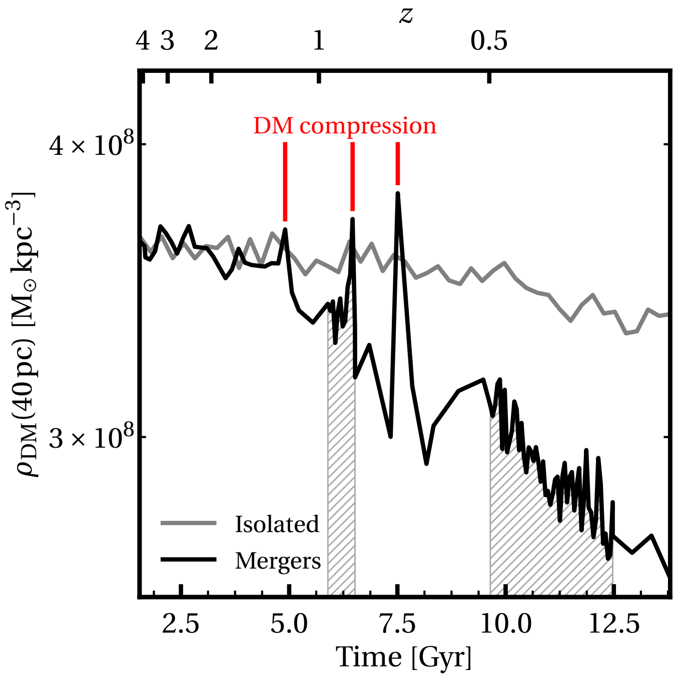

Figure 4.7: The evolution of the 3D DM density at 40 pc in the GRIFFIN simulations. I start the x-axis at redshift $z = 4$ to mimic the age of the reference RAMSES simulation. The grey line shows a control GRIFFIN simulation run to $z = 0$ without any mergers. The black line shows the same simulation including 38 mergers. The hatched grey areas mark time intervals over which the output cadence is increased by an order of magnitude to resolve high-frequency effects. Notice that the DM density is lowered substantially in the simulation with mergers as compared to the control simulation. Notice, further, the three DM density spikes marked in red. These correspond to close subhalo passages, suggesting that the 'DM heating' effect seen here is driven by repeated gravitational shocks from merging subhaloes (see Figure 4.9).

the central density of the simulation with mergers of $\approx 9.1 \times 10^7\,\mathrm{M}_\odot\,\mathrm{kpc}^{-3}$. The small heating present in the isolated simulation is not immediately obvious in any of the non-GM EDGE dwarfs, and the differences in numerical setup and lack of cosmological growth may be contributing to this. I do not run any EDGE dwarfs without cosmological accretion, so a strict comparison is difficult.

Finally, notice the three prominent 'spikes' in the inner DM density at ~ 4.9, ~ 6.5 and ~ 7.5 Gyr, as marked on Figure 4.7 in red. These times correspond to close subhalo passages, suggesting that the 'DM heating' effect is driven by repeated gravitational shocks from merging subhaloes. I discuss this further in Section §4.5.

4.4.4 Cusp replenishment

Along with mechanisms that flatten the central DM density, there are mechanisms that can rebuild it. Laporte & Penarrubia (2015) investigate a scenario where dense mergers can reintroduce dynamically cold DM into a cored parent halo, thereby rebuilding the central density cusp. These events require that the merger is able to fall into the centre of the parent halo intact, which would demand the merging structures are resistant to the tidal disruption of the parent galaxy.

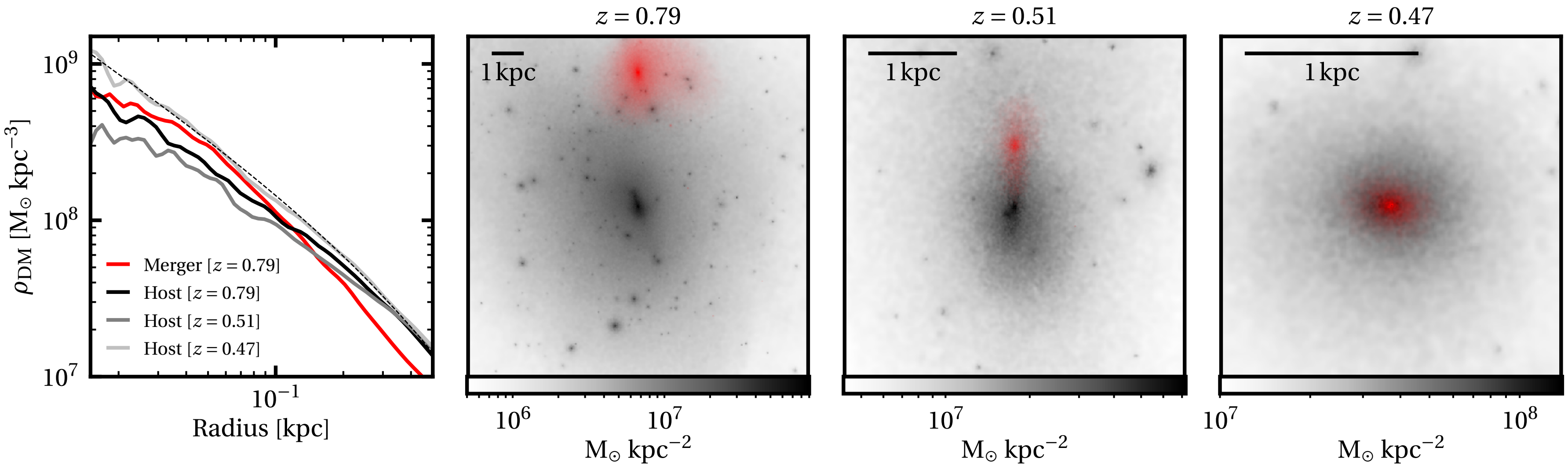

Figure 4.8: This plot illustrates how the reintroduction of denser DM material to the Halo1459 GM:Latest simulation erases the effect of earlier DM heating. *Leftmost panel:* The central 3D DM density profiles of a cuspy subhalo (red line) and of the parent halo evolution (black, dark grey and light grey lines). The density profile of the host at $z = 0.51$ is centred on only the host particles to avoid any bias due to the merger. Removing the merger particles from the density profile calculation does not qualitatively change the results. A black dashed line represents a NFW profile fit to the parent halo at $z = 0.79$ (Navarro et al., 1997). *Right panels:* The evolution of the merger system shown in three panels, where the parent halo is in grey-scale and the merging halo is red. The merging halo has permanently fallen into the central 100 pc of the parent halo by $z = 0.47$. In all cases, the merger system has been oriented such that the centres of both haloes are in the xy-plane.

In Figure 4.8, I show an example of such a merger in Halo1459 GM:Latest. The left panel shows the central DM densities of the merging system at several key times. The merging halo is shown in red at $z = 0.79$, by which time it has permanently crossed over the r_{200c} radius of the parent halo. The parent halo is shown at the same time in black, and has already begun to depart from a primordial density cusp (black dotted line), primarily due to the action of minor mergers as in Section §4.4.2. By $z = 0.51$, the dark grey line shows that the central density of the parent halo has continued to decline to its lowest point. Finally, the light grey line shows the parent and merging halo combined at $z = 0.47$, with the central density returning to a steep primordial cusp (which is coincidentally well described by the cuspy profile fit made at $z = 0.79$).

The right three panels show the progression of the merger event in surface density plots, with the accreted material highlighted in red. The outer regions of the merging halo have been stripped away between $z = 0.79$ and $z = 0.51$, but the central density is retained. The final panel conveys how the increase in central density at $z = 0.47$ is correlated with the central deposition of the merger material.

4.5 Discussion

We have established that gas flows driven by star formation are able to drive sufficiently large potential fluctuations to erode central density cusps in the EDGE dwarfs (Section §4.4.1). However, this is seen only at early times when star formation rates exceed $10^{-4}\,\mathrm{M_\odot yr^{-1}}$ and fluctuate on a timescale of order the local dynamical time. Despite the late-time rejuvenation of star formation in several of the simulations, this second phase of star formation is not sufficient to drive significant gas flows and the central DM density is unaffected.

However, bursty star formation is not the only means by which the central gravitational force can be varied. I have also shown that passing subhaloes act to fluctuate the central density driving DM heating (Section §4.4.2). In Figure 4.9, I show an example orbit of one merging subhalo taken from the GRIFFIN simulation. Notice that this merger repeatedly punctures the inner region (0.1 kpc) of its host galaxy on a timescale shorter than the local dynamical time (red). The first close passage of this subhalo corresponds to the DM density spike at 6.5 Gyr shown in Figure 4.7. Shortly before this passage at ~ 6 Gyr, the mass enclosed within 0.1 kpc of the host halo is $7.92 \times 10^5\,\mathrm{M_\odot}$. In comparison, the merging subhalo contains $6.54 \times 10^5\,\mathrm{M_\odot}$ within 0.1 kpc of its centre, which is among the most massive of the mergers I model. This suggests the heating effect is greatest when the interacting masses are similar, as expected for impulsive heating (Hills, 1980). The other density spikes in that Figure correspond to close passages from different merging subhaloes. Taken together, this indicates that the late time DM heating is being driven by tidal shocks from the merging subhaloes on their host.

The above late time DM heating due to minor mergers occurs in both baryonic and DMO RAMSES simulations (Figure 4.6). However, in the DMO simulations the inner DM density, while lower, remains cuspy (Figure 4.6, bottom panel). By contrast, in the baryonic simulation – and in the GRIFFIN replica of this simulation – these minor mergers flatten the cusp. This occurs because in these simulations, the cusp is already weakened at early times by DM heating due to star formation (Figure 4.6, upper panel).

Previous literature has suggested that minor mergers can “heat up” a host DM profile. Naab et al. (2009) propose a mechanism by which the central concentrations of massive elliptical galaxies are reduced through repeated minor mergers, with Bédorf & Portegies Zwart (2013) finding the same for massive compact galaxies. Similarly, Boldrini et al.

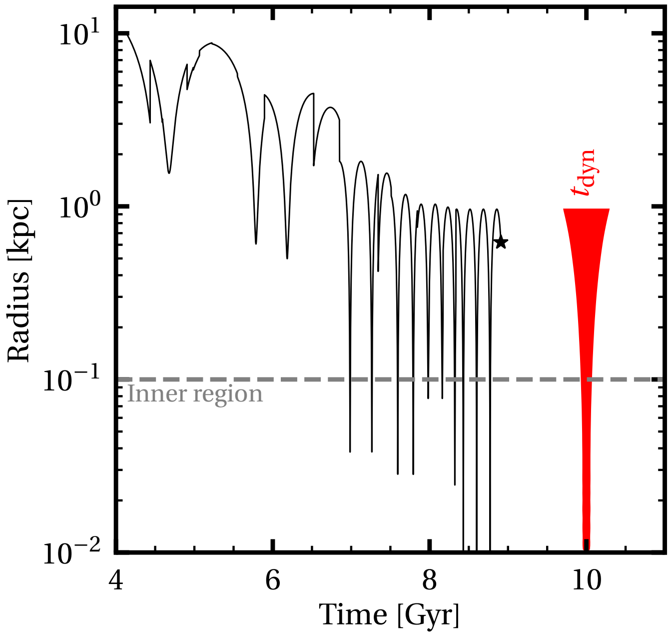

Figure 4.9: The orbit of one example merger from the 'Mergers' GRIFFIN simulation. The orbit between each simulation output has been reconstructed with a two-body integration in AGAMA, assuming a spherically symmetric background potential and using a multipole fit to each simulation snapshot. Whilst these orbit reconstructions are imperfect due to perturbations from other subhaloes and triaxiality, they provide a reasonable estimate for my purposes. A red bar shows the width of one dynamical time $t_{\rm dyn} = 2\pi\sqrt{3/4\pi G\rho(r)}$ over a range of orbital radii, and a black star marks the time at which the merger dissolves. The approximate inner region is indicated at 0.1 kpc with a horizontal dashed line.

(2020b) are able to enact a cusp-core transition in a model of M31 via the accretion of both minor and major mergers on highly eccentric orbits. Towards the scale of dwarf galaxies, Macciò et al. (2017) show that minor mergers can boost star formation, exciting DM heating via the usual gas-flow mechanism. This effect cannot be important for ultra-faint dwarfs, since they do not show evidence for late-time star formation. However, Boldrini et al. (2020a) find that minor mergers can directly heat the central DM density in a model of the Fornax dwarf via dynamical friction. Finally, Leung et al. (2020) propose that mergers could expand the orbits of GCs in the Fornax dwarf spheroidal galaxy, solving a long-standing puzzle as to why they have not sunk to the centre of Fornax via dynamical friction. This same mechanism would also expand the orbits of the DM particles.

4.6 Conclusions

I have presented a suite of cosmological zoom simulations of the ultra-faint dwarf galaxies performed with the adaptive mesh refinement code RAMSES as part of the EDGE project. These simulations have a spatial and mass resolution of 3 pc and 120 $\mathrm{M}_\odot$, respectively, sufficient to resolve the formation of very small DM cores.

My key result is that I uncover two distinct pathways to DM core formation at sub-kpc scales in the $10^9 < M_{200c}/\mathrm{M}_\odot < 5\times10^9$ halo mass regime. These are able to drive reductions in the central (40 pc) DM density of up to approximately a factor of two as compared to pure DM simulations. The first pathway is stellar feedback, in agreement with previous literature. This requires a sufficiently high star-formation rate over an extended period of time, which in EDGE simulations only occurs at high redshift prior to reionisation. At these early times, I found that the star formation rate fluctuated on the order of the local dynamical time with an average amplitude of $\sim 1 \times 10^{-4}\,\mathrm{M}_\odot\,\mathrm{yr}^{-1}$. This caused the orbits of DM particles to migrate outwards, lowering the dwarf's inner DM density.

However, even after quenching by reionisation, I found that a second mechanism can cause DM cores to continue to grow: impulsive heating from minor mergers. To demonstrate this, I 'genetically modified' the ICs for one dwarf such that it assembled later from many minor mergers. I found that, in this case, the dwarf's inner DM density continued to drop long after star formation ceased. I tested the veracity of this result by running an independent 'replica' simulation using the GRIFFIN N-body code, finding excellent agreement between the GRIFFIN and RAMSES calculations.

While all of the dwarfs experienced some DM heating prior to reionisation, I showed that dense major mergers can replenish kinematically cold DM, thereby reintroducing a density cusp at late times. This demonstrates that the central density of the smallest dwarf galaxies at $z = 0$ is sensitive to both their mass assembly histories and their star-formation histories. This will drive stochasticity in the central DM densities of isolated ultra-faint dwarfs. I will study this in more detail in future work.

Finally, none of the simulated EDGE dwarfs experienced sufficient DM heating to produce a flat density core. In the next chapter, I will consider whether the DM heating found in EDGE is sufficient to explain the survival and properties of the lone SC in Eridanus II.

Star clusters as probes of dark matter cores in ultra-faint dwarfs

5.1 Abstract

There is growing evidence that at least some ultra-faint dwarf galaxies have central DM cores. A prime example is the Eridanus II dwarf galaxy that appears to require a DM core in order for its lone star cluster to survive. Such cores are challenging to explain in a ΛCDM cosmology because galaxies like Eridanus II have too few stars to produce any significant coring. However, in Chapter 4, I showed that dwarf galaxies in the EDGE project can form cored DM profiles through a combination of early heating due to star formation, followed by late-time heating from minor mergers. In this chapter, I show that these same EDGE simulations naturally produce low mass SCs like that in Eridanus II. I perform a suite of 720 follow-up direct N-body simulations to test whether the coring seen in EDGE is sufficient to explain the size, projected shape, orientation and survival of Eridanus II's lone SC. I find that whilst the coring seen in EDGE is sufficient to support the long-term survival of SCs, a much shallower and larger core appears to be required to reproduce the properties of the SC in Eridanus II.

5.2 Introduction

The Standard ΛCDM Cosmological Model provides an excellent match to the observed growth of cosmic structure on large scales (e.g. Springel et al., 2006; Clowe et al., 2006; Tegmark et al., 2006; Dawson et al., 2013; Oka et al., 2014; Planck Collaboration et al., 2014; Wang et al., 2016). However, pure DM simulations in a ΛCDM cosmology begin to deviate from observations on galactic and sub-galactic scales where the role of 'baryonic physics' take effect (Carignan & Freeman, 1988; Flores & Primack, 1994; Moore, 1994; Klypin et al., 1999; Moore et al., 1999; McGaugh et al., 2001; Sand et al., 2002; Okamoto & Frenk, 2009; Boylan-Kolchin et al., 2011). The earliest such tension has become known as the CC problem and concerns the central densities of DM haloes in dwarf galaxies. Pure DM simulations in a ΛCDM cosmology predict the formation of a complex web of cosmic structure punctuated by dense haloes that have a self-similar density profile[1] (Navarro et al., 1997). These density profiles are well-fit at ∼10% accuracy by the NFW profile in Equation 1.6.

Analysis of real galaxies reveals a more complicated picture. Many dwarf galaxies favour a much lower central density than predicted by the NFW profile (Carignan & Freeman, 1988; Flores & Primack, 1994; Moore, 1994; McGaugh et al., 2001; Read et al., 2017), while some are consistent with a dense NFW cusp (Richardson & Fairbairn, 2014; Strigari et al., 2017; Read et al., 2018; Shi et al., 2021). In Chapter 4 I found that the densest dwarfs are those with the least star formation, while the dwarfs with lower central densities have experienced the most star formation, with similar results in the literature

---

[1] This self-similarity is predicted to end at around an Earth-mass for a $\sim 100\,\mathrm{GeV/c^2}$ Weakly Interacting Massive Particle due to the free-streaming limit (Hofmann et al., 2001; Diemand et al., 2005; Wang et al., 2020). This is currently far below the resolution limit of most cosmological simulations.

(Oñorbe et al., 2015; Dutton et al., 2019). This is exactly what was predicted by models where DM cusps are transformed to lower density 'cores' by repeated gravitational potential fluctuations driven by gas inflow/outflow through the star formation cycle (Navarro et al., 1996a; Mashchenko et al., 2006; Read & Gilmore, 2005; Mashchenko et al., 2008; Pontzen & Governato, 2012).

While gas cooling and stellar feedback can transform DM cusps to cores, it is energetically challenging for this process to create significant cores ($> 500\,\mathrm{pc}$) in ultra-faint dwarfs since they form so few stars (Peñarrubia et al., 2012; Garrison-Kimmel et al., 2013; Di Cintio et al., 2014a; Madau et al., 2014; Maxwell et al., 2015; Tollet et al., 2016; Read et al., 2016a, 2017; Contenta et al., 2018). Simulations to date have found that these dwarfs remain cuspy despite their star formation (Governato et al., 2012; Di Cintio et al., 2014b; Oñorbe et al., 2015). Yet, there is mounting observational evidence for DM cores in at least some ultra-faint dwarfs, with the most compelling evidence coming from the Eridanus II dwarf (Amorisco, 2017; Contenta et al., 2018).

Eridanus II, discovered by the Dark Energy Survey (DES, Bechtol et al., 2015; Koposov et al., 2015), has a stellar mass of $8.3^{+1.7}_{-1.4} \times 10^4$ and a dynamical mass estimate of $1.2^{+0.4}_{-0.3} \times 10^7$ within its half light radius (Li et al., 2017). This makes Eridanus II highly DM dominated at all radii. Its low metallicity also implies an old stellar population and it is a good candidate for being a 'fossil' galaxy that was quenched by reionisation (Simon et al., 2021b).

Deep imaging of Eridanus II has revealed a lone SC offset from the galactic photometric centre (Koposov et al., 2015; Crnojević et al., 2016; Simon et al., 2021b), making it the smallest known galaxy to host a SC. This SC lies at a projected $23 \pm 3\,\mathrm{pc}$ from the centre of Eridanus II (Simon et al., 2021b), and has a large projected half light radius, with the authors in Crnojević et al. (2016) finding $13 \pm 1\,\mathrm{pc}$ and further observations in Simon et al. (2021b) finding an even larger $15 \pm 1\,\mathrm{pc}$. This extended distribution makes it particularly vulnerable to destruction by tidal forces (Amorisco, 2017; Contenta et al., 2018).

Amorisco (2017) and Contenta et al. (2018) show that Eridanus II is likely to contain a central density core by using the SC as a probe of the potential profile slope. The long-term survival of SCs are highly dependent on the inner potential profile slope of their host galaxy, therefore the existence and properties of SCs can be used to constrain the potential they inhabit (Read et al., 2006a; Goerdt et al., 2006; Petts et al., 2016). SCs orbiting in cuspy potentials sink rapidly to the centre via dynamical friction, and experience accelerated mass loss due to enhanced tidal stripping (Orkney et al., 2019). By contrast, SCs orbiting in a cored potential experience no tidal mass loss while their orbit stalls on the edge of the core, no longer decaying due to dynamical friction (Read et al., 2006a; Inoue, 2009; Goerdt et al., 2010; Kaur & Sridhar, 2018; Banik & van den Bosch, 2021). Furthermore, a "dynamical bouyancy" effect pushes SCs on shallower orbits out towards the edge of the core (Cole et al., 2012; Banik & van den Bosch, 2021). A large suite of N-body simulations in Amorisco (2017); Contenta et al. (2018) show that a central core in Eridanus II allows for an older and more extended SC, in agreement with the observed properties of the cluster.

In Chapter 4 I show that ultra-faint dwarf galaxies in the EDGE project can form cored DM profiles through a combination of early heating due to star formation, followed by late-time heating from minor mergers (Orkney et al., 2021a). In this chapter I first show that SCs similar to that found in Eridanus II form naturally in the EDGE dwarfs. I then investigate whether such SCs can survive within their host galactic potentials for a Hubble time. To achieve this, I sample a range of initial orbits for the SCs (see Table 5.2) and run 720 NBODY6DF simulations of their tidal disruption. I consider a static core,

Name	**Physics**	**Resolution** $[m_{\mathrm{DM}}, m_*, m_{\mathrm{gas}}]/\mathbf{M}_\odot$	$M_{200\mathrm{c}}$ **[M$_\odot$]** **(At $z = 0$)**	**Contamination fraction** **(At $z = 0$)**
Halo1445 DMO	DM-only	[139, -, -]	1.65×10^9	4.75×10^{-6}
Halo1459 DMO	DM-only	[139, -, -]	1.71×10^9	2.47×10^{-5}
Halo1459 GM:Later DMO	DM-only	[139, -, -]	1.74×10^9	5.95×10^{-5}
Halo1459 GM:Latest DMO	DM-only	[139, -, -]	1.74×10^9	9.12×10^{-5}
Halo1445	Agertz+2020	[117, 18, 300]	1.32×10^9	5.07×10^{-5}
Halo1459	Agertz+2020	[117, 18, 300]	1.43×10^9	2.58×10^{-5}
Halo1459 GM:Later	Agertz+2020	[117, 18, 300]	1.43×10^9	4.34×10^{-5}
Halo1459 GM:Latest	Agertz+2020	[117, 18, 300]	1.38×10^9	5.08×10^{-5}

Table 5.1: Description of the subset of EDGE dwarfs presented in this chapter, chosen for their likeness to the ultra-faint dwarf Eridanus II. From left to right are the simulation names, the physics scheme employed, the mass resolution, the total halo $M_{200\mathrm{c}}$ mass at $z = 0$ and the contamination fraction of the main halo at $z = 0$. The contamination fraction is defined as the fraction of DM particles within the virial radius $r_{200\mathrm{c}}$ that have masses greater than the DM particle resolution limit.

cusp and time-evolving potential that transitions from a cusp to a core similarly to one of the EDGE dwarfs. I then quantitatively compare these simulated SCs to the lone SC in Eridanus II to make inferences about Eridanus II's underlying central DM density profile, and to test whether the EDGE simulations can explain the puzzlingly large size and central offset of Eridanus II's SC.

This chapter is organised as follows. In Section §5.3 I describe the motivation and setup for the N-body simulation suite which I use to simulate SC evolution. I compare the properties of the EDGE simulations to those of Eridanus II in Section §5.4.1. In Section §5.4.2 and Section §5.4.3, I discuss the evolution and central density evolution of the EDGE simulations. In Section §5.4.4, I show examples of SCs which form naturally in the EDGE simulations. I present my results for the N-body simulation suite in Section §5.4.6. I discuss possible evolutionary pathways for the SC in Eridanus II in and the corresponding implications for DM cores in ultra-faint dwarfs in Section §5.5. Finally, I conclude in Section §5.6.

5.3 Method

RAMSES simulations

I analyse a selection of ultra-faint dwarf galaxy simulations taken from the wider suite of cosmological zoom-in simulations that form the EDGE project (debuted in Agertz et al., 2020), modelled using the AMR tool RAMSES (Teyssier, 2002). A detailed description of this suite is included in Chapter 3.

All simulations are initialised with the GENETIC code (Stopyra et al., 2021b) which allows for forensic investigation using the GM approach (Roth et al., 2016; Rey & Pontzen, 2018). This involves altering the ICs of a cosmological simulation in a way that maximises the chance that those alterations arise from a random Gaussian draw from a ΛCDM cosmology. See Rey et al. (2019) for an example of how GM can be used to investigate the history of a simulated galaxy.

I analyse four haloes chosen for their similarity to Eridanus II in stellar mass, size, metallicity and stellar velocity dispersion (see Table 5.3). All four are simulated both with and without baryonic physics. Halo1459 GM:Later and Halo1459 GM:Latest are based upon the ICs of Halo1459 which have undergone GM treatment. Halo1459 GM:Later

N	$\mathbf{M}_{\rm ini}$ $[\mathbf{M}_\odot]$	$R_{\rm halfmass,ini}$ **[pc]**			$R_{\rm g}$ **[pc]**			$v_{\rm ini}/v_{\rm circ}$				**Host** γ				
2^{16}	4.18×10^4	2.5	5	10	45	100	200	1	0.75	0.50	0.25	0(Fcore)	0	$0(t)$	0.75	1
2^{15}	2.08×10^4	2.5	5	10	45	100	200	1	0.75	0.50	0.25	0(Fcore)	0	$0(t)$	0.75	1
2^{14}	1.00×10^4	2.5	5	10	45	100	200	1	0.75	0.50	0.25	0(Fcore)	0	$0(t)$	0.75	1
2^{13}	5.14×10^3	2.5	5	10	45	100	200	1	0.75	0.50	0.25	0(Fcore)	0	$0(t)$	0.75	1

Table 5.2: Description of the NBODY6DF simulation suite. From left to right are the initial star numbers in the cluster, the corresponding total mass, the initial 3D half mass radius used to initialise the cluster, the initial galactocentric distance of the cluster orbit, the initial tangential orbital velocity, and the central slope parameter γ of the Dehnen model used for the host potential (where $\gamma = 0$ is a core and $\gamma = 1$ is a cusp). In total, this table is representative of 720 unique simulations.

(Halo1459 GM:Latest) differs from Halo1459 in that its formation history has been delayed such that it is 3× (2×) less massive at the time of reionisation ($z = 8.5$).

Some of these haloes are able to form a small SC close to their density centres (the physics of this SC formation will be investigated in future work). Due to practical limitations, RAMSES employs ‘force softening’ for the stellar component to avoid divergent gravitational forces of close encounters. Force softening places an upper bound on the gravitational force within some critical radius, which in the case of RAMSES is of the order of the grid-cell side length ($\sim 3\,$pc). This results in inaccurate modelling of close stellar orbits within a SC. Therefore, any SC that develops in RAMSES (and similar cosmological codes) is prone to artificial dissolution due to its diminished intra-gravitational force, independent of any physical effects within the host galaxy. As such, I do not attempt to draw any conclusions from the survival of these SCs. Instead, I will model the survival and properties of these SCs using follow-up simulations with an accurate direct summation code. I describe these follow-up simulations, next.

Direct summation N-body simulations

I simulate the evolution of SCs in the EDGE dwarfs using a direct summation N-body tool. This sacrifices accurate representation of the cosmological context and host potential for a more precise representation of the SC evolution. I run these simulations using a variant of the NBODY6 code (Aarseth, 1999), a Graphics Processing Unit (GPU) enabled direct N-body simulation tool (Nitadori & Aarseth, 2012), which uses regularisation to multiple-order stellar encounters. Stellar evolution is implemented with the standard ‘Eggleton, Tout and Hurley’ option in NBODY6 (Eggleton et al., 1989; Tout et al., 1997; Hurley et al., 2000, 2002; Hurley, 2008).

My chosen variant is NBODY6DF (Petts, Gualandris, & Read, 2015; Petts, Read, & Gualandris, 2016), which introduces the effects of dynamical friction (first described in Chandrasekhar, 1943). Dynamical friction is a drag force which acts on a body as it passes through a background of lighter bodies, and would normally manifest as a result of interactions between a SC and background stars, gas and DM. However, in the default NBODY6 the background potential is modelled as a spherically symmetric profile and does not respond to the gravity of an orbiting SC. NBODY6DF uses a semi-analytic approach to calculate the orbital decay of a SC due to dynamical friction, which eliminates the need for simulating the full galactic context. The code depends upon a distribution function to properly calculate the dynamical friction force, which is analytic for a Dehnen potential

(Dehnen, 1993):

$$\rho_{\text{Dehnen}}(r) = \rho_0 \left(\frac{r}{r_{\text{s}}}\right)^{-\gamma} \left(1 + \frac{r}{r_{\text{s}}}\right)^{\gamma-4}, \tag{5.1}$$

where ρ_0 is the central density, r_{s} is the scale radius and γ is a variable used to set the logarithmic slope of the inner density profile ($\gamma = 0$ corresponds to a core and $\gamma = 1$ corresponds to a cusp). A range of options for the variable γ are implemented in NBODY6DF based on analytic solutions from Dehnen (1993). Since the code uses a spherically symmetric Dehnen profile, I fit this to the EDGE dwarf density profiles in Section §5.4.3.

Critically, the core-stalling phenomenon is reproduced whereby dynamical friction ceases within some radius, which is typically the time at which the orbital radius approaches the tidal radius of the orbiting SC (Goerdt et al., 2010; Petts et al., 2015, 2016). For a Dehnen potential, this radius can be estimated as:

$$r_{\text{stall}} = \left[\frac{M_{\text{SC}}}{M_{\text{g}}}\left(r_{\text{s}}^{2-\gamma} + r_{\text{s}}\gamma\right)\right]^{1/(3-\gamma)}, \tag{5.2}$$

where $M_{\text{SC}}/M_{\text{g}}$ is the ratio of the SC mass to the host galaxy mass.

The ICs for each SC were constructed with the tool McLuster (Küpper et al., 2011) using a Plummer density model (Plummer, 1911), a Kroupa IMF (Küpper et al., 2010) with stellar masses $0.1 \leqslant \text{M}_{\odot} \leqslant 100$. This equates to a mean stellar mass of $\sim 0.63\,\text{M}_{\odot}$. I use an initial mean metallicity of 1×10^{-4}, the lowest available in native NBODY6. I assume zero primordial binaries and stars which evolve into black holes have no natal kick velocity. Both of these choices remove potential sources of dynamical heating, and so maximise SC survival. I retain unbound stars in the full integration of the system, as I find that these can often become rebound to the SC at later times.

I create ICs for SCs over a grid of masses (star numbers $N = 2^{13}, 2^{14}, 2^{15}, 2^{16}$, yielding the initial masses given in Table 5.2), initial half mass radii ($R_{\text{half}}/\text{pc} = 2.5, 5, 10$), orbital radii ($R_{\text{g}}/\text{pc} = 45, 100, 200$), and orbital eccentricities ($v_{\text{ini}}/v_{\text{circ}} = 0.25, 0.50, 0.75, 1.00$). Eccentric orbits are produced by setting the initial tangential velocity to fractions of the circular velocity in a Dehnen potential:

$$v_{\text{circ}}^2(r) = \frac{GM_{\text{g}}r^{2-\gamma}}{(r + r_{\text{s}})^{3-\gamma}}. \tag{5.3}$$

The combinations of initial parameters are described in Table 5.2. Each permutation is then inserted into a Dehnen profile fit to the haloes described in Table 5.1.

This simulation suite was run for either a Hubble time (13.8 Gyr) or until SC dissolution, which was determined as the time when the number of bound cluster stars drops below 10. I consider only the surviving SCs in my results.

5.4 Results

5.4.1 Comparison of EDGE ultra-faint dwarfs with Eridanus II

I begin by comparing the EDGE galaxy properties with those of Eridanus II (see Table 5.3). For the metallicities in the EDGE dwarfs, I first perform a surface brightness cut on the halo stars using a Markov Chain Monte Carlo (MCMC) maximum likelihood method described in Appendix C. This shows that for Halo1459, stellar mass and stellar metallicity drop as formation time is delayed (see GM:Later and GM:Latest). A delayed formation also leads to a larger half light radius and stellar velocity dispersion. These trends are a

Name	$M_{200\mathrm{c}}$ **[M$_\odot$]**	M_* **[M$_\odot$]**	$R_{1/2}$ **[kpc]**	**[Fe/H]**	σ_{LOS} **[km/s]**	$\rho(40\,\mathrm{pc})$ [M$_\odot$/kpc^3]	$M(<R_{1/2})$ [M$_\odot$]	t_{form} **[Gyr]**
Eridanus II	$4.7^{+6.9}_{-2.6} \times 10^{8\mathrm{a}}$	$8.3^{+1.7}_{-1.4} \times 10^{4\mathrm{b}}$	$0.277 \pm 0.014^{\mathrm{c}}$	$-2.38 \pm 0.13^{\mathrm{d}}$	$6.9^{+1.2\mathrm{d}}_{-0.9}$	1.418×10^{8a}	$1.2^{+0.4}_{-0.3} \times 10^{7\mathrm{d}}$	-
Halo1445	1.316×10^9	1.348×10^5	0.101	-2.383	4.992 ± 0.513	4.781×10^8	9.927×10^5	3.788
Halo1459	1.429×10^9	3.770×10^5	0.099	-1.988	5.660 ± 0.454	6.887×10^8	1.914×10^6	2.830
Halo1459 GM:Later	1.426×10^9	1.110×10^5	0.200	-2.493	5.709 ± 0.525	3.425×10^8	2.922×10^6	3.191
Halo1459 GM:Latest	1.375×10^9	8.646×10^4	0.304	-2.760	6.071 ± 0.464	3.623×10^8	7.261×10^6	3.547

Table 5.3: Comparison between the properties of Eridanus II and those of the EDGE dwarfs. From left to right are the galaxy name, the virial mass, the total stellar mass, the projected half light radius, the stellar metallicity, the stellar velocity dispersion, the galactic density at 40 pc, the mass within the half light radius using the mass estimator from Wolf et al. (2010), and the formation time measured as the time when the main progenitor reaches 50% of the final $M_{200\mathrm{c}}$. For simulations, the velocity dispersion and uncertainty are determined using a bootstrapping technique with $\sigma_\star = \sqrt{\sigma^2_{\star,\mathrm{x}} + \sigma^2_{\star,\mathrm{y}} + \sigma^2_{\star,\mathrm{z}}}/\sqrt{3}$. Properties for Eridanus II are gathered from the literature, a: (Contenta et al., 2018), b: (Bechtol et al., 2015), c: (Crnojević et al., 2016), d: (Li et al., 2017).

direct result of the assembly history, and are described fully in Rey et al. (2019). Eridanus II itself is a particularly extended, low-metallicity and high-dispersion galaxy. These properties are best matched by Halo1459 GM:Later, and support the notion that Eridanus II is itself a late-former. I also include the central densities at 40 pc (where I use the best fit potential from Contenta et al. (2018) for Eridanus II) and the mass contained within the half light radius as calculated using the mass estimator from Wolf et al. (2010). Once again, the closest comparison is with Halo1459 GM:Later.

Though the Halo1459 GM:Latest simulation is in many ways the best match for the properties of Eridanus II, I do not consider it for SC survival. There is less early core-formation due to diminished star formation activity, and whilst the central density begins to decline at late times as in Halo1459 GM:Later, a late cuspy merger rebuilds the central density (as shown in Chapter 4 and Orkney et al. 2021a). The final central potential at $z = 0$ is degenerate with Halo1459, but it could have hosted the most substantial core if it were not for the cuspy merger.

5.4.2 Mass assembly and star formation

The haloes described in Table 5.1 attain $M_{200\mathrm{c}}$ halo masses of approximately $1.5 \times 10^9\,\mathrm{M}_\odot$ by $z = 0$. This places the EDGE dwarfs in a similar mass regime to the ultra-faint dwarf galaxy Eridanus II, with the authors in Contenta et al. (2018) deriving $M_{200\mathrm{c}} = 4.7^{+6.9}_{-2.6} \times 10^8\mathrm{M}_\odot$ from NFW profile fits. All haloes form stars when baryonic physics is switched on, although it is isolated to early times ($z < 4$). Star formation continues for some time after the onset of reionization at $z = 8.5$, but is quenched after the remaining cool gas within the halo is exhausted (as in Rey et al. 2020).

The star formation and mass growth histories up to $z = 3$ are shown in figure 5.1. The mass growth is defined as the mass enclosed within 1 kpc rather than the virial mass $M_{200\mathrm{c}}$, because the central mass is most important for the survival of low-orbit SCs, and because $M_{200\mathrm{c}}$ undergoes a pseudo-growth due to the lowering background density of the Universe as it expands (Diemand et al., 2007; Diemer et al., 2013). There is no star formation in any of the haloes after $z = 4$, and the overall mass internal to 1 kpc remains roughly constant after 1 Gyr. The star formation in all haloes is bursty, which is a necessary quality in driving the gaseous flows responsible for DM core formation. Indeed, there is a fluctuating gas mass in all haloes at early times. Halo1459 assembles its central mass most rapidly and has the highest final central mass, along with the most substantial star

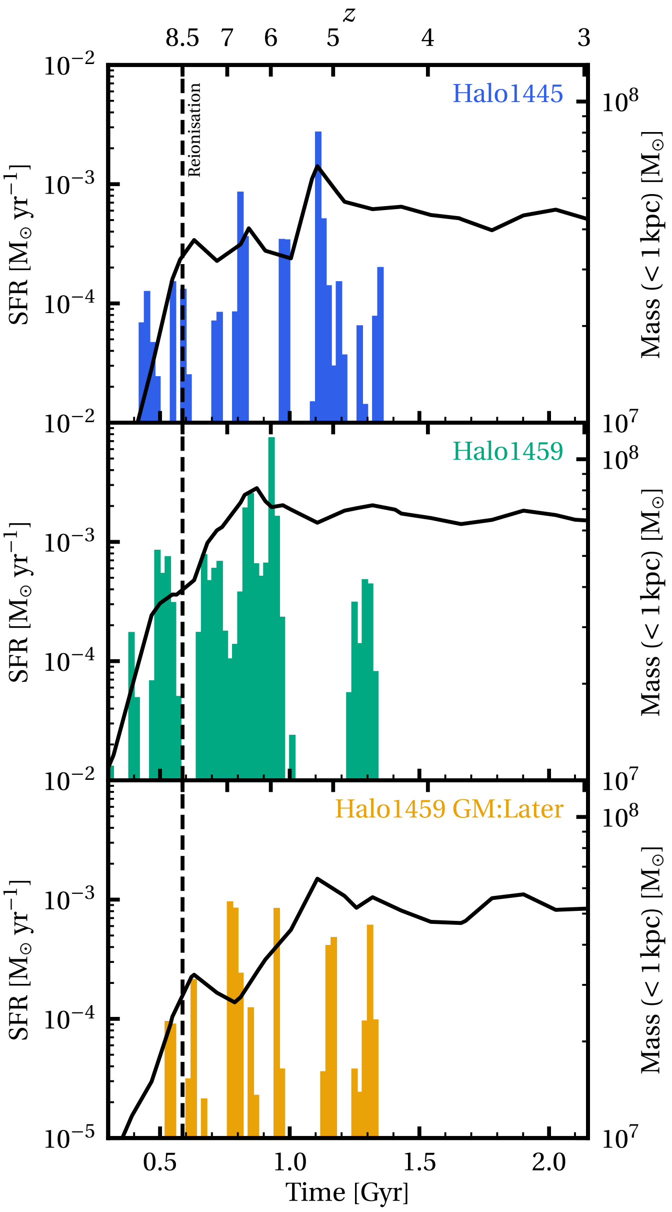

Figure 5.1: The star formation and mass assembly history for the baryonic EDGE simulations. The star formation rate (left y-axis) is averaged over bin sizes of 20 Myr, and takes into account stars formed within the virial radius R_{200c} of the main progenitor halo. The mass assembly history (right y-axis) considers the total mass contained within the inner 100 pc of the main progenitor halo. A vertical dashed line indicates the onset of reionisation at $z = 8.5$.

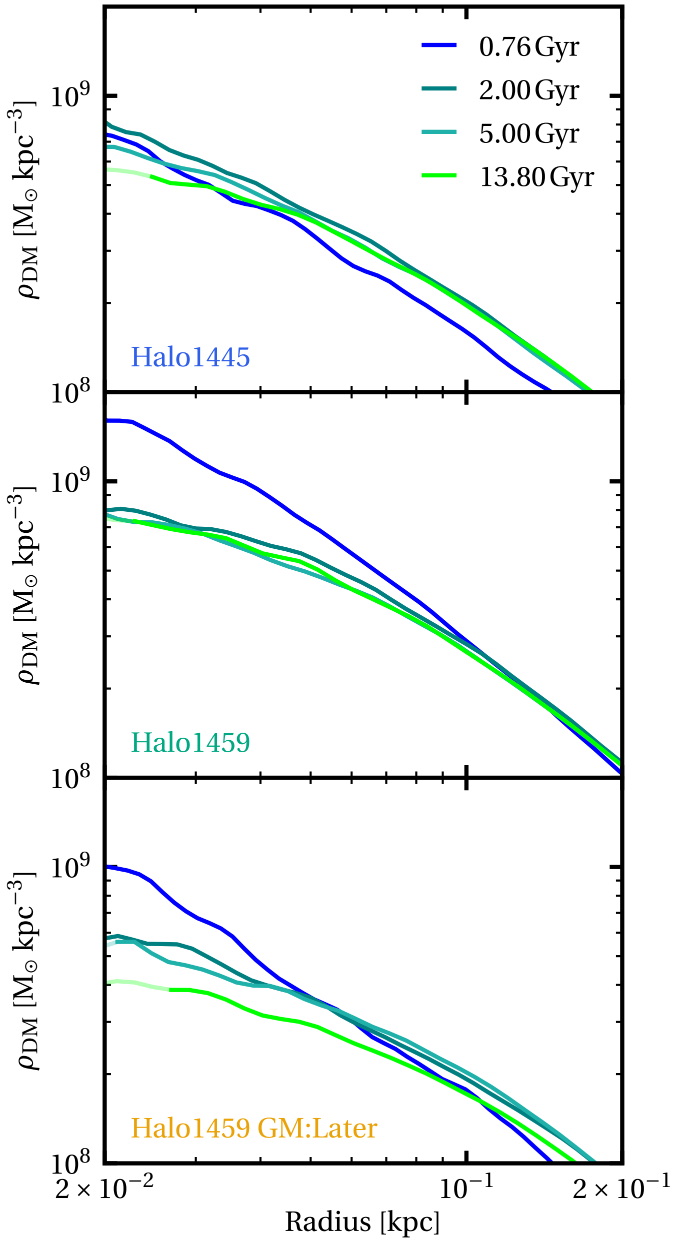

Figure 5.2: 3D DM density profiles for the main progenitor halo in the baryonic EDGE simulations. These are shown at four different times throughout the evolution of the halo, where the density has been averaged over the preceding three simulation outputs and passed through a Gaussian filter to reduce noise. Faint lines are used to indicate the radius within which numerical relaxation may have contaminated the result (see Appendix B).

formation. This relation appears causal in nature, with a higher early mass aiding in the compression of gas into star-forming clouds.

Note that these results are qualitatively the same when using the M_{200c} mass and/or the combined star formation from all progenitors.

5.4.3 Density profiles

Density profiles for the major progenitor branch of each halo are shown in Figure 5.2. A faint line indicates where the DM distribution is likely dominated by two-body relaxation (see Appendix B). All haloes experience a shallowing of their central density profile slopes, occurring predominantly over the period when the galaxy is forming stars. The magnitude of this early-time shallowing is most significant in Halo1459, which owes to its more intense star formation.

The central profile in Halo1445 changes only marginally between 0.76 and 2 Gyr. This is not the case, however, for the DM profile in Halo1459. This exhibits substantial shallowing by 2 Gyr that remains mostly unchanged throughout the rest of the halo evolution. In this case, it is clear that the DM heating is baryonic in origin, and that it is large enough that it has dominated any heating due to two-body relaxation. Halo1459 GM:Later shows the most significant shallowing of the simulations shown here, with a portion occurring after the cessation of star formation. In Chapter 4, I show that this owes to impulsive heating from late-time minor mergers similar to the mechanism described in Naab et al. (2009); Boldrini et al. (2020b).

In figure 5.3, I show Dehnen profile fits to the *total* mass distribution of each RAMSES halo (these are distinct from the DM density profiles of Figure 5.2). I consider only the portion of the profile beyond the numerical relaxation limit. These fits are produced with the python module LMFIT (Newville et al., 2014), and maximise the goodness of fit within 0.2 kpc. For Halo1445 and Halo1459 I fit the halo density profiles at $z = 3.2$, because this time is late enough that the inner halo is assembled whilst minimising two-body relaxation. For Halo1459 GM:Later I make a fit both at $z = 4$ and $z = 0$ and interpolate between them to approximate a varying potential profile which best matches the simulation data at all times, as in Orkney et al. (2019). I also produce a fit for Halo1459 DMO to provide a $\gamma = 1$ cusp reference, but do not fit profiles to the other DM-only simulations. I include the cored Dehnen profile from Contenta et al. (2018) that is best able to host N-body SC simulations with properties comparable to that in Eridanus II. This profile is named 'Fcore'.

The fits for Halo1459 DMO and Halo1445 accurately reproduce the simulation density over the ranges shown and beyond. The fit for Halo1459 and Halo1459 GM:Later deviate from the density data in the outer regions because a Dehnen profile density varies as r^{-4} in its outskirts whereas the EDGE haloes vary as r^{-3}. These fits are suitable for my purposes here, since I limit my analysis to orbital radii of 200 pc or less.

I also plot constraints for the DM density profile of Eridanus II in red, based upon a Hernquist-Zhao profile (Hernquist, 1990; Zhao, 1996) fit performed by the authors in Zoutendijk et al. (2021). This fit is performed using pyGravSphere (Read & Steger, 2017) with stellar line-of-sight velocities as measured by the MUSE-Faint survey. The shaded bands correspond to 68% and 95% confidence limits. This demonstrates that all profiles fit to EDGE dwarfs are within the 68% limit, and even the flat core profile 'Fcore' is within the 95% limit.

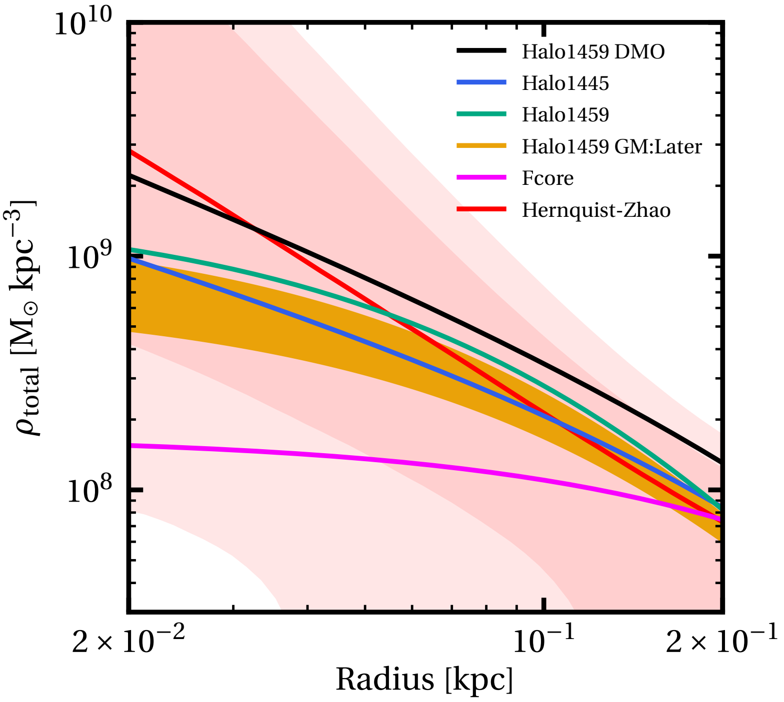

Figure 5.3: Fits to the 3D density profiles of RAMSES simulations shown in Table 5.1 at $z = 3.2$. The fits to Halo1459 GM:Later are shown as a filled region, with the upper (lower) limit representing the fit at $z = 4$ ($z = 0$). A central dense SC, which would otherwise manifest as a central density spike within 0.01 kpc, has been removed from Halo1459 prior to fitting. This has minimal effect on the Dehnen profile fit, and is only present at early times. The 'Fcore' line represents the profile from Contenta et al. (2018) best able to host N-body simulations with Eridanus II SC properties. I include constraints to the density profile of Eridanus II based on a Hernquist-Zhao profile fit from Zoutendijk et al. (2021), where the shaded bands correspond to 68% and 95% confidence limits.

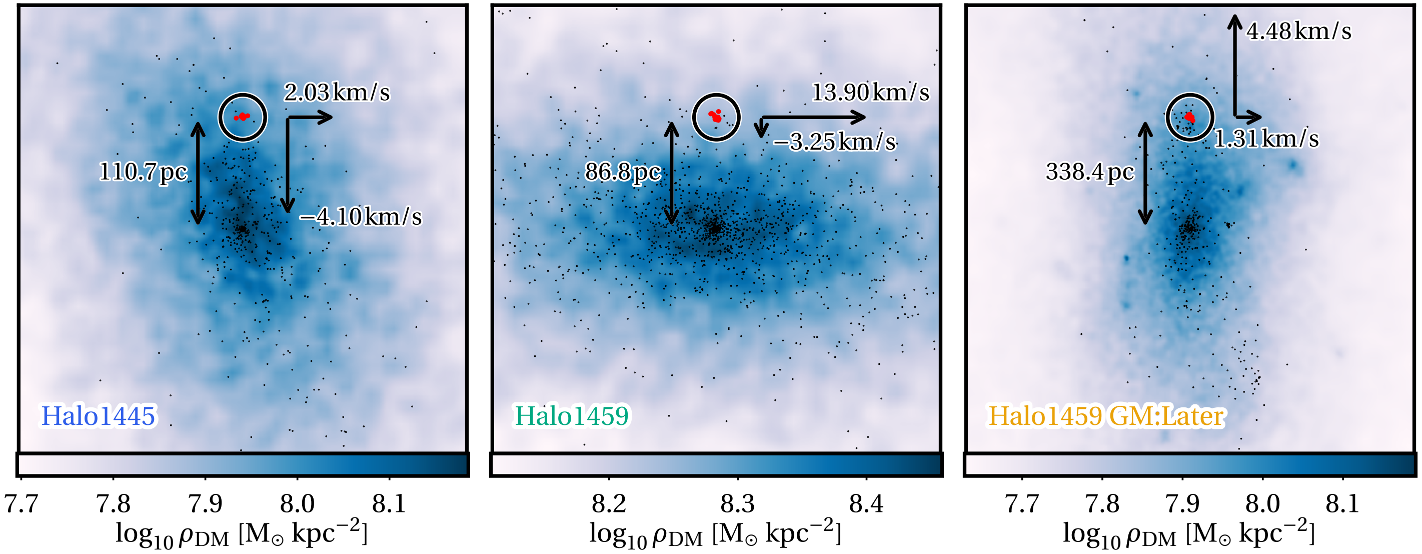

Figure 5.4: Plot of SCs in orbit around their host galaxy at $z = 4$. The DM surface density is shown in blue, with star particles over-plotted as black pixels. Stars deemed as belonging to the SC are shown as red dots, and are highlighted by a circle. Also marked on the plot are the distance between the mass-weighted SC centre and the centre of the stellar distribution in the host galaxy, as found by the shrinking spheres method (Power et al., 2003) implemented in PYNBODY, and the mass-weighted mean velocity of the SC. The simulation frame has been oriented such that the x and z distances are 0, and the z-component of the velocity is 0.

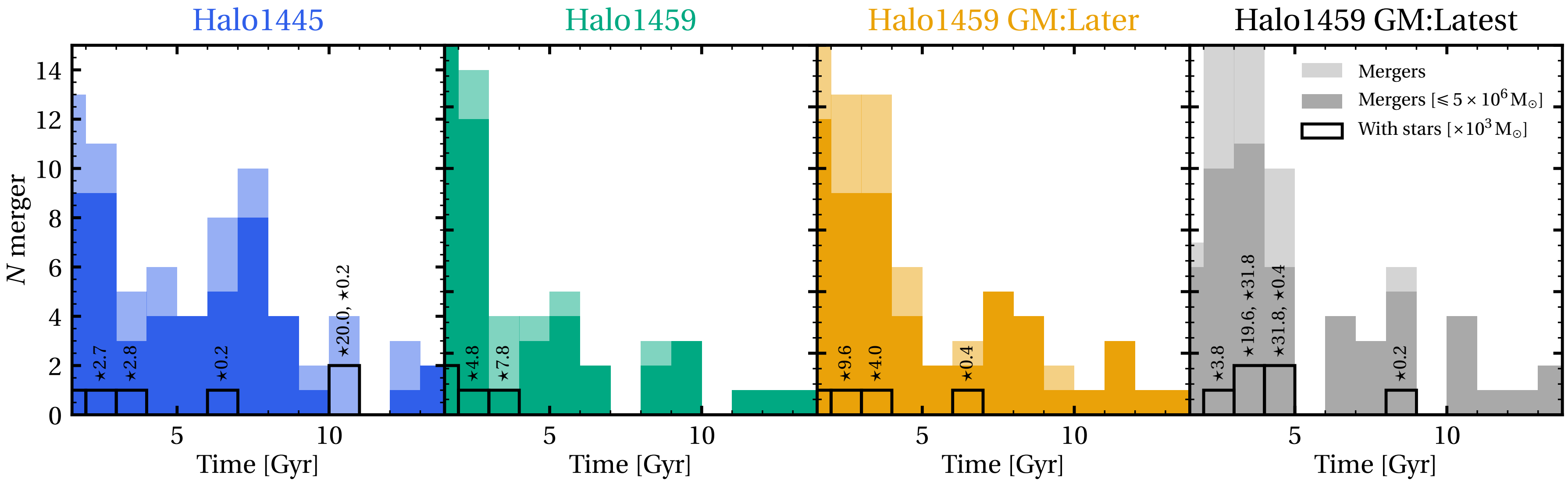

Figure 5.5: Histograms with the total number of mergers after $z = 4$ with $M_{200\mathrm{c}} \geqslant 10^6\,\mathrm{M}_\odot$. Faint bars correspond to all mergers, whereas solid bars correspond only to mergers with $M_{200\mathrm{c}} \leqslant 5 \times 10^6\,\mathrm{M}_\odot$. Hollow black histograms highlight mergers with stellar material, where the total stellar masses are included as annotations. Note that the merging time is defined as when the merging subhalo crosses over the $R_{200\mathrm{c}}$ radius of the host

5.4.4 Star clusters in RAMSES

In Figure 5.4, I show example plots of SCs found in the EDGE haloes at $z = 4$. The DM surface density of the host galaxy is shown in blue, with background stars over-plotted as black pixels. Stars identified as belonging to the SC are plotted in red and have been highlighted with a circle. The SC stars form at high redshift ($6 \leqslant z \leqslant 9$).

The SCs in Halo1445 and Halo1459 represent in-situ formation, the stars are born well within the virial radius R_{200c} of their host galaxies and are not associated with any significant local DM overdensity. The SC highlighted in Halo1459 GM:Later begins life outside of R_{200c} in its own DM halo, and continues to form stars as it falls onto the host galaxy. This DM halo disintegrates prior to $z = 4$ and leaves a SC with no associated dark matter. The details surrounding the births and properties of SCs in EDGE will be investigated in future work (Taylor et al. in prep).

The total stellar masses at the time of their birth are $5.1 \times 10^3 \mathrm{M}_\odot$ for the SC in Halo1445, $9.2 \times 10^3 \mathrm{M}_\odot$ for the SC in Halo1459 and $4.0 \times 10^3 \mathrm{M}_\odot$ for the SC in Halo1459 GM:Later, with all on highly eccentric orbits. The positions shown in Figure 5.4 are not representative of the orbital apo/pericentres.

All SCs gradually dissolve due, primarily, to numerical effects and are entirely dispersed before $z = 0$. The SCs are comprised of only a few stellar particles due to the stellar mass resolution in these simulations ($\sim 300\,\mathrm{M}_\odot$ at the time of birth), and so their evolution and dissolution are unreliable. Regardless, it is worth noting that the EDGE dwarfs naturally form SCs within dwarf galaxies.

5.4.5 Merger histories

Whilst the EDGE dwarfs assemble at early times, there are still a significant number of mergers throughout their lives. These mergers may contribute to sub-dominant DM heating as with Halo1459 GM:Later, but could also act as vehicles for SCs. A SC that is donated via a subhalo merger would be somewhat shielded from the destructive forces of gravitational tides until the DM envelope is stripped (e.g. Mashchenko & Sills, 2005a,b). If the SC in Eridanus II was accreted at late times then this could alleviate the need for a fully cored host potential.

In Figure 5.5, I show histograms for the total number of mergers with $M_{200c} \geqslant 10^6\,\mathrm{M}_\odot$ occurring after $z = 4$. Less massive mergers with $M_{200c} \leqslant 5 \times 10^6\,\mathrm{M}_\odot$ are shown in darker colours. Mergers that host stars prior to infall are shown with hollow black bars, where the stellar masses are included as annotations. The EDGE dwarfs are situated in isolated cosmic environments, and yet there are still some stellar mergers that occur at later times. Even in this small sample, there is one example of a $m > 10^4\,\mathrm{M}_\odot$ stellar mass merger after 10 Gyr.

The N-body analysis in Section §5.4.6 considers only the case of in-situ SCs. SCs formed in their own ex-situ DM haloes experience stronger dynamical friction forces and are shielded from the effects of gravitational tides, but will also be exposed to steeper potential slopes upon their infall, and so may not have a comparable evolution. Whilst I note that it is entirely possible that the SC in Eridanus II was formed ex-situ, analysis of the colour magnitude diagrams in Eridanus II cannot distinguish between host and SC – suggesting similar origins (Simon et al., 2021b).

	$\mu(\mathbf{R}_\mathrm{g})$ [pc]			$\sigma(\mathbf{R}_\mathrm{g})$ [pc]		
$\mathbf{M}_\mathrm{ini}$ [$\mathbf{M}_\odot$]	**0(Fcore)**	**0**	**0(t)**	**0(Fcore)**	**0**	**0(t)**
4.18×10^4	42.47	7.27	13.14	11.00	3.53	5.00
2.08×10^4	35.06	4.88	9.22	8.25	2.56	4.01
1.00×10^4	31.58	3.00	5.38	9.85	1.71	2.95
5.14×10^3	30.78	1.81	3.40	22.96	1.18	1.97

Table 5.4: Summary of the final mean orbital radii for the NBODY6DF simulation suite. The first column indicates the initial SC mass, and sub-columns of the second and third columns indicate the slope γ of the host potential. The second column includes the mean orbital radii averaged over the most recent orbit. The standard deviation of orbital radii for the SCs in each group are included in the third column. More massive SCs tend to infall more rapidly, but then stall at larger radii.

5.4.6 *N*-body simulations of SC survival in the EDGE dwarfs

Final SC properties

Of all simulations described in Table 5.2, I find that only those hosted by $\gamma = 0$ cored potentials are able to survive for a full Hubble time. Only two SCs in a semi-cored potential (Halo1445) survive longer than 6 Gyr, and no SC in a cuspy potential (Halo1459 DMO) survives longer than 1.5 Gyr. SCs with an initial $N = 2^{15}$ stars are best able to reproduce the estimated mass of the SC in Eridanus II ($2.7 \times 10^3 \leqslant M/\mathrm{M}_\odot \leqslant 8.2 \times 10^3$, assuming $M/L_v = 2$).

Properties for all surviving SCs after 13.8 Gyr are presented in Figure 5.6. In the upper panel I plot the projected half light radius against the final orbital radius, where the orbital radius is averaged over the last pericentre to apocentre passage. The most recent pericentre and apocentre are denoted with error bars. The projected half light radii are evaluated with the MCMC fitting described in Appendix C. The observed properties of the SC in Eridanus II, with uncertainties, are indicated by a red region.

The orbital response to dynamical friction is so strong that SCs rapidly approach their core-stalling limit, with most SCs reaching that limit within 1 Gyr. Only some SCs in the ‘Fcore’ potential are yet to reach this limit by a Hubble time. The orbital radius then continues to decay as the SC is stripped of mass, as predicted by equation 5.2. SCs orbiting the ‘Fcore’ potential are able to adopt a wide range of final orbital radii depending on the initial orbital eccentricity, and bracket the projected orbital distance of the SC in Eridanus II. SCs at larger orbital radii should not be discounted, because the offset observed in Eridanus II is a projected distance and the full distance is unknown. SCs in the ‘Fcore’ potential also retain a larger degree of their initial orbital eccentricity, whereas the orbits of SCs in other host potentials are rapidly circularised. Despite their stronger response to dynamical friction, the most massive SCs maintain slightly higher orbital radii due to their increased core-stalling radius (see Table 5.4). This sub-dominant effect may be important for the relatively small offset observed in Eridanus II.

Only SCs within the ‘Fcore’ potential are able to approach the extended size of that in Eridanus II, with $R_\mathrm{halfmass,ini} = 10$ consistently producing the largest sizes. Trial simulations with more extended initial half mass radii ($R_\mathrm{halfmass,ini} = 15\,\mathrm{pc}$) were all extremely short-lived.

Prompted by Figure 5.5, I also investigated the SC properties over a Hubble time in increments of 2 Gyr. Whilst a larger portion of SCs survive at earlier times, they are more

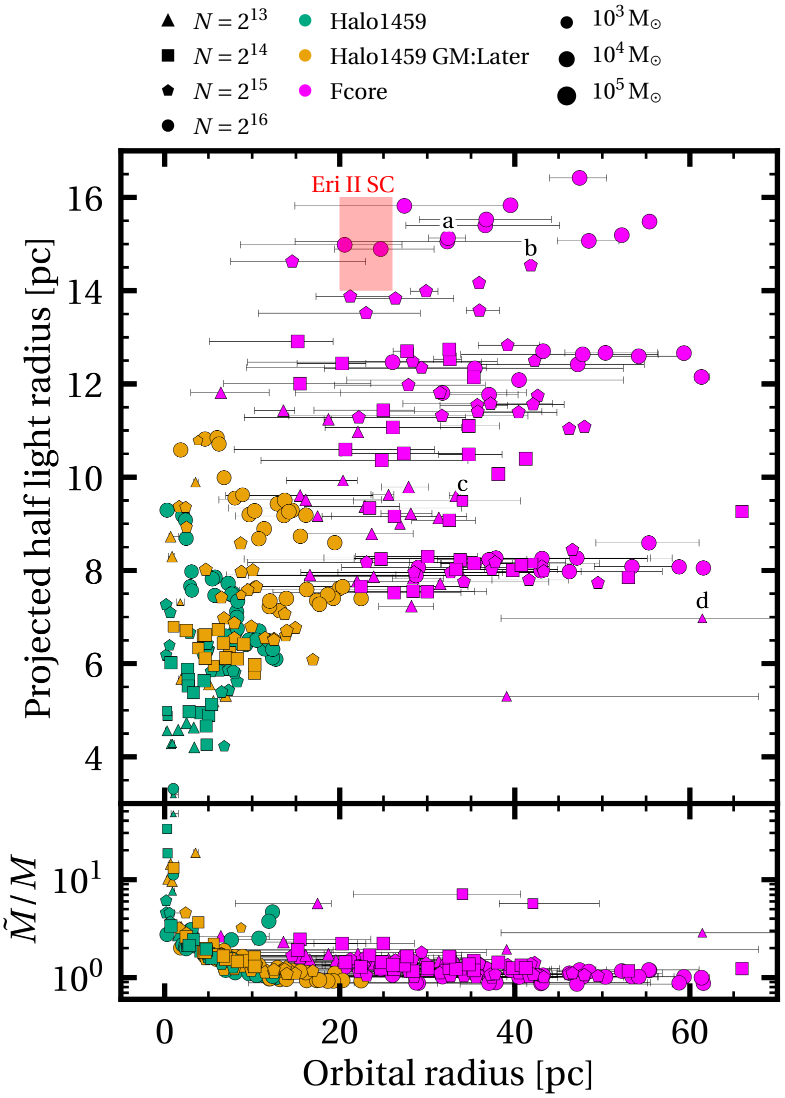

Figure 5.6: *Upper panel:* This plot shows the projected half mass radius versus the orbital radius of the surviving NBODY6DF simulation suite after a Hubble time. Marker style indicates the initial membership N of each SC, colour the host profile, and size the final bound mass in solar units. Each point represents the average radius on the most recent orbit, with error bars indicating the orbital apocentre and pericentre. Also included is a red band representing the parameter space expected for the SC in Eridanus II, using the data from Simon et al. (2021b). Some host haloes are not represented because they did not support SC survival, and others lie beyond the 70 pc shown here. Letter labels indicate the locations of the sample SCs shown in Figure 5.10. *Lower panel:* The ratio $\tilde{M}/M$ for all surviving NBODY6DF simulations against final orbital radius.

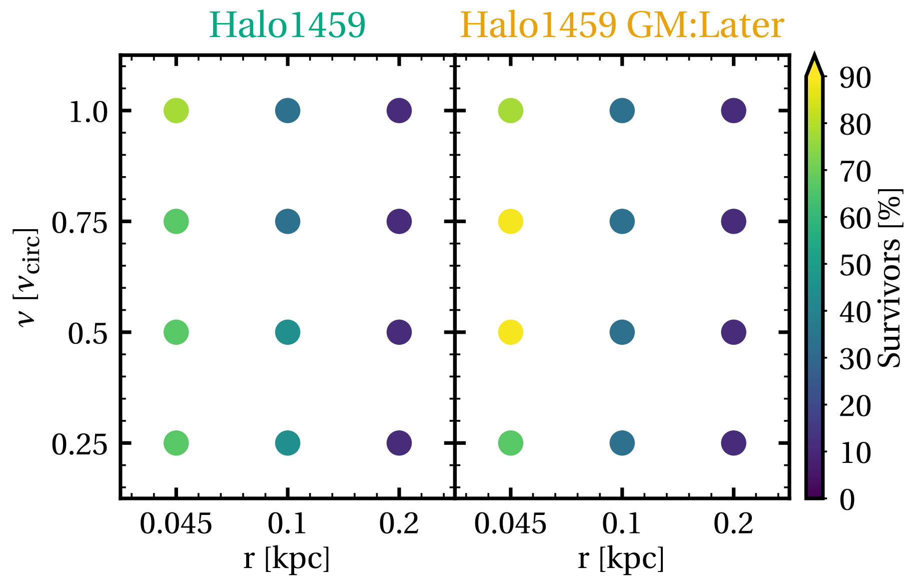

Figure 5.7: The Hubble time survival percentage of SCs between 2^{13} and 2^{15} initial star particles, orbiting within Halo1459 and Halo1459 GM:Later. I have omitted 2^{16} SCs and the 'Fcore' potential because most SCs survive regardless of their initial orbital properties.

compact and are less able to reproduce the extended size seen in Eridanus II.

The lower panel of Figure 5.6 includes the mass ratio $\tilde{M}/M$, which I define now. The velocity dispersion of a self-gravitating system can be approximated using the virial theorem as:

$$\sigma^2 \approx \frac{GM(<r)}{r}. \tag{5.4}$$

By rearranging this equation, the stellar velocity dispersion can be used to estimate the mass within the half light radius. By comparing this dynamical mass estimate to the stellar mass of the system, a measurement can be made of the DM content. This ratio will be higher for a SC that has dynamically relaxed at the centre of a DM halo.

I use the formula provided in Wolf et al. (2010) to find an analytic mass within the half mass radius, which I call $\tilde{M}$. The ratio of $\tilde{M}$ to the SC stellar half mass reveals by how much the SC mass is dominated by the background potential, where $\tilde{M}/M = 1$ implies zero influence and $\tilde{M}/M \gg 1$ implies a central SC. The lower panel in Figure 5.6 shows that SCs situated further than ~ 5 pc from the host centre typically have a mass ratio of $1 \leqslant \tilde{M}/M \leqslant 2$. As predicted, the ratio peaks for SCs that have fallen into the host centre.

SC survival in the EDGE dwarfs

Following the basic premise that harsher gravitational tides act to destroy orbiting SCs more rapidly, it is natural to assume that there are simple relationships between SC survival and the initial orbital parameters. Traditionally it is expected that more eccentric orbits, which plunge the SC in and out of a stronger background potential, result in shorter-lived SCs due to the impact of tidal shocks (Weinberg, 1994; Kundic & Ostriker, 1995; Gnedin et al., 1999; Baumgardt & Makino, 2003; Webb et al., 2019).

In Figure 5.7 I compare the survival of the lower initial mass SCs in two of my host potentials, sorted by initial orbital velocity and radius. As expected, survival is improved with lower initial orbital radii. However, survival is *not* always improved with increasingly

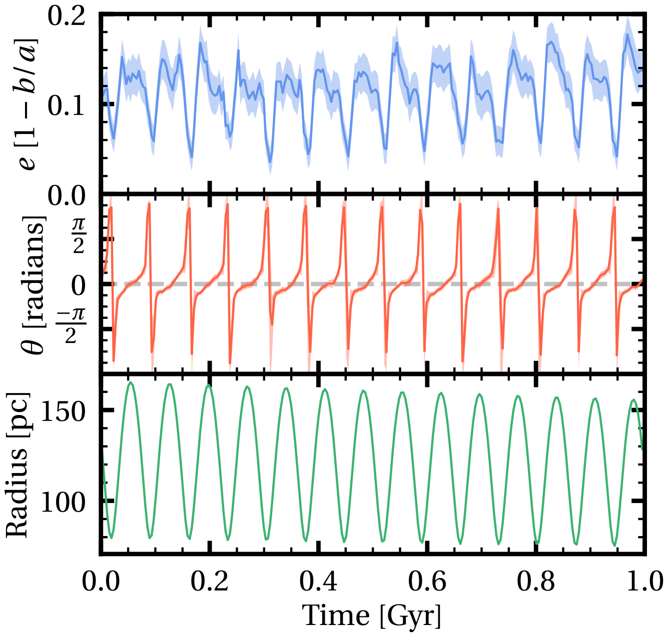

Figure 5.8: The evolution of the SC shape for an example simulation over a Gyr (from $\sim 3 - 4$ Gyr in physical time). The upper panel shows the ellipticity e, the middle panel shows the orientation θ (where $\theta = -\pi, 0, \pi$ is aligned with the galactic centre), and the lower panel shows the galactocentric orbital radius. Filled regions are the 1σ uncertainty determined from bootstrapping. For eccentric orbits, the SC shape is highly dependent on the position in the orbit.

circular orbits. In Halo1459, SCs starting at 0.1 kpc are slightly more likely to survive with eccentric orbits. In Halo1459 GM:Later, moderately eccentric ($v_{\rm circ} = 0.75, 0.5$) orbits starting at 0.045 kpc are likely to survive, with the survival dropping off for both extremely eccentric and circular orbits ($v_{\rm circ} = 0.25, 1$).

Whilst it is generally true that more eccentric orbits encourage the dissolution of the SC, it is also true that dynamical friction is stronger for plunging orbits, which in turn acts to circularise the orbit. SC dissolution is reduced as the SC approaches the shallower slope near the centre of the host potential, with SCs that survive infall being most likely to survive long-term. Therefore, there is competition between whether the increased dissolution or increased orbital decay will destroy or protect the SC. The orbital decay for SCs in the Halo1459 and Halo1459 GM:Later potentials occurs over timescales of less than a Gyr, and long-term survival is decided early.

SC shape

Observations in Simon et al. (2021b) have shown that the SC in Eridanus II has a highly elliptical shape ($e = 0.31^{+0.05}_{-0.06}$) and the direction of the major axis is almost aligned with the photometric centre of the galaxy ($\theta = 15 \pm 6°$).

In Figure 5.8 I plot the evolution of the ellipticity e and alignment θ for an example SC over a Gyr using the shape finder I will describe in Chapter 6, modified for projected stellar distributions. I consider all stars within a projected radius set by the Roche volume, where I exclude stars with $L \geqslant 100\,{\rm L}_\odot$ and black holes/compact remnants. This example SC was chosen because it clearly exhibits evolutionary trends, but the results are consistent throughout the simulation suite. This plot shows that e (upper panel) and θ (middle panel)

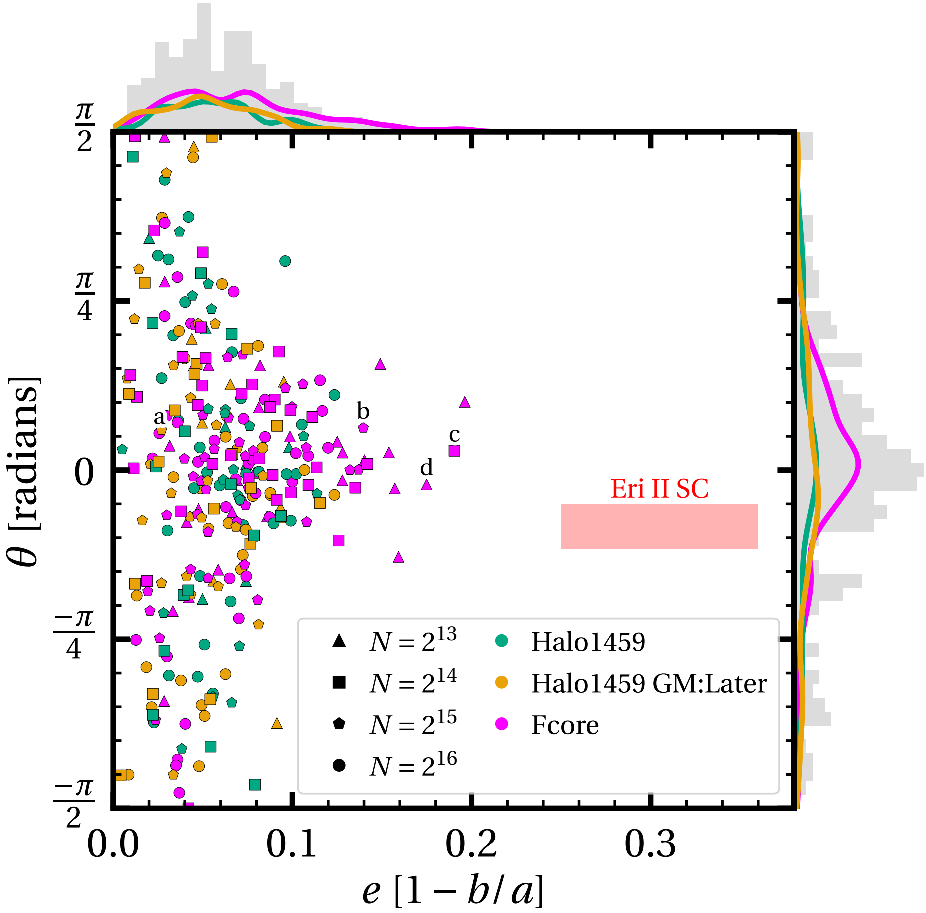

Figure 5.9: The alignment angle θ versus ellipticity e for all surviving SC simulations, calculated at the orbital apocentre (maximising θ and e). Histograms, including normalised distributions for each host profile, are plotted at the borders. The red region indicates the observed properties of the SC in Eridanus II from Simon et al. (2021b). Letter labels indicate the locations of the sample SCs shown in Figure 5.10.

vary periodically with the orbital radius (lower panel). e is maximised during apocentre passage, at which time the cluster is also most aligned with the galactic centre ($\theta = 0$). Note, however, that e can still be high for SCs on circular orbits, and that there is little preference for increased SC ellipticity with orbital eccentricity. There are also long-term evolutionary trends in all simulations, but they are dwarfed by the impact of the orbit periodicity and by the orbital eccentricity.

Hereafter I calculate e and θ using a MCMC fit – which I describe in Appendix C – viewed top-down on the orbital plane. The apparent ellipticity is maximised when viewed in the $x - y$ plane, and I do not consider alternative orientations. This method is more computationally demanding than simple numerical calculation, but provides a more direct comparison to observational data.

I plot e and θ for all surviving SC simulations at 13.8 Gyr in Figure 5.9. Motivated by the results in Figure 5.8, I fit the SC shape at the most recent orbital apocentre. This shows that SCs tend to align with the host galactic centre with increasing ellipticity (y-axis histogram), and that SC ellipticity e is rarely in excess of 0.1. Coloured Gaussian kernel density estimations show the contributions from the different host potential profiles.

Both Halo1459 and Halo1459 GM:Later are almost identical, with low e and incoherent alignment. SCs evolved in the 'Fcore' potential trend towards higher e and are significantly more aligned with their host.

Visual impression

In Figure 5.10 I present four sample SC simulations from the survivors at 13.8 Gyr. Examples **a, b** are chosen to represent feasible matches to the SC in Eridanus II in terms of their size and orbital radius, whereas examples **c, d** are chosen to represent the most feasible matches in terms of SC ellipticity and alignment angle. Of *all* simulations, **b** is the best match when all properties are considered together (although as for all the simulations, the ellipticity is still too low). Contours show the shape and alignment of each SC, where each band is annotated with the surface brightness in units of mag/arcsec^2. The surface brightness is defined based on the MCMC fit to the cluster body, and does not account for tidal debris. In all cases, the brightness of the bound SC are in excess of 20mag/arcsec^2, and easily meet the limiting magnitudes of current surveys (25.5 mag/arcsec^2 Drlica-Wagner et al. 2020, 32 mag/arcsec^2 Crnojevic 2020).

At these late times, the tidal debris from each SC has become well phase-mixed. Only in **d** is there visible tidal structure, though at low level. This is similar to the observed spatial distribution of Eridanus II stars in Figure 9 of Simon et al., 2021b. In all simulations, it takes at least multiple Gyrs for tidal debris to become visually phase-mixed, but with substantial variation between simulations. Whilst much of the faint tidal tail could be undetectable, the surface brightness from my simulations remains above limiting magnitudes near the SC vicinity ($\sim 5 - 10 \times R_{\mathrm{half}}$).

5.5 Discussion

5.5.1 Scenarios for a star cluster in Eridanus II

Eridanus II hosts a central dark matter core

There are three main implications if the potential profile of Eridanus II contains a substantial DM core. Firstly, the reduced gravitational tides support SCs with low initial masses ($\sim 5 \times 10^3\,\mathrm{M}_\odot$). Secondly, the reduced background potential encourages SC expansion and could support the extended distribution that is observed for the SC in Eridanus II. Thirdly, the core-stalling radius (Equation 5.2) would be larger and support a wider range of final orbital radii. These conclusions can be drawn from the 'Fcore' pink data points in Figure 5.6. A smaller core, as in Halo1459, is unable to explain the observed size and orbital radius of the SC in Eridanus II. There is marginal improvement if the potential is lowered further with time, as in Halo1459 GM:Later.

Whilst the 'Fcore' potential can justify both extended sizes and higher orbital radii, I am still unable to reproduce SCs with the high ellipticity seen in Eridanus II. This particular SC property may be caused by details that I do not consider in my simulations (i.e. gravitational perturbations from halo substructure/triaxiality or heating from stellar binaries). In Appendix D I consider whether the observed ellipticity is subject to bias from the host stellar distribution, but find it unlikely.

A new challenge arises in justifying the presence of a large, flat core in a galaxy as faint as Eridanus II. I consider this further in Section §5.5.2.

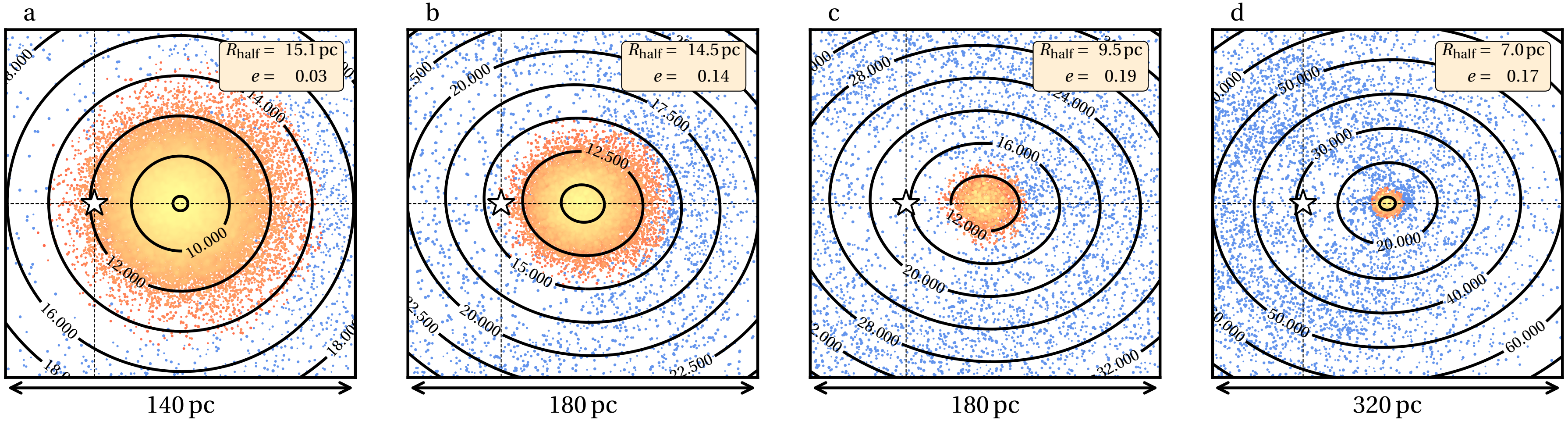

Figure 5.10: Example plots of N-body SC simulations, shown at orbital apocentre and viewed in the $x-y$ orbital plane. Initial simulation properties N, R_{half}, R_g, v/v_{circ} and γ are as follows: **a**: 2^{16}, 10 pc, 45 pc, 0.75, 0(Fcore); **b**: 2^{15}, 10 pc, 100 pc, 1, 0(Fcore); **c**: 2^{14}, 10 pc, 200 pc, 0.5, 0(Fcore); **d**: 2^{13}, 2.5 pc, 200 pc, 0.5, 0(Fcore). The locations of each SC are indicated with labels in Figures 5.6 and 5.9. A white star and dashed black lines represent the centre of the host potential. Stars within the spherical Roche region of the SC are shown in orange, with denser regions in lighter orange, whereas stripped stars are shown in blue. Surface brightness contours are included with units of mag/arcsec^2, which are produced using the method described in Appendix C. A physical scale is included beneath each panel, and the contemporary half light radius and ellipticity are attached as an annotation.

Star cluster donation

The SC in Eridanus II may have been donated via a merger. In this case, the modern-day properties of the SC can be decoupled from its present dynamical state. Eridanus II is considered an isolated system and is one of the Milky Way's most distant satellites, however the authors in Li et al. (2017) predict that it is most likely on its second passage around the Milky Way. Therefore, interactions several Gyr ago may allow for SCs to be implanted into Eridanus II.

The N-body simulations do not produce better matches to the observed properties of the SC in Eridanus II when viewed at earlier times, see Appendix E. This is primarily because the half light radius of the SC has not had sufficient time to expand. Nevertheless, a donated SC could be fine-tuned to produce the desired properties.

Interaction with mergers

The failure of the N-body simulations to produce SCs with an ellipticity in excess of $e = 0.2$ could be due to the smooth background potential. Interactions with substructure could perturb a SC orbit and shape, and may be required to explain the SC in Eridanus II.

Such interactions may dynamically heat low-orbit SCs or even expand their orbits, with the authors in Leung et al. (2020) showing that a late major merger can widen the orbits of the globular clusters in the Fornax dSph galaxy. This could alleviate the need for an extremely flat host potential to explain large sizes and orbital radii.

Tidal interactions

Following the idea that Eridanus II may have been less isolated in the past, close passages with other substructures orbiting the Milky Way could have tidally heated its SC as in Oh et al. (2000). This could encourage SC growth by removing mass from Eridanus II, thereby lowering the background potential, and encourage the SC to adopt a wider orbit.

Eridanus II hosts a nuclear star cluster

If the SC in Eridanus II is located at the centre of the potential then its survival is likely no matter the host potential of the galaxy, even in the case of severe cusps as in Amorisco (2017); Contenta et al. (2018). However, the SC would need to be born extremely close to, or at, the potential centre. In my N-body simulations, even a small offset of 45 pc in cuspy host potentials results in total SC dissolution within 1.5 Gyr.

This possibility is made very unlikely by the recent observations in Simon et al. (2021b), which place the SC at 23 ± 3 pc from the photometric centre of Eridanus II. Failing some mechanism which kicks nuclear SCs out to wider orbits, like mergers as in Leung et al. (2019, 2020), this would rule out a nuclear SC.

5.5.2 Forming cores in ultra-faint galaxies

I find that late-forming haloes combined with high rates of bursty star formation are the most likely to contain shallow density cores in EDGE. However, as shown in Section §5.4.6, the size and density of these cores cannot support SCs with the extended half light radius observed in Eridanus II. None of the EDGE dwarfs considered here are outside the 68% confidence intervals of mass assembly in ΛCDM, and more extreme late-forming galaxies may perform even better.

Name	$E_{\rm SN}$ **[erg]**	ΔW **[erg]**	$\epsilon_{\rm DM}$
Halo1445	7.688×10^{53}	1.636×10^{50}	2.128×10^{-4}
Halo1459	1.251×10^{54}	1.526×10^{50}	1.220×10^{-4}
Halo1459 GM:Later	2.715×10^{53}	7.273×10^{49}	2.679×10^{-4}

Table 5.5: Comparison of the estimated total SNe energy ($E_{\rm SN}$), the energy required to lower the central density cusp (cusp gravitational binding energy minus core gravitational binding energy, ΔW), and the coupling efficiency ($\epsilon_{\rm DM}$) for the two haloes in Table 5.1 at $z = 4$. For the calculation of $E_{\rm SN}$ I consider only stars within a core radius (taken from coreNFW profile fits, Read et al. 2016a), as stars exterior to this radius will not be contributing to the heating of the DM cusp.

The relationship between mass and star formation rate must also be considered. Halo1459 and Halo1459 GM:Later are able to form a remarkably similar density profile at early times (which can be seen from the profile fits in Figure 5.3), despite Halo1459 GM:Later forming less than a third of the stars that Halo1459 forms (Table 5.3). This is because the halo mass of Halo1459 GM:Later accumulates later and is more vulnerable to the impact of bursty star formation, which I investigate further next. Usually, less star formation results in less coring, and both early-time coring through stellar feedback and late-time coring through minor mergers are required to form the most substantial core. A later assembly does not guarantee a more significant core.

Pontzen et al. (2021b) find that cores form more efficiently if star formation is burstier. EDGE could be modified in many ways such that burstier star formation is favoured. The numerical resolution may contribute, and I note that the subgrid models are missing physics including magnetic fields, ionising radiation via radiative transfer, and more (see Agertz et al., 2020). Therefore, it is very possible that more realistic dwarf galaxies could form larger cores than in EDGE.

Energetics

I perform a simple comparison of the energies required to unbind DM cusps to that provided by SNe explosions, following the technique in Peñarrubia et al. (2012); Read et al. (2016a); Contenta et al. (2018); Trujillo-Gomez et al. (2020). I make this comparison at $z = 4$ because this is the point at which star formation has quenched in the EDGE dwarfs, although I note that this does not account for the continued coring in Halo1459 GM:Later.

I estimate the SNe energy from the IMF as follows:

$$E_{\rm SF} = \frac{M_* \xi E_{\rm SN}}{\langle m_* \rangle}, \tag{5.5}$$

where M_* is the total stellar mass of the galaxy at $z = 4$, $\langle m_* \rangle$ is the expectation value for the stellar mass, ξ is the number fraction of stars that become SNe ($m_* > 8\,{\rm M}_\odot$) and $E_{\rm SN} = 10^{51}$ erg is the energy per SNe. My implementation of RAMSES utilizes a Chabrier IMF (Chabrier, 2003), for which I evaluate $\langle m_* \rangle$ and ξ by integrating over the range $0.1 < m_*/{\rm M}_\odot < 120$ as 0.680 and 0.00802 respectively. This is an imperfect representation of the SNe energy because it does not consider that some SNe could have occurred whilst an accreted stellar particle was still ex-situ, and may not have contributed directly to the heating of the main progenitor.

The energy needed to depress the central density as in Figure 5.2 can be found by

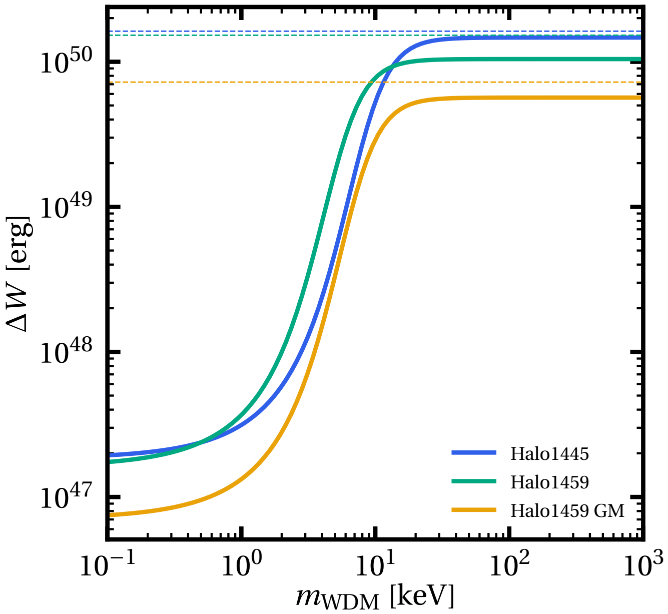

Figure 5.11: Equivalent energies required to lower the central density cusp (ΔW) assuming different halo concentration parameters corresponding to WDM over a range of particle masses. Horizontal dashed lines mark the values of ΔW from Table 5.5.

analysing the enclosed mass profiles of the haloes at $z = 4$. I fit a coreNFW profile (Read et al., 2016a) where the concentration parameter c is calculated as in Dutton & Macciò (2014). A cuspy profile is approximated by setting the parameter $n = 0$ (equivalent to an NFW profile Navarro et al., 1997). Then, the energy difference ΔW between the cuspy and fitted profile is calculated as in Equation 22 of Read et al. (2016a). A coupling efficiency between the SNe energy and DM is defined as $\Delta W/E_{\rm SF}$. The results are summarised in Table 5.5.

Although Halo1459 and Halo1459 GM:Later are the same galaxy with modified ICs, Halo1459 GM:Later has a lower energy required to unbind its DM cusp. This is because the later assembly of Halo1459 GM:Later has left it with a diminished central density at the earliest times (Figure 5.1 at $t = 0.76\,$Gyr). Halo1445 exhibits a similar coupling efficiency to Halo1459 GM:Later, which also owes to its slower mass growth.

Alternative cosmologies

As discussed in Contenta et al. (2018), cosmologies beyond ΛCDM can support lower central densities in galaxies like Eridanus II without relying on gravitational fluctuations driven by stellar feedback. For example, WDM does not in itself produce significant cores, but lowers the concentration of DM haloes such that core formation is more easily facilitated (Macciò et al., 2012; Fitts et al., 2019).

I now consider the implication of a WDM cosmology on ΔW in Figure 5.11. Plotted is the ΔW derived from coreNFW profile fits to the EDGE dwarfs, where the concentration parameter c has been posthumously varied according to predictions from the mass of a WDM particle (see Schneider et al., 2012). This shows that ΔW plummets by ~ 3 orders of magnitude for WDM particle energies $\lesssim 20\,$KeV. Whilst this would facilitate easier core formation, the reduction in central density could also result in delayed star formation (as in Lovell et al., 2020) – which would make core formation more difficult again.

Different cosmologies can also impact the evolution of SCs in ultra-faint galaxies. As an example, the authors in Schive et al. (2020) consider ultralight bosonic DM with a particle energy of $\sim 10^{-22}\,\mathrm{eV}$, in which the de Broglie wavelike nature of the particle results in a soliton core residing in the centre of Eridanus II. Whereas the formation of a core in itself aids with SC survival, the soliton core undergoes a random walk which acts to agitate and disrupt SCs. This limits the lifetime of SCs within Eridanus II to between 1 and 5 Gyr, depending on its interactions with the Milky Way.

5.6 Conclusions

I have presented analysis of several high resolution (spatial and mass resolution of 3 pc and $120\,\mathrm{M}_{\odot}$) cosmological zoom simulations of dwarf galaxies from the EDGE project, selected to best match the isolated ultra-faint Eridanus II. I have shown that these simulations are capable of forming small central cores ($\sim 40\,\mathrm{pc}$), and spontaneously form bound SCs at high redshift with both in-situ and ex-situ origins.

I ran a comprehensive suite of direct summation N-body SC simulations, orbiting at low radii in a selection of host galaxy potentials. Four of these host potentials are fit to the EDGE dwarfs, and one is taken from Contenta et al. (2018) which is best able to host SCs simulations with properties comparable to that in Eridanus II. In agreement with previous literature (Amorisco, 2017; Contenta et al., 2018), I find that SCs are unable to survive long-term within a cuspy potential. SCs survive long-term in cored potentials, but cannot reproduce the observed properties of the SC in Eridanus II (namely the extended size and high ellipticity). I find that only the extremely shallow host potential from Contenta et al. (2018) can support the extended size of the SC in Eridanus II, but still fails to meet the high ellipticity.

The EDGE dwarf that best matches the observed properties of Eridanus II, and best supports SC survival, is a late-former. The late assembly results in an extended half light radius (0.2 kpc) and lower central density. This could suggest that Eridanus II, which has an even wider half light radius (0.277 kpc), may itself be a more extreme late-former.

I suggest that interactions with minor mergers may be able to explain the properties of the SC in Eridanus II. Such mergers could dynamically bouy up a low-orbit SC, disrupt a spherical shape, and are consistent with a late-formation scenario. I leave further investigation of such a scenario to future work.

The shape and phase space of dark matter haloes at the edge of galaxy formation

6.1 Abstract

A consistent prediction of hierarchical structure formation is that DM haloes have triaxial shapes. For DMO simulations in a cosmological context, it is established that haloes are prolate at their centres and increasingly spherical towards their outskirts. The introduction of baryons adds an additional complication, with the condensation of gas transforming the central shape into something much rounder. In this chapter, I investigate the halo shape in the EDGE project. Some of the EDGE dwarfs are reionisation fossils with exceedingly low gas fractions ($< 0.001\%$ within the half light radius), and it is unclear whether baryonic effects are still relevant in this regime. I find that the shapes of haloes with $M_{200} < 2 \times 10^9$ are degenerate between DMO and baryonic simulations, suggesting a lower limit to the impact of baryonic effects on the halo shape. There is no sign that DM heating mechanisms are directly responsible for changing the halo shape.

6.2 Introduction

In the ΛCDM paradigm, the Universe is predominantly comprised of an invisible DM. DM undergoes hierarchical collapse under gravity to form a cosmic web of structure comprising of sheets, filaments and nodes (Press & Schechter, 1974; White & Rees, 1978; Peebles, 1982). It is in these nodes, called DM haloes, that galaxies are born and evolve. DM haloes are often described with spherical symmetry (i.e. the half light radius, virial radius). Indeed, throughout this work I have calculated profile properties in spherical bins. Nonetheless, DM haloes are actually complex shapes that are better described by a sequence of nested triaxial ellipsoids (Bardeen et al., 1986; Frenk et al., 1988; Dubinski & Carlberg, 1991; Jing & Suto, 2002; Allgood et al., 2006).

In an isolated environment, a pure DM halo tends towards a prolate (cigar) shape over all radii (Gustafsson et al., 2006; Macciò et al., 2008). This shape is energetically favoured because it minimises the angular momentum in a dissipationless system. The picture is complicated in fully cosmological environments, where simulations show that halo shapes are sculpted by their dynamical interactions and accretion from filaments (Bett et al., 2007; Zolotov et al., 2015; Tomassetti et al., 2016; Wu et al., 2018), and depend on halo mass (Allgood et al., 2006; Padilla & Strauss, 2008; Zhang et al., 2019)[1]. In cosmological environments, DM haloes are prolate in their central regions and increasingly oblate (pancake) shaped in their outskirts (Frenk et al., 1988; Jing & Suto, 2002; Vera-Ciro et al., 2011). This can be interpreted as a consequence of the central halo being constructed from highly anisotropic accretion from thin filaments at early times, contrasting with more isotropic build-up of the outer halo at later times (Tormen, 1997; Vera-Ciro et al., 2011; Shao et al., 2018; Ganeshaiah Veena et al., 2018).

---

[1] The reasoning behind this dynamic sculpting is discussed in Moore et al. (2004).

It is well established that the introduction of baryonic physics affects halo shapes, with simulations showing that a usual prolate halo is made more spherical and oblate (Katz & Gunn, 1991; Dubinski, 1994; Gustafsson et al., 2006; Debattista et al., 2008; Pato et al., 2010). Simulations and theory agree that the prolate triaxial halo shape is comprised of particles on 'box' orbits which pass arbitrarily close to the halo centre (Gerhard & Binney, 1985; Udry & Martinet, 1994; Merritt & Valluri, 1999). As gas cools and condenses into halo centres, it acts to scatter DM particles onto more tube-like orbits (Tissera & Dominguez-Tenreiro, 1998; Kazantzidis et al., 2010; Zhu et al., 2017), which adopt a more spherical overall shape. This transformation is most efficient within ~ 20 half light radii, where the majority of the gas resides (Springel et al., 2004; Debattista et al., 2008). Whether these processes are operating within the smallest dwarf galaxies, where gas fractions are proportionally lower, is still questionable.

Baryons can also impact the inner density profile of dwarf galaxies. Condensation of gas encourages higher halo concentrations as the DM contracts in response to the increased central potential (Young, 1980; Blumenthal et al., 1986; Gnedin et al., 2011; Dutton et al., 2016). On the other hand, a variety of baryonic heating mechanisms can flatten the central density profile (Navarro et al., 1996a; El-Zant et al., 2001; Read & Gilmore, 2005; Weinberg & Katz, 2007; Orkney et al., 2021b).

Observations of real galaxies suggest a diversity of halo shapes (i.e. Peters et al., 2017), but such measurements are fraught with uncertainty. Massive galaxies and galaxy clusters can be examined with gravitational lensing (Treu, 2010; van Uitert et al., 2012; Bruderer et al., 2016), but this only returns the projected halo shape. Tracers of the gravitational potential, such as stellar streams (Ibata et al., 2001; Helmi, 2004; Lux et al., 2012; Deg & Widrow, 2013; Vera-Ciro & Helmi, 2013) and GCs (Lux et al., 2012; Posti & Helmi, 2019), can reveal the 3D halo shape over the radii probed by the tracers. Alternatively, edge-on galaxies provide a unique means of measuring the halo shape by analysis of the rotation and flaring in their HI discs (Olling & van Gorkom, 1995; Weijmans et al., 2008; O'Brien et al., 2010; Peters et al., 2017; Leung et al., 2021). This can also reveal the 3D halo shape, but only in the region close to the gas disc. Only the HI flaring technique is effective in the dwarf regime, and it remains difficult to detect triaxiality. However, with measurements of $> 10,000$ velocities it may be possible (Read & Steger, 2017).

In this chapter I investigate, for the first time, DM halo shapes in the smallest galaxies. For this I use the EDGE simulation suite presented in Chapter 3. My key aim is to study whether the halo shapes in reionisation fossils, which are gas deficient, are still able to be transformed by baryons. Furthermore, I aim to study whether DM cusp-core transformations have any appreciable effect on the halo shape within the half light radius. The chapter is organised as follows: In Section §6.3 I describe my method for calculating the halo shape, and for filtering substructure. In Section §6.4 I present the shape with radius, and the central shape evolution with time, and analyse the velocity anisotropy for the primary EDGE suite. I discuss my findings in Section §6.5, and finally conclude in Section §6.6.

6.3 Method

I refer the reader to Chapter 3 for a full description of the EDGE simulation suite. In this chapter, I analyse only the higher resolution non-GM dwarf galaxies in Table 3.1. This is because testing in Section §6.3.1 shows that an accurate shape fit requires particles of $\mathcal{O}(1000)$ or greater, limiting the minimum radius that can be probed at my fiducial resolution. Only the higher resolution EDGE simulations provided enough central particles

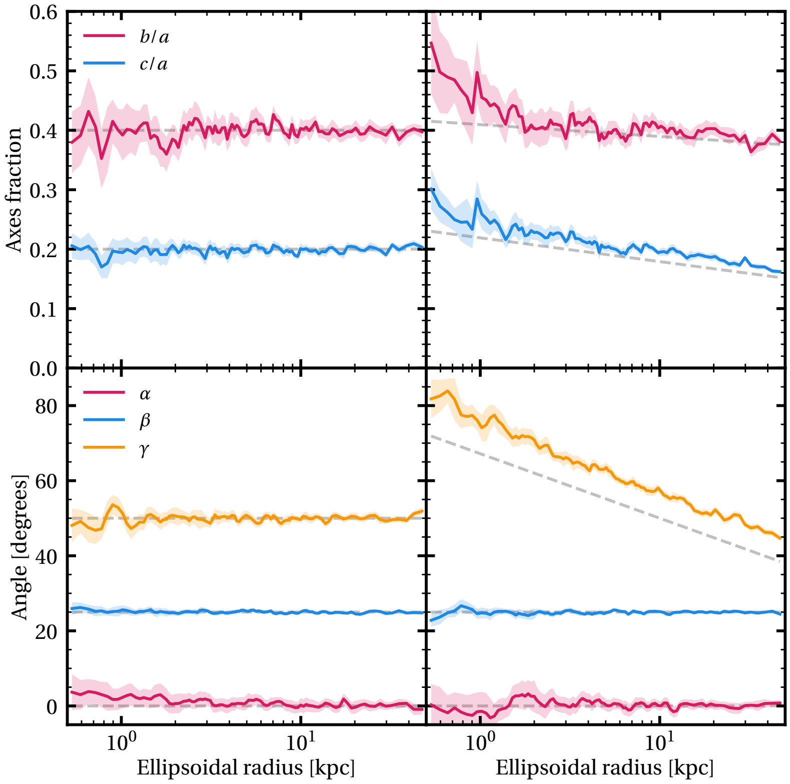

Figure 6.1: Shape fits using the algorithm described in Section §6.3 to mock Hernquist profiles of a known shape. The profile is sampled by $100,000$ equal mass particles. Grey dashed lines indicate the expected shape of the profiles. The upper panels show the axis ratio, and the lower panels the corresponding Euler angles. These shape parameters are plotted over an arbitrary range of radii in 100 bins, where each bin (initially) contains an equal number of particles. The left panels show the fit to a Hernquist profile with constant axis ratios and rotation over all radii, whereas I vary these parameters in the right panels. The shaded regions correspond to the 1σ scatter from a bootstrapping analysis.

to satisfactorily measure their shape within the half light radius. The GM simulations are excluded purely because they offer no significant shape differences when compared to the non-GM variant.

6.3.1 Shape algorithm

I estimate the shape of DM haloes using the moment of inertia method described in (Katz, 1991; Dubinski & Carlberg, 1991; Warren et al., 1992, and references therein). This fits homoeoidal shells with variable axis ratios and rotations to the particle distribution. The advantages of using ellipsoidal shells as opposed to ellipsoidal volumes are explored in Zemp et al. (2011), where it is found that thinner shells provide better fits to the *local* particle distribution. However, these are more sensitive to deviations from ellipsoidal symmetry due to substructure.

The fitting process groups the halo particle distribution into an initial set of spherical shells. These shells are then adjusted to fit the underlying particle distribution by solving the “shape tensor” S:

$$S_{ij} = \frac{\sum_k m_k (r_k)_i (r_k)_j}{\sum_k m_k}, \tag{6.1}$$

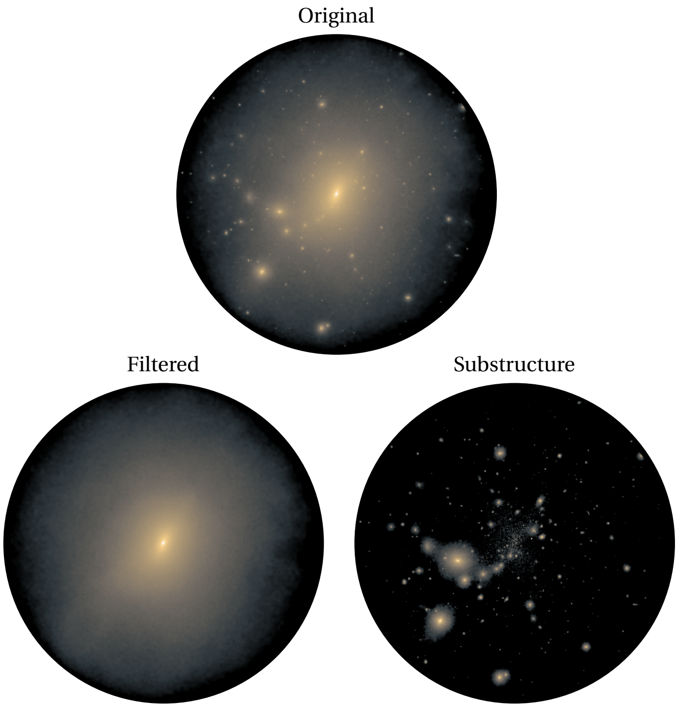

Figure 6.2: *Upper panel:* The total DM surface density within r_{200c} for Halo1445. *Lower panels:* On the left, the filtered DM halo. Zero visible substructures remain, and the parent halo is unaffected. On the right, the removed substructure.

where the right-hand-side refers to the elements of S in terms of a DM particle k with mass m and radial distances r. Axial ratios a, b, c are derived from the eigenvalues of S in the form $e_x = Mx^2/3$ (where M is the total mass in the enclosed region and $x = a, b, c$). The eigvenvectors of S are then the rotation matrix for each shell. This calculation is iterated, using the preceding shape as the new shell, until convergence criterion are met. I consider the shape fit to be converged when the difference between axial ratios vary by less than 10^{-4} between iterations. The authors in Zemp et al. (2011) also investigate whether a weighting function on S can reduce bias caused by halo substructure. They find that zero weighting consistently returns the most accurate fits, and so no weighting is used here.

Figure 6.1 demonstrates the success of the algorithm in reproducing the shape of example Hernquist (Hernquist, 1990) particle distributions with known axial ratios and rotations. The fits show extremely good adherence to the underlying particle distribution when there are constant shape parameters. However, there is a small but noticeable systematic bias when the shape parameters vary with radius. This bias is not affected by increasing/decreasing the number of radial bins. The authors in Zemp et al. (2011) report a similar bias, which appears to be an innate weakness of the algorithm, and I defer further improvement to future work.

This algorithm is now included in the public distribution of PYNBODY.

6.3.2 Filtering

As mentioned in Section §6.2, the shape fitting algorithm is extremely sensitive to the presence of substructure. Substructure is common throughout DM haloes, and these should be purged before performing shape fits. I found that halo finders struggled to remove all visible substructure in a way that preserved the uniformity of the background density, so I use the shape algorithm itself to identify over-densities.

First, I run the shape algorithm on the EDGE haloes using a small number of radial bins (~ 10), yielding a shape estimate that is insensitive to local substructure. The method is successful so long as subhaloes are proportionally light, which is the case for EDGE at $z = 0$. This shape is interpolated to 100 homoeoidal shells and smoothed with a Gaussian filter, providing a higher resolution and extremely smooth shape profile. Rotation matrices cannot be safely interpolated, and so I convert them to quaternions which can themselves be interpolated and smoothed without issue.

I then histogram the local densities (determined in PYNBODY) for the particles in each homoeoidal shell, and tag all particles that are 2σ above a Normal distribution fit to the main local density peak (in log-density space). This is very effective at identifying particles which deviate from the expected logarithmic slope in ΛCDM haloes.

The tagged particles are removed from the simulation using an accept/reject method, such that the density is lowered to the peak of the Gaussian density distribution. This avoids leaving 'holes' in the density distribution. I demonstrate this filtering technique in Figure 6.2 on Halo1445. All shape results are cross-checked with and without this filtering.

This technique is similar to that laid out by Ayromlou et al. (2019), except more rudimentary in that I do not use velocity information to distinguish subhalo particles from those belonging to the host. However, it is capable of removing the overdensities that would otherwise bias halo shape fits.

6.4 Results

6.4.1 The internal shape

The axial ratios b/a and c/a for the EDGE simulation suite at $z = 0$ are presented in the upper panels of Figure 6.3, over the range $50\,\mathrm{pc} \leqslant r \leqslant r_{200\mathrm{c}}$. For Halo1445 and Halo1459, there is good agreement between DMO and baryonic simulations over all radii. This shows that, for reionisation fossils, the presence of baryons does not notably change the DM haloes from their primordial shape. Both haloes tend towards a more spherical shape (higher axial ratios) towards their outskirts ($> 10\,\mathrm{kpc}$). This is in line with expectations for more massive haloes.

Halo600, Halo605 and Halo624 have good agreement between DMO and baryonic simulations only at higher radii. The shape in the baryonic simulation deviates from the DMO simulations within $\sim 1\,\mathrm{kpc}$, and begins to adopt a more spherical shape. The onset of this deviation begins well outside of the half light radius, suggesting that feedback from bursty star formation cannot be the main driver.

In the lower panels of Figure 6.3 I quantify whether the haloes are prolate or oblate with the triaxiality parameter T:

$$T = \frac{1 - b^2/a^2}{1 - c^2/a^2}, \tag{6.2}$$

where $T > 2/3$ is prolate, $T < 1/3$ is oblate, and $1/3 < T < 2/3$ is triaxial. The DM haloes in Halo1445 DMO and Halo1459 DMO are more prolate than their higher-mass siblings, even without the addition of baryons. This suggests Halo1445 and Halo1459 are constructed from more anisotropic accretion (see Vera-Ciro et al., 2011).

In Figure 6.4 I plot the alignment of the DM minor axis c, where the halo has first been aligned on the angular momentum of the central cool gas ($< 1\,\mathrm{kpc}$, $< 10^4\,\mathrm{K}$). This is oriented such that an angle of 0 corresponds to perfect alignment between halo shape and

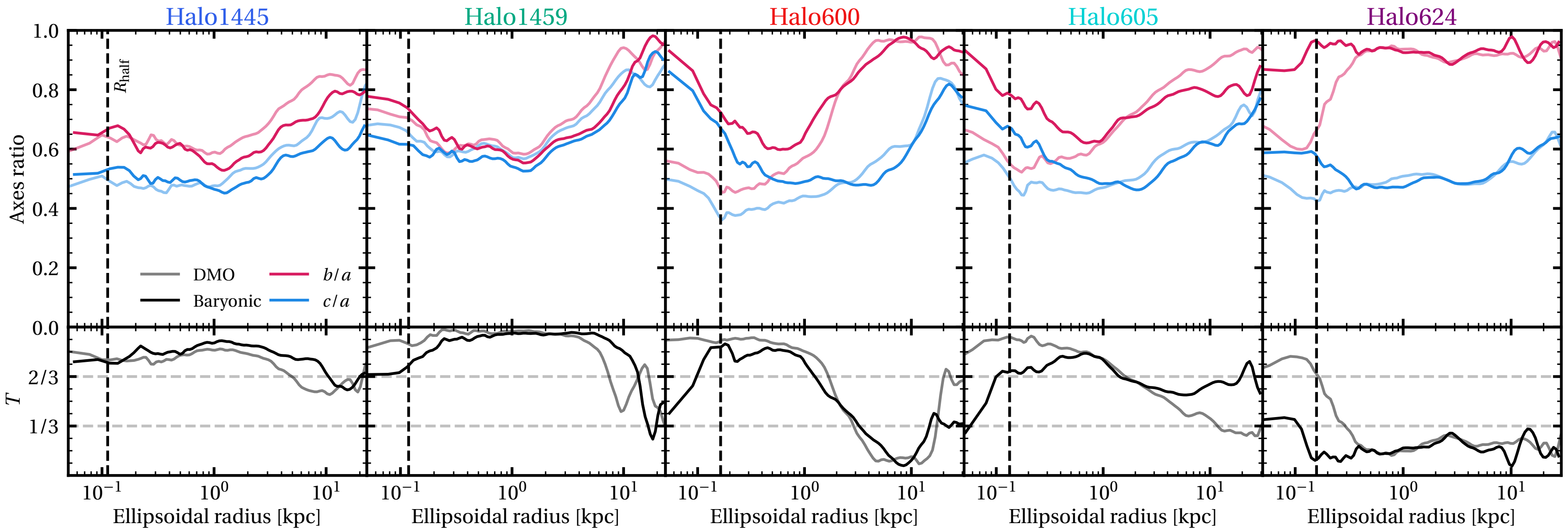

Figure 6.3: *Upper panels:* The axial ratios b/a (blue) and c/a (red) for the DM component in each of the EDGE dwarf galaxies over a range in radii $0.05 \geqslant r \geqslant r_{200c}$. *Lower panels:* The triaxiality parameter T (Equation 6.2) over the same radial ranges. DMO simulations are shown with faint lines, and Agertz+2020 physics with opaque lines. A vertical dashed black line marks the stellar 3D half light radius in the baryonic simulation, averaged over the five most recent simulation outputs. The radial binning used for the shape algorithm has at minimum 5k particles per bin, and the result is smoothed with a Gaussian filter of $\sigma = 1$.

gas angular momentum. This shows that the angular alignment is relatively consistent throughout the halo. Halo624, which is the only halo to possess a gas disc (see Figure 4.1), has exceedingly good alignment. The other EDGE dwarfs are not aligned, which is unsurprising given the lack of coherence in their gas.

6.4.2 Central shape evolution

In Figure 6.5 I investigate the evolution of the central halo shape. In the upper panels I plot the averaged central ($0 - 0.2\,\mathrm{kpc}$) DM halo shape with time. In the lower panels I plot the gas to DM mass ratio within 500 pc alongside the star formation history. The halo shape is extremely stochastic during the rapid early assembly phase of each halo. There is very little disruption to Halo1459, but the late-forming Halo600 is still turbulent until 5 Gyr. It is at this early time that the DM haloes experience the most heating from bursty SNe, as described in Chapter 4, and so it is difficult to decipher the impact of early heating on the halo shape.

For Halo1445 and Halo1459, the halo shape evolution is relatively static for both DMO and baryonic simulations. Correspondingly, the gas mass is extremely low and there is no star formation after 2 Gyr. The implication is that there is insufficient gas condensation to perturb DM particle orbits. I do not show the GM resimulations of Halo1459 because they are degenerate with Halo1459.

Halo600 with baryons shows some clear evolution towards a more spherical shape between 5 Gyr and 8 Gyr, which is correlated with the rapid condensation of gas into the halo centre. This evolution is suddenly halted by a gas blowout driven by SNe at 8 Gyr. It is difficult to decipher the shape evolution before 5 Gyr due to stirring from mergers, but there appears to be little difference between baryonic and DMO simulations until 3 Gyr.

Halo605 with baryons exhibits mild evolution towards a more spherical shape between 2 Gyr and 7 Gyr. This is correlated with repeated gas inflow/outflow resulting from successive periods of SNe blowout and condensation. These gas flows could be interpreted both as gas condensation and DM heating, and it is difficult to decouple the two mechanisms. However, as is shown in Figure 4.3, there is barely any change in the inner density ($< 40\,\mathrm{pc}$) of Halo605 after 2 Gyr, and so it seems likely that the halo shape change is dominated by gas dissipation rather than cusp-core transformations.

Halo624 with baryons retains an extremely oblate shape throughout its evolution, in contrast with its DMO counterpart. As can be seen in Figure 6.3, this discrepancy extends to just $\sim 400\,\mathrm{pc}$ at $z = 0$. This is a similar scale to the gaseous disc – that is only present in Halo624 – which starts to be established at 2 Gyr. This suggests that the halo shape transformation in this simulation proceeds similarly to that in larger scale discs (Debattista et al., 2008).

There are no clear signs that shape evolution can be attributed to DM heating processes, but rather the standard gas condensation mechanism. Halo600 in particular shows no correlation between the central DM heating in Figure 4.3 and its shape evolution. In fact, the large starburst at 8 Gyr – which causes a sudden drop in the central DM density – yields a slight reduction in the axial ratios.

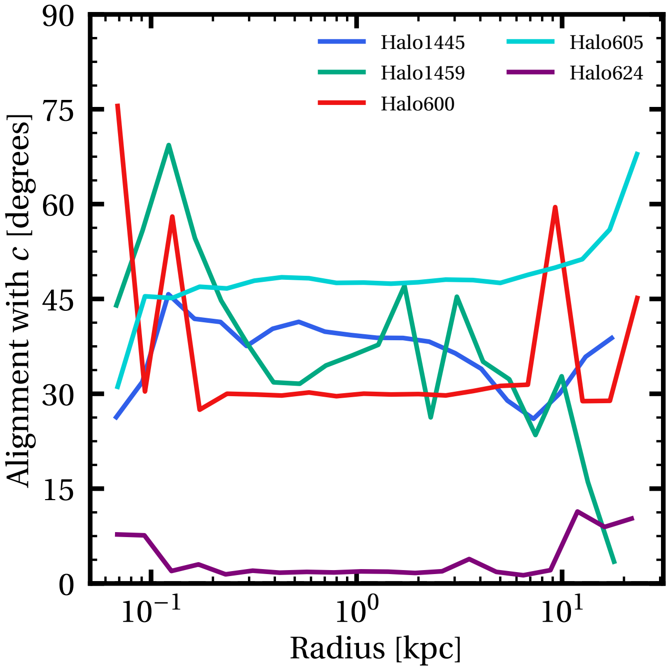

Figure 6.4: The alignment angle between the short-axis c and the angular momentum of the cold central gas ($< 1\,\mathrm{kpc}$, $< 10^4\,\mathrm{K}$), in twenty logarithmic bins. An angle of 0 corresponds to perfect alignment. Only Halo624 has a well-defined rotating gas disc.

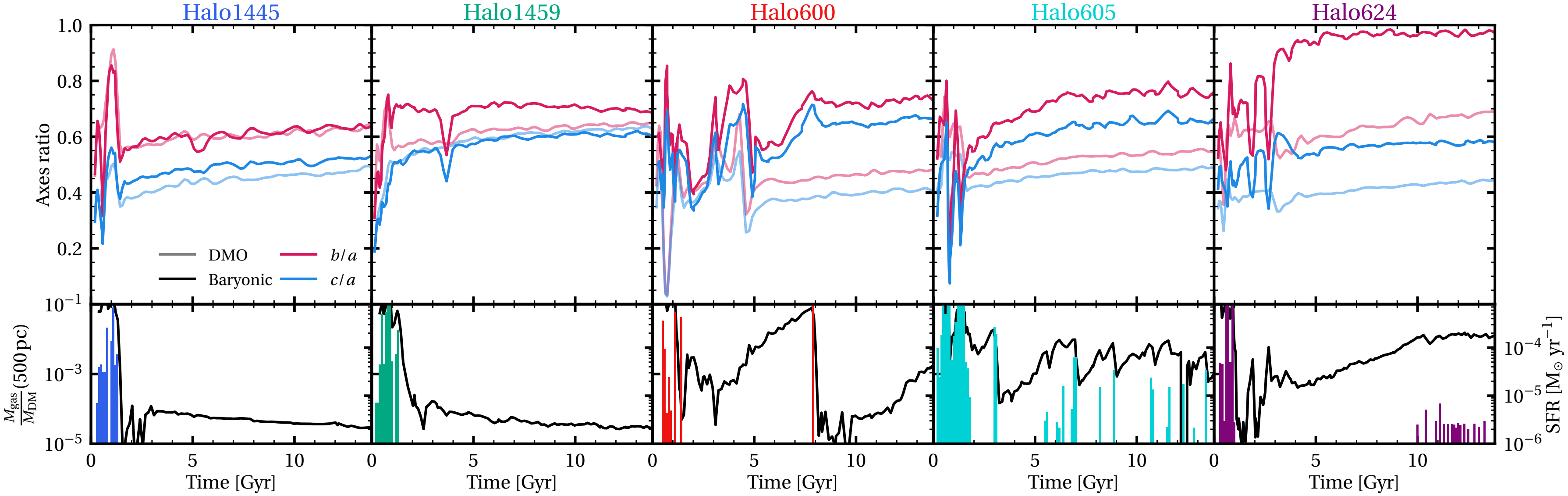

Figure 6.5: *Upper panels:* The axial ratios b/a (blue) and c/a (red) for the DM component in each of the EDGE dwarf galaxies with time. *Lower panels:* The ratio of gas to DM mass within 500 pc (black line, left axis) and the star formation history of the main progenitor halo in 100 Myr bins (coloured histogram, right axis) with time.

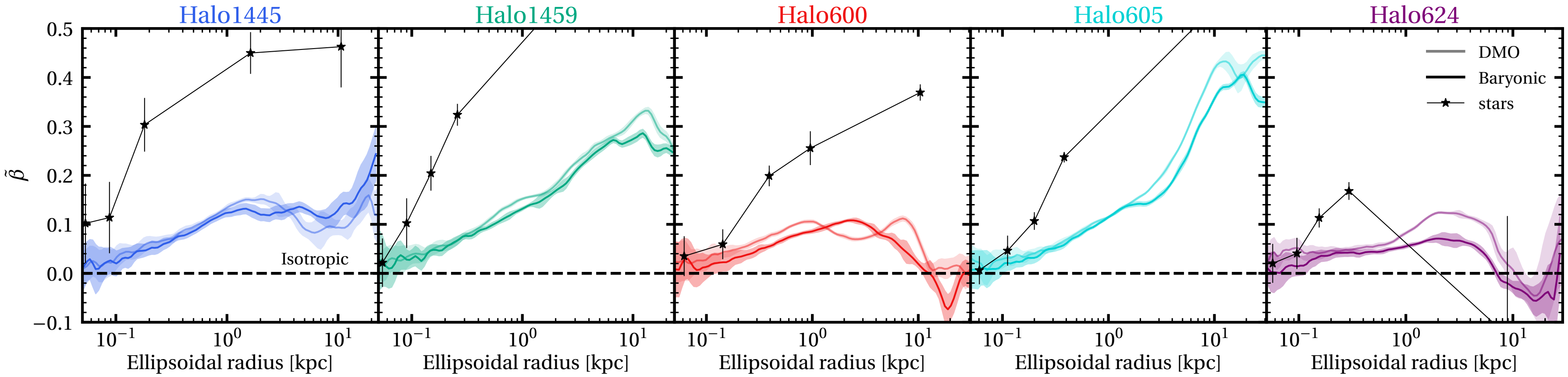

Figure 6.6: The symmetrised anisotropy parameter $\tilde{\beta}$ over the range 50 pc to $r_{200\mathrm{c}}$ for the stars (black stars) and DM (shaded bands) for the baryonic (darker lines) and DMO (lighter lines) EDGE simulations. The results shown are the median over the penultimate ten simulation outputs ($0.1 \leqslant z \leqslant 0$). Shaded regions or error bars indicate the standard deviation of those ten outputs, demonstrating the reduced certainty at the lowest and highest radii. At low radii this uncertainty stems from lower particle numbers (which are more easily overwhelmed by passing subhaloes), whereas at high radii the uncertainty is caused by subhaloes which wander through the host potential. A black dashed line marks $\beta = 0$, which represents isotropy. No attempt is made to remove substructure. DM results are smoothed with a Gaussian filter using $\sigma = 1$.

6.4.3 Velocity anisotropy

The velocity anisotropy parameter relates tangential velocities (circular orbits) to radial orbits (plunging orbits) as follows (Binney, 1980; Binney & Tremaine, 2008):

$$\beta = 1 - \frac{\sigma_t^2}{2\sigma_r^2}, \tag{6.3}$$

where σ_t is the transverse velocity dispersion and σ_r is the radial velocity dispersion. Here, I use the symmetrised variant of β as in Read & Steger (2017):

$$\tilde{\beta} = \frac{\sigma_r^2 - \sigma_t^2}{\sigma_r^2 + \sigma_t^2} = \frac{\beta}{2 - \beta}, \tag{6.4}$$

where $\tilde{\beta} = -1$ corresponds to fully tangential velocities, $\tilde{\beta} = 0$ corresponds to fully isotropic velocities and $\tilde{\beta} = 1$ corresponds to fully radial velocities.

Here, I use $\tilde{\beta}$ to investigate the anisotropy in the DM haloes of the EDGE dwarfs. Previous research has shown that DM haloes of varying scales are described by near-isotropic central regions that grow more tangentially biased towards the virial radius (Lemze et al., 2012; Sparre & Hansen, 2012; Cataldi et al., 2021). The authors in Tormen et al. (1997) link this trend to the anisotropic accretion of substructure and DM from the cosmic web, which tend to bias the velocities towards anisotropy in the halo outskirts.

In Figure 6.6 I present $\tilde{\beta}$ for the stars (black stars) and DM (shaded bands) for the baryonic (darker lines) and DMO (lighter lines) EDGE simulations. For simplicity, I perform this calculation in spherical bins. I do not attempt to filter substructure, because the contribution of substructure velocities is important to the overall anisotropy profile. I will investigate the anisotropy without substructure in future work. I take the median of the results over the penultimate ten simulation outputs ($0.1 \leqslant z \leqslant 0$), which reduces the bias from any wandering subhaloes. The individual anisotropy profiles over this timeframe show little evolution. Shaded regions indicate the standard deviation over those ten outputs.

The $\tilde{\beta}$ trends are similar for both DMO and baryonic simulations, particularly within the central regions ($< 100\,\mathrm{pc}$). One might expect the scattering of DM particle orbits due to baryons would increase the velocity isotropy over the regions that were sphericalised in Figure 6.3. The baryonic Halo600, Halo605 and Halo624 are all slightly more isotropic in their central regions than their DMO counterparts, but this difference is within the standard deviation and the DMO simulations are already very isotropic at their centres.

Halo1445, Halo1459 and Halo605 exhibit trends of increasing $\tilde{\beta}$ with radius, as expected for cosmological haloes that assemble from filamentary structure (particularly for isolated haloes). Halo600 and Halo624 suddenly depart from a radial bias at $\sim 10\,\mathrm{kpc}$, briefly adopting more tangential velocities. These two haloes are also the most oblate in their outskirts. A common process, possibly involving the angular momentum of accreted material, could be responsible for both properties (Tormen, 1997; Vera-Ciro et al., 2011; Shao et al., 2018; Ganeshaiah Veena et al., 2018). This will be investigated in future work.

The $\tilde{\beta}$ for the stellar component of each dwarf approaches 0 at low radii, and then climbs towards more radial orbits with increasing radius. The outermost stars are more tangentially anisotropic in Halo624, though this is subject to a great degree of variance across time. This can be an indicator of strong tidal effects (see Read et al., 2006c) and/or of the presence of substructure/tidal debris in the outer halo (see Loebman et al., 2018; Cunningham et al., 2019). The baryonic simulation of Halo624 at $z = 0$ is moments away from a major merger, a merger which has already occurred in the DMO simulation (see Figure 4.2). The tidal influence of this merger is the likely culprit for the outermost stellar anisotropy.

6.5 Discussion

6.5.1 A minimum scale for shape transformation

My results have confirmed previous literature in that DM halo shapes are prolate in their centres, and become increasingly spherical towards their outer edges. Then, the condensation of gas into the halo centre acts to transform the inner prolate shape into a rounder, more oblate shape from within a few half light radii. I find that this mechanism no longer operates for halo masses $M_{200c} < 2 \times 10^9\,\mathrm{M}_\odot$ due to the lack of available gas. Therefore, I predict that observations of gas poor ultra-faint dwarf galaxies should reveal primordial triaxial potentials that are prolate on average. I note, however, that the low numbers of dwarfs in EDGE may under-sample the variety of galaxy types in the field, and there may be exceptions.

In one simulation (Halo624), a clear cold gas disc forms. In this case, the inner halo becomes oblate and aligned with the angular momentum vector of the cold gas, similarly to the halo shape change behaviour reported for more massive disc galaxies (e.g. Debattista et al., 2008). It is unclear whether the gas disc forms as a result of the oblate halo shape, or if the halo shape becomes oblate in response to the gas disc. The halo shape remains oblate out to the virial radius, far outside the influence of the gas disc.

6.5.2 Observational possibilities

The velocity anisotropy parameter of observed stellar velocities is often used to constrain galactic potentials (Zait et al., 2008; Hunter, 2014; Genina et al., 2020b and see Łokas & Mamon, 2003; Read & Steger, 2017). Triaxial halo shapes can be inferred through analysis of the velocities of tracers, i.e. stars. The authors in Read & Steger (2017) find that, on average, $> 10,000$ velocities are needed to detect triaxiality in the ultra-faint regime.

Recently, Leung et al. (2021) investigated the central density and shape of the isolated dwarf irregular galaxy WLM using joint stellar and gas dynamics. WLM, with a stellar mass of $M_* \approx 1-4 \times 10^7\,\mathrm{M}_\odot$ (Jackson et al., 2007; McConnachie, 2012) and a halo mass of order $10^{10}\,\mathrm{M}_\odot$ (Leaman et al., 2012), is in a higher mass category than any EDGE dwarf. It also has a rich star formation history (i.e. Albers et al., 2019). The authors in Leung et al. (2021) find evidence favouring a DM core, consistent with having formed through bursty stellar feedback, and a prolate halo shape. Following my results here, I would expect a rounding of the halo within multiples of the half light radius, especially given that WLM is by no means gas-deficient (Jackson et al., 2004; Kepley et al., 2007). However, in that paper the authors are concerned with much more substantial shape transformations that could be evidence for self-interacting DM schemes, and smaller shape transformations may exist within the uncertainties.

6.6 Conclusions

I have analysed five ultra-faint dwarf galaxies from the EDGE simulation suite, run with a DM mass resolution of $100\,\mathrm{M}_\odot$. This resolution is sufficient to precisely analyse the shape of the DM profile at radii $\ll 100\,\mathrm{pc}$, which is lower than the half light radii of the dwarfs in this mass regime. In Chapter 4, I show that a combination of heating mechanisms can lower the central density in these dwarf galaxies. Here, I have also investigated whether the halo shape contains clues as to whether these heating mechanisms are active.

For dwarfs of mass $M_{200} > 3 \times 10^9$, the condensation of baryons into the centres of DM haloes transforms an otherwise prolate shape into a spherical or oblate shape. This transformation occurs on scales several times greater than the 3D stellar half light radius. DM heating driven by bursty star formation has no noticeable impact on the halo shape, although successive inflows of gas can themselves contribute to the shape transformation – regardless of whether there is any associated DM heating. Further investigation with more idealised setups would be needed to confirm the magnitude of this effect. Whilst it is not a direct sign of DM heating, a dwarf galaxy with excessively round inner shape could be indicative of successive gaseous flows.

For dwarfs of mass $M_{200} < 2 \times 10^9$, the addition of baryons yields no appreciably difference in the DM halo shapes. Therefore, I predict that future observations of gas-poor ultra-faint dwarfs will find an increased prevalence of primordial, prolate DM haloes.

Analysis of the velocity anisotropy reveals similar trends to those reported elsewhere in the literature, but further investigation is warranted.

Conclusions and future work

In this thesis I have presented my work relating to the EDGE project, a suite of cosmological zoom simulations of dwarf galaxies over the halo mass range $10^9 < M_{200}/\mathrm{M}_\odot < 4\times10^9$. These have given me a unique perspective on the CC problem and galaxy formation physics in the smallest galaxies. In this final chapter, I summarise my conclusions and set the scene for future work.

7.1 The cusp-core problem in the ultra-faint regime

In Chapter 4, I investigate the central densities in the EDGE simulation suite. Critically, the high resolution in the EDGE project allows for detailed modelling of SNe events and resulting gas flows, which have historically been described as the dominant mechanism flattening the central potentials of dwarf galaxies (Navarro et al., 1996a; Read & Gilmore, 2005; Pontzen & Governato, 2012; Governato et al., 2012; Pontzen & Governato, 2014; Teyssier et al., 2013; Di Cintio et al., 2014a; Oñorbe et al., 2015; Dutton et al., 2016). The high resolution of EDGE has also allowed me to probe the inner potential at very low radii ($\sim 40\,\mathrm{pc}$), for which contamination from numerical relaxation remains negligible.

I find that the central densities in EDGE are stochastic, depending on assembly and star formation history. Over a Hubble time, the central ($\sim 40\,\mathrm{pc}$) densities are reduced by a factor of 2 when compared with DMO simulations, even in this faint regime where stellar masses never exceed $10^6\,\mathrm{M}_\odot$. This transformation occurs from within the half light radius, as predicted for the gas flow mechanism. I show that this is primarily dependant on a fluctuating central gas mass fraction, but that the DM density is only affected when star formation rates exceed an average of $\sim 10^{-4}\,\mathrm{M}_\odot\,\mathrm{yr}^{-1}$. Whilst several EDGE dwarfs rejuvenate after being quenched by reionisation, they are subsequently unable to exceed this critical star formation rate.

I then present evidence for an additional sub-dominant heating mechanism that arises in dwarf galaxies with delayed formation. I design an idealised simulation in the GRIFFIN N-body code, which reproduces a delayed assembly history in an otherwise isolated DMO halo. I show that impulsive heating from subhalo mergers is able to lower the central density. Whilst this mechanism does not directly depend on baryonic physics, the density reduction is maximised when the host halo is pre-flattened by gas flows. This mechanism has been previously described in the literature (Naab et al., 2009; Bédorf & Portegies Zwart, 2013; Boldrini et al., 2020b), but only in Boldrini et al. (2020a) is the mechanism considered in ultra-faint dwarfs. Crucially, the mechanism can depress density cusps without continued star formation, and may offer an explanation for the shallow cores predicted in ultra-faints like Eridanus II (Amorisco, 2017; Contenta et al., 2018).

Finally, I confirm that DM cores are vulnerable to contamination from cuspy mergers, where a central cusp can be rebuilt if a sufficiently dense merger is deposited in the halo. This may introduce additional scatter in the central densities of dwarf galaxies.

7.2 Explaining the mysterious nature of Eridanus II

In Chapter 5, I focus on the EDGE dwarfs which are the best analogues of the ultra-faint dwarf Eridanus II (Bechtol et al., 2015; Koposov et al., 2015). Ultra-faint galaxies such as Eridanus II have so few stars that they could not have supported substantial gas flows during their evolution, and the central halo densities likely remain very steep. However, Eridanus II is the faintest galaxy known to host a SC, which has an extended distribution and is offset by $23 \pm 3\,\mathrm{pc}$ (Simon et al., 2021b). This is difficult to reconcile with a cuspy central density, because gravitational tides and accelerated dynamical friction would have either torn the SC apart or deposited it at the peak of the potential. The authors in (Amorisco, 2017; Contenta et al., 2018) use the properties of the SC in Eridanus II to argue for a significant central density core.

The EDGE dwarf analogues exhibit a trend whereby the metallicity, size, stellar mass and central densities compare best with Eridanus II when their formation is delayed (compared to the scatter of assembly histories in ΛCDM). Thanks to the GM technique, I can be sure that this is not a selection artefact. This trend suggests that Eridanus II may itself be a late-former, with an assembly much more extreme than any of the EDGE simulations.

I also note that low-mass SCs form spontaneously within the EDGE dwarfs, with both in-situ and ex-situ origins. The origin of SCs has long been debated (e.g. Peebles & Dicke, 1968; Fall & Rees, 1985, 1988; Kang et al., 1990; Forbes et al., 1997; Cen, 2001; Barton et al., 2015), and there is renewed interest now that simulations can resolve their formation in cosmological settings (Renaud et al., 2017; Forbes et al., 2018). EDGE member Ethan Taylor will investigate the physics behind the formation of these SC in future work (Taylor et al. in prep), with the aim of finding distinguishing features between SCs that form within DM haloes and those that do not.

I investigate whether the central density profiles in these EDGE dwarfs could support the survival of SCs with properties comparable to that in Eridanus II. For this, I design a suite of direct summation N-body simulations of SCs with a variety of initial masses, half light radii and orbits. I run these simulations in a selection of host potentials which represent the EDGE dwarfs and a best-fit potential for Eridanus II from Contenta et al. (2018), including a semi-analytic implementation for dynamical friction. I find that SCs can survive in several host potentials for a Hubble time. However, only SCs in the best-fit potential from Contenta et al. (2018) can grow to the extended size of the SC in Eridanus II, and can retain high orbital offsets.

Only SCs on wide orbits are able to adopt an ellipticity comparable to that reported in the SC of Eridanus II. This suggests that either the SC in Eridanus II is at a high offset but viewed in projection, or that unmodelled substructure in the host potential is disrupting the SC. The former of these scenarios could support a wider variety of host potentials, but requires the SC to be fine-tuned. The latter scenario is more robust, and future codes that are able to resolve complex background potentials could be used to test it further. One such example is RAMBODY (Delorme et al. in prep), which marries the NBODY6 and RAMSES codes, and reproduces the dynamical friction effect self-consistently. Combined with increasingly detailed observational constraints regarding the density and history of Eridanus II (Zoutendijk et al., 2021; Gallart et al., 2021b), the future is bright for ultra-faint dwarfs.

7.3 The shape of the smallest galaxies

Finally, in Chapter 6 I investigate the DM halo shapes of the EDGE dwarfs. DM haloes are generally approximated as spheres for convenience. However, it is well established that DM haloes in cosmological environments have prolate inner shapes and increasingly spherical/oblate shapes towards their outskirts (Frenk et al., 1988; Jing & Suto, 2002; Vera-Ciro et al., 2011). The inner shape can then be modified by baryons, with gas condensation scattering DM particle orbits and transforming a prolate shape into a spherical shape (Katz & Gunn, 1991; Dubinski, 1994; Gustafsson et al., 2006; Debattista et al., 2008; Pato et al., 2010).

I show that the EDGE dwarfs follow similar trends, but that the lightest galaxies ($M_{200} < 2 \times 10^9\,\mathrm{M_\odot}$) retain their primordial prolate inner shape. This is because they have lower central gas mass fractions, which are quickly boiled off by reionisation and never replenished. Furthermore, there is no evidence that DM heating has any additional impact on the halo shape. It is exceedingly difficult to constrain galactic triaxiality with observation, and measurements of $\mathcal{O}(10,000)$ velocities would be needed to properly investigate the shapes of dwarf galaxies (Read & Steger, 2017). This would prove extremely challenging for the ultra-faint regime, where total luminosities are typically $\leqslant 10^5\,\mathrm{L_\odot}$ (Simon, 2019).

I also analyse the velocity anisotropy within EDGE, finding isotropic centres and radially anisotropic outskirts. These profiles have been used to help define lower bounds for the mass of fermionic DM Alvey et al. (2021). Future investigation will determine to what extent the anisotropy profile is set by the anisotropic accretion of subhaloes and DM from the cosmic web. This could then provide a link between the anisotropy and halo triaxiality in halo outskirts, which are set by the local environment.

The structural properties of the EDGE dwarfs, albeit in a different context, will be compared to observational analogues in Goater et al (in prep). This will focus on the faint and extended stellar haloes that are predicted to surround ultra-faint dwarfs, and highlight any similarities between simulation and observation.

7.4 The future of EDGE

The success of EDGE has prompted the development of a new generation of simulations, hereafter EDGE2.0, for which I have continued involvement. This new project will take advantage of a wider collaboration and refine the subgrid physics. Other improvements include the calculation of potentially limitless metal species and modelling of tracer particles to track gas flows. EDGE2.0 extends the halo mass range to $10^{10}\,\mathrm{M_\odot}$, connecting to the faint end of galaxies that are better represented in observational surveys. This will confirm whether the subgrid physics are robust to a wider range of halo masses, and whether they compare well with the latest observational constraints (Read et al., 2019a). Whereas EDGE has focused on the ΛCDM paradigm, EDGE2.0 will also investigate a range of WDM cosmologies – which are often overlooked in simulations (see discussion in Brooks, 2014, 2019).

7.5 Final thoughts

This thesis has demonstrated the exciting role of dwarf galaxies in the investigation of galactic evolution and the properties of DM. I have run high resolution simulations of the smallest galaxies in a ΛCDM cosmology, with detailed subgrid physics recipes that compare favourably to all known observational constaints. Although the primary simulation suite contains just five fully-resolved dwarfs, artful use of the GM technique has allowed the EDGE collaboration to scrutinise key results with multiple follow-up simulations. Through analysis of this simulation suite, I have shown that baryonic processes are active in sculpting the central density and shape of ultra-faint dwarfs. This has ramifications on their visible components, searches for DM annihilation signals and the long-term survival of satellites. The low-mass dwarf galaxies in EDGE are incredibly sensitive to the physical processes that mould them, and to their unique assembly histories.

Appendix

A Simulation convergence

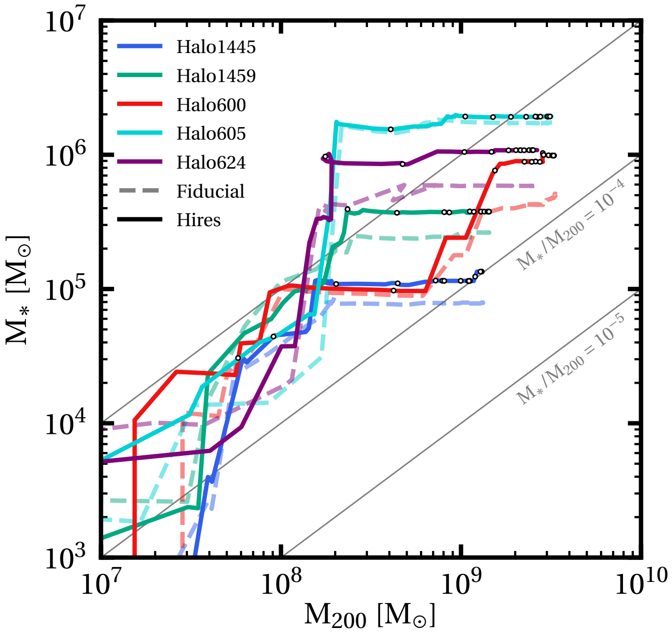

Figure 1: The SMHM relation through time for the primary EDGE simulation suite, where I compare fiducial resolution simulations (faint dashed lines) to high resolution simulations (solid lines). The black circles on the high resolution lines mark intervals of 1 Gyr in time. The grey diagonal lines show constant ratios of $M_*/M_{200\mathrm{c}}$ in powers of ten, as marked

The DM particle mass resolution used in this paper is an order of magnitude smaller than used in the fiducial EDGE simulations (Rey et al., 2019; Agertz et al., 2020; Rey et al., 2020; Pontzen et al., 2020). In this Appendix, I perform a convergence study to determine how my results are impacted by DM resolution. As previously in this paper, I distinguish between the lower and higher resolution simulations by appending the labels ‘fiducial’ and ‘hires’, respectively, to their name.

In Figure 1, I plot the total stellar mass within $r_{200\mathrm{c}}$ versus $M_{200\mathrm{c}}$ as a function of time for the fiducial (faint dashed) and hires (opaque solid) EDGE simulations. I find good convergence in shape of the general evolution of each simulated dwarf. The higher resolution simulations form systematically more stars (as first noted in Agertz et al. 2020). However, the final stellar masses typically agree within $\sim 30\%$ and at worst differ by a factor of ~two (for Halo600). This is within the expected uncertainties due to modelling galaxy formation (Agertz et al., 2020).

In Figure 2, I compare the 3D DM density profiles for the main simulation suite at two redshifts, $z = 4$ (top panels) and $z = 0$ (bottom panels). The DMO simulations are marked by the faint lines, the baryonic simulations by the opaque lines. The fiducial and

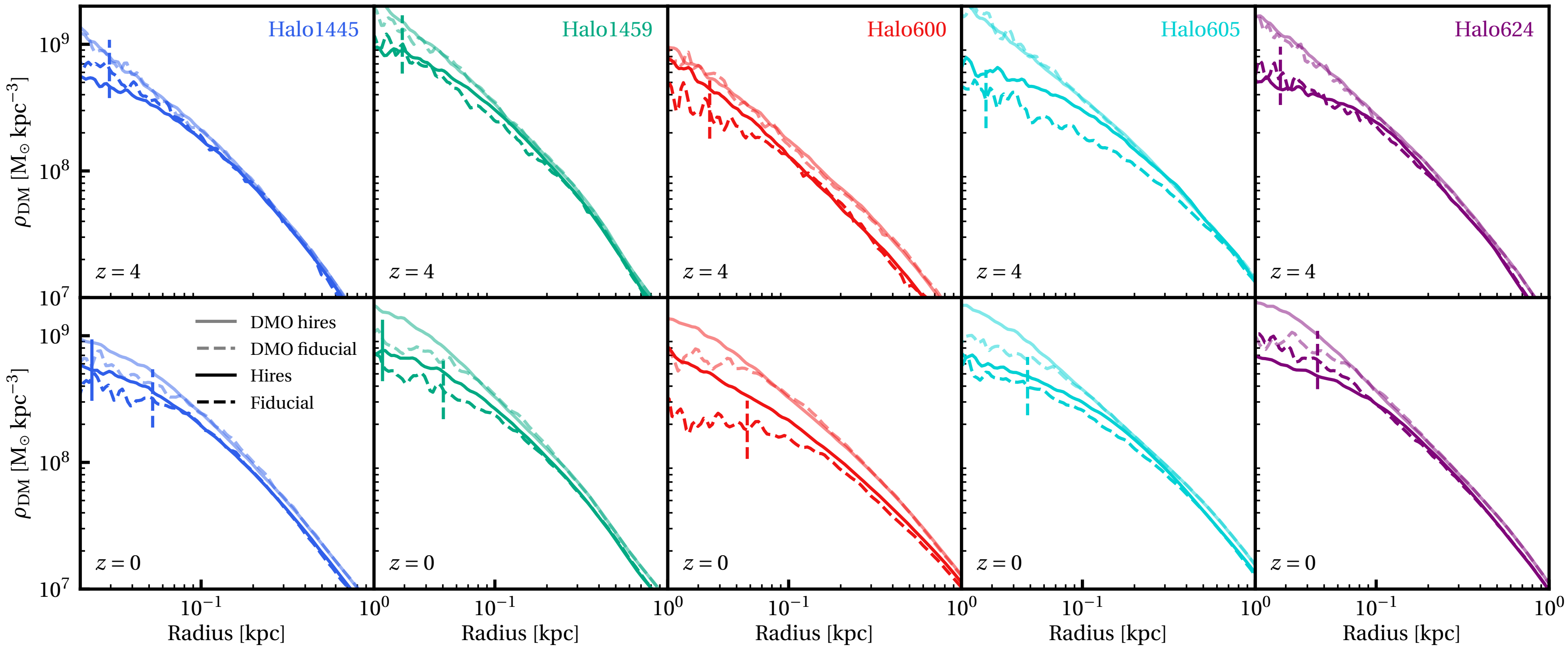

Figure 2: The 3D DM density profiles of the main simulation suite, where I compare DM-only simulations (faint lines) and baryonic simulations (opaque lines) at fiducial (dashed lines) and high (solid lines) resolution. The upper panels show this comparison at $z = 4$, by which time all haloes are quenched due to reionisation (some will later reignite their star formation). The lower panels show this comparison at $z = 0$. The numerical relaxation radius, as defined in Appendix B, is indicated by a short vertical line for the baryonic simulations. This limit is similar for the corresponding DMO simulations.

hires simulations are marked by dashed and solid lines, respectively.

Overall, there is good convergence between the fiducial and hires simulations. The DMO simulations are all converged for $r > r_{\mathrm{relax}}$ (vertical lines), and there is good agreement also for the baryonic simulations Halo1445, Halo1459 and Halo624, at both $z = 4$ and $z = 0$. However, two EDGE simulations show poor convergence. Halo600 fiducial substantially rejuvenates its star formation after $z = 1$, forming 17% of its final stellar mass after this time. This extended period of star formation is replaced by a singular burst in Halo600 hires. As a result, Halo600 fiducial undergoes significantly more DM heating that causes its final inner density profile to be substantially lower than Halo600 hires. Similarly, Halo605 fiducial forms a larger DM core than Halo605 hires at early times. However, this disparity is largely resolved before $z = 0$ due to a late cuspy merger in Halo605 fiducial (see Section 4.4.4 for a discussion of this cusp reintroduction mechanism).

The above results highlight an important point. It is often stated in the literature that whether a galaxy will be cusped or cored is determined by the stellar mass-to halo mass ratio, $M_*/M_{200\mathrm{c}}$ (e.g. Peñarrubia et al., 2012; Di Cintio et al., 2014a; Read et al., 2019a). This is true to leading order. However, it also matter *how* those stars form, as illustrated by Halo600 fiducial versus Halo600 hires. The latter actually forms more stars, but because at late time they form in a single burst, this leads to less DM heating. And, at least at the very edge of galaxy formation, it also matters what the merger history is. Halo605 fiducial goes on to partially lose its DM core due to a late cuspy merger.

B Deriving the relaxation radius for the EDGE simulations

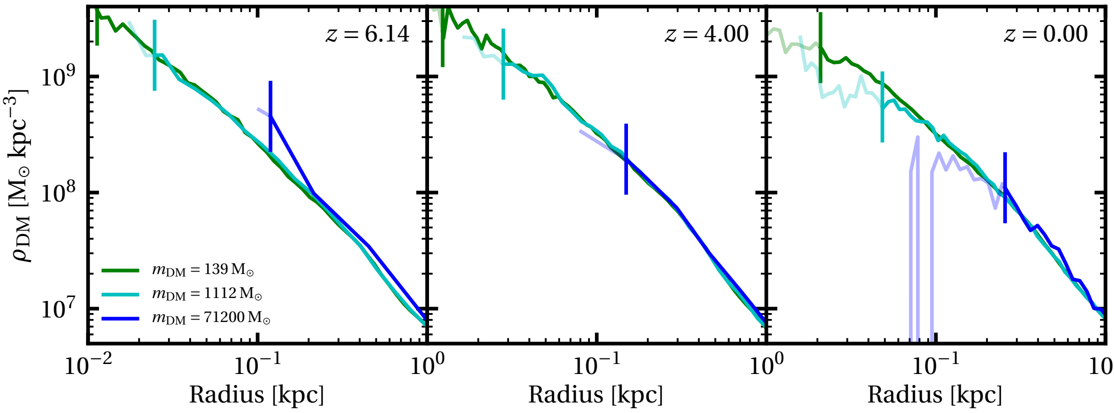

Figure 3: The evolution of the 3D density profiles for Halo1459 DMO at three DM particle resolutions, as stated in the legend. The two lowest particle masses (green and cyan lines) correspond to the high resolution and fiducial resolutions, respectively (see Table 3.1). The fainter lines indicate the radii within which at least one relaxation time (estimated using equation 1) has passed, with the transition marked using an additional vertical line for clarity. In some cases, the density profiles are not plotted at smaller radii because there are insufficient particles.

The DM 'particles' in collisionless cosmological simulations like RAMSES are really 'super-particles' that represent unresolved patches of the DM fluid. This approximation leads to overly large two-body relaxation that causes an artificial reduction in the inner DM density of a halo over time (e.g. Power et al., 2003; Diemand et al., 2004c,a; Dehnen & Read, 2011).

The two-body relaxation timescale is given by Binney & Tremaine (1987):

$$t_{\rm relax} = \frac{N t_{\rm orb}}{16\pi \log \Lambda}, \tag{1}$$

where N is the number of particles within some radius r, $t_{\rm orb}$ is the orbital time of the system given by $t_{\rm orb} = 2\pi\sqrt{R^3/GM}$ and Λ is the 'Coulomb logarithm' given by $\Lambda = b_{\rm max}/b_{\rm min}$. The maximum impact parameter $b_{\rm max}$ and the minimum impact parameter $b_{\rm min}$ define the largest and smallest scales at which particles are expected to interact with each other. The relaxation time gives the time taken for the particle velocities to change by 90°, and can be considered as the time taken for a system to lose dynamical memory of its ICs. A large relaxation time is preferred because this implies two-body relaxation has a minimal influence on the particle kinematics. For standard N-body methods, the simplest way to increase the relaxation time is by increasing the number of DM particles, N, that sample the system (e.g. Dehnen & Read, 2011).

There is some debate in the literature over the best choices for the impact parameters $b_{\rm max}$ and $b_{\rm min}$. Here, I define $b_{\rm max}$ to be the total virial size of the system r_{200}, and $b_{\rm min}$ to be the side length of the highest resolution grid cell in RAMSES. This is the approximate distance above which Newtonian gravity is recovered. Although multiple resolutions of grid cell are used throughout the simulated haloes, the central regions that are of interest here are predominantly at the highest resolution.

We now perform a brief resolution study in order to determine at what radius numerical relaxation effects become important. In Figure 3, I plot DM density profiles from a DM-only simulation at three different resolutions. These three resolutions each exhibit a different amount of central density flattening due to numerical relaxation, with the flattening becoming stronger with increasing particle mass and with time. At $z = 0$, all three resolutions are converged beyond $\sim 300\,$pc, but begin to deviate from the expected NFW form within some critical radius.

We define the 'relaxation radius', $r_{\rm relax}$, to be the radius at which the relaxation time (equation 1) for the enclosed DM particles is equal to the simulation age for any particular simulation output:

$$\left(\frac{r_{\rm relax}}{\rm kpc}\right) = \eta \left(\frac{t_{\rm sim}}{\rm Gyr}\right)^{\alpha} \left(\frac{M(< r_{\rm relax})}{\rm M_\odot}\right)^{-\frac{1}{3}} \left(\frac{\langle m \rangle}{\rm M_\odot}\right)^{\frac{2}{3}} \tag{2}$$

where I have substituted $t_{\rm relax}$ for the total run time of the simulation, $\langle m \rangle$ is the mean particle mass and η and α are fitting parameters. From the data in Figure 3, I find $\alpha = 1/3$ and $\eta = 64G \log \Lambda/100^2$. The mass within the relaxation radius, $M(r_{\rm relax})$, is calculated directly from the simulation data and so equation 2 can be solved numerically to find $r_{\rm relax}$. This is then used to predict the resolution limit for the EDGE simulations in this paper. The relaxation radii, calculated in this way, are marked on Figure 3 by the vertical lines. Notice that the DM density profiles are shallower leftwards of $r_{\rm relax}$ in the lower resolution simulations as compared to the higher resolution simulations.

C MCMC fitting

The shape fits in Chapter 5, unless otherwise stated, are designed to mimic that used in observational astronomy to recover structural properties of dwarf galaxies (see Martin et al., 2008, 2016). The method was developed by Alex Goater (Goater et al. in prep). It uses the affine-invariant Markov chain Monte Carlo ensemble sampler EMCEE (Foreman-Mackey et al., 2013). Here, I use this algorithm as a general purpose shape-finder for dwarf galaxy and SC alike. I cross-check the results with the halo shape finder algorithm that I develop in Chapter 6, finding good agreement.

The method assumes a surface brightness profile which is fit to the simulated stellar data. Once appropriately normalised, it represents the mass-weighted probability of finding a star, i, at a given position, r_i, as,

$$l_i = \frac{882N}{625\pi r_{\text{half}}^2(1-\epsilon)} \exp\left(\frac{-42r_i}{25r_{\text{half}}}\right)\frac{m_i}{M}, \tag{3}$$

where N is the number of stars in the sample, M is the total stellar mass, m_i the individual stellar mass, ϵ is the ellipticity defined as $\epsilon = 1 - b/a$, with b/a as the minor-to-major-axis ratio of the system, and r_{half} is the projected half light radius of the exponential radial profile. The elliptical radius is related to the stellar positions as:

$$r_i = \left[\left(\frac{1}{1-\epsilon}(x_i\cos\theta - y_i\sin\theta)\right)^2 + (x_i\sin\theta + y_i\cos\theta)^2\right]^{\frac{1}{2}}, \tag{4}$$

where θ is the position angle of the major axis.

The total likelihood is the product of all probabilities, which is then calculated as:

$$\ln\mathcal{L} = \sum_i \ln l_i. \tag{5}$$

I place flat priors for ϵ, θ and r_h such that the $0 \leqslant \epsilon < 1$, $-\pi \leqslant \theta \leqslant \pi$, and $r_{\text{half}} > 0$. When fitting SCs I use the additional constraint that $r_{\text{half}} \leqslant 5r_{\text{half,numerical}}$, where $r_{\text{half,numerical}}$ is the true projected half light radius of the system.

This function is technically fit to the stellar mass distribution rather than the light distribution, but it is often assumed that observed systems have uniform stellar populations unaffected by mass segregation (Martin et al., 2016). Whilst this is a potentially dubious approximation for GC systems (see Bolte, 1989; Bonnell & Davies, 1998; Allison et al., 2009), I reiterate that the results of this MCMC are well reproduced by comparable numerical calculation.

D Ellipticity bias

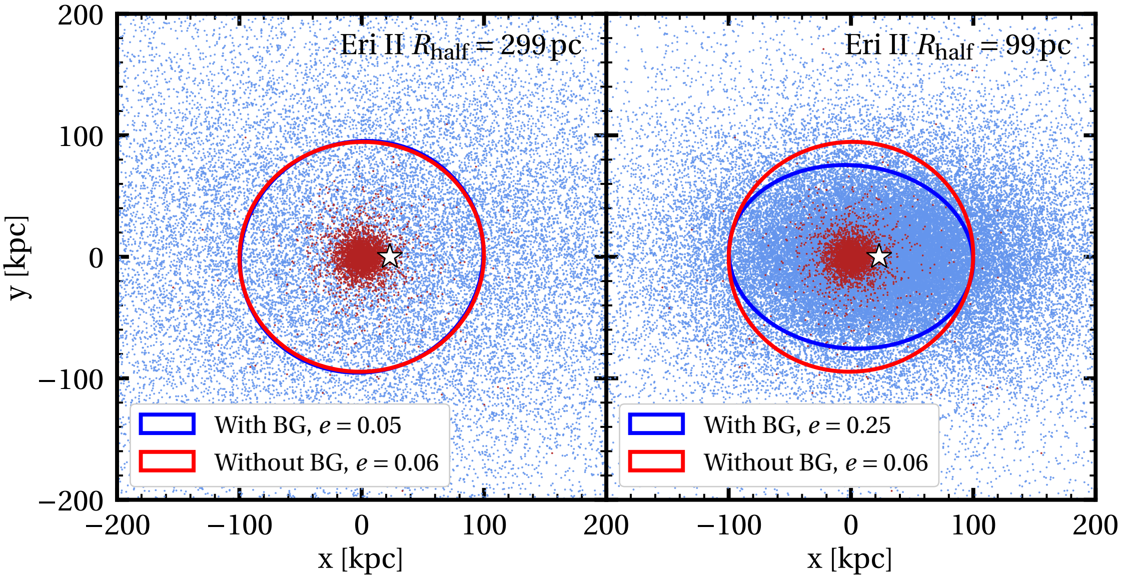

Figure 4: Mock stellar distributions for the ultra-faint Eridanus II (blue points) and its lone SC (crimson points). The centre of the host is marked with a white star. Rings represent shape fits to the projected stellar distributions of the SC, where the blue ring includes all stars and the red ring excludes the blue host stars. The ellipticity of each ring is shown in the legend. In the left panel, the stellar distribution of Eridanus II is fit to observational constraints. In the right panel, the half light radius is a third of its observed size.

The shape calculations in Simon et al. (2021b) are not performed on the SC alone, but on the total stellar distribution in Eridanus II. The structural properties of both host and SC are then determined in unison. Ideally, if the shape of the host is recovered then there will be no bias on the shape of the SC. However, as noted in Simon et al. (2021b), their observations have limited coverage and the correct host properties may not be recovered[1]. There is also no consideration of more complex triaxiality in the stellar distribution, such as a variable ellipticity or orientation. Therefore, there remains some possibility that the shape of the SC in Eridanus II is biased by the high ellipticity of the host.

Here, I consider this bias by reproducing mock-data of the stellar distribution in Eridanus II. For the host, I model the stars as a Plummer profile (Plummer, 1911) with half light radius of 299 pc, stellar mass of $8.3 \times 10^4\,{\rm M}_\odot$, alignment of $77.8\,°$, and ellipticity of 0.45. These choices are in line with observations from Bechtol et al. (2015); Simon et al. (2021b). For the SC I use a spherically symmetric Plummer profile with half light radius of 15 pc and stellar mass of $4 \times 10^3\,{\rm M}_\odot$, offset from the host profile by 23 pc. These profiles are populated by $1\,{\rm M}_\odot$ stars. Then, I fit the shape of the SC out to two half light radii – both including and excluding background stars – using the shape finder that I develop in Chapter 6. The results are shown in the left panel of Figure 4.

The left panel of Figure 4 shows that, even in this worst-case scenario where the shape fit to the SC includes all background stars, the bias is negligible. In the right panel I show

---

[1] Muñoz et al. (2012) show that a coverage equal or exceeding three half light radii is needed to accurately determine structural properties.

that a significant bias can be produced for a more concentrated host (one third of the half light radius). A similar increased bias results from using the Hernquist profile. For the distribution observed in Eridanus II, it is extremely unlikely that the high SC ellipticity observed in Simon et al. (2021b) could be caused by background bias.

E Early star cluster simulation results

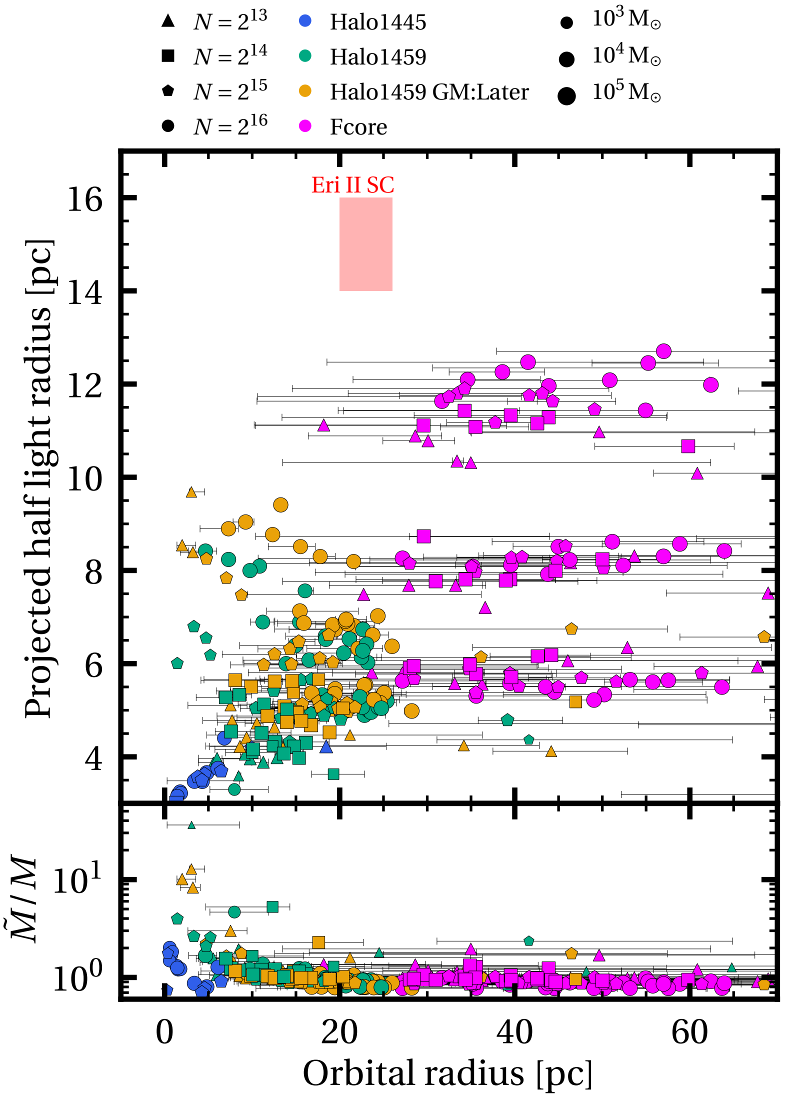

Figure 5: *Upper panel:* This plot shows the projected half mass radius versus the orbital radius of the surviving NBODY6DF simulation suite after 1.8 Gyr. Marker style indicates the initial membership N of each SC, colour the host profile, and size the final bound mass in solar units. Each point represents the average radius on the most recent orbit, with error bars indicating the orbital apocentre and pericentre. Also included is a red band representing the parameter space expected for the SC in Eridanus II, using the data from Simon et al. (2021b). Some host haloes are not represented because they did not support SC survival, and others lie beyond the 70 pc shown here. *Lower panel:* The ratio $\tilde{M}/M$ for all surviving NBODY6DF simulations against orbital radius.

In Figure 5 I present orbital offsets and size for all SC simulations from Table 5.2 after 1.8 Gyr. The methods used to produce this plot are described in Chapter 5. This figure is twinned with Figure 5.6, which shows the same results after 13.8 Gyr. At this much earlier time, the SCs sizes have changed little from their ICs.

Unlike at later times, there are still some SCs surviving in the Halo1445 ($\gamma = 0.75$)

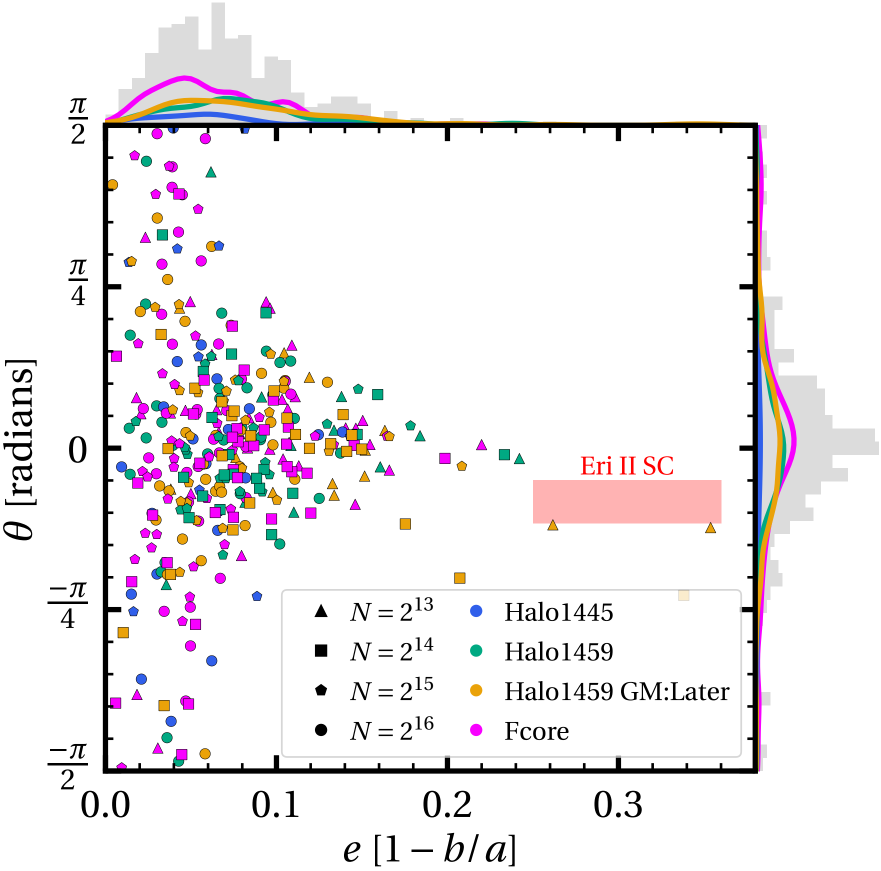

Figure 6: The alignment angle θ versus ellipticity e for all surviving SC simulations, calculated at the orbital apocentre (maximising θ and e). Histograms, including Gaussian kernel density estimations for each host profile, are plotted at the borders. The red region indicates the observed properties of the SC in Eridanus II from Simon et al. (2021b).

host potential. These simulations have been heavily stripped, yielding tiny half light radii. Despite having fallen into the potential centre of their host, their $\tilde{M}/M$ ratios remain low. In some cases this is because the SC orbits have decayed so rapidly that they have not had sufficient time to dynamically relax. For others, it is because the SCs are on the verge of dissolution.

In Figure 6 I present the shape properties for the same simulations at 1.8 Gyr. The results are qualitatively similar to those in the twin figure (Figure 5.9), but skew towards higher ellipticities. This high-ellipticity tail ($e > 0.2$) is populated predominantly by SCs on wide orbits.

At these early times, the initial SC size could be fine-tuned to reproduce that seen in Eridanus II. However, tides would still need to be elicited to reproduce the high ellipticity. Only SCs at wide orbits are able to survive and become highly elliptical, therefore the observed projection would need to be fine-tuned to reproduce the apparent offset in Eridanus II. The confluence of fine-tuning required for this scenario is unlikely. The SC properties at other times provide no additional insights.

F Stellar accelerations as probes of dark matter structure

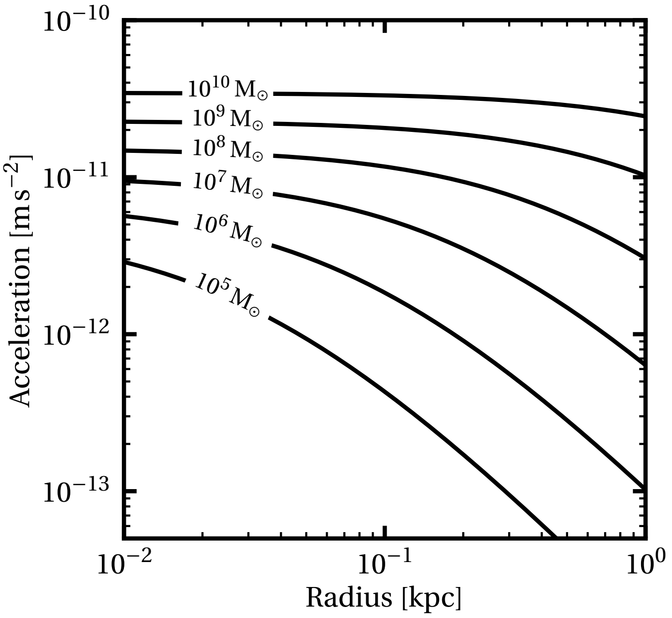

Figure 7: The central accelerations for NFW DM haloes, calculated over a range of halo masses.

During the first year of my postgraduate studies, while the EDGE simulation suite was still running, I worked on testing various novel ideas to hunt for DM substructure. For completeness, I present some of that work in this Appendix.

In ΛCDM, DM haloes have a near constant central DM cusp. The central density changes only by a factor of a few – even for large changes in halo mass – because of the mass-concentration relation (e.g. Read et al., 2019a). Baryonic processes can lower this inner density even in the very smallest dwarf galaxies (Section §1.5.1 and Chapter 4), but haloes/subhaloes become dark below $M_{200} \sim 10^{8-9}\,\mathrm{M}_\odot$, and are almost completely devoid of stars and gas. These subhaloes are predicted to have pristine DM densities that may be larger than their hosts. Furthermore, the densities of these pristine subhaloes will be comparable even down to very low masses.

Central DM cusps have a density $\rho \propto r^{-1}$, and therefore have an associated central acceleration $a \propto M/r^2 \sim$ constant. This is illustrated in Figure 7, which shows the central acceleration for NFW haloes over the mass range $10^5 < M_{200}/\mathrm{M}_\odot < 10^{10}$. If we can detect accelerations of order $a \sim 10^{-10}\,\mathrm{m\,s^{-2}}$, then we will be sensitive to a broad spectrum of subhalo mass. Here, I explore whether this could provide a novel and sensitive probe of the nature of DM.

Measuring stellar accelerations depends on the precision of velocity measurements from spectrographs, from which accelerations can then be determined after continuous measurement for a set period of time (i.e. over one decade). The precision of spectrographs has seen continuous improvement over time, which is shown in Figure 8, and future decades may see instruments capable of probing the dwarf regime in detail.

To explore this further, I create a mock NFW DM halo with realistic NFW substructure by fitting to relationships derived from the Aquarius project simulations (Springel et al., 2008). This mock halo assumes spherical symmetry, a host mass of $M_{\mathrm{host}} = 10^{10}\,\mathrm{M}_\odot$, a half light radius of 1 kpc, a concentration parameter of 10, with 12% of its mass contained

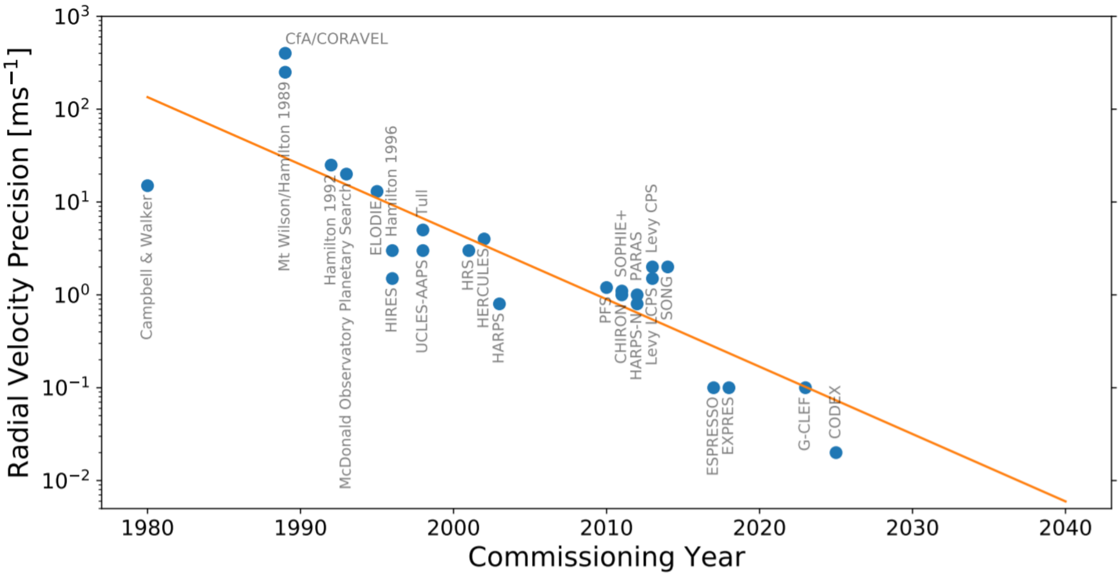

Figure 8: This graph, taken from Silverwood & Easther (2019), shows the improvements in spectrographic precision over the last few decades – and extrapolates this improvement into the future. These can be converted into accelerations by considering the change in velocity over a certain time period. For example, a precision of $6 \times 10^{-3}\,\mathrm{m\,s^{-1}}$ equates to an acceleration precision of roughly $2 \times 10^{-11}\,\mathrm{m\,s^{-2}}$ over a decade of measurements.

in substructure.

Subhaloes are generated with masses of $10^5 \leqslant M_{\mathrm{sub}}/\mathrm{M}_{\odot} \leqslant 0.12 \times M_{\mathrm{host}}$. The subhalo mass distribution, radial distribution, and concentration distribution (including scatter) are generated randomly based upon probability density functions fit to Springel et al. (2008). The three dimensional locations of each subhalo are then generated randomly, normalised for the surface of a sphere.

I approximate the effect of WDM with particle masses $m_{\mathrm{WDM}} = 10, 3\,\mathrm{keV}$ by careful treatment of the subhalo concentrations and mass function. These adjustments are informed by relations from (Schneider et al., 2012), who derive the mass scale where WDM affects hierarchical structure formation based on the particle free-streaming length. The outcome is to both lower subhalo concentrations and decrease the prevalence of subhaloes towards the lower end of the mass spectrum. This reduces the total % of mass in substructure. I use the same random seed in each scenario to improve cross comparison.

I calculate the z-axis accelerations experienced by a uniform grid of 10^6 tracer particles. This is not a true approximation of a realistic stellar distribution, which would instead be extremely sparse in the halo outskirts. To find the residual accelerations due exclusively to substructure, I subtract the accelerations due to a smooth host potential (accounting for the fraction of the potential locked-up in substructure mass). The final accelerations are missing contributions from surrounding cosmology, but this is a minor inaccuracy.

I plot the resulting acceleration fields in Figure 9. In descending rows I have added increasing levels of noise drawn from a Normal distribution, which is intended to simulate instrumental uncertainty. Different cosmologies are shown in each column. The acceleration fields show that tracer particles experience higher accelerations around subhaloes, with the heightened accelerations never exceeding $10^{-12}\,\mathrm{m/s^2}$ when averaged over the plotting resolution ($\sim 0.64\,\mathrm{kpc}$). Larger subhaloes dominate the acceleration field, but smaller subhaloes in the 'CDM' scenario can still cause significant localised perturbations. The

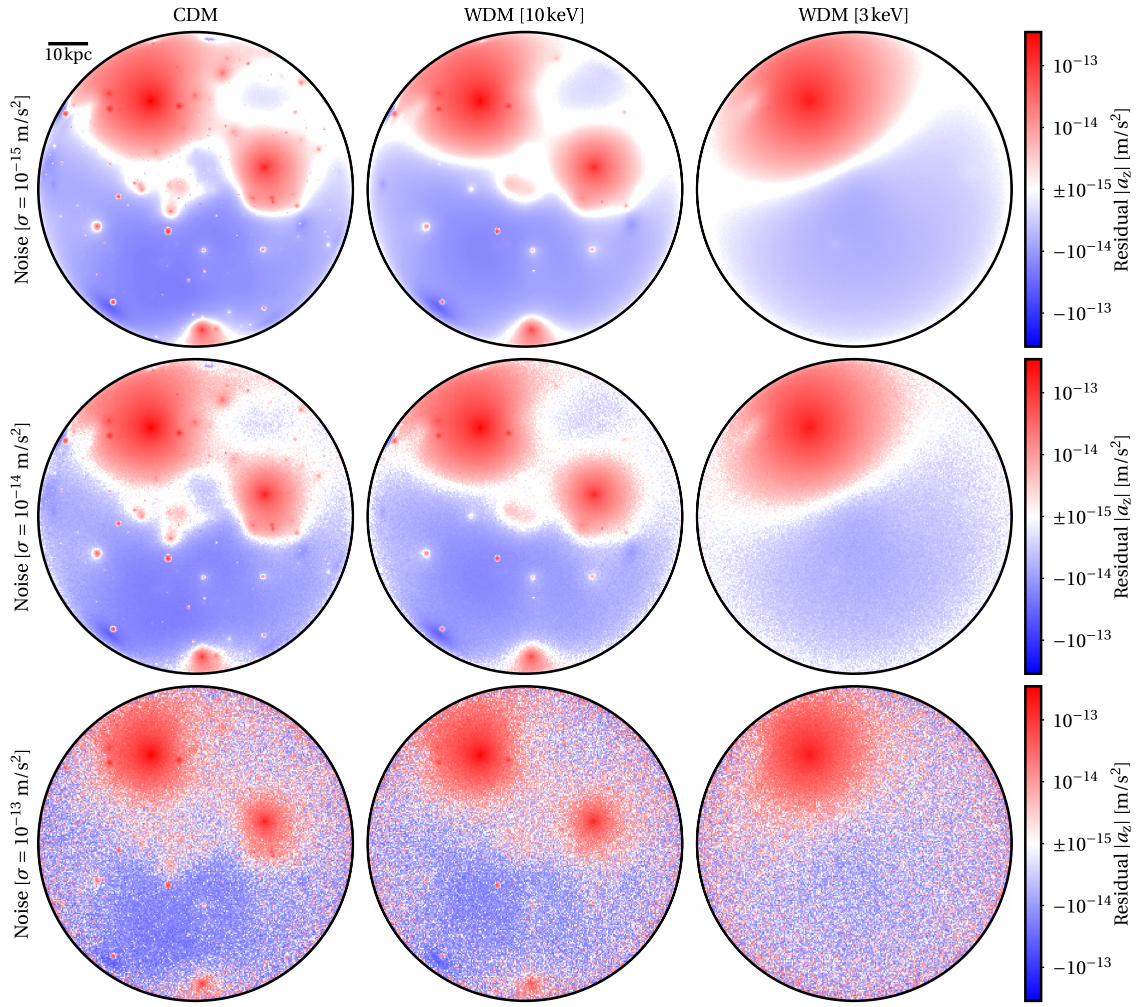

Figure 9: Plots of the uniformly sampled residual z-axis acceleration field for a mock NFW halo out to the r_{200} radius. Each column represents a different cosmology, and each row includes the addition of different Gaussian noise. Each panel has been generated based upon the same random seed. A physical scale has been added to the upper left corner.

prevalence of these smaller subhaloes is diminished for WDM of increasingly light particle mass. Increasing the level of background noise similarly acts to wash-out the acceleration perturbations of substructures.

The contribution from perturbations of different sizes is analysed by way of the power spectrum in Figure 10. The form of the power spectra are near identical for large frequencies ($k < 0.2$) independent of the background noise, but there are some notable differences depending on the chosen cosmology. However, it is important to note that the contribution at large scales becomes dependent on the random seed used for the mock NFW halo. The differences are exaggerated at higher frequencies, with CDM having proportionally more significant power $P(k)$. These distinctions become contaminated by noise at the highest frequencies ($k > 0.6$). For a noise level of $\sigma = 10^{-13}\,\mathrm{m/s^2}$, the power spectra are degenerate for $k > 0.4$.

Assuming data acquisition periods of one decade, current generation spectrographs would not be sensitive enough to perceive the accelerations caused by this substructure (CODEX Pasquini et al., 2008, ESPRESSO Pepe et al., 2021, and Figure 8), and it may

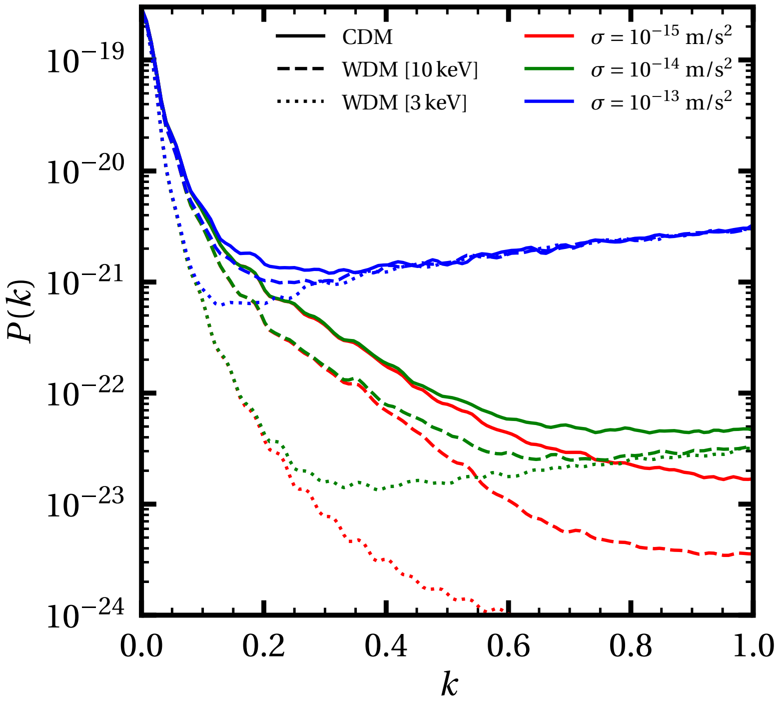

Figure 10: The power spectra for each panel of Figure 9, where the frequency k has been normalised between 0 and 1. A frequency of 0 corresponds to the largest scales ($\sim$ 80 kpc) and 1 to the smallest scales ($\sim$ 0.64 kpc, the resolution provided by the uniform stellar field in this example).

be many decades before such an instrument exists. However, if the DM particle remains undetected via any of the other fundamental forces, measuring these small gravitational accelerations could become the only way to progress our understanding of the nature of DM.

Bibliography

Aarseth S. J., 1999, Publications of the ASP, 111, 1333
Aarseth S. J., 2003, Gravitational N-Body Simulations
Aarseth S. J., Gott, J. R. I., Turner E. L., 1979, ApJ, 228, 664
Abazajian K., Fuller G. M., Tucker W. H., 2001, ApJ, 562, 593
Abazajian K. N., 2019, in Illuminating Dark Matter, Essig R., Feng J., Zurek K., eds., Vol. 56, p. 1
Abel T., Norman M. L., Madau P., 1999, ApJ, 523, 66
Agertz O., Kravtsov A. V., Leitner S. N., Gnedin N. Y., 2013, ApJ, 770, 25
Agertz O. et al., 2020, MNRAS, 491, 1656
Agertz O., Romeo A. B., Grisdale K., 2015, MNRAS, 449, 2156
Aguirre A., Hernquist L., Schaye J., Weinberg D. H., Katz N., Gardner J., 2001, ApJ, 560, 599
Aihara H. et al., 2018, PASJ, 70, S4
Akins H. B., Christensen C. R., Brooks A. M., Munshi F., Applebaum E., Engelhardt A., Chamberland L., 2021, ApJ, 909, 139
Albers S. M. et al., 2019, MNRAS, 490, 5538
Alcock C. et al., 1997, ApJ, 491, 436
Alcock C. et al., 1998, ApJ, 499, L9
Alcock C. et al., 1996, ApJ, 461, 84
Allgood B., Flores R. A., Primack J. R., Kravtsov A. V., Wechsler R. H., Faltenbacher A., Bullock J. S., 2006, MNRAS, 367, 1781
Allison R. J., Goodwin S. P., Parker R. J., de Grijs R., Portegies Zwart S. F., Kouwenhoven M. B. N., 2009, ApJ, 700, L99
Alpher R. A., Bethe H., Gamow G., 1948, Physical Review, 73, 803
Alvey J. et al., 2021, MNRAS, 501, 1188
Amorisco N. C., 2017, ApJ, 844, 64
Amorisco N. C., Agnello A., Evans N. W., 2013, MNRAS, 429, L89
Amorisco N. C., Zavala J., de Boer T. J. L., 2014, ApJ, 782, L39
Anderson M. E., Churazov E., Bregman J. N., 2015, MNRAS, 452, 3905
Angus G. W., Gentile G., Diaferio A., Famaey B., van der Heyden K. J., 2014, MNRAS, 440, 746
ANTARES Collaboration, 2013, , 11, 032
Applebaum E., Brooks A. M., Christensen C. R., Munshi F., Quinn T. R., Shen S., Tremmel M., 2021, ApJ, 906, 96
Applebaum E., Brooks A. M., Quinn T. R., Christensen C. R., 2020, MNRAS, 492, 8
Aubert D. et al., 2018, ApJ, 856, L22
Aubert D., Teyssier R., 2008, MNRAS, 387, 295
Avila-Reese V., Colín P., Valenzuela O., D'Onghia E., Firmani C., 2001, ApJ, 559, 516
Ayromlou M., Nelson D., Yates R. M., Kauffmann G., White S. D. M., 2019, MNRAS, 487, 4313
Babcock H. W., 1939, Lick Observatory Bulletin, 19, 41
Bagla J. S., 2005, Current Science, 88, 1088
Baldassare V. F., Reines A. E., Gallo E., Greene J. E., 2017, ApJ, 836, 20

Banik N., Bovy J., Bertone G., Erkal D., de Boer T. J. L., 2019, arXiv e-prints, arXiv:1911.02663

Banik U., van den Bosch F. C., 2021, arXiv e-prints, arXiv:2103.05004

Bardeen J. M., Bond J. R., Kaiser N., Szalay A. S., 1986, ApJ, 304, 15

Barkana R., Haiman Z., Ostriker J. P., 2001, ApJ, 558, 482

Barkana R., Loeb A., 1999, ApJ, 523, 54

Barnes J., Hut P., 1986, Nature, 324, 446

Barrena R., Biviano A., Ramella M., Falco E. E., Seitz S., 2002, A&A, 386, 816

Barton A., Brandenberger R. H., Lin L., 2015, , 2015, 022

Battaglia G., Helmi A., Tolstoy E., Irwin M., Hill V., Jablonka P., 2008, ApJ, 681, L13

Baumgardt H., Côté P., Hilker M., Rejkuba M., Mieske S., Djorgovski S. G., Stetson P., 2009, MNRAS, 396, 2051

Baumgardt H., Makino J., 2003, MNRAS, 340, 227

Baur J., Palanque-Delabrouille N., Yèche C., Boyarsky A., Ruchayskiy O., Armengaud É., Lesgourgues J., 2017, , 2017, 013

Baur J., Palanque-Delabrouille N., Yèche C., Magneville C., Viel M., 2016, , 2016, 012

Bechtol K. et al., 2015, ApJ, 807, 50

Bédorf J., Portegies Zwart S., 2013, MNRAS, 431, 767

Begeman K. G., 1987, PhD thesis, , Kapteyn Institute, (1987)

Begeman K. G., Broeils A. H., Sanders R. H., 1991, MNRAS, 249, 523

Behroozi P. S., Wechsler R. H., Conroy C., 2013, ApJ, 770, 57

Bekki K., Couch W. J., 2003, ApJ, 596, L13

Bekki K., Forbes D. A., Beasley M. A., Couch W. J., 2002, MNRAS, 335, 1176

Bekki K., Freeman K. C., 2003, MNRAS, 346, L11

Bel J. et al., 2014, A&A, 563, A37

Bellovary J. M., Cleary C. E., Munshi F., Tremmel M., Christensen C. R., Brooks A., Quinn T. R., 2019, MNRAS, 482, 2913

Benítez-Llambay A., Navarro J. F., Abadi M. G., Gottlöber S., Yepes G., Hoffman Y., Steinmetz M., 2015, MNRAS, 450, 4207

Bennett C. L. et al., 2003, ApJS, 148, 97

Benson A. J., Bower R. G., Frenk C. S., Lacey C. G., Baugh C. M., Cole S., 2003, ApJ, 599, 38

Bernadich M. C. i., Pérez de los Heros C., 2019, arXiv e-prints, arXiv:1912.04585

Bertone G., Hooper D., 2018, Reviews of Modern Physics, 90, 045002

Bertone G., Hooper D., Silk J., 2005, Phys. Rep., 405, 279

Bessel F. W., 1844, MNRAS, 6, 136

Bett P., Eke V., Frenk C. S., Jenkins A., Helly J., Navarro J., 2007, MNRAS, 376, 215

Bhattacharjee P., Majumdar P., Biswas S., Joarder P. S., 2019, , 2019, 028

Bialek J. J., Evrard A. E., Mohr J. J., 2001, ApJ, 555, 597

Binney J., 1980, MNRAS, 190, 873

Binney J., de Vaucouleurs G., 1981, MNRAS, 194, 679

Binney J., Tremaine S., 1987, Galactic dynamics

Binney J., Tremaine S., 2008, Galactic Dynamics: Second Edition

Birchall K. L., Watson M. G., Aird J., 2020, MNRAS, 492, 2268

Blake C., Glazebrook K., 2003, ApJ, 594, 665

Blakeslee J. P., Cantiello M., 2018, Research Notes of the American Astronomical Society, 2, 146

Blanton M., 2008, Sdss, "sdss galaxy map.". http://www.sdss.org/science/orangepie/, accessed: 28/01/2021

Blumenthal G. R., Faber S. M., Flores R., Primack J. R., 1986, ApJ, 301, 27

Bode P., Ostriker J. P., Turok N., 2001, ApJ, 556, 93

Boehm C., Schaeffer R., 2005, A&A, 438, 419

Boldrini P., Mohayaee R., Silk J., 2020a, MNRAS, 492, 3169

Boldrini P., Mohayaee R., Silk J., 2020b, arXiv e-prints, arXiv:2002.12192

Boley A. C., Lake G., Read J., Teyssier R., 2009, ApJ, 706, L192

Bolte M., 1989, ApJ, 341, 168

Bond J. R., Efstathiou G., Silk J., 1980, Phys. Rev. Lett., 45, 1980

Bond J. R., Kofman L., Pogosyan D., 1996, Nature, 380, 603

Bondi H., Gold T., 1948, MNRAS, 108, 252

Bonnell I. A., Davies M. B., 1998, MNRAS, 295, 691

Bonnivard V. et al., 2015, MNRAS, 453, 849

Bose S. et al., 2019, MNRAS, 486, 4790

Boyarsky A., Drewes M., Lasserre T., Mertens S., Ruchayskiy O., 2019, Progress in Particle and Nuclear Physics, 104, 1

Boyarsky A., Lesgourgues J., Ruchayskiy O., Viel M., 2009a, , 2009, 012

Boyarsky A., Ruchayskiy O., Iakubovskyi D., Franse J., 2014, Phys. Rev. Lett., 113, 251301

Boyarsky A., Ruchayskiy O., Shaposhnikov M., 2009b, Annual Review of Nuclear and Particle Science, 59, 191

Boylan-Kolchin M., Bullock J. S., Kaplinghat M., 2011, MNRAS, 415, L40

Bradford J. D. et al., 2011, ApJ, 743, 167

Brandt T. D., 2016, ApJ, 824, L31

Bringmann T., Hofmann S., 2007, , 2007, 016

Bromm V., Clarke C. J., 2002, ApJ, 566, L1

Brook C. B., Di Cintio A., 2015, MNRAS, 450, 3920

Brook C. B., Di Cintio A., Knebe A., Gottlöber S., Hoffman Y., Yepes G., Garrison-Kimmel S., 2014, ApJ, 784, L14

Brooks A., 2014, Annalen der Physik, 264, 294

Brooks A. M., 2019, in Illuminating Dark Matter, Essig R., Feng J., Zurek K., eds., Vol. 56, p. 19

Brooks A. M., Kuhlen M., Zolotov A., Hooper D., 2013, ApJ, 765, 22

Brooks A. M., Papastergis E., Christensen C. R., Governato F., Stilp A., Quinn T. R., Wadsley J., 2017, ApJ, 850, 97

Brooks A. M., Zolotov A., 2014, ApJ, 786, 87

Brown T. M. et al., 2014, ApJ, 796, 91

Bruderer C., Read J. I., Coles J. P., Leier D., Falco E. E., Ferreras I., Saha P., 2016, MNRAS, 456, 870

Bulbul E., Markevitch M., Foster A., Smith R. K., Loewenstein M., Randall S. W., 2014, ApJ, 789, 13

Bullock J. S., 2010, ArXiv e-prints

Bullock J. S., Boylan-Kolchin M., 2017, ARA&A, 55, 343

Burbidge E. M., Burbidge G. R., Fowler W. A., Hoyle F., 1957, Reviews of Modern Physics, 29, 547

Cameron A. G. W., 1955, ApJ, 121, 144

Carignan C., Freeman K. C., 1988, ApJ, 332, L33

Carlson E. D., Machacek M. E., Hall L. J., 1992, ApJ, 398, 43

Carroll B. W., Ostlie D. A., 2006, An introduction to modern astrophysics and cosmology. Cambridge University Press

Cataldi P., Pedrosa S. E., Tissera P. B., Artale M. C., 2021, MNRAS, 501, 5679
Cen R., 2001, ApJ, 560, 592
Ceverino D., Klypin A., 2009, ApJ, 695, 292
Chabrier G., 2003, PASP, 115, 763
Chambers K. C. et al., 2016, arXiv e-prints
Chan T. K., Kereš D., Oñorbe J., Hopkins P. F., Muratov A. L., Faucher-Giguère C. A., Quataert E., 2015, MNRAS, 454, 2981
Chandrasekhar S., 1943, ApJ, 97, 255
Chatterjee A., Dayal P., Choudhury T. R., Hutter A., 2019, MNRAS, 487, 3560
Chauhan G., Lagos C. d. P., Obreschkow D., Power C., Oman K., Elahi P. J., 2019, MNRAS, 488, 5898
Choi J.-H., Nagamine K., 2009, MNRAS, 393, 1595
Clementini G., Cignoni M., Contreras Ramos R., Federici L., Ripepi V., Marconi M., Tosi M., Musella I., 2012, ApJ, 756, 108
Clowe D., Bradač M., Gonzalez A. H., Markevitch M., Randall S. W., Jones C., Zaritsky D., 2006, ApJ, 648, L109
Cole D. R., Dehnen W., Read J. I., Wilkinson M. I., 2012, MNRAS, 426, 601
Cole D. R., Dehnen W., Wilkinson M. I., 2011, MNRAS, 416, 1118
Collins M. L. M. et al., 2013, ApJ, 768, 172
Colombi S., 2001, New Astronomy Reviews, 45, 373
Conroy C., Loeb A., Spergel D. N., 2011, ApJ, 741, 72
Contenta F. et al., 2018, MNRAS, 476, 3124
Correa C. A., 2021, MNRAS
Cowan, C. L. J., Reines F., Harrison F. B., Kruse H. W., McGuire A. D., 1956, Science, 124, 103
Crnojevic D., 2020, in American Astronomical Society Meeting Abstracts, Vol. 235, American Astronomical Society Meeting Abstracts #235, p. 207.13
Crnojević D., Sand D. J., Zaritsky D., Spekkens K., Willman B., Hargis J. R., 2016, ApJ, 824, L14
Croft R. A. C., Weinberg D. H., Katz N., Hernquist L., 1998, ApJ, 495, 44
Croton D. J. et al., 2006, MNRAS, 365, 11
Cunningham E. C. et al., 2019, ApJ, 879, 120
Cusano F. et al., 2016, ApJ, 829, 26
Dalla Vecchia C., Schaye J., 2012, MNRAS, 426, 140
Dark Energy Survey Collaboration et al., 2016, MNRAS, 460, 1270
Dashyan G., Silk J., Mamon G. A., Dubois Y., Hartwig T., 2018, MNRAS, 473, 5698
Davis A. J., Khochfar S., Dalla Vecchia C., 2014, MNRAS, 443, 985
Dawoodbhoy T. et al., 2018a, MNRAS, 480, 1740
Dawoodbhoy T. et al., 2018b, MNRAS, 480, 1740
Dawson K. S. et al., 2013, AJ, 145, 10
Debattista V. P., Moore B., Quinn T., Kazantzidis S., Maas R., Mayer L., Read J., Stadel J., 2008, ApJ, 681, 1076
Deg N., Widrow L., 2013, MNRAS, 428, 912
Dehnen W., 1993, MNRAS, 265, 250
Dehnen W., 2014, Computational Astrophysics and Cosmology, 1, 1
Dehnen W., Read J. I., 2011, European Physical Journal Plus, 126, 55
Dekel A., Silk J., 1986, ApJ, 303, 39
Del Popolo A., Pace F., 2016, Ap&SS, 361, 162
della Ceca R., Griffiths R. E., Heckman T. M., MacKenty J. W., 1996, ApJ, 469, 662

Di Cintio A., Brook C. B., Dutton A. A., Macciò A. V., Stinson G. S., Knebe A., 2014a, MNRAS, 441, 2986
Di Cintio A., Brook C. B., Macciò A. V., Stinson G. S., Knebe A., Dutton A. A., Wadsley J., 2014b, MNRAS, 437, 415
Dicke R. H., Peebles P. J. E., Roll P. G., Wilkinson D. T., 1965, ApJ, 142, 414
Diemand J., Kuhlen M., Madau P., 2007, ApJ, 667, 859
Diemand J., Moore B., Stadel J., 2004a, MNRAS, 353, 624
Diemand J., Moore B., Stadel J., 2004b, MNRAS, 352, 535
Diemand J., Moore B., Stadel J., 2005, Nature, 433, 389
Diemand J., Moore B., Stadel J., Kazantzidis S., 2004c, MNRAS, 348, 977
Diemer B., More S., Kravtsov A. V., 2013, ApJ, 766, 25
Dodelson S., 2011, International Journal of Modern Physics D, 20, 2749
Draine B. T., 1978, ApJS, 36, 595
Drewes M., 2013, International Journal of Modern Physics E, 22, 1330019
Drlica-Wagner A. et al., 2020, ApJ, 893, 47
Dubinski J., 1994, ApJ, 431, 617
Dubinski J., Carlberg R. G., 1991, ApJ, 378, 496
Dunkley J. et al., 2009, ApJS, 180, 306
Dutton A. A., Macciò A. V., 2014, MNRAS, 441, 3359
Dutton A. A., Macciò A. V., Buck T., Dixon K. L., Blank M., Obreja A., 2019, MNRAS, 486, 655
Dutton A. A. et al., 2016, MNRAS, 461, 2658
Dyer C. C., Ip P. S. S., 1993, ApJ, 409, 60
Edwards T. D. P., Kavanagh B. J., Visinelli L., Weniger C., 2020, arXiv e-prints, arXiv:2011.05378
Efstathiou G., 1992, MNRAS, 256, 43P
Efstathiou G., 2000, MNRAS, 317, 697
Efstathiou G., Davis M., White S. D. M., Frenk C. S., 1985, ApJS, 57, 241
Eggleton P. P., Fitchett M. J., Tout C. A., 1989, ApJ, 347, 998
Einstein A., de Sitter W., 1932, Proceedings of the National Academy of Science, 18, 213
Eisenstein D. J., Hut P., 1998, ApJ, 498, 137
Eisenstein D. J. et al., 2005, ApJ, 633, 560
El-Badry K., Wetzel A., Geha M., Hopkins P. F., Kereš D., Chan T. K., Faucher-Giguère C.-A., 2016, ApJ, 820, 131
El-Zant A., Shlosman I., Hoffman Y., 2001, Astrophysical Journal, 560, 636
Ellis J., Hagelin J. S., Nanopoulos D. V., Olive K., Srednicki M., 1984, Nuclear Physics B, 238, 453
Emerick A., Mac Low M.-M., Grcevich J., Gatto A., 2016, ApJ, 826, 148
Escala I. et al., 2018, MNRAS, 474, 2194
Evans, Neal J. I., Heiderman A., Vutisalchavakul N., 2014, ApJ, 782, 114
Faber S. M., Gallagher J. S., 1979, ARA&A, 17, 135
Fall S. M., Rees M. J., 1985, ApJ, 298, 18
Fall S. M., Rees M. J., 1988, in The Harlow-Shapley Symposium on Globular Cluster Systems in Galaxies, Grindlay J. E., Philip A. G. D., eds., Vol. 126, pp. 323–330
Famaey B., McGaugh S. S., 2012, Living Reviews in Relativity, 15, 10
Fan X., Narayanan V. K., Strauss M. A., White R. L., Becker R. H., Pentericci L., Rix H.-W., 2002, AJ, 123, 1247
Feldmann R., Faucher-Giguère C.-A., Kereš D., 2019, ApJ, 871, L21

Ferland G. J., Korista K. T., Verner D. A., Ferguson J. W., Kingdon J. B., Verner E. M., 1998, PASP, 110, 761

Ferrara A., Loeb A., 2013, MNRAS, 431, 2826

Ferreira E. G. M., 2020, arXiv e-prints, arXiv:2005.03254

Ferrero I., Abadi M. G., Navarro J. F., Sales L. V., Gurovich S., 2012, MNRAS, 425, 2817

Fielder C. E., Mao Y.-Y., Newman J. A., Zentner A. R., Licquia T. C., 2019, MNRAS, 486, 4545

Fillingham S. P., Cooper M. C., Pace A. B., Boylan-Kolchin M., Bullock J. S., Garrison-Kimmel S., Wheeler C., 2016, MNRAS, 463, 1916

Finlator K., Davé R., 2008, MNRAS, 385, 2181

Fitts A. et al., 2019, MNRAS, 490, 962

Fitts A. et al., 2017, MNRAS, 471, 3547

Fixsen D. J., 2009, ApJ, 707, 916

Flores R. A., Primack J. R., 1994, ApJ, 427, L1

Forbes D. A. et al., 2018, Proceedings of the Royal Society of London Series A, 474, 20170616

Forbes D. A., Brodie J. P., Grillmair C. J., 1997, AJ, 113, 1652

Foreman-Mackey D., Hogg D. W., Lang D., Goodman J., 2013, PASP, 125, 306

Freeman K. C., 1970, ApJ, 160, 811

Frenk C. S., White S. D. M., 2012, Annalen der Physik, 524, 507

Frenk C. S., White S. D. M., Davis M., Efstathiou G., 1988, ApJ, 327, 507

Friedland A., Giannotti M., Wise M., 2013, Phys. Rev. Lett., 110, 061101

Friedmann A., 1999, General Relativity and Gravitation, 31, 1991

Gallart C. et al., 2021a, arXiv e-prints, arXiv:2101.04464

Gallart C. et al., 2021b, ApJ, 909, 192

Ganeshaiah Veena P., Cautun M., van de Weygaert R., Tempel E., Jones B. J. T., Rieder S., Frenk C. S., 2018, MNRAS, 481, 414

Garrison-Kimmel S., Boylan-Kolchin M., Bullock J. S., Lee K., 2014, MNRAS, 438, 2578

Garrison-Kimmel S., Rocha M., Boylan-Kolchin M., Bullock J. S., Lally J., 2013, MNRAS, 433, 3539

Garrison-Kimmel S. et al., 2017, MNRAS, 471, 1709

Garzilli A., Boyarsky A., Ruchayskiy O., 2017, Physics Letters B, 773, 258

Garzilli A., Magalich A., Ruchayskiy O., Boyarsky A., 2021, MNRAS, 502, 2356

Geiger B., Schneider P., 1998, MNRAS, 295, 497

Genina A., Read J. I., Fattahi A., Frenk C. S., 2020a, arXiv e-prints, arXiv:2011.09482

Genina A. et al., 2020b, MNRAS, 498, 144

Gerhard O. E., Binney J., 1985, MNRAS, 216, 467

Geringer-Sameth A., Koushiappas S. M., Walker M. G., Bonnivard V., Combet C., Maurin D., 2018, ArXiv e-prints

Ghigna S., Moore B., Governato F., Lake G., Quinn T., Stadel J., 1998, MNRAS, 300, 146

Gilman D., Birrer S., Nierenberg A., Treu T., Du X., Benson A., 2020, MNRAS, 491, 6077

Gilman D., Birrer S., Treu T., Nierenberg A., Benson A., 2019, MNRAS, 487, 5721

Gnedin N. Y., Abel T., 2001, New Astronomy, 6, 437

Gnedin N. Y., Kravtsov A. V., Chen H.-W., 2008, ApJ, 672, 765

Gnedin N. Y., Ostriker J. P., 1997, ApJ, 486, 581

Gnedin O. Y., Ceverino D., Gnedin N. Y., Klypin A. A., Kravtsov A. V., Levine R., Nagai D., Yepes G., 2011, arXiv e-prints, arXiv:1108.5736

Gnedin O. Y., Hernquist L., Ostriker J. P., 1999, ApJ, 514, 109

Gnedin O. Y., Kravtsov A. V., Klypin A. A., Nagai D., 2004, ApJ, 616, 16
Goerdt T., Moore B., Read J. I., Stadel J., 2010, ApJ, 725, 1707
Goerdt T., Moore B., Read J. I., Stadel J., Zemp M., 2006, MNRAS, 368, 1073
Gonzalez A. H., Sivanandam S., Zabludoff A. I., Zaritsky D., 2013, ApJ, 778, 14
Governato F. et al., 2012, MNRAS, 422, 1231
Grand R. J. J. et al., 2017, MNRAS, 467, 179
Graus A. S., Bullock J. S., Kelley T., Boylan-Kolchin M., Garrison-Kimmel S., Qi Y., 2019, MNRAS, 488, 4585
Grebel E. K., Gallagher, John S. I., Harbeck D., 2003, AJ, 125, 1926
Grisdale K., Agertz O., Renaud F., Romeo A. B., Devriendt J., Slyz A., 2019, MNRAS, 486, 5482
Gualandris A., Read J. I., Dehnen W., Bortolas E., 2017, MNRAS, 464, 2301
Guo Q., White S., Li C., Boylan-Kolchin M., 2010, MNRAS, 404, 1111
Gustafsson M., Fairbairn M., Sommer-Larsen J., 2006, Phys. Rev. D, 74, 123522
Haardt F., Madau P., 1996, ApJ, 461, 20
Hagmann C. et al., 1998, Phys. Rev. Lett., 80, 2043
Hahn O., Abel T., 2011, MNRAS, 415, 2101
Harvey D., Massey R., Kitching T., Taylor A., Tittley E., 2015, Science, 347, 1462
Haslbauer M., Dabringhausen J., Kroupa P., Javanmardi B., Banik I., 2019, Astronomy and Astrophysics, 626, A47
Hausammann L., Revaz Y., Jablonka P., 2019, A&A, 624, A11
Hayashi E., Navarro J. F., Springel V., 2007, MNRAS, 377, 50
Heggie D. C., 1979, MNRAS, 76, 525
Heggie D. C., Hut P., 1996, in Dynamical Evolution of Star Clusters: Confrontation of Theory and Observations, Hut P., Makino J., eds., Vol. 174, p. 303
Helmi A., 2004, ApJ, 610, L97
Henderson B., Bekki K., 2016, ApJ, 822, L33
Hernquist L., 1990, ApJ, 356, 359
Hernquist L., Katz N., Weinberg D. H., Miralda-Escudé J., 1996, ApJ, 457, L51
Hezaveh Y. D. et al., 2016, ApJ, 823, 37
Hilker M., Richtler T., 2000, A&A, 362, 895
Hills J. G., 1980, ApJ, 235, 986
Hinshaw G. et al., 2009, ApJS, 180, 225
Hirtenstein J. et al., 2019, ApJ, 880, 54
Hockney R. W., Eastwood J. W., 1981, Computer Simulation Using Particles
Hoekstra H., Yee H. K. C., Gladders M. D., 2004, ApJ, 606, 67
Hoffman Y., Ribak E., 1991, ApJ, 380, L5
Hofmann S., Schwarz D. J., Stöcker H., 2001, Phys. Rev. D, 64, 083507
Hogan C. J., Dalcanton J. J., 2000, Phys. Rev. D, 62, 063511
Hogan C. J., Rees M. J., 1988, Physics Letters B, 205, 228
Hook A., Kahn Y., Safdi B. R., Sun Z., 2018, Phys. Rev. Lett., 121, 241102
Hopkins P. F., Kereš D., Oñorbe J., Faucher-Giguère C.-A., Quataert E., Murray N., Bullock J. S., 2014, MNRAS, 445, 581
Hoyle F., 1948, MNRAS, 108, 372
Hsueh J. W., Enzi W., Vegetti S., Auger M. W., Fassnacht C. D., Despali G., Koopmans L. V. E., McKean J. P., 2020, MNRAS, 492, 3047
Hubble E., 1929, Proceedings of the National Academy of Science, 15, 168
Hunter D. R., 2014, , 2014, 023

Hurley J. R., 2008, in Lecture Notes in Physics, Berlin Springer Verlag, Vol. 760, The Cambridge N-Body Lectures, Aarseth S. J., Tout C. A., Mardling R. A., eds., p. 283

Hurley J. R., Pols O. R., Tout C. A., 2000, MNRAS, 315, 543

Hurley J. R., Tout C. A., Pols O. R., 2002, MNRAS, 329, 897

Ibata R., Lewis G. F., Irwin M., Totten E., Quinn T., 2001, ApJ, 551, 294

Ibata R., Nipoti C., Sollima A., Bellazzini M., Chapman S. C., Dalessandro E., 2013a, MNRAS, 428, 3648

Ibata R., Sollima A., Nipoti C., Bellazzini M., Chapman S. C., Dalessandro E., 2011, ApJ, 738, 186

Ibata R. A. et al., 2013b, Nature, 493, 62

Inoue S., 2009, MNRAS, 397, 709

Iocco F., Mangano G., Miele G., Pisanti O., Serpico P. D., 2009, Phys. Rep., 472, 1

Iršič V. et al., 2017, Phys. Rev. D, 96, 023522

Irwin M. J. et al., 2007, ApJ, 656, L13

Islam T., Dutta K., 2019, Phys. Rev. D, 100, 104049

Jackson D. C., Skillman E. D., Cannon J. M., Côté S., 2004, AJ, 128, 1219

Jackson D. C., Skillman E. D., Gehrz R. D., Polomski E., Woodward C. E., 2007, ApJ, 656, 818

Janesh W., Rhode K. L., Salzer J. J., Janowiecki S., Adams E. A. K., Haynes M. P., Giovanelli R., Cannon J. M., 2019, AJ, 157, 183

Jeon M., Besla G., Bromm V., 2017, ApJ, 848, 85

Jeon M., Bromm V., Pawlik A. H., Milosavljević M., 2015, MNRAS, 452, 1152

Jesseit R., Naab T., Burkert A., 2002, ApJ, 571, L89

Jethwa P., Erkal D., Belokurov V., 2018, MNRAS, 473, 2060

Jing Y., Wang C., Li R., Liao S., Wang J., Guo Q., Gao L., 2019, Monthly Notices of the Royal Astronomical Society, 488, 3298

Jing Y. P., Suto Y., 2002, ApJ, 574, 538

Johnston K. V., Spergel D. N., Hernquist L., 1995, ApJ, 451, 598

Jowett Chan H. Y., Ferreira E. G. M., Hayashi K., 2021, arXiv e-prints, arXiv:2102.05300

Kang H., Shapiro P. R., Fall S. M., Rees M. J., 1990, ApJ, 363, 488

Kaplinghat M., Tulin S., Yu H.-B., 2016, Phys. Rev. Lett., 116, 041302

Karachentsev I. D., Kaisina E. I., Makarov D. I., 2018, MNRAS, 479, 4136

Kato K., Mori M., Ogiya G., 2016, in IAU Symposium, Vol. 317, The General Assembly of Galaxy Halos: Structure, Origin and Evolution, Bragaglia A., Arnaboldi M., Rejkuba M., Romano D., eds., pp. 312–313

Katz N., 1991, ApJ, 368, 325

Katz N., 1992, ApJ, 391, 502

Katz N., Gunn J. E., 1991, ApJ, 377, 365

Katz N., Quinn T., Bertschinger E., Gelb J. M., 1994, MNRAS, 270, L71

Katz N., White S. D. M., 1993, ApJ, 412, 455

Kauffmann G., 2014, MNRAS, 441, 2717

Kauffmann G., White S. D. M., Guiderdoni B., 1993, MNRAS, 264, 201

Kaur K., Sridhar S., 2018, ApJ, 868, 134

Kavanagh B. J., Edwards T. D. P., Visinelli L., Weniger C., 2020, arXiv e-prints, arXiv:2011.05377

Kaviraj S. et al., 2017, MNRAS, 467, 4739

Kazantzidis S., Abadi M. G., Navarro J. F., 2010, ApJ, 720, L62

Keating L. C., Weinberger L. H., Kulkarni G., Haehnelt M. G., Chardin J., Aubert D., 2020, MNRAS, 491, 1736

Kent S. M., 1986, AJ, 91, 1301
Kepley A. A., Wilcots E. M., Hunter D. A., Nordgren T., 2007, AJ, 133, 2242
Kim C.-G., Ostriker E. C., 2015, ApJ, 802, 99
Kim S. Y., Peter A. H. G., Hargis J. R., 2018, Phys. Rev. Lett., 121, 211302
Kimm T., Cen R., Devriendt J., Dubois Y., Slyz A., 2015, MNRAS, 451, 2900
Kirby E. N., Bullock J. S., Boylan-Kolchin M., Kaplinghat M., Cohen J. G., 2014, MNRAS, 439, 1015
Kirby E. N., Cohen J. G., Guhathakurta P., Cheng L., Bullock J. S., Gallazzi A., 2013, ApJ, 779, 102
Klypin A., Karachentsev I., Makarov D., Nasonova O., 2015, MNRAS, 454, 1798
Klypin A., Kravtsov A. V., Valenzuela O., Prada F., 1999, ApJ, 522, 82
Klypin A. A., Trujillo-Gomez S., Primack J., 2011, ApJ, 740, 102
Knollmann S. R., Knebe A., 2009, ApJS, 182, 608
Kodama H., Sasaki M., 1984, Progress of Theoretical Physics Supplement, 78, 1
Kolb E. W., Tkachev I. I., 1993, Phys. Rev. Lett., 71, 3051
Komatsu E. et al., 2011, ApJS, 192, 18
Koposov S. E., Belokurov V., Torrealba G., Evans N. W., 2015, ApJ, 805, 130
Kormendy J., 1985, ApJ, 295, 73
Krauss L. M., Srednicki M., Wilczek F., 1986, Phys. Rev. D, 33, 2079
Kronberger T., Kapferer W., Ferrari C., Unterguggenberger S., Schindler S., 2008, A&A, 481, 337
Kroupa P., 2001, MNRAS, 322, 231
Kroupa P., Theis C., Boily C. M., 2005, A&A, 431, 517
Krumholz M. R., Federrath C., 2019, Frontiers in Astronomy and Space Sciences, 6, 7
Kuhlen M., Vogelsberger M., Angulo R., 2012, Physics of the Dark Universe, 1, 50
Kundic T., Ostriker J. P., 1995, ApJ, 438, 702
Kunkel W. E., Demers S., Dickens R. J., Perry J. E., Smith F. G., King I. R., 1976, Royal Greenwich Observatory Bulletins, 182, 241
Küpper A. H. W., Kroupa P., Baumgardt H., Heggie D. C., 2010, MNRAS, 401, 105
Küpper A. H. W., Maschberger T., Kroupa P., Baumgardt H., 2011, MNRAS, 417, 2300
Kuzio de Naray R., Kaufmann T., 2011, MNRAS, 414, 3617
Lada C. J., Lombardi M., Alves J. F., 2010, ApJ, 724, 687
Lake G., 1990, Nature, 346, 39
Laporte C. F. P., Agnello A., Navarro J. F., 2019, Monthly Notices of the Royal Astronomical Society, 484, 245
Laporte C. F. P., Penarrubia J., 2015, MNRAS, 449, L90
Larson R. B., 1974, MNRAS, 169, 229
Leaman R. et al., 2012, ApJ, 750, 33
Lee J., Yepes G., 2016, ApJ, 832, 185
Leitherer C. et al., 1999, ApJS, 123, 3
Lemaître G., 1927, Annales de la Société Scientifique de Bruxelles, 47, 49
Lemons S. M., Reines A. E., Plotkin R. M., Gallo E., Greene J. E., 2015, ApJ, 805, 12
Lemze D. et al., 2012, ApJ, 752, 141
Lesgourgues J., Pastor S., 2006, Phys. Rep., 429, 307
Leung G. Y. C., Leaman R., Battaglia G., van de Ven G., Brooks A. M., Peñarrubia J., Venn K. A., 2021, MNRAS, 500, 410
Leung G. Y. C., Leaman R., van de Ven G., Battaglia G., 2019, MNRAS, 3112
Leung G. Y. C., Leaman R., van de Ven G., Battaglia G., 2020, MNRAS, 493, 320
Li P., Wang H., Mo H. J., Wang E., Hong H., 2020, ApJ, 902, 75

Li T. S. et al., 2017, ApJ, 838, 8
Li Y., Mo H. J., van den Bosch F. C., Lin W. P., 2007, MNRAS, 379, 689
Lightman A. P., Fall S. M., 1978, ApJ, 221, 567
Limousin M., Kneib J.-P., Natarajan P., 2005, MNRAS, 356, 309
Lin D. N. C., Faber S. M., 1983, ApJ, 266, L21
Lo K. Y., Sargent W. L. W., Young K., 1993, AJ, 106, 507
Loebman S. R. et al., 2018, ApJ, 853, 196
Łokas E. L., Mamon G. A., 2003, MNRAS, 343, 401
Lovell M. R., Hellwing W., Ludlow A., Zavala J., Robertson A., Fattahi A., Frenk C. S., Hardwick J., 2020, MNRAS, 498, 702
Lux H., Read J. I., Lake G., 2010, MNRAS, 406, 2312
Lux H., Read J. I., Lake G., Johnston K. V., 2012, MNRAS, 424, L16
Lynden-Bell D., 1976, MNRAS, 174, 695
Lynds C. R., Sandage A. R., 1963, ApJ, 137, 1005
Lynds R., 1971, ApJ, 164, L73
Lynn B. W., Nelson A. E., Tetradis N., 1990, Nuclear Physics B, 345, 186
Ma X., Hopkins P. F., Kasen D., Quataert E., Faucher-Giguère C.-A., Kereš D., Murray N., Strom A., 2016, MNRAS, 459, 3614
Ma X., Quataert E., Wetzel A., Faucher-Giguère C.-A., Boylan-Kolchin M., 2020, arXiv e-prints, arXiv:2006.10065
Macciò A. V., Dutton A. A., van den Bosch F. C., 2008, MNRAS, 391, 1940
Macciò A. V., Frings J., Buck T., Penzo C., Dutton A. A., Blank M., Obreja A., 2017, MNRAS, 472, 2356
Macciò A. V., Paduroiu S., Anderhalden D., Schneider A., Moore B., 2012, MNRAS, 424, 1105
Madau P., 2017, ApJ, 851, 50
Madau P., Ferrara A., Rees M. J., 2001, ApJ, 555, 92
Madau P., Haardt F., Rees M. J., 1999, ApJ, 514, 648
Madau P., Shen S., Governato F., 2014, ApJ, 789, L17
Malhan K., Valluri M., Freese K., 2020, MNRAS
Marcolini A., Brighenti F., D'Ercole A., 2003, MNRAS, 345, 1329
Marinacci F., Vogelsberger M., 2016, MNRAS, 456, L69
Martel H., Shapiro P. R., 1998, MNRAS, 297, 467
Martin N. F., Collins M. L. M., Longeard N., Tollerud E., 2018, ApJ, 859, L5
Martin N. F., de Jong J. T. A., Rix H.-W., 2008, ApJ, 684, 1075
Martin N. F. et al., 2016, ApJ, 833, 167
Mashchenko S., Couchman H. M. P., Wadsley J., 2006, Nature, 442, 539
Mashchenko S., Sills A., 2005a, ApJ, 619, 243
Mashchenko S., Sills A., 2005b, ApJ, 619, 258
Mashchenko S., Wadsley J., Couchman H. M. P., 2008, Science, 319, 174
Massey R., Kitching T., Richard J., 2010, Reports on Progress in Physics, 73, 086901
Mateo M. L., 1998, ARA&A, 36, 435
Maxwell A. J., Wadsley J., Couchman H. M. P., 2015, ApJ, 806, 229
Mayer L., Mastropietro C., Wadsley J., Stadel J., Moore B., 2006, MNRAS, 369, 1021
McConnachie A. W., 2012, AJ, 144, 4
McGaugh S. S., Rubin V. C., de Blok W. J. G., 2001, AJ, 122, 2381
McNamara B. R. et al., 2006, ApJ, 648, 164
McQuinn K. B. W. et al., 2015, ApJ, 812, 158
Meiksin A. A., 2009, Reviews of Modern Physics, 81, 1405

Meneghetti M., Yoshida N., Bartelmann M., Moscardini L., Springel V., Tormen G., White S. D. M., 2001, MNRAS, 325, 435
Merrifield M. R., Kent S. M., 1990, AJ, 99, 1548
Merritt D., Valluri M., 1999, AJ, 118, 1177
Mesinger A., Perna R., Haiman Z., 2005, ApJ, 623, 1
Meurer G. R., Freeman K. C., Dopita M. A., Cacciari C., 1992, AJ, 103, 60
Mezcua M., Civano F., Marchesi S., Suh H., Fabbiano G., Volonteri M., 2018, MNRAS, 478, 2576
Mihalas D., Mihalas B. W., 1984, Foundations of radiation hydrodynamics
Mihos J. C., Hernquist L., 1994, ApJ, 437, 611
Milgrom M., 1983, ApJ, 270, 365
Milgrom M., 2020, Studies in the History and Philosophy of Modern Physics, 71, 170
Miller G. E., Scalo J. M., 1979, ApJS, 41, 513
Mo H. J., Mao S., 2004, MNRAS, 353, 829
Mocz P. et al., 2019, Phys. Rev. Lett., 123, 141301
Mohapatra R. N., Senjanovic G., 1980, Phys. Rev. Lett., 44, 912
Moore B., 1994, Nature, 370, 629
Moore B., 1996, ApJ, 461, L13
Moore B., Ghigna S., Governato F., Lake G., Quinn T., Stadel J., Tozzi P., 1999, ApJ, 524, L19
Moore B., Governato F., Quinn T., Stadel J., Lake G., 1998, ApJ, 499, L5
Moore B., Kazantzidis S., Diemand J., Stadel J., 2004, MNRAS, 354, 522
More S., Diemer B., Kravtsov A. V., 2015, ApJ, 810, 36
Moscardini L., Matarrese S., Lucchin F., Messina A., 1991, MNRAS, 248, 424
Moster B. P., Naab T., White S. D. M., 2013, MNRAS, 428, 3121
Moster B. P., Somerville R. S., Maulbetsch C., van den Bosch F. C., Macciò A. V., Naab T., Oser L., 2010, ApJ, 710, 903
Muñoz R. R., Padmanabhan N., Geha M., 2012, ApJ, 745, 127
Muanwong O., Thomas P. A., Kay S. T., Pearce F. R., 2002, MNRAS, 336, 527
Mukhanov V. F., Feldman H. A., Brandenberger R. H., 1992, Phys. Rep., 215, 203
Müller O., Pawlowski M. S., Jerjen H., Lelli F., 2018, Science, 359, 534
Munshi F., Brooks A., Applebaum E., Christensen C., Sligh J. P., Quinn T., 2021, arXiv e-prints, arXiv:2101.05822
Munshi F., Brooks A. M., Applebaum E., Weisz D. R., Governato F., Quinn T. R., 2017, arXiv e-prints, arXiv:1705.06286
Munshi F., Brooks A. M., Christensen C., Applebaum E., Holley-Bockelmann K., Quinn T. R., Wadsley J., 2019, ApJ, 874, 40
Munshi F. et al., 2013, ApJ, 766, 56
Murgia R., Iršič V., Viel M., 2018, Phys. Rev. D, 98, 083540
Murgia R., Merle A., Viel M., Totzauer M., Schneider A., 2017, , 2017, 046
Naab T., Johansson P. H., Ostriker J. P., 2009, ApJ, 699, L178
Nadler E. O. et al., 2021, Phys. Rev. Lett., 126, 091101
Nadler E. O. et al., 2020, ApJ, 893, 48
Nasim I., Gualandris A., Read J., Dehnen W., Delorme M., Antonini F., 2020, MNRAS
Nasim I. T., Gualandris A., Read J. I., Antonini F., Dehnen W., Delorme M., 2021, Monthly Notices of the Royal Astronomical Society, stab435
Natarajan P., Zhao H., 2008, MNRAS, 389, 250
Navarro J. F., Eke V. R., Frenk C. S., 1996a, MNRAS, 283, L72
Navarro J. F., Frenk C. S., White S. D. M., 1996b, ApJ, 462, 563

Navarro J. F., Frenk C. S., White S. D. M., 1997, ApJ, 490, 493

Navarro J. F., White S. D. M., 1993, MNRAS, 265, 271

Navarro J. F., White S. D. M., 1994, MNRAS, 267, 401

Newville M., Stensitzki T., Allen D. B., Ingargiola A., 2014, LMFIT: Non-Linear Least-Square Minimization and Curve-Fitting for Python

Nicastro F. et al., 2018, Nature, 558, 406

Niederste-Ostholt M., Belokurov V., Evans N. W., 2012, MNRAS, 422, 207

Nightingale J. W., Massey R. J., Harvey D. R., Cooper A. P., Etherington A., Tam S.-I., Hayes R. G., 2019, MNRAS, 489, 2049

Nipoti C., Binney J., 2015, MNRAS, 446, 1820

Nishikawa H., Boddy K. K., Kaplinghat M., 2020, Phys. Rev. D, 101, 063009

Nitadori K., Aarseth S. J., 2012, MNRAS, 424, 545

Nuñez-Castiñeyra A., Nezri E., Bertin V., 2019, , 2019, 043

Oñorbe J., Boylan-Kolchin M., Bullock J. S., Hopkins P. F., Kereš D., Faucher-Giguère C.-A., Quataert E., Murray N., 2015, MNRAS, 454, 2092

Oñorbe J., Garrison-Kimmel S., Maller A. H., Bullock J. S., Rocha M., Hahn O., 2014, MNRAS, 437, 1894

Oñorbe J., Hennawi J. F., Lukić Z., 2017, ApJ, 837, 106

O'Brien J. C., Freeman K. C., van der Kruit P. C., 2010, A&A, 515, A63

Ogiya G., Burkert A., 2015, MNRAS, 446, 2363

Oh K. S., Lin D. N. C., Richer H. B., 2000, ApJ, 531, 727

Oka A., Saito S., Nishimichi T., Taruya A., Yamamoto K., 2014, MNRAS, 439, 2515

Okamoto T., Frenk C. S., 2009, MNRAS, 399, L174

Olling R. P., van Gorkom J. H., 1995, in American Institute of Physics Conference Series, Vol. 336, Dark Matter, Holt S. S., Bennett C. L., eds., pp. 121–124

Oman K. A. et al., 2015, MNRAS, 452, 3650

Oman K. A., Navarro J. F., Sales L. V., Fattahi A., Frenk C. S., Sawala T., Schaller M., White S. D. M., 2016, MNRAS, 460, 3610

Omukai K., 2000, ApJ, 534, 809

Omukai K., 2001, Ap&SS, 276, 807

Oort J. H., 1940, ApJ, 91, 273

Orkney M. D. A., Read J. I., Petts J. A., Gieles M., 2019, MNRAS, 488, 2977

Orkney M. D. A. et al., 2021a, arXiv e-prints, arXiv:2101.02688

Orkney M. D. A. et al., 2021b, arXiv e-prints, arXiv:2101.02688

Ostriker J. P., Peebles P. J. E., Yahil A., 1974, ApJ, 193, L1

Ott J., Walter F., Brinks E., Van Dyk S. D., Dirsch B., Klein U., 2001, AJ, 122, 3070

Paardekooper J.-P., Khochfar S., Dalla Vecchia C., 2015, MNRAS, 451, 2544

Padilla N. D., Strauss M. A., 2008, MNRAS, 388, 1321

Pal P. B., Wolfenstein L., 1982, Phys. Rev. D, 25, 766

Papastergis E., Giovanelli R., Haynes M. P., Shankar F., 2015, A&A, 574, A113

Papastergis E., Shankar F., 2016, A&A, 591, A58

Pardo K. et al., 2016, ApJ, 831, 203

Pardo K., Spergel D. N., 2020, Phys. Rev. Lett., 125, 211101

Pasquini L. et al., 2008, in Society of Photo-Optical Instrumentation Engineers (SPIE) Conference Series, Vol. 7014, Ground-based and Airborne Instrumentation for Astronomy II, McLean I. S., Casali M. M., eds., p. 70141I

Pato M., Agertz O., Bertone G., Moore B., Teyssier R., 2010, Phys. Rev. D, 82, 023531

Pavlidou V., Tomaras T. N., 2014, , 2014, 020

Pawlowski M. S., Kroupa P., 2020, MNRAS, 491, 3042

Pawlowski M. S., Pflamm-Altenburg J., Kroupa P., 2012, MNRAS, 423, 1109
Peñarrubia J., Pontzen A., Walker M. G., Koposov S. E., 2012, ApJ, 759, L42
Peccei R. D., 1999, Nuclear Physics B Proceedings Supplements, 72, 3
Peccei R. D., Quinn H. R., 1977a, Phys. Rev. D, 16, 1791
Peccei R. D., Quinn H. R., 1977b, Phys. Rev. Lett., 38, 1440
Peebles P. J. E., 1982, ApJ, 263, L1
Peebles P. J. E., 1984, ApJ, 277, 470
Peebles P. J. E., Dicke R. H., 1968, ApJ, 154, 891
Peeples M. S., Shankar F., 2011, MNRAS, 417, 2962
Penzias A. A., Wilson R. W., 1965, ApJ, 142, 419
Pepe F. et al., 2021, A&A, 645, A96
Peter A., 2001, Living Reviews in Relativity, 4, 2
Peters S. P. C., van der Kruit P. C., Allen R. J., Freeman K. C., 2017, MNRAS, 464, 65
Petkova M., Springel V., 2009, MNRAS, 396, 1383
Petts J. A., Gualandris A., Read J. I., 2015, MNRAS, 454, 3778
Petts J. A., Read J. I., Gualandris A., 2016, MNRAS, 463, 858
Pineda J. C. B., Hayward C. C., Springel V., Mendes de Oliveira C., 2017, MNRAS, 466, 63
Planck Collaboration et al., 2016a, A&A, 596, A108
Planck Collaboration et al., 2014, A&A, 571, A16
Planck Collaboration et al., 2016b, A&A, 594, A13
Plummer H. C., 1911, MNRAS, 71, 460
Pontzen A., Governato F., 2012, MNRAS, 421, 3464
Pontzen A., Governato F., 2014, Nature, 506, 171
Pontzen A., Rey M. P., Cadiou C., Agertz O., Teyssier R., Read J., Orkney M. D. A., 2020, MNRAS
Pontzen A., Rey M. P., Cadiou C., Agertz O., Teyssier R., Read J., Orkney M. D. A., 2021a, MNRAS, 501, 1755
Pontzen A., Rey M. P., Cadiou C., Agertz O., Teyssier R., Read J., Orkney M. D. A., 2021b, MNRAS, 501, 1755
Pontzen A., Roškar R., Stinson G. S., Woods R., Reed D. M., Coles J., Quinn T. R., 2013, pynbody: Astrophysics Simulation Analysis for Python. Astrophysics Source Code Library, ascl:1305.002
Pontzen A., Tremmel M., 2018a, ApJS, 237, 23
Pontzen A., Tremmel M., 2018b, ApJS, 237, 23
Posti L., Helmi A., 2019, A&A, 621, A56
Power C., Navarro J. F., Jenkins A., Frenk C. S., White S. D. M., Springel V., Stadel J., Quinn T., 2003, MNRAS, 338, 14
Preskill J., Wise M. B., Wilczek F., 1983, Physics Letters B, 120, 127
Press W. H., Schechter P., 1974, ApJ, 187, 425
Press W. H., Spergel D. N., 1985, ApJ, 296, 679
Press W. H., Teukolsky S. A., Vetterling W. T., Flannery B. P., 1992, Numerical recipes in C. The art of scientific computing
Pshirkov M. S., Popov S. B., 2009, Soviet Journal of Experimental and Theoretical Physics, 108, 384
Puchwein E., Springel V., 2013, MNRAS, 428, 2966
Raffelt G. G., Dearborn D. S. P., 1987, Phys. Rev. D, 36, 2211
Raiteri C. M., Villata M., Navarro J. F., 1996, A&A, 315, 105

Randall S. W., Markevitch M., Clowe D., Gonzalez A. H., Bradač M., 2008, ApJ, 679, 1173

Read J. I., Agertz O., Collins M. L. M., 2016a, MNRAS, 459, 2573

Read J. I., Erkal D., 2019, MNRAS, 487, 5799

Read J. I., Gilmore G., 2005, MNRAS, 356, 107

Read J. I., Goerdt T., Moore B., Pontzen A. P., Stadel J., Lake G., 2006a, MNRAS, 373, 1451

Read J. I., Iorio G., Agertz O., Fraternali F., 2016b, MNRAS, 462, 3628

Read J. I., Iorio G., Agertz O., Fraternali F., 2017, MNRAS, 467, 2019

Read J. I., Lake G., Agertz O., Debattista V. P., 2008, MNRAS, 389, 1041

Read J. I., Steger P., 2017, MNRAS, 471, 4541

Read J. I., Walker M. G., Steger P., 2018, MNRAS, 481, 860

Read J. I., Walker M. G., Steger P., 2019a, MNRAS, 484, 1401

Read J. I., Walker M. G., Steger P., 2019b, MNRAS, 484, 1401

Read J. I., Wilkinson M. I., Evans N. W., Gilmore G., Kleyna J. T., 2006b, MNRAS, 367, 387

Read J. I., Wilkinson M. I., Evans N. W., Gilmore G., Kleyna J. T., 2006c, MNRAS, 366, 429

Recchi S., Kroupa P., Ploeckinger S., 2015, MNRAS, 450, 2367

Renaud F., Agertz O., Gieles M., 2017, MNRAS, 465, 3622

Revaz Y., Jablonka P., 2018, A&A, 616, A96

Rey M. P., Pontzen A., 2018, MNRAS, 474, 45

Rey M. P., Pontzen A., Agertz O., Orkney M. D. A., Read J. I., Rosdahl J., 2020, MNRAS, 497, 1508

Rey M. P., Pontzen A., Agertz O., Orkney M. D. A., Read J. I., Saintonge A., Pedersen C., 2019, ApJ, 886, L3

Rhee G., Valenzuela O., Klypin A., Holtzman J., Moorthy B., 2004, ApJ, 617, 1059

Richardson J. C. et al., 2011, ApJ, 732, 76

Richardson T., Fairbairn M., 2014, MNRAS, 441, 1584

Richer M., McCall M. L., Stasińska G., 1998, A&A, 340, 67

Ricotti M., 2002, MNRAS, 336, L33

Ricotti M., Gnedin N. Y., 2005, ApJ, 629, 259

Ricotti M., Parry O. H., Gnedin N. Y., 2016, ApJ, 831, 204

Rieder M., Teyssier R., 2017, MNRAS, 471, 2674

Rodriguez-Gomez V. et al., 2015, MNRAS, 449, 49

Rodriguez Wimberly M. K., Cooper M. C., Fillingham S. P., Boylan-Kolchin M., Bullock J. S., Garrison-Kimmel S., 2019a, MNRAS, 483, 4031

Rodriguez Wimberly M. K., Cooper M. C., Fillingham S. P., Boylan-Kolchin M., Bullock J. S., Garrison-Kimmel S., 2019b, MNRAS, 483, 4031

Rogers K. K., Peiris H. V., 2021, Phys. Rev. Lett., 126, 071302

Romano-Díaz E., Shlosman I., Heller C., Hoffman Y., 2009, ApJ, 702, 1250

Rosen A., Bregman J. N., 1995, ApJ, 440, 634

Roth N., Pontzen A., Peiris H. V., 2016, MNRAS, 455, 974

Rubin V. C., 1983, Scientific American, 248, 96

Rubin V. C., Burstein D., Ford, Jr. W. K., Thonnard N., 1985, ApJ, 289, 81

Rubin V. C., Ford, W. Kent J., 1970, ApJ, 159, 379

Salpeter E. E., 1955, ApJ, 121, 161

Saltzman J., 1994, Journal of Computational Physics, 115, 153

Salvadori S., Ferrara A., 2009, MNRAS, 395, L6

Sameie O., Yu H.-B., Sales L. V., Vogelsberger M., Zavala J., 2020, Phys. Rev. Lett., 124, 141102
Sand D. J., Treu T., Ellis R. S., 2002, ApJ, 574, L129
Sandage A., Binggeli B., 1984, AJ, 89, 919
Sanders J. L., Evans N. W., Dehnen W., 2018, MNRAS, 478, 3879
Schaller M., Dalla Vecchia C., Schaye J., Bower R. G., Theuns T., Crain R. A., Furlong M., McCarthy I. G., 2015, MNRAS, 454, 2277
Schive H.-Y., Chiueh T., Broadhurst T., 2014a, Nature Physics, 10, 496
Schive H.-Y., Chiueh T., Broadhurst T., 2020, Phys. Rev. Lett., 124, 201301
Schive H.-Y., Liao M.-H., Woo T.-P., Wong S.-K., Chiueh T., Broadhurst T., Hwang W. Y. P., 2014b, Phys. Rev. Lett., 113, 261302
Schmidt M., 1959, ApJ, 129, 243
Schneider A., Smith R. E., Macciò A. V., Moore B., 2012, MNRAS, 424, 684
Schramm D. N., Turner M. S., 1998, Reviews of Modern Physics, 70, 303
Seiler J., Hutter A., Sinha M., Croton D., 2019, MNRAS, 1578
Shanks T. et al., 2015, MNRAS, 451, 4238
Shao S., Cautun M., Frenk C. S., Grand R. J. J., Gómez F. A., Marinacci F., Simpson C. M., 2018, MNRAS, 476, 1796
Shi Y., Zhang Z.-Y., Wang J., Chen J., Gu Q., Yu X., Li S., 2021, arXiv e-prints, arXiv:2101.01282
Sikivie P., 1983, Phys. Rev. Lett., 51, 1415
Silk J., 2017, ApJ, 839, L13
Silk J., Olive K., Srednicki M., 1985, Phys. Rev. Lett., 55, 257
Silverwood H., Easther R., 2019, Publ. Astron. Soc. Aus., 36, e038
Simon J. D., 2019, ARA&A, 57, 375
Simon J. D. et al., 2021a, ApJ, 908, 18
Simon J. D. et al., 2021b, ApJ, 908, 18
Simon J. D., Geha M., 2007, ApJ, 670, 313
Sitwell M., Mesinger A., Ma Y.-Z., Sigurdson K., 2014, MNRAS, 438, 2664
Skordis C., Zlosnik T., 2020, arXiv e-prints, arXiv:2007.00082
Slosar A., Melchiorri A., Silk J. I., 2005, Phys. Rev. D, 72, 101301
Smith M. C., Sijacki D., Shen S., 2018, MNRAS, 478, 302
Smoot G. F. et al., 1992, ApJ, 396, L1
Snaith O. N., Bailin J., Knebe A., Stinson G., Wadsley J., Couchman H., 2017, MNRAS, 472, 2694
Sparre M., Hansen S. H., 2012, , 10, 049
Sparre M., Hayward C. C., Feldmann R., Faucher-Giguère C.-A., Muratov A. L., Kereš D., Hopkins P. F., 2017, MNRAS, 466, 88
Spergel D. N., Steinhardt P. J., 2000, Phys. Rev. Lett., 84, 3760
Springel V., 2000, MNRAS, 312, 859
Springel V., Frenk C. S., White S. D. M., 2006, Nature, 440, 1137
Springel V., Hernquist L., 2002, MNRAS, 333, 649
Springel V. et al., 2008, MNRAS, 391, 1685
Springel V., White S. D. M., Hernquist L., 2004, in IAU Symposium, Vol. 220, Dark Matter in Galaxies, Ryder S., Pisano D., Walker M., Freeman K., eds., p. 421
Steenbeck M., Krause F., Rädler K. H., 1966, Zeitschrift Naturforschung Teil A, 21, 369
Steigman G., 2007, Annual Review of Nuclear and Particle Science, 57, 463
Stewart K. R., Bullock J. S., Barton E. J., Wechsler R. H., 2009, ApJ, 702, 1005
Steyrleithner P., Hensler G., Boselli A., 2020, MNRAS, 494, 1114

Stinson G., Seth A., Katz N., Wadsley J., Governato F., Quinn T., 2006, MNRAS, 373, 1074

Stopyra S., Pontzen A., Peiris H., Roth N., Rey M. P., 2021a, ApJS, 252, 28

Stopyra S., Pontzen A., Peiris H., Roth N., Rey M. P., 2021b, ApJS, 252, 28

Strigari L. E., Frenk C. S., White S. D. M., 2017, ApJ, 838, 123

Su K.-Y. et al., 2021, arXiv e-prints, arXiv:2102.02206

Tanaka M., Chiba M., Hayashi K., Komiyama Y., Okamoto T., Cooper A. P., Okamoto S., Spitler L., 2018, ApJ, 865, 125

Tegmark M. et al., 2006, Phys. Rev. D, 74, 123507

Teyssier R., 2002, A&A, 385, 337

Teyssier R., Pontzen A., Dubois Y., Read J. I., 2013, MNRAS, 429, 3068

Thacker R. J., Couchman H. M. P., 2000, ApJ, 545, 728

Theis C., 1998, A&A, 330, 1180

Thomson W., Kelvin B., 2010, Baltimore Lectures on Molecular Dynamics and the Wave Theory of Light. Cambridge University Press

Thoul A. A., Weinberg D. H., 1996, ApJ, 465, 608

Tissera P. B., Dominguez-Tenreiro R., 1998, MNRAS, 297, 177

Tisserand P. et al., 2007, A&A, 469, 387

Tollet E. et al., 2016, MNRAS, 456, 3542

Tomassetti M. et al., 2016, MNRAS, 458, 4477

Tormen G., 1997, MNRAS, 290, 411

Tormen G., Bouchet F. R., White S. D. M., 1997, MNRAS, 286, 865

Tout C. A., Aarseth S. J., Pols O. R., Eggleton P. P., 1997, MNRAS, 291, 732

Tremmel M., Wright A. C., Brooks A. M., Munshi F., Nagai D., Quinn T. R., 2020, MNRAS, 497, 2786

Treu T., 2010, ARA&A, 48, 87

Trujillo-Gomez S., Klypin A., Primack J., Romanowsky A. J., 2011, ApJ, 742, 16

Trujillo-Gomez S., Kruijssen J. M. D., Keller B. W., Reina-Campos M., 2020, arXiv e-prints, arXiv:2010.05930

Tulin S., Yu H.-B., 2018, Phys. Rep., 730, 1

Udry S., Martinet L., 1994, A&A, 281, 314

van Albada T. S., Bahcall J. N., Begeman K., Sancisi R., 1985, ApJ, 295, 305

van Dokkum P., Danieli S., Abraham R., Conroy C., Romanowsky A. J., 2019, The Astrophysical Journal, 874, L5

van Dokkum P. et al., 2018, Nature, 555, 629

van Uitert E., Hoekstra H., Schrabback T., Gilbank D. G., Gladders M. D., Yee H. K. C., 2012, A&A, 545, A71

Vasiliev E., 2018, AGAMA: Action-based galaxy modeling framework

Vegetti S., Koopmans L. V. E., Auger M. W., Treu T., Bolton A. S., 2014, MNRAS, 442, 2017

Vera-Ciro C., Helmi A., 2013, ApJ, 773, L4

Vera-Ciro C. A., Sales L. V., Helmi A., Frenk C. S., Navarro J. F., Springel V., Vogelsberger M., White S. D. M., 2011, MNRAS, 416, 1377

Vikhlinin A., Kravtsov A., Forman W., Jones C., Markevitch M., Murray S. S., Van Speybroeck L., 2006, ApJ, 640, 691

Villaescusa-Navarro F., Dalal N., 2011, , 2011, 024

Vogel J. K. et al., 2013, arXiv e-prints, arXiv:1302.3273

Vogelsberger M. et al., 2014, MNRAS, 444, 1518

Vogelsberger M., Zavala J., 2013, MNRAS, 430, 1722

Volders L. M. J. S., 1959, Bull. Astron. Inst. Netherlands, 14, 323

Wagoner R. V., Fowler W. A., Hoyle F., 1967, ApJ, 148, 3

Walker M. G., Mateo M., Olszewski E. W., Peñarrubia J., Wyn Evans N., Gilmore G., 2009, ApJ, 704, 1274

Walker M. G., Peñarrubia J., 2011, ApJ, 742, 20

Wang J., Bose S., Frenk C. S., Gao L., Jenkins A., Springel V., White S. D. M., 2020, Nature, 585, 39

Wang L., Dutton A. A., Stinson G. S., Macciò A. V., Penzo C., Kang X., Keller B. W., Wadsley J., 2015, MNRAS, 454, 83

Wang W., White S. D. M., Mandelbaum R., Henriques B., Anderson M. E., Han J., 2016, MNRAS, 456, 2301

Warren M. S., Quinn P. J., Salmon J. K., Zurek W. H., 1992, ApJ, 399, 405

Webb J. J., Reina-Campos M., Kruijssen J. M. D., 2019, MNRAS, 486, 5879

Wechsler R. H., Bullock J. S., Primack J. R., Kravtsov A. V., Dekel A., 2002, ApJ, 568, 52

Weijmans A.-M., Krajnović D., van de Ven G., Oosterloo T. A., Morganti R., de Zeeuw P. T., 2008, MNRAS, 383, 1343

Weinberg M. D., 1994, AJ, 108, 1403

Weinberg M. D., Katz N., 2007, MNRAS, 375, 460

Weisz D. R. et al., 2011a, ApJ, 739, 5

Weisz D. R. et al., 2011b, ApJ, 743, 8

Weisz D. R. et al., 2012a, ApJ, 744, 44

Weisz D. R. et al., 2012b, ApJ, 748, 88

Wetzel A. R., Hopkins P. F., Kim J.-h., Faucher-Giguère C.-A., Kereš D., Quataert E., 2016, ApJ, 827, L23

Wetzel A. R., Tollerud E. J., Weisz D. R., 2015, ApJ, 808, L27

Wheeler C., Oñorbe J., Bullock J. S., Boylan-Kolchin M., Elbert O. D., Garrison-Kimmel S., Hopkins P. F., Kereš D., 2015, MNRAS, 453, 1305

White M., Carlstrom J. E., Dragovan M., Holzapfel W. L., 1999, ApJ, 514, 12

White S. D. M., Rees M. J., 1978, MNRAS, 183, 341

Whiting A. B., Irwin M. J., Hau G. K. T., 1997, AJ, 114, 996

Witten E., 1984, Phys. Rev. D, 30, 272

Wolf J., Martinez G. D., Bullock J. S., Kaplinghat M., Geha M., Muñoz R. R., Simon J. D., Avedo F. F., 2010, MNRAS, 406, 1220

Wright A. C., Brooks A. M., Weisz D. R., Christensen C. R., 2019, MNRAS, 482, 1176

Wright A. C., Tremmel M., Brooks A. M., Munshi F., Nagai D., Sharma R. S., Quinn T. R., 2021, MNRAS, 502, 5370

Wu P., Zhang S., Lee C., Primack J., 2018, in American Astronomical Society Meeting Abstracts, Vol. 231, American Astronomical Society Meeting Abstracts #231, p. 356.06

Wu X., McQuinn M., Eisenstein D., 2021, , 2021, 042

Yoo J., Chanamé J., Gould A., 2004, ApJ, 601, 311

York D. G. et al., 2000, AJ, 120, 1579

Young L. M., 2000, AJ, 119, 188

Young P., 1980, ApJ, 242, 1232

Yozin C., Bekki K., 2015, MNRAS, 453, 14

Zait A., Hoffman Y., Shlosman I., 2008, ApJ, 682, 835

Zeldovich I. B., Einasto J., Shandarin S. F., 1982, Nature, 300, 407

Zemp M., Gnedin O. Y., Gnedin N. Y., Kravtsov A. V., 2011, ApJS, 197, 30

Zentner A. R., Bullock J. S., 2003, ApJ, 598, 49

Zentner A. R., Kravtsov A. V., Gnedin O. Y., Klypin A. A., 2005, ApJ, 629, 219
Zhang H. et al., 2019, MNRAS, 484, 5170
Zhao D. H., Mo H. J., Jing Y. P., Börner G., 2003, MNRAS, 339, 12
Zhao H., 1996, MNRAS, 278, 488
Zhu Q., Hernquist L., Marinacci F., Springel V., Li Y., 2017, MNRAS, 466, 3876
Zolotov A. et al., 2015, MNRAS, 450, 2327
Zoutendijk S. L., Brinchmann J., Bouché N. F., den Brok M., Krajnović D., Kuijken K., Maseda M. V., Schaye J., 2021, arXiv e-prints, arXiv:2101.00253
Zwicky F., 1933, Helvetica Physica Acta, 6, 110
Zwicky F., 1937, ApJ, 86, 217